HIGH NUCLEARITY POLYOXOMETALATES AS WATER OXIDATION CATALYSTS: FROM EXPERIMENTS TO THEORY

Joaquín Soriano López

DOCTORAL THESIS

High Nuclearity Polyoxometalates as Water Oxidation Catalysts: From Experiments to Theory

Joaquín Soriano López

Supervised by

Prof. Dr. José Ramón Galán Mascarós

and Prof. Dr. Josep Maria Poblet

Institut Català d'Investigació Química (ICIQ)

Universitat Rovira i Virgili (URV)

Tarragona, March 2016

UNIVERSITAT ROVIRA i VIRGILI

UNIVERSITAT ROVIRA I VIRGILI
HIGH NUCLEARITY POLYOXOMETALATES AS WATER OXIDATION CATALYSTS: FROM EXPERIMENTS TO THEORY
Joaquín Soriano López

Prof. Dr. Josep Maria Poblet i Rius, Tenure Professor of the Physical Chemistry and Inorganic Department of the Universitat Rovira i Virgili (URV), and Prof. Dr. José Ramón Galán Mascarós, Group Leader of the Institute of Chemical Research of Catalonia (ICIQ) and Research Professor of the Catalan Institution for Research and Advances Studies (ICREA),

CERTIFY that the present Doctoral Thesis entitled: **"High Nuclearity Polyoxometalates as Water Oxidation Catalysts: From Experiments to Theory"**, presented by Joaquín Soriano López to receive the PhD degree in Chemistry, has been carried out under our supervision, in the Institute of Chemical Research of Catalonia (ICIQ), and in the Universitat Rovira i Virgili (URV).

Tarragona, 1 February 2016

PhD Thesis supervisors

Prof. Dr. Josep Maria Poblet i Rius

Prof. Dr. José Ramón Galán Mascarós

UNIVERSITAT ROVIRA I VIRGILI
HIGH NUCLEARITY POLYOXOMETALATES AS WATER OXIDATION CATALYSTS: FROM EXPERIMENTS TO THEORY
Joaquín Soriano López

The work performed in the present doctoral thesis has been possible thanks to the funding of:

- Institut Català d'Investigació Química (ICIQ)
- Universitat Rovira i Virgili (URV)
- European Cooperation in Science and Technology (COST)
- Ministerio de Economía y Competitividad: CTQ2012-34088

UNIVERSITAT ROVIRA I VIRGILI
HIGH NUCLEARITY POLYOXOMETALATES AS WATER OXIDATION CATALYSTS: FROM EXPERIMENTS TO THEORY
Joaquín Soriano López

A José Manuel, t'estime, t'estimo, t'estim...

UNIVERSITAT ROVIRA I VIRGILI
HIGH NUCLEARITY POLYOXOMETALATES AS WATER OXIDATION CATALYSTS: FROM EXPERIMENTS TO THEORY
Joaquín Soriano López

«Si la humanidad no es capaz de pensar como especie, si sigue pensando apenas como país, y como clase social, y pensando sólo en lo nuestro, entonces la civilización está condenada.»

—José Mujica

UNIVERSITAT ROVIRA I VIRGILI
HIGH NUCLEARITY POLYOXOMETALATES AS WATER OXIDATION CATALYSTS: FROM EXPERIMENTS TO THEORY
Joaquín Soriano López

Acknowledgements

Als meus supervisors, JR i Poblet, no podria estar més agraït per haver-me donat l'oportunitat de formar part d'aquest projecte del qual em vaig enamorar el primer dia. Gràcies per la vostra paciència i per saber animar-me i motivar-me quan la cosa es complicava. Gràcies per no tractar-me simplement com un estudiant, sino com un company o un amic. Gràcies per tot el que m'heu ensenyat, i per haver-me ajudat a arribar més lluny del que mai haguera imaginat. Espere que això no siga un final, sino un principi de moltes col·laboracions i de molts més bons moments. No menys important ha sigut la inestimable ajuda de Jordi Carbó. Sempre has estat disposat a ajudar-me en tots els dubtes que he tingut i sempre has sabut resoldre'ls. Tots sabem que aquesta tesi també et correspon. A tots tres, moltíssimes gràcies!!!

Thanks to Prof. Greta R. Patzke for giving me the opportunity to carry on part of my research in her laboratory during my stay at the University of Zurich. I also want to thank Prof. Lee Cronin for letting me to work in his group during my stay at the University of Glasgow. I really appreciate your interest in this Thesis and all the nice discussions we had. I have learned a lot of science from you both.

Gràcies als meus companys i companyes de laboratori, tant de l'ICIQ com de la URV. Han sigut molts el moments que em viscut junts al llarg d'aquestos quatre anys que mai oblidaré. Ha estat un plaer treballar i compartir laboratori amb vosaltres.

Als dos manterazos, Nelson i Guillem, més que companys de carrera sou dos grans amics. Per totes les hores d'estudi, de rialles i de plors. Vos estime, manteros. Diuen que els inicis no són fàcils. No és cert si el primer amic que fas a una ciutat nova es diu Jordi Ampurdanés. Gràcies per estar sempre dispost a ajudar-me, sense importar en què. Al meu company de pis Antonio Bazzo, junts ens vam convertir en rockstars, encara que fos per cinc minuts. Als quatre vos reservaré un ministeri a l'illa de Barbados!

A mis padres, porque siempre me han apoyado y me han animado a que siguiera estudiando. Porque nunca han dudado de que lo conseguiría y se han dejado el alma para que llegara hasta aquí. Porque por muchas veces que me cayera ellos han estado a mi lado para levantarme, darme los mejores consejos y guiarme en mi camino. Porque todo lo que soy, todo lo que he sido y todo lo que seré se lo debo a ellos. A mi hermano, mi ojo derecho, mi mejor amigo. Por revolucionar mi mundo desde que naciste. Te he visto crecer y convertirte en un hombre del que no podría estar más orgulloso. Porque pocas personas hay en el mundo que tengan un corazón tan grande como el tuyo. Te quiero con locura y no pasa un día en el que no te eche de menos. Recuerda que pase lo que pase, nunca estarás solo. A mis abuelos José María y Ángeles, todo un ejemplo de lucha, sacrificio y amor. No ha habido muro lo suficientemente alto en esta puta vida que os haya podido parar. No lleváis capa, pero sois mis héroes. A mi abuelo Manolo, por enseñarme a trabajar la tierra, y que para recoger los frutos primero hay que cuidar la siembra. A mi abuela Vicenta, el vacío que dejaste cada día es más grande. Allá donde estés quiero que sepas que te echo mucho de menos y que no te olvido. Muchas gracias por todos tus buenos consejos.

A Dolores, mi amor, por regalarme los mejores años de mi vida. Por hacerme sentir la persona más especial en todo momento y por hacer único cada día que pasamos juntos. Por apoyarme en los buenos momentos, pero sobretodo por apoyarme en los momentos más difíciles. Porque no importa ni el dónde ni el cómo, si es contigo, meu ben, soy feliz.

UNIVERSITAT ROVIRA I VIRGILI
HIGH NUCLEARITY POLYOXOMETALATES AS WATER OXIDATION CATALYSTS: FROM EXPERIMENTS TO THEORY
Joaquín Soriano López

UNIVERSITAT ROVIRA I VIRGILI
HIGH NUCLEARITY POLYOXOMETALATES AS WATER OXIDATION CATALYSTS: FROM EXPERIMENTS TO THEORY
Joaquín Soriano López

Contents

UNIVERSITAT ROVIRA I VIRGILI
HIGH NUCLEARITY POLYOXOMETALATES AS WATER OXIDATION CATALYSTS: FROM EXPERIMENTS TO THEORY
Joaquín Soriano López

List of Publications

The results of this PhD thesis have delivered the following publications:

1. Goberna-Ferrón, S., Soriano-López, J., Galán-Mascarós, J. R., and Nyman, M. Solution Speciation and Stability of Cobalt-Polyoxometalates Water Oxidation Catalysts by X-ray Scattering. *Eur. J. Inorg. Chem.* **2015**, 2833-2840 (2015).

2. Soriano-López, J., Goberna-Ferrón, S., Vigara, L., Carbó, J. J., Poblet, J. M., and Galán-Mascarós, J. R. Cobalt Polyoxometalates as Heterogeneous Water Oxidation Catalysts. *Inorg. Chem.* **52**, 4753-4755 (2013).

3. Goberna-Ferrón, S., Vigara, L., Soriano-López, J., Galán-Mascarós, J. R. Identification of a Nonanuclear $\{Co^{II}_9\}$ Polyoxometalate Cluster as a Homogeneous Catalyst for Water Oxidation. *Inorg. Chem.* **51**, 11707-11715 (2012).

Manuscripts in preparation:

1. Soriano-López, J., Patzke, G. R., Carbó, J. J., Poblet, J. M., and Galán-Mascarós, J. R. Heterogeneous Light-Driven Water Oxidation Catalysis with Cobalt Polyoxometalates.

2. Soriano-López, J., Carbó, J. J., Musaev, D. G., Hill, C. L., Poblet, J. M., and Galán-Mascarós, J. R. Reaction Mechanism of Water Oxidation Catalyzed by Co-Containing Polyoxometalates.

Publications non related with this thesis:

1. Goberna-Ferrón, S., Soriano-López, J., and Galán-Mascarós, J. R. Activity and Stability of the Tetramanganese Polyanion $[Mn_4(H_2O)_2(PW_9O_{34})_2]^{10-}$ during Electrocatalytic Water Oxidation. *Inorganics* **3**, 332-340 (2015).

2. von Allmen, K., Moré, R. Müller, R., Soriano-López, J., Linden, A., and Patzke, G. R. Nickel-Containing Keggin-Type Polyoxometalates as Hydrogen Evolution Catalysts: Photochemical Structure-Activity Relationships. *ChemPlusChem* **80**, 1389-1398 (2015).

3. Goberna-Ferrón, S., Peña, B., Soriano-López, J., Carbó, J. J., Zhao, H., Poblet, J. M., Dunbar, K. R., and Galán-Mascarós, J. R. A Fast Metal-Metal Bonded Water Oxidation Catalyst. *J. Catal.* **315**, 25-32 (2014)

Abbreviations

%yr^{-1}	Percentage per year
η	Overpotential
μ	Micro
ρ	Spin density
Φ	Quantum yield
AC	Amorphous carbon
aq	Aqueous
ATP	Adenosine triphosphate
bpp	Bis(2-pyridyl)-3,5-pyrazolate
bpy	2,2'-bipyridine
CAN	Cerium(IV) ammonium nitrate
CASPT2	Complete active space perturbation theory
CH_2O	Carbohydrate
CoX-C	Cobalt oxide modified carbon paste electrodes
Cp*	Pentamethylcyclopentadienyl
CY	Chemical yield

DFT	Density functional theory
dG	Dried graphene
DLS	Dynamic light scattering
dmiz	1,3-dimethylimidazole
$\mathbf{e^-}$	Electron
E^0	Thermodynamic potential
E	Nerstian potential
ECP	Effective core potential
EDX	Electron dispersive X-ray spectroscopy
EPR	Electron paramagnetic resonance
ES	Earth system
eV	Electronvolt
FTO	Fluorine-doped tin oxide
G20	Group of twenty
GC	Gas chromatography or Glassy carbon electrode
$\mathbf{h\nu}$	Photon of light
$\mathbf{H^+}$	Proton
$\mathbf{H_2bda}$	2,2'-bipyridine-6,6'-dicarboxilyc acid
HEXS	High energy X-ray scattering
HOMO	Highest occupied molecular orbital
ICP-OES	Inductively coupled plasma optical emission spectromety
IR	Infrared spectroscopy
isoq	Isoquinoline
ITO	Indium-doped tin oxide
j	Current density
j_0	Exchange current
L	Ligand
LHCII	Light harvesting complex II
LUMO	Lowest unoccupied molecular orbital

M	Molar or Metal
mA/cm^2	Milliampere per square centimeter
MCN	Mesoporous carbon nitride
Me	Methyl
MJ kg	Megajoules per kilogram
mm	Millimeter
MO$_x$	Metal oxide
MS	Mass spectroscopy
MWCNT	Multiwalled carbon nanotube
NADPH	Reduced pyridine nucleotide
NHE	Normal hydrogen electrode
nm	Nanometer
NMR	Nuclear magnetic resonance
n$_{O2}$	Number of mols of oxygen
n$_{S2O8}$	Number of mols of persulfate
OAc	Acetate
OEC	Oxygen evolving center
OER	Oxygen evolving reaction
PAMAM	Polyamidoamine
PB	Planet boundaries
PBAs	Prussian blue analogues
PCET	Proton-coupled electron transfer
P$_i$	Phosphate
pic	4-picoline
POM	Polyoxometalate
POM-C	Polyoxometalate modified carbon paste electrodes
ppm	Parts-per-million
ppy	2-phenylpyridine
PS	Photosensitizer

PSI	Photosystem I
PSII	Photosystem II
PXRD	Powder X-ray diffraction
Py5	2,6-(bis(bis-2-pyridyl)methoxymethane)pyridine
QM/MM	Quantum mechanics/molecular mechanics
SAXS	Small angle X-ray scattering
SEM	Scanning electron microscopy
$\mathbf{S}_i$	Species i
SPC	Screen-printed carbon
SWCNT	Single-walled carbon nanotube
taml	Tetraamido macrocyclic ligand
TBA	Tetrabutylammonium
terpy	2,2':6,2"-terpyridine
TGA	Thermogravimetry analysis
toe	Tones of oil equivalent
TOF	Turnover frequency
TON	Turnover number
trpy	2,2':6',2"-terpyridine
TW	Terawatt
$\mathbf{TWyr}^{-1}$	Terawatt per year
UV-vis	Ultraviolet-visible spectroscopy
V	Volt
wG	Wet graphene
$\mathbf{Whkg}^{-1}$	Watt-hour per kilogram
$\mathbf{Wkg}^{-1}$	Watt per kilogram
$\mathbf{Wm}^{-2}$	Watts per square meter
WOC	Water oxidation catalyst
XANES	X-ray absorption near edge structure spectroscopy
XPS	X-ray photoelectron spectroscopy

UNIVERSITAT ROVIRA I VIRGILI
HIGH NUCLEARITY POLYOXOMETALATES AS WATER OXIDATION CATALYSTS: FROM EXPERIMENTS TO THEORY
Joaquín Soriano López

UNIVERSITAT ROVIRA I VIRGILI
HIGH NUCLEARITY POLYOXOMETALATES AS WATER OXIDATION CATALYSTS: FROM EXPERIMENTS TO THEORY
Joaquín Soriano López

Chapter 1

General Introduction

UNIVERSITAT ROVIRA I VIRGILI
HIGH NUCLEARITY POLYOXOMETALATES AS WATER OXIDATION CATALYSTS: FROM EXPERIMENTS TO THEORY
Joaquín Soriano López

1.1 Motivation: Global Energy Consumption and Planetary Boundaries

Population growth and living standards are creating an increase on the global energy consumption projected to be at least 2-fold in the following decades relative to the present. The world population in 2001 was close to 6.1 billion, with a projected increase rate of *ca.* 0.9 %yr^{-1}, what means that the population by 2050 will probably reach 9.4 billion. Moreover, the world energy consumption rate is projected to grow by 1.5 %yr^{-1}, from 13.5 terawatt (TW) in 2001 to *ca.* 27 TW by 2050, and *ca.* 43 TW by 2100, in other words, at the end of the century the energy consumption will have been quadrupled. With no doubt meeting this huge demand of energy in a competitive, reliable, clean, and sustainable manner is so far the most important scientific and technical challenge that humanity is facing in the 21st century.[1]

According to European Commission, in 2009 the worldwide gross consumption of energy was 12140.9 tonnes of oil equivalent (toe), which supposes an increase of 21 % with respect the consumption recorded in 2000. In this period of time China's gross inland consumption more than doubled while, on the other hand, the United States together with Japan were the only G20 members that recorded a lower gross inland consumption in 2010 than in 2000.[2]

As shown in Figure 1.1, in 2009 the use of coal and ignite as source of energy supposed the 27.2 % of worldwide gross consumption, a 32.8 % was crude oil and oil products, and a 20.9 % was gas; so thus combined these three fuels accounted for the 80.9 % of global energy consumption. On the contrary nuclear energy, and renewable energies and waste accounted just for a 5.8 % and a 13.3 %, respectively.

Data clearly show the huge dependence of humanity on fossil fuels for energy production. This dependence does not represent an issue in terms of availability of fossil reserves and processability of raw materials at some reasonable cost. Based

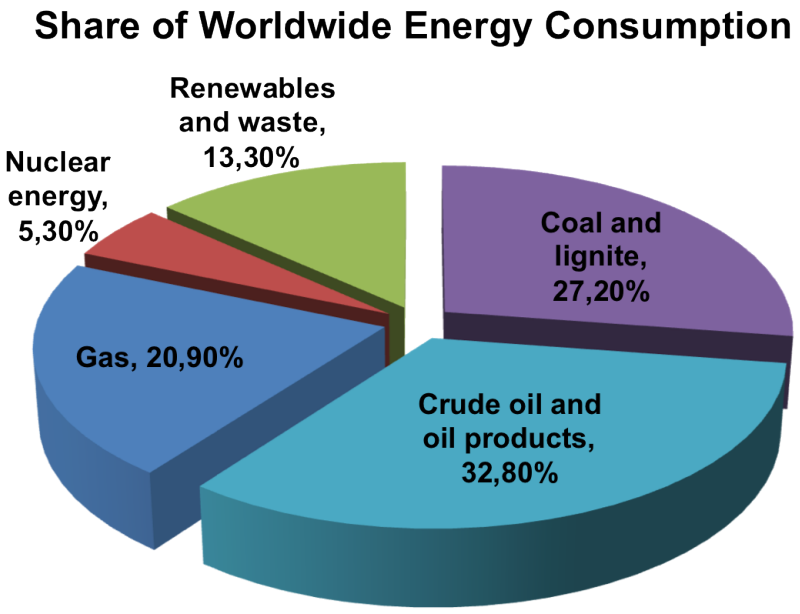

Figure 1.1: Provenance of worldwide energy gross consumption in 2009.[2]

on 1998 consumption rates, availability of oil reserves (including estimated resource base) will exist globally for 50-150 years. Reserves of natural gas will be present for 60-160 years, and between 200-590 years of gas resources. Moreover, a 1000-2000 years supply of coal, shales and tar sands is in the estimated resource base. Therefore, taking into account all the estimated fossil energy resources would support the high energy consumption of 25-30 $TWyr^{-1}$ for at least several centuries.[1] Unfortunately, consumption of fossil fuels is producing a potentially significant global issue, since it leads to carbon emissions in the form of CO_2. The absence of natural mechanisms of CO_2 destruction in the atmosphere causes a concentration increase of this gas, with negative effects not only in human health but also in the resilience of Holocene-like state of the planet, that has been in equilibrium for the last 12000 years. Such state is the only state that we know for certain can support contemporary human societies.[1,3] Therefore, with no active intervention, any environmental effect caused by atmospheric CO_2 accumulation during the next 40-50 years, will remain globally for the next 500-2000 years. Scientific evidences indicate that atmospheric CO_2 concentration during the past 650000 years has kept stable between

210 and 300 ppm, while has been recorded an evident increase during the last 50 years due to anthropogenic CO_2 emissions from fossil fuels consumption, until an excess of 380 ppm.

In this scenario, Rockström and collaborators proposed in 2009, and revised later in 2015, a planetary boundaries (PB) framework in order to prevent a deviation from the Holocene-like state that might cause a destabilization of the Earth system (ES).[3,4] *The planetary boundaries framework defines a safe operating space for humanity based on the intrinsic biophysical process that regulate the stability of the Earth system.* In the PB framework, nine processes that are being modified by human action are studied: Climate change (atmospheric CO_2 concentration, and energy imbalance at top-of-atmosphere), Biosphere integrity (extinction rate, and functional diversity), Land-system change (area of forested land), Freshwater use, Biogeochemical flows (phosphorous and nitrogen flows), Ocean acidification (carbonate ion concentration), Atmospheric aerosol loading, Stratospheric ozone depletion, and introduction of Novel entities (Figure 1.2).

Climate change and biosphere integrity are recognized as "core" boundaries due to their capacity of driving the ES into a new state of uncertainty stability. Figure 1.2 shows that some of the boundaries are already transgressed, as in the case of biogeochemical flows (*i.e.*, phosphorous, and nitrogen cycles), and genetic diversity, while land-system change and climate change are found in the zone of uncertainty with an increasing risk of regime shifts. These data should alert the society that it is time to react to avoid the change to an uncomfortable system much less hospitable to the development of human societies.

Proposed boundaries on climate change are an atmospheric CO_2 concentration of 350 ppm, and an energy imbalance at top-of-atmosphere of $+1.0$ Wm^{-2} relative to preindustrial levels. Current values for the control variables show that the atmospheric CO_2 concentration in 2014 was 399 ppm, and in 2011 the energy imbalance at top-of-atmosphere was $+2.3$ Wm^{-2} relative to 1750. Evidence of these high lev-

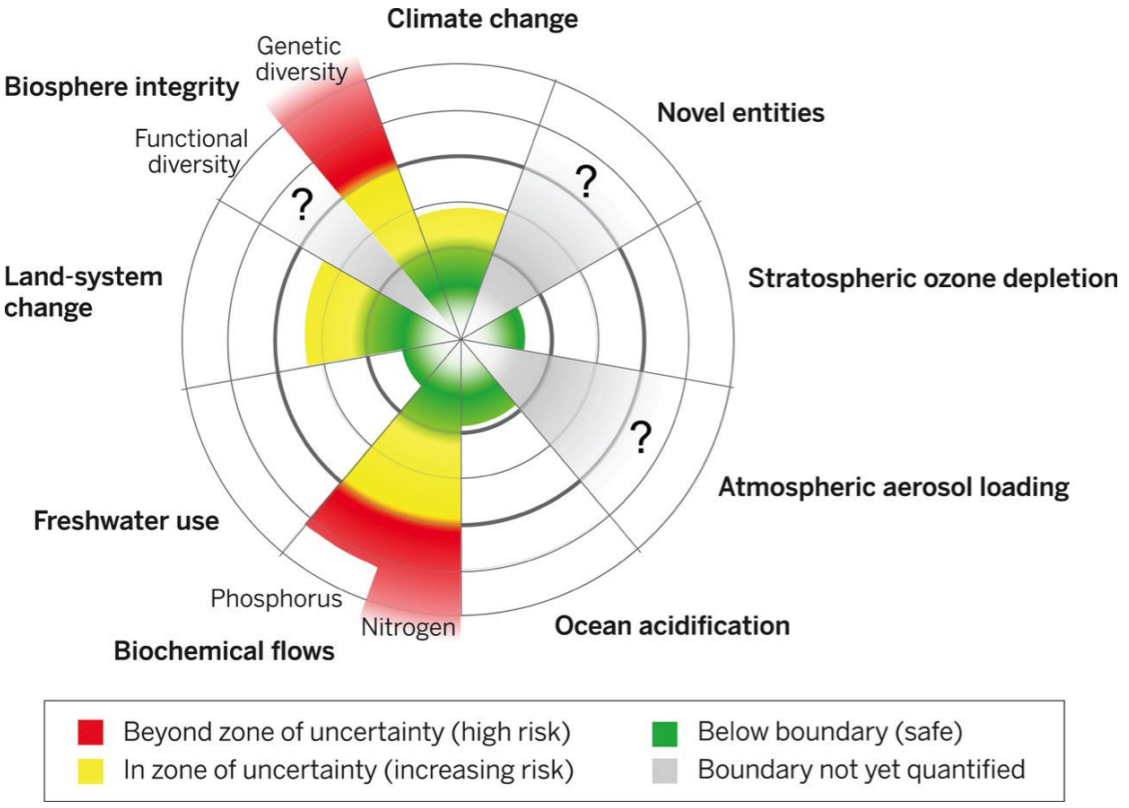

Figure 1.2: Current status of the control variables for seven of the planetary boundaries. The green zone is the safe operating space, the yellow represents the zone of uncertainty (increasing risk), and the red is a high-risk zone.[3]

els have been observed in climate change, as there is an obvious global increase in the intensity, frequency, and duration of heat waves, the number of heavy rainfall events in many regions, changes in atmospheric circulation patterns, and the rate of combined mass loss from the Greenland and Antarctic ice sheets.[3]

Given the problem that humanity is about to deal, it is of imperious importance the invention, development, and deployment of carbon-neutral energy sources and technology. The most prominent renewable energies are hydroelectric, geothermal, wind, tides, ocean thermal energy conversion, and solar. Being the latter the most exploitable resource, due to it is clean, abundant, economically affordable, and the only one with sufficient capacity to produce energy for all the planet.[1,5,6]

1.2 The Use of Solar Energy

All the energy consumed by humans in an entire year corresponds to the solar energy that reaches Earth in one hour. This fact makes sunlight the most promising carbon-neutral energy source for the future, as solar radiation is available at any location on the surface of the Earth. Regardless of location, the maximum power density of sunlight on Earth is *ca.* 1000 watts per square meter. The solar source is commonly described in terms of insolation, *i.e.* the energy available per unit of area and per unit of time, such a kilowatt-hours per square meter a year. Depending on location, the annual insolation can vary over the Earth by a factor of 3, as an example in northern Scandinavia and Canada the insolation is about 800 kilowatt-hours per square meter a year, on the contrary a maximum of 2500 kilowatt-hours per square meter a year can be reached in some dry desert areas.[7]

On this regard, it is well documented that solar energy has the sufficient potential to supply current and projected energy consumption in the next century. The use of solar energy as primary energy source requires three factors that will determine the extent to which it is used in the longer run: (i) capture and conversion of the energy contained in solar photons; (ii) solar energy storage; and (iii) cost-effective implementation into the global energy markets.[5,7,8] Capture and conversion of solar photons is accomplished by photovoltaics, which generally cannot compete with conventional power plants in grid-connected applications. Photovoltaic electricity production costs vary between $0.3-1.5 a kilowatt-hour, depending on solar insolation, turnkey costs, depreciation periods, and interest rate. Under favorable conditions and at favorable sites, the lowest cost figure may come down to $0.05-0.06 a kilowatt-hour.[7]

It is necessary a robust, and cost-effective storage system to convert solar energy in the primary energy source for society. There are different technologies and methods for solar energy storage, distinguished by the time scales on which en-

ergy is stored and their intrinsic power and energy densities. These methods are of four forms: (i) chemical energy (batteries or fuels), (ii) thermal energy (concentrated solar thermal, geothermal), (iii) potential energy (pumped-hydroelectric, compressed-air, electric charge in super/ultra capacitors), and (iv) kinetic energy (flywheels). Among these methods, chemical fuels have the highest energy density (Figure 1.3). This characteristic of chemical fuels is reflected in a rapid adoption of solar-derived chemical fuels of current prevalent technologies and infrastructures.[5,8]

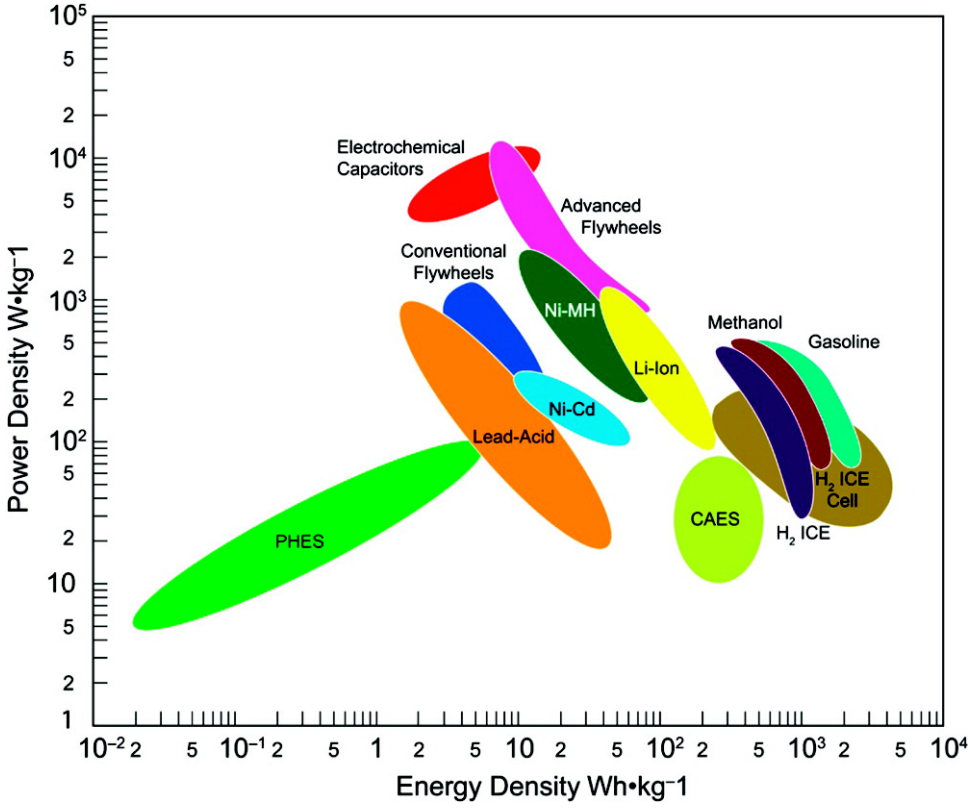

Figure 1.3: Ragone plot of specific power density versus energy density of various storage methods.[5]

A sustainable solution to small-scale distributed energy storage are chemical fuels, due to their high energy densities through the storage of electrons in the small volume of a two-electron bond between light elements (*i.e.*, C−H, N−H, and H−H bonds). At this point, it is important to compare the energy densities offered by these three (hydrocarbon, nitrogen and hydrogen) fuels as a function of weight and volume,

so thus: (i) hydrogen (H_2) has the largest energy density by mass (143 MJ kg) but suffers in volumetric energy density because it is a gas, (ii) nitrogen-based fuels have modestly high energy content by mass and volume, and (iii) hydrocarbon fuels provide the optimum energy supply in terms of volumetric energy density. This latter point, along with the economic availability of fossil fuels, provides the basis for the choice of hydrocarbon-based fuels as the energy currency of modern society. Changing the view of chemical fuels from carbon-based energy source to renewable energy storage, is a challenge that our society is facing nowadays.

UNIVERSITAT ROVIRA I VIRGILI
HIGH NUCLEARITY POLYOXOMETALATES AS WATER OXIDATION CATALYSTS: FROM EXPERIMENTS TO THEORY
Joaquín Soriano López

1.3 Natural Photosynthesis

Evolution over billions of years from primitive non-oxygenic-evolving photosynthetic organisms to advanced eukaryotic life forms is one of the key steps in the development of life on Earth.[9] The overall equation of oxygenic photosynthesis is given in Eq. 1.1, where (CH_2O) represents carbohydrate.[10] The aim of artificial photosynthesis is to reproduce at large scale the processes of oxygen-evolving photosynthesis that take place in higher green plants, cyanobacteria, and algae. Therefore it is of interest the understanding of the reaction mechanisms present in natural photosynthesis for developing technologies for fuel production directly powered by solar energy.[11]

$$CO_2 + H_2O \xrightarrow{h\nu} (CH_2O) + O_2 \tag{1.1}$$

Natural photosynthesis process is splitted in two different stages, known as "light" and "dark" reactions. In the first one, antenna molecules, such a chlorophylls placed in the cell membrane (thylakoid), harvest the light energy, which is driven to the reaction center, where charge separation takes place. At this point electrochemical reactions start generating two energy-rich compounds: adenosine triphosphate (ATP), and reduced pyridine nucleotide (NADPH). During this process oxygen is produced as byproduct and released to the atmosphere (Eq. 1.2). These firsts steps serve essentially to convert the trapped light energy into electrical energy stored in cell membranes. In this light reaction two different photosystems operate in serie to photochemically "charge" the membrane, the so-called photosystem I (PSI), and photosystem II (PSII).[10,12,13] In the dark reactions, carbon dioxide is reduced to form carbohydrates (sugars) using the ATP and the NADPH produced in the light stage. The reaction employs the enzyme Rubisco to catalyze the carboxilation of ribulose diphosphate. This process is of high importance for the progressive formation of sugars molecules from carbon dioxide and water.[13]

$$2H_2O + 2\ plastoquinones + 4H^+_{stroma} \xrightarrow{h\nu} O_2 + 4H^+_{lumen} + 2\ plastoquinols \quad (1.2)$$

Therefore, PSI and PSII, together with cytochrome b_6f are involved in the primary transduction of light energy to electrical energy, and generate an electron flux and an associated electrochemical gradient across the thylakoid membrane. The source of the electrons comes from the water oxidation reaction to molecular oxygen, that occurs within the oxygen-evolving complex (OEC) located in PSII (Figure 1.4).[14]

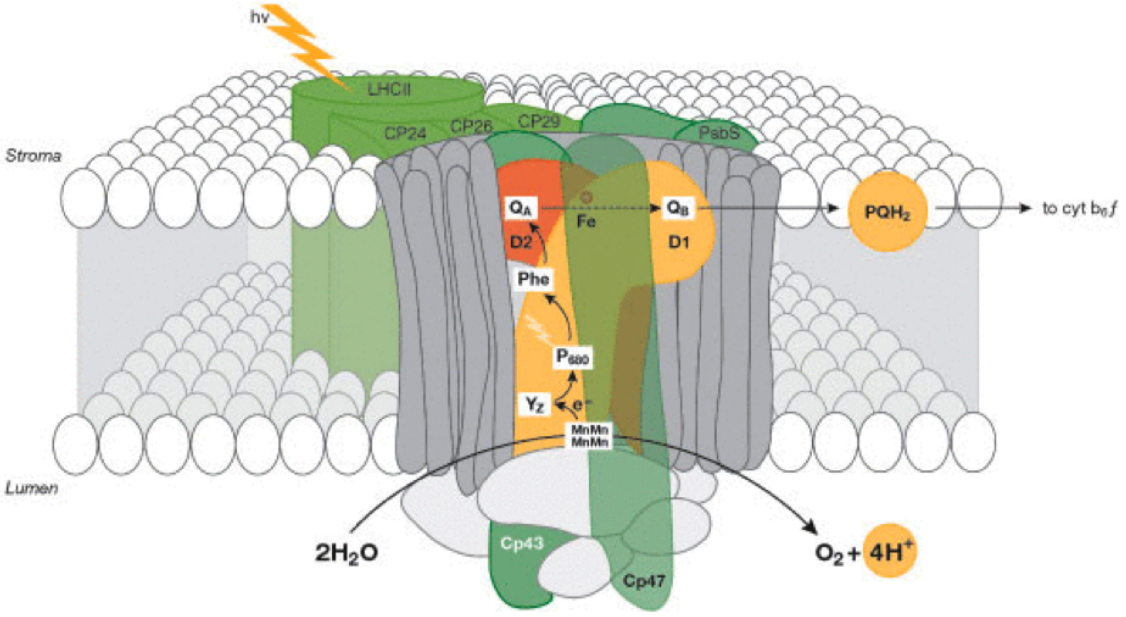

Figure 1.4: Organization of photosystem II and light-harvesting complex II in the thylakoid membrane. Cp43, Cp47: internal antenna chlorophyll-protein complexes. D1, D2: main components of reaction centers with binding sites for electron acceptor quinones (Q_B, Q_A). P_{680}: chlorophyll special pair. Other cofactors associated with D1/D2: pheophytin (Phe), non-haem iron (Fe), Mn-cluster. Accessory chlorophylls and β-carotene are not shown. Chl, chlorophyll; PQH_2, plastoquinone pool; cyt b_6f, cytochrome b_6f complex; Y_Z, D1-Tyr161.[15]

The water oxidation process starts when light is harvested by the photosynthetic pigments (chlorophylls and carotenoids) present in the light-harvesting complex II (LHCII). Light energy is converted then into electric energy and rapidly transferred to the reaction center (P_{680}), resulting in its oxidation to the cation radical P_{680}^{+} and the reduction of a pheophytin molecule, producing a charge separation. The P_{680} state is recovered by a rapid electron injection from tyrosine 161, Y_Z, placed on the D1 peptide, which is an oxidizable protein side-chain intermediate that stabilizes the charge separation. The ultimate source of electrons comes from the oxidation of water to molecular oxygen within the OEC.[10,13]

The structure of the OEC from cyanobacterial PSII was solved recently employing crystallographic techniques.[16] It consists in a Mn_4CaO_5 cluster with a cubane-like structure formed by three manganese, one calcium, and four oxygen atoms placed in the corners, with the oxygen atoms serving as oxo bridges linking the metal atoms. The fourth manganese atom is placed outside the cluster, linked to two manganeses within the cubane by one vertex oxygen and the fifth oxygen *via* a di-μ-oxo bridge (Fig. 1.5). In addition, four water molecules are associated to the Mn_4CaO_5 cluster, of which two of them are coordinated to the calcium atom, and the other two are coordinated to the manganese atom placed outside the cubane structure. A significant structural feature of the cluster is its distorted chair form caused by the existence of the calcium atom within the cubane-like structure. This distortion may be important for elucidating the mechanism of the water-splitting reaction.

The water oxidation catalysis performed within the OEC is the most energetically demanding reaction performed by nature. Working close to the thermodynamic limit under mild temperature and pH conditions, it requires a redox potential of at least 0.8 V vs NHE (herein all potentials will be referenced to the normal hydrogen electrode, unless otherwise noted), with a maximum turnover rate of *ca.* 10^3 s^{-1}, for the reaction $2H_2O \longrightarrow O_2 + 4H^+ + 4e^-$. The water oxidation mechanism in PSII, known as Kok cycle (Fig. 1.6), proceeds *via* four sequential one-electron transfer

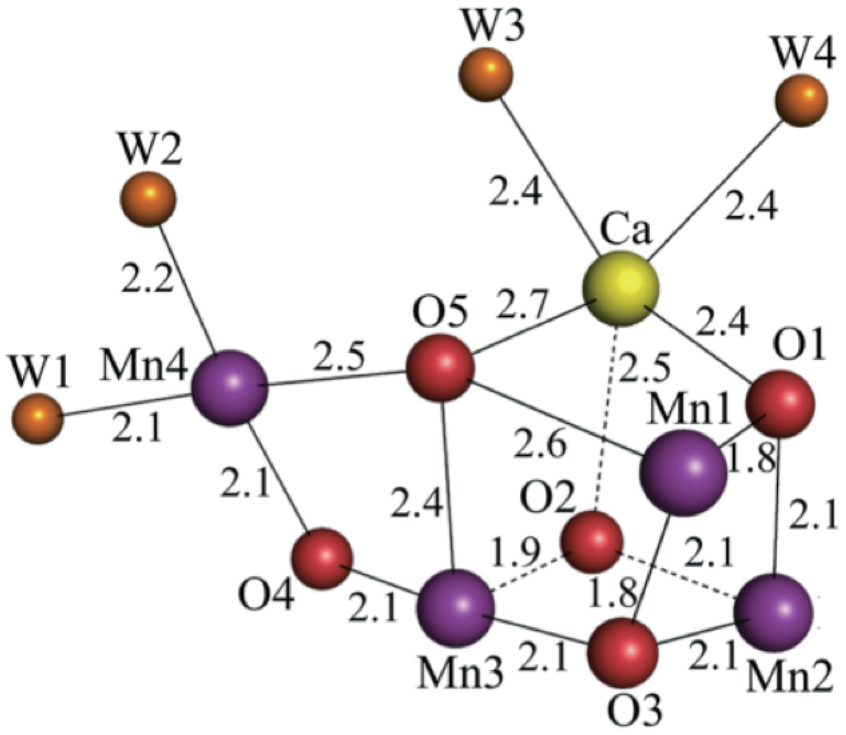

Figure 1.5: Structure of the Mn_4CaO_5. Distances (in ångströms) between metal atoms and oxo bridges or water molecules.[16]

driven upon the oxidation of P_{680} to the cation radical P_{680}^+ produced thanks to the successive absorption of four photons. This cation radical P_{680}^+ is the strongest known biological oxidizing agent with a redox potential of 1.26 V. Four electrons are sequentially subtracted, together with four protons, process known as proton-coupled electron transfer (PCET), from the lowest state (S_0) progressively to reach the S_4 state, where oxygen is evolved and the initial S_0 state is spontaneously recovered. The protein environment adjusts the proton chemical potential to the OEC catalytic sites and the resting state of the PSII is the S_1 state, with one electron extracted from the OEC, stabilized by proton release. During the S-cycle the release of protons into the protein environment keeps the charge neutrality during the electron transfer events.[11,17] The OEC and surrounding structures are damaged as a consequence of the highly energetic reactions carried out during the Kok cycle. These molecules are restored *via* sophisticated self-repair mechanisms, without them

the OEC would degrade in about 30 minutes.[18]

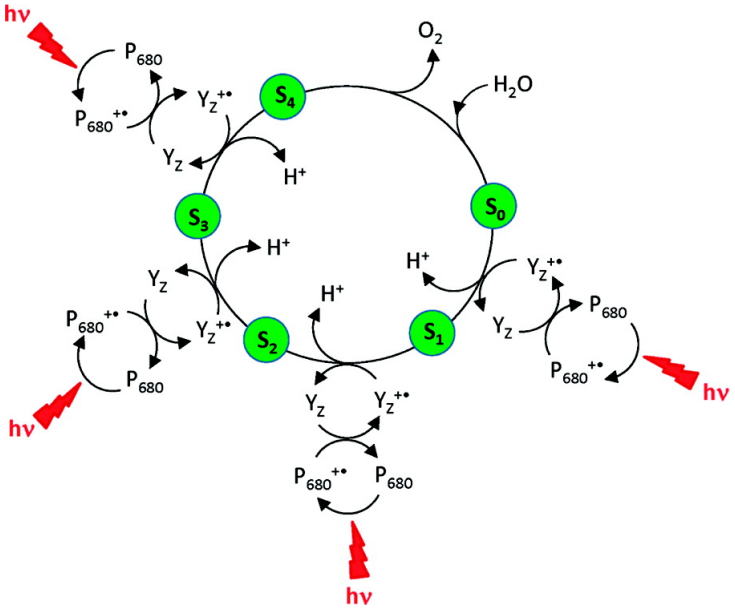

Figure 1.6: The S-state (Kok) cycle showing how the absorption of four photons of light (hν) by P_{680} drives the splitting of two water molecules and formation of O_2 through a consecutive series of five intermediates (S_0, S_1, S_2, S_3, and S_4). The S-states represent the various oxidation states of Mn in PSII-OEC. Electron donation from the PSII-OEC to the cation radical P_{680}^{+} is mediated by tyrosine, Y_Z.[19]

The understanding of the processes involved in light harvesting and its conversion into stored energy in chemical bonds, from water to hydrocarbons, performed by photosynthetic organisms is of high importance on the development of photocatalytic systems able to capture sunlight and convert it into electric energy by using water as raw material. Current technology employed for the conversion of solar energy into electric energy can be improved by mimicking (if not improving) the ability of natural photosynthetic organisms of storing energy. These systems will not only capture and convert the solar energy but, in addition, will also store this electric energy into chemical bonds, producing H_2 as green chemical fuel from water splitting.

UNIVERSITAT ROVIRA I VIRGILI
HIGH NUCLEARITY POLYOXOMETALATES AS WATER OXIDATION CATALYSTS: FROM EXPERIMENTS TO THEORY
Joaquín Soriano López

1.4 Artificial Photosynthesis and Water Splitting

The pioneer of modern photochemistry is considered to be the italian chemist Professor Giacomo Ciamician. He was the first scientist that investigated the photochemical reactions in a systematic way. In his visionary work, presented in 1912, he suggested to replace "fossil solar energy" (*i.e.*, coal) with sunlight energy, particularly the production of fuels (dihydrogen) by means of artificial photochemical reactions (artificial photosynthesis).[20,21] His proposal is still one of the most important goals of current research of many scientists.

In natural photosynthesis the solar light is used to rearrange the bonds of water to oxygen and hydrogen (Eq. 1.3). Subsequently the hydrogen is fixed by its combination with carbon dioxide to produce carbohydrate (Eq. 1.4). Thermodynamic energies of both processes show that it is water splitting and not carbohydrate production the core reaction in any solar energy storage.

$$H_2O \longrightarrow H_2 + \frac{1}{2}O_2 \qquad E^0 = 1.23V \tag{1.3}$$

$$CO_2 + H_2O \longrightarrow \frac{1}{6}C_6H_{12}O_6 + O_2 \qquad E^0 = 1.24V \tag{1.4}$$

Where, based on an electron equivalency, the production of the carbohydrate stores only 0.01 eV more energy than water splitting. Therefore, water splitting is used in photosynthesis for solar energy storage, while carbohydrate production is the method used by nature to store the hydrogen that is released from the water splitting reaction.[19]

In artificial photosynthesis, sunlight is converted into spatially separated electron/hole pairs employing a photovoltaic cell, and charges are captured with catalysts that mediate water splitting. Oxygen is produced by the catalyst at the anode when it captures four holes, while hydrogen is produced in a separate catalyst at the cathode when it captures four electrons.[22] So thus, solar energy is stored in chemical

bonds in the form of H_2 and O_2. On this regard, efficient electrocatalysts for water splitting must operate close to the Nerstian potentials (E) for both, water oxidation and proton reduction, semi-reactions involved in water splitting:

$$2H_2O \rightleftharpoons O_2 + 4H^+ + 4e^- \qquad E_{anodic} = 1.23 - 0.059(pH)\ V\ vs\ NHE \qquad (1.5)$$

$$4H^+ + 4e^- \rightleftharpoons 2H_2 \qquad E_{cathodic} = 0.00 - 0.059(pH)\ V\ vs\ NHE \qquad (1.6)$$

Of these two reactions, the water oxidation reaction is considered the bottle-neck reaction in water splitting, since it requires a four-electron oxidation of two water molecules coupled to the removal of four protons to form a relatively weak oxygen-oxygen bond. Moreover, in addition to the thermodynamic demands of water splitting, additional potential is needed to overcome activation barriers, concentration effects and voltage drops, due to resistence, to attain a given catalytic activity. This is known as overpotential. Furthermore, water oxidation catalysts must be stable under strong oxidizing environments, since, even at the thermodynamic limit, most chemical functional groups degrade due to the oxidizing power required by the oxidation of water.[22]

Nevertheless, solar water splitting is not a strictly scientific problem. Indeed, there are several large-scale projects working on the combination of renewable energy sources with commercially available water electrolyzers. But it is needed a financially attractive green alternative to fossil fuels to make the solar energy storage process competitive. The main reason for the low commercial impact of water electrolysis is the lack of a stable and inexpensive water oxidation catalyst able to work under mild conditions. Most of the existing catalysts are based on noble metals, or require the use of highly alkaline conditions working at low efficiencies. Therefore, the main challenge is the search for a robust, efficient, and inexpensive water oxidation catalyst.[23]

1.5 Water Oxidation Catalysts

A large number of organometallic complexes have been described as homogeneous water oxidation catalysts since Meyer, in 1982, reported the catalytic oxidation of water by a μ-oxo-bridged ruthenium dimer coordinated by polypyridil ligands, known as *blue dimer*.[24] These complexes have shown high performance in terms of rates and efficiency,[25–28] and they are easy to optimize and process. However, long-term stability is an important issue, since the organic ligands, which some of them are adequately stable in photovoltaic devices,[29] are unstable toward oxidative deactivation due to the strong oxidizing conditions during the water splitting process. Therefore, organometallic complexes have null options to be implemented into water-splitting devices.

The state-of-the art in terms of feasible industrial applications is lead by heterogeneous noble metal oxides, such as IrO_2, and RuO_2.[19,22,30–38] Probably, the most remarkable heterogeneous water oxidation catalyst based in abundant metals is the one reported by Nocera,[22] where a phosphate oxide cobalt layer (Co-P_i) was electrodeposited onto the anode of a sillicon-based solar cell, yielding a robust, monolithic, photo-assisted anode able to split water by direct irradiation with sunlight working at neutral pH. This catalyst shows pH-dependent degradation, making it too costly to compete with other hydrogen production procedures.

1.5.1 Molecular Water Oxidation Catalysts

Ruthenium-based Catalysts

Ruthenium complexes have been subject of research during the last years as water oxidation catalysts, although they are too expensive to be implemented into a real water splitting device. As already said, in 1982 Meyer reported the first example of a well-defined homogeneous water oxidation catalyst, the μ-oxo-bridged cis,cis-

$[(bpy)_2(H_2O)Ru^{III}(\mu\text{-}O)Ru^{III}(H_2O)(bpy)_2]^{4+}$ referred as the *blue dimer* due to its characteristic color.[24] As shown in Figure 1.7, the two halves of the oxo-bridged dimer are related by the 2-fold symmetry through the bridging oxygen atom. Both ruthenium centers are approximately octahedrally coordinated with a cis, cis arrangement with respect to the bpy ligands, allowing the coordinated water to align in parallel through free-rotation along the bridging oxide.[39] Due to steric constraints imposed by the bpy ligands is observed a nearly linear geometry of the Ru atoms through the μ-oxo bridge. Employing cerium(IV) ammonium nitrate (CAN) as chemical oxidant, in strong acidic conditions the *blue dimer* performs a turnover frequency (TOF) and a turnover number (TON) of 0.0042 s^{-1} and 13.2, respectively, and with a O_2 yield of 60 % based on the moles of oxidant.[40]

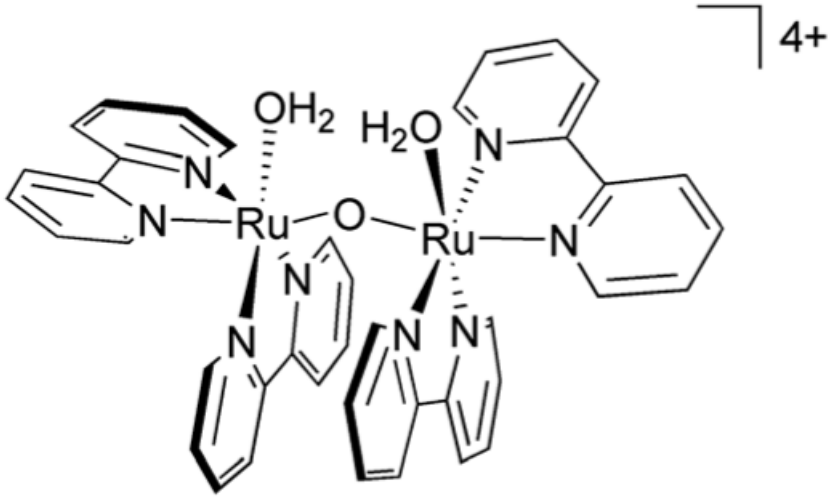

Figure 1.7: Structure of the blue dimer, cis,cis-$[(bpy)_2(H_2O)Ru^{III}(\mu\text{-}O)Ru^{III}(H_2O)(bpy)_2]^{4+}$ in the salt $[(bpy)_2(H_2O)Ru^{III}(\mu\text{-}O)Ru^{III}(H_2O)(bpy)_2](ClO_4)_4{\cdot}2H_2O$.

The *blue dimer* and its structurally related derivatives have been the field of study during the last three decades to shed some light into the mechanisms of water oxidation catalyzed by this complex.[39,41–48] Meyer et al. emphasized that PCET could be the key to catalytic water oxidation by the blue dimer[49,50] which allow many

oxidative equivalents to accumulate sequentially at one site without the buildup of highly charged species.[51,52] Mechanistic and kinetic studies of the water oxidation reaction by the *blue dimer* revealed the high complexity of the reaction mechanism, since it does involve not only multiple PCET events reaching high oxidation states of the central Ru-O-Ru core, and cross electron transfer between non-adjacent oxidation states but also different intermediate acid-base equilibrium reactions and some anion exchanges between the surrounding solution and the coordinated water molecules. As depicted in Figure 1.8, latests mechanistic studies employing CAN as chemical oxidant in strong acidic conditions, suggest that the ($[Ru^{III}-O-Ru^{III}]^{4+}$) core is oxidized *via* four successive PCET events, reaching the highest oxidation state ($[O=Ru^{V}-O-Ru^{V}=O]^{4+}$). At this point an ancillary water molecule attacks the core producing a hydroperoxo species, which is oxidized intramolecularly by the second $Ru^{V}=O$ group, thus releasing O_2.[53] A different study suggests the participation of the bpy ligands in the O_2-releasing step (Figure 1.9).[54] In this case a water molecule oxidizes the bpy ligand by attacking the α-position of the pyridine ring. Such attack could be relevant for explaining the observed degradation of the bpy ligands under strong oxidative conditions. After the water nucleophillic addition, the radical formed in the pyridine ring is neutralized when a second molecule of water attacks the β-position, so thus leading to O-O bond formation after oxidation by the Ru-centers. The recovery of the aromaticity of the ligand serves as a driving force for the release of a molecule of dioxygen.

As a consequence of the low water oxidation activity performed by the *blue dimer*, and the instability of the bpy ligands towards oxidative conditions, many researchers have focused in trying to solve these problems. As an example, Llobet et al. in 2004 reported a new ruthenium dimer, $[(Ru^{II}(trpy)(H_2O))_2(\mu\text{-bpp})]^{3+}$ (where trpy = 2,2':6',2"-terpyridine; and bpp = bis(2-pyridyl)-3,5-pyrazolate), which was called the *bpp dimer* (Figure 1.10).[56] The bridging bpp ligand enforces a cis geometry of the two ruthenium centers with the two bounded aqua ligands facing each other in

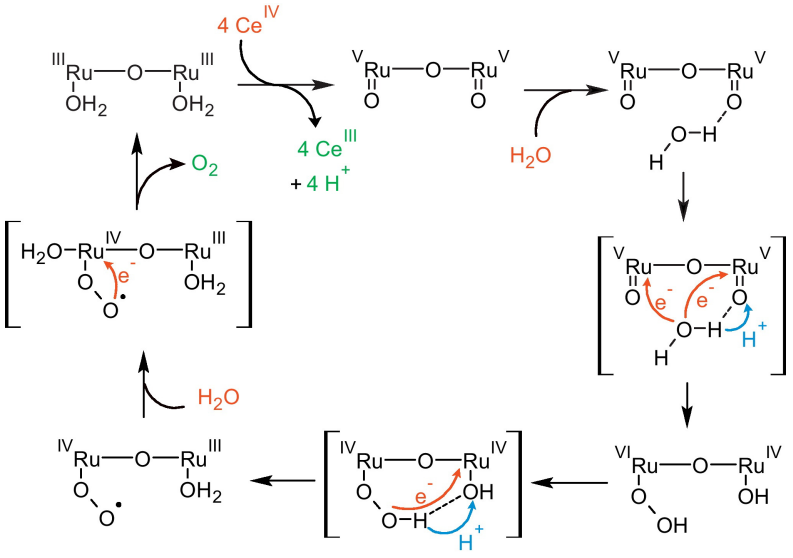

Figure 1.8: Proposed mechanism of the *blue dimer* catalyst.[55]

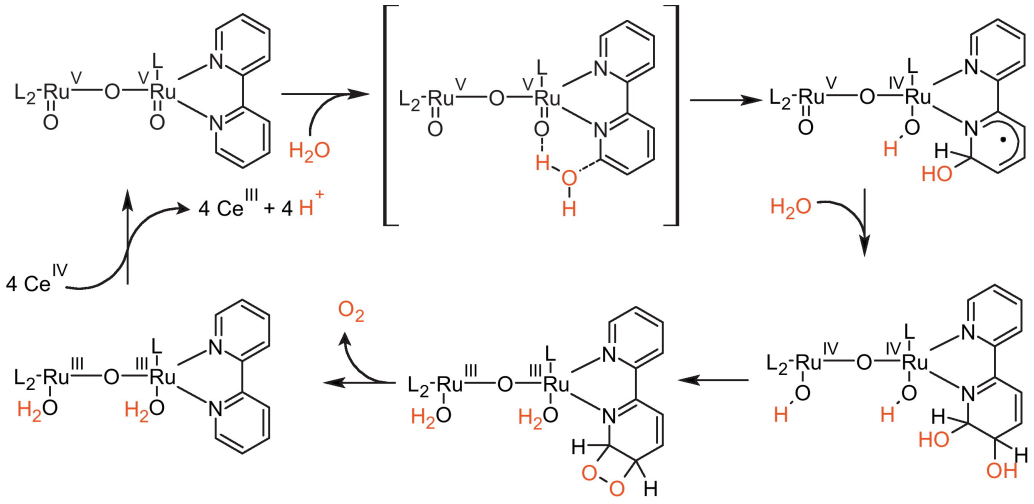

Figure 1.9: Mechanism of O_2 release by [O=Ru^V-O-Ru^V=O], *via* ligand participation. L = 2,2'-bipyridine.[55]

close proximity. Water oxidation experiments with this complex were conduct with CAN in a pH 1 solution of 0.1 M triflic acid. Contrary to the *blue dimer*, the starting species of the *bpp dimer* was $Ru^{II}-Ru^{II}$, and it reached the highest oxidation state of $Ru^{IV}-Ru^{IV}$ quickly upon oxidation. Due to the rigid coordination geometry the oxygen evolution rate increased to 0.014 s^{-1}, compared with the *blue dimer*.[57] A

TON of 18 was achieved, corresponding to a catalyst efficiency of 70 % according to the moles of oxidant consumed. Kinetic analysis combined with ^{18}O-labeling experiments, and DFT and CASPT2 modeling, provided evidences that once the highest oxidation state is reached, the mechanism follows an "intramolecular O−O bond formation" in preference of a "H_2O nucleophillic attack".[57,58] Separately DFT studies reported by Baik et al. concluded that intramolecular O−O coupling, despite of being affordable, is unproductive toward dioxygen evolution since substitution of the peroxo group to afford the peroxo/aqua intermediate would demand a prohibitively high energy, whereas the water nucleophillic attack to one of the Ru^{IV}=O moieties to afford a peroxo intermediate seems to be plausible regarding the energy barrier found, being the rate-determining step in the reaction mechanism.[59]

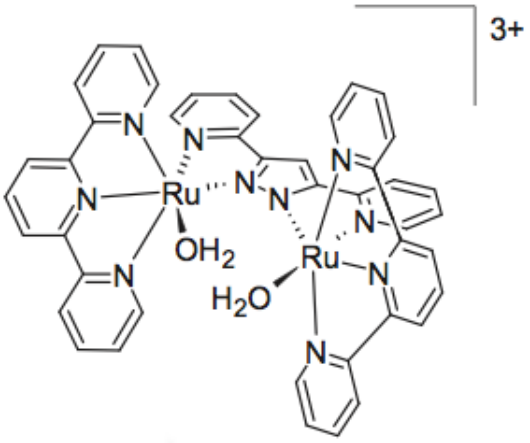

Figure 1.10: Drawn structure of the *bpp dimer*.[58]

During long time, it was thought that only multinuclear water oxidation catalysts could carry on oxygen evolution, by dividing the four PCET steps required for the water oxidation reaction over several metal centers in close proximity. However, Zong and Thummel[60] and Meyer et al.[52] demonstrated that mononuclear ruthenium complexes were also active as water oxidation catalysts. These complexes were able to successively accumulate the four PCET events necessary to oxidize water. Since then, a huge number of active mononuclear ruthenium complexes toward oxygen

evolution appeared in the literature.[25,55,61] One of the most remarkable examples was reported by Sun and Llobet, where they studied the activity of [Ru(bda)(isoq)$_2$] (where H_2bda = 2,2'-bipyridine-6,6'-dicarboxilyc acid; isoq = isoquinoline) (here noted as **Ru(isoq)**) (Figure 1.11).[26,62–64] Addition of the catalyst to an aqueous solution of 0.1 M triflic acid (pH 1) containing an excess of CAN as chemical oxidant, led to a rapid oxygen evolution with a TOF of 303 s^{-1}, and a maximum TON of 8360. In the same report authors also investigated the activity of a similar complex, where the aromatic isoquinolines are substituted by a more electrondonating and less aromatic 4-picolines (pic), [Ru(bda)(pic)$_2$] (herein **Ru(pic)**) (Figure 1.11).

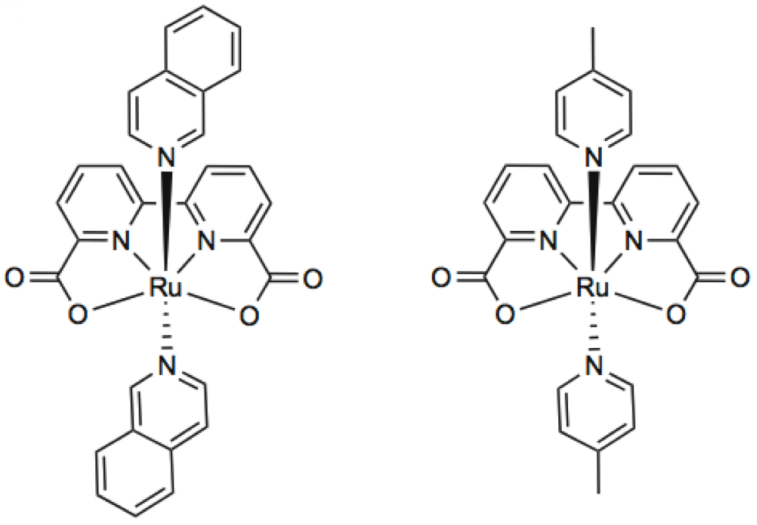

Figure 1.11: Drawn structure of [Ru(bda)(isoq)$_2$] (left) and of [Ru(bda)(pic)$_2$] (right).[26]

In this case the catalytic activity decreased one order of magnitude but important similarities were found experimentally for the two complexes, under the same experimental conditions. In both cases the oxygen evolution was second order in catalyst concentration, suggesting a rate increase within a common reaction mechanism. Therefore, for solubility reasons, it was easier to perform stopped-flow kinetic measurements with the **Ru(pic)** complex. In the proposed reaction mechanism, under stoichiometric CAN conditions, the stating species $Ru^{II}-OH_2$ rapidly oxidizes

to $Ru^{III}-OH_2$ when the solution is exposed to air, therefore this first step could no be investigated. After two PCET events the highly oxidized species $Ru^{V}=O$ were obtained, which dimerizes (radical coupling) forming a Ru^{IV}-peroxodimer, and then molecular oxygen evolves. In addition, when the experiment is carried out under excess of oxidant the Ru^{IV}-peroxodimer is further oxidized reaching a formally Ru^{IV}-superperoxodimer, which is weakly bound and responsible for the subsequent liberation of O_2 (Figure 1.12). Spectroscopic, electrochemical and kinetics studies, suggested a seven-coordinate environment of the ruthenium center towards oxidation, thanks to the properties of the bda^{2-} ligand. As already said, authors also observed a second-order reaction kinetics in catalyst for oxygen production, with a bi-nuclear radical coupling pathway for O−O bond formation. DFT studies support that stacking of isoquinolines facilitates the formation of the O−O bond in the radical dimerization of $Ru^{V}=O$ active species, thus making **Ru(isoq)** far superior in activity than **Ru(pic)**.

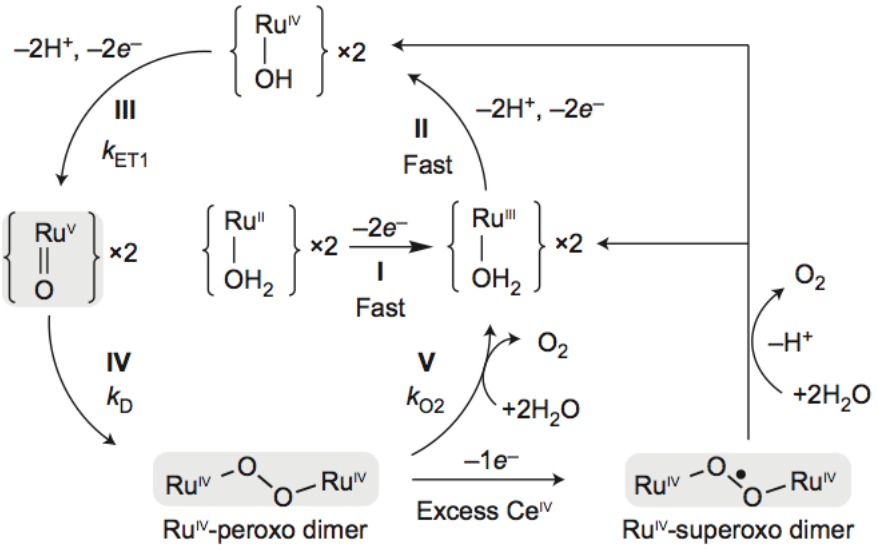

Figure 1.12: O_2 generation pathways of the $[Ru(bda)(pic)_2]$ complex with stoichiometric and excess amount of CAN at pH 1 (the circular pathway in the middle and further to the right, respectively).[26]

Recently, our group in collaboration with K. R. Dunbar, reported the water oxidation activity of the first metal-metal bonded diruthenium(II,II) tetracetate complex, [$Ru_2(\mu$-$O_2CCH_3)_4$] (**Ru_2**; Figure 1.13).[65] This compound catalyzes water electrolysis over a wide pH range (1-10) and at high catalytic rates with quantitative efficiencies even in diluted solutions. With an estimated TOF = 77 s^{-1}, the diruthenium compound is one of the fastest Ru-based catalyst reported to date, with the notable exception being the family of the **Ru(isoq)**, and with the difference that **Ru_2** does not require strict pH conditions. We detected slow oxidative deactivation due to the instability of the acetate ligands at high potentials. As shown in Figure 1.14, DFT calculations were carried out to investigate the intermediates involved in the plausible mechanism for water oxidation, where the initial PCET event emerges as the most energetic demanding step, which is in good agreement with the experimental results. The highly oxidized species Ru^V=O is prone to nucleophilic attack of an external water molecule yielding the formation of the O−O bond. In addition, we found that the **Ru_2** can act as single-site catalyst with the adjacent Ru behaving as an auxiliary ligand that tunes reactivity providing a remarkably active catalyst.

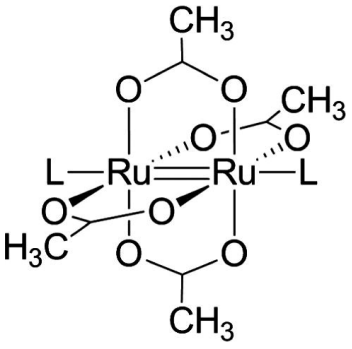

Figure 1.13: Schematic representation of the molecular structure of **Ru_2**. The acetate ligands are bound to the $Ru_2{}^{4+}$ core in the equatorial positions; L denotes open axial positions for solvent or anion binding.[65]

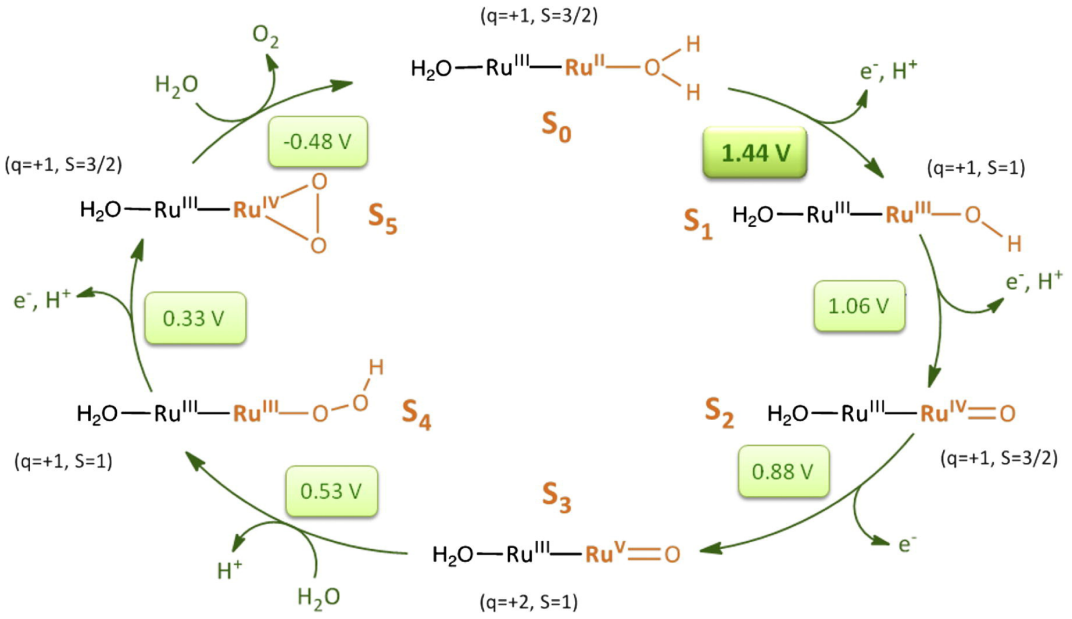

Figure 1.14: Proposed water oxidation mechanism catalyzed by $[Ru_2(\mu\text{-}O_2CCH_3)_4(H_2O)_2]^+$ catalyst based on DFT calculations. The potentials reported are relative to NHE at pH 0.[65]

Iridium-based Catalysts

The use of iridium complexes as water oxidation catalysts have been relevant since 2008, when Bernhard and co-workers reported a group of cyclometalated iridium(III) complexes which were suitable catalyst precursors (Figure 1.15a).[66] These complexes contain 2-phenylpyridine-type (ppy) ligands, leaving two cis open sites where two water molecules are able to coordinate the complex. Stoichiometric consumption of CAN lead to oxygen evolution, confirmed by gas chromatography, with maximum TOF and TON of 0.0015 s^{-1} and 2500, respectively.

Afterwards, in 2009 the group of Crabtree published the use of pentamethylcyclopentadienyl (Cp*) complexes as molecular precatalysts for water oxidation employing CAN as chemical oxidant (Figure 1.15b and 1.15c).[67] These type of complexes, $[(Cp^*)IrL_3]$ (where L = any monodentate ar bidentate ligand), demonstrated that stronger donating ligands improve the catalytic activity. They are the most ex-

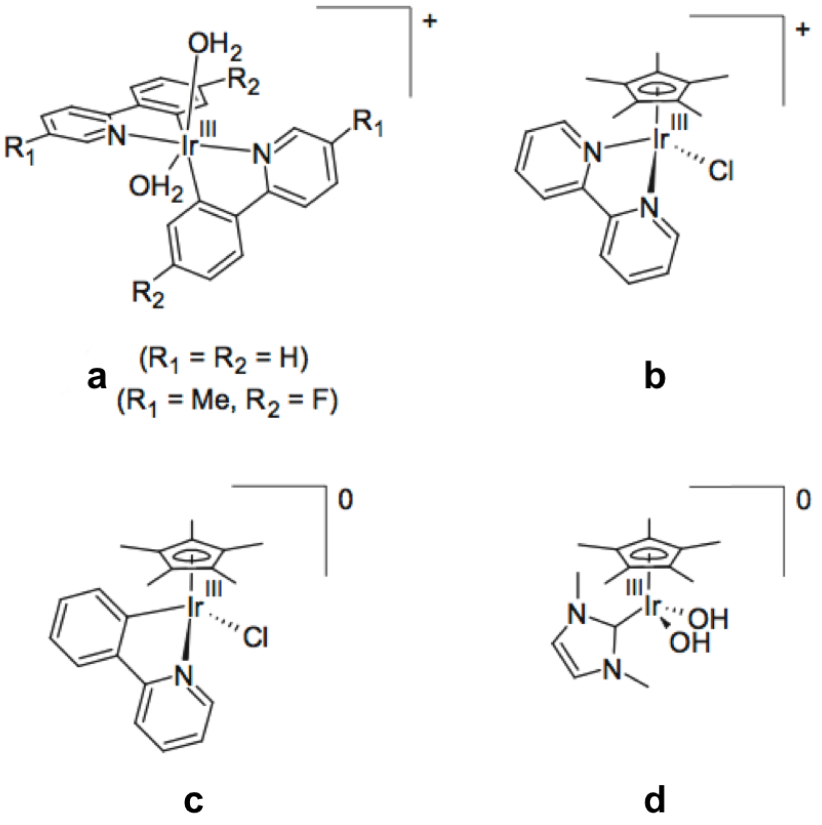

Figure 1.15: Drawn structure of some representative Ir-based complexes.[66–68]

tensively studied iridium-based water oxidation catalysts, reaching oxygen-evolution rates as high as 1.5 s^{-1} and maximum TON of 2000, when employing N-heterocycilc carbene ligands, [(Cp*)Ir(dmiz)$(OH)_2$] (where dmiz = 1,3-dimethylimidazole) (Figure 1.15d), as reported by Hetterscheid and Reek.[68] On the basis of fist-order dependence of oxygen evolution on the concentration of iridium precatalyst, it was proposed a reaction mechanism for a single-site catalysis by means of DFT calculations. The mechanism described the electronic structure of an iridium(V) oxo complex as a possible intermediate (Figure 1.16), although this species was not observed experimentally.[67,69]

The molecular nature of these iridium-based complexes under turnover conditions is not obvious, since large amounts of CAN create quite extreme chemical

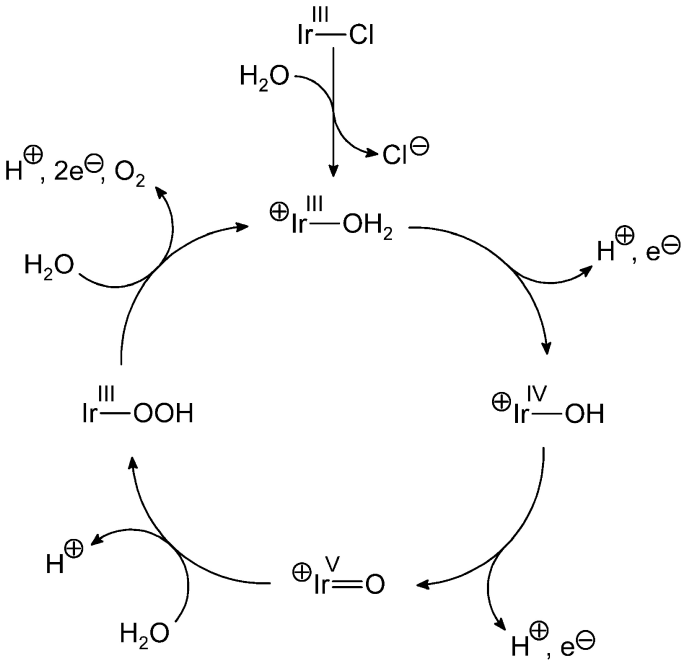

Figure 1.16: Reaction mechanism postulated for Ir-catalyzed water oxidation.[69]

conditions causing ligand degradation that may lead to metal oxide nanoparticles, which may be responsible of the water oxidation catalysis.[70–73] As demonstrated by Crabtree et al. with an electrochemical Quartz Crystal Nanobalance, under water oxidizing conditions a layer of carbon-containing iridium oxide material deposits on the electrode, which gives a blue color to the electrode and showed excellent catalytic water oxidation properties.[73] In addition, Grotjahn et al. performed tunneling electron microscopy, powder X-ray diffraction, and UV-vis spectroscopy experiments that revealed the presence of IrO_x nanoparitcles of ∼2-10 nm of diameter when mixing some reported iridium complexes with large amounts of CAN.[71]

Manganese-based Catalysts

Manganese plays an essential role in natural photosynthesis since is within the active site of the OEC in PSII, therefore many researchers have focused in the preparation of Mn complexes that mimic the structure of the OEC and catalyze water oxida-

tion.[74,75] In addition, the use of Mn is attractive because it is Earth abundant and relatively nontoxic compared with the other more active catalysts. A large number of manganese complexes have been studied as models of the OEC, however it is not always clear what the actual catalytic species is or whether they are true molecular catalysts, as most suffer from poor stability under the experimental conditions. Additionally, these complexes require the use of oxygen transfer and/or two-electron oxidizing agents as oxidants (such as ClO^-, and $HSO_5{}^-$) to evolve O_2 catalytically in a homogeneous solution.

Binuclear complexes have been reported to catalyze water oxidation in homogeneous conditions. Among them, one of the most studied is the dimeric complex $[(terpy)(H_2O)Mn^{III}(\mu\text{-}O)_2Mn^{IV}(terpy)(H_2O)]^{3+}$ (where terpy = 2,2':6,2"-terpyridine, Figure 1.17), reported by Crabtree et al. in 1999.[76] This complex oxidizes water employing NaClO as chemical oxidant with a maximum TON of 4 after 6 h, with an initial TOF of 0.67 s^{-1}. Authors postulated that during the catalytic cycle, the Mn(III)/(IV) dimer form a Mn^V=O species, which is a key intermediate for the O−O bond fomation, involving an attack by OH^- to produce a peroxy intermediate. The Mn(V)/(V) intermediate is reduced to Mn(III)/(III) upon O_2 releasing, which is oxidized by the oxidant to the original Mn(IV)/(IV) dimer (Figure 1.17), as demonstrated by electron paramagnetic resonance (EPR), and UV-vis spectroscopy. However, the complex suffers of dissociation to $MnO_4{}^-$, that was proposed to coincide with catalyst deactivation. Later, it was demonstrated that impregnation of this complex into a clay mineral lead to an increase of the number of turnovers by nearly 4-fold.[77]

Tetranuclear manganese complexes have also been studied as water oxidation catalysts, motivated by the structure of the OEC in the PSII. Dismukes et al. reported these tetranuclear complexes as $Mn_4O_4L_6$ and $[Mn_4O_4L_6]^+$ (where L = $(Ph)_2PO_2{}^-$, $(p\text{-}MePh)_2PO_2{}^-$, or $(p\text{-}MeOPh)_2PO_2{}^-$, Figure 1.18), that are able to evolve oxygen when irradiated with UV light.[78–80] This cubane structure self-assembles sponta-

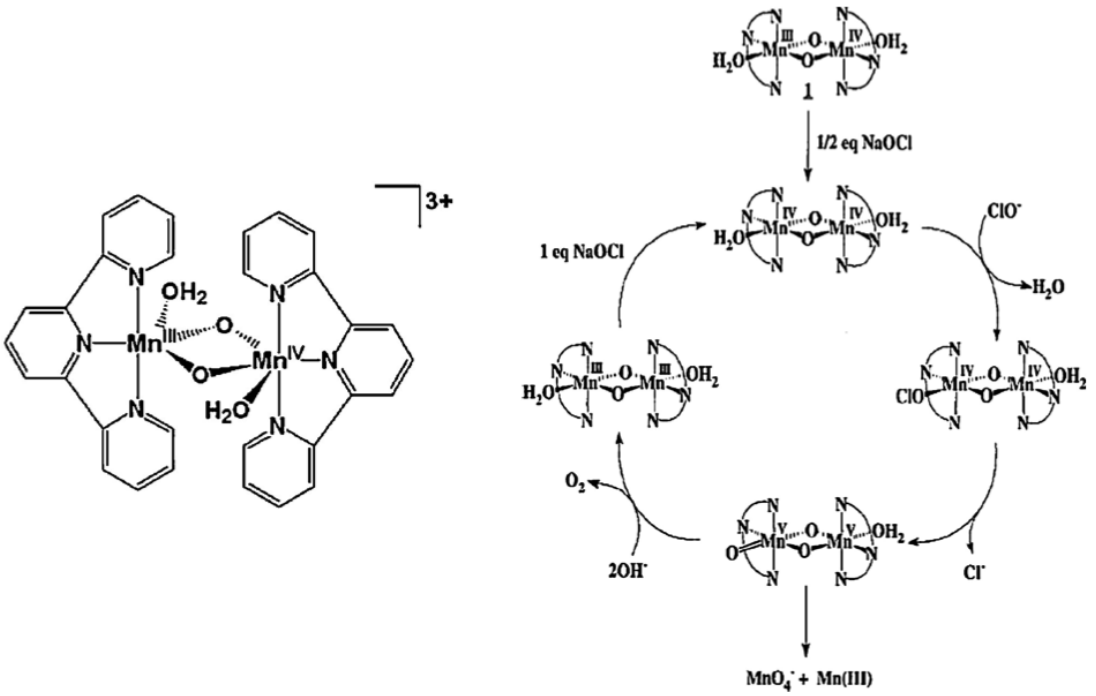

Figure 1.17: Structure of the Mn dimer reported by Crabtree et al. (left), and the proposed reaction mechanism of the formation of O_2 using NaClO as chemical oxidant (right).[76]

neously from Mn(II) and permanganate salts in high yield in non-aqueous solvent, and the oxidized cubane ($[Mn_4O_4L_6]^+$) is obtained by oxidation of $Mn_4O_4L_6$ using electrochemical or chemical methods. Irradiation of $Mn_4O_4L_6$ with UV light leads to oxygen evolution. Isotope labeling experiments indicate that under UV light one of the bridging phosphinate ligands dissociates, thus forming the open "butterfly" $[Mn_4O_4L_5]^{2+}$ and the O−O bond forms through coupling of two corner oxygen atoms. In addition, $[Mn_4O_4L_6]^+$ (where L = $(p\text{-MePh})_2PO_2^-$) was incorporated into a Nafion-coated electrode, thereby heterogenizing the catalyst.[81,82] This electrode was able to oxidize water under UV light irradiation and application of 1.2 V vs NHE. However, posterior studies from Spiccia et al.,[30] and from Young et al.,[83] separately, demonstrated that the molecular manganese complex in the electrode assembly was not a genuine catalyst, but manganese oxide formed in situ was identify as the true catalyst.

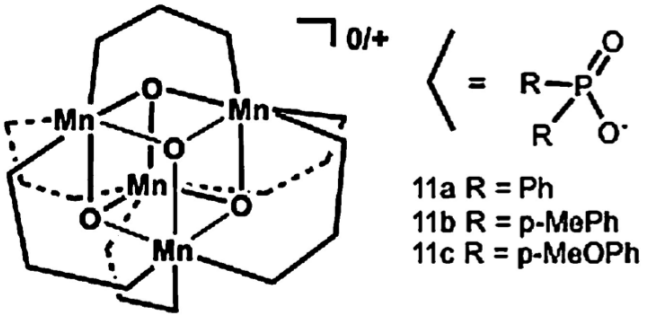

Figure 1.18: Structure of the $Mn_4O_4L_6$ complex.[84]

In general, low stability and low TONs (< 25) are obtained among all reported Mn complexes acting as water oxidation catalysts due to the labile coordination of the manganese. Decomposition products beginning from Mn^{2+} ions, normally permanganate ions or manganese oxide nanoparticles may be catalytically active, depending on the structure and size.

Iron-based Catalysts

Bernhad and Collins et al. reported in 2010 a series of Fe-macrocyclic complexes, $[Fe^{III}(taml)]^-$ (where taml = tetraamido macrocyclic ligand, Figure 1.19a). Four of them were able to oxidize water to O_2 employing CAN as chemical oxidant.[28] Substitution of the ligands either with electron donating or electron withdrawing groups could modulate the water oxidation activity of the complex. That is, when employing R_1 = H, R_2 = CH_3, the complex does not have any catalytic activity, whereas using R_1 = Cl, R_2 = F, the catalyst exhibited the highest TOF and TON of the series, being $> 1.3\ s^{-1}$ and > 16, respectively. However, the compound is quickly (within seconds) deactivated, most likely due to oxidation of the ligand. Moreover, the mechanism of the O_2 generation remains unclear.

In 2011, Lloret Fillol and Costas et al. reported a series of tetraaza complexes of Mn, Fe, Co and Ni for water oxidation catalysis employing CAN or $NaIO_4$ as

primary oxidants.[85] Oxygen evolution was observed when employing Fe, and with the tetradentate ligands allowing for a cis coordination of two labile sites (Figure 1.19b). On the contrary, when the ligand yields a trans coordination and for pentadentate ligands, again using Fe, complexes did not show any catalytic activity. In the proposed mechanism high valent Fe(V)−oxo species are responsible for the O−O bond formation. The most active complex reached a TON $>$ 1000 when employing $NaIO_4$ at pH 2.

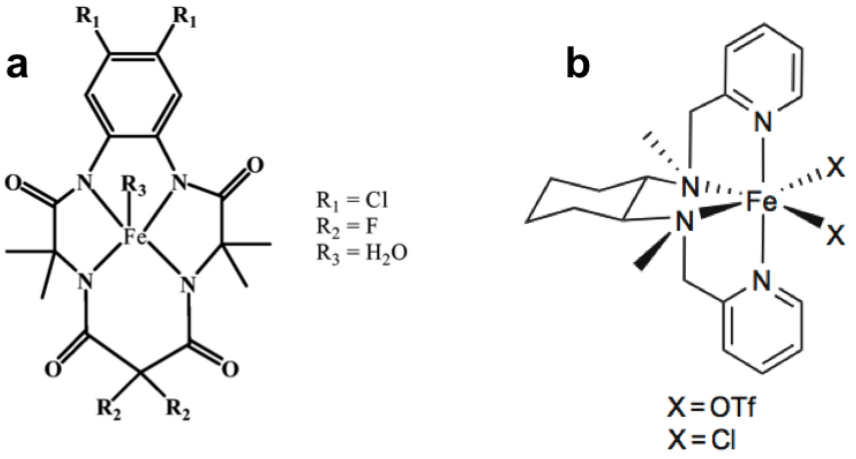

Figure 1.19: Structures of: (a) the Fe-macrocyclic complexes,[28] and (b) the Fe tetracoordinated active complex.[85]

Cobalt-based Catalysts

During the last years researchers have been interested in developing molecular cobalt catalyst for water oxidation. Cobalt phthalocyanine,[86] fluorinated cobalt corrole,[87] and cobalt porphyrins[88] have been reported as active water oxidation catalysts. For example, Nocera et al. reported a series of cobalt hangman corrole complexes,[87] which incorporated into a Nafion membrane were able to catalytically oxidize water. Paticularly, best oxygen evolution rates were obtained with β-octofluoro Co(III) xanthene hangman corrole, bearing 5,15-bis(pentafluorophenyl) substituents (Figure 1.20), reaching a TOF of 0.81 s^{-1} at an applied potential of 1.6 V vs NHE in 0.1 M

potassium phosphate buffer at pH 7.

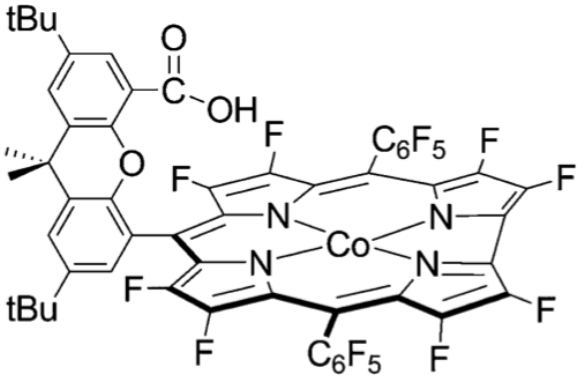

Figure 1.20: Structures of β-octofluoro Co(III) xanthene hangman corrole.[87]

Catalytic activity of polypyridyl complexes of cobalt have also been studied. Berlinguette et al. reported that under basic conditions the complex $[Co(Py5)(OH_2)]^{2+}$ (where Py5 = 2,6-(bis(bis-2-pyridyl)methoxymethane)pyridine) evolved oxygen (Figure 1.21).[89,90] Oxygen evolution was measured with a fluorescence optical probe immersed in solution at an applied potential of 1.59 V vs NHE over 10 minutes in basic media. Experiments suggest a TOF of 79 s^{-1}. Beginning from $[Co^{II}-OH_2]^{2+}$ species, the proposed reaction mechanism is initiated with a PCET event reaching the $[Co^{III}-OH]^{2+}$ species, which is oxidized to $[Co^{IV}-OH]^{3+}$, being the responsible species for the O−O bond formation when is nucleophilically attacked by the base (*e.g.* OH^-, phosphate), as shown in Figure 1.21. However, it was difficult to conclusively rule out the possibility of nanoparticles formation near the electrode, being the responsible for the catalytic current.

Tetranuclear Co_4O_4 cubane compounds have recently been proposed as molecular water oxidation catalysts. Two groups reported, separately, the catalytic activity of the $[Co_4O_4(OAc)_4(py)_4]$ complex (where OAc = acetate) (Figure 1.22).[91–93] During light-driven water oxidation experiments, employing $[Ru(bpy)_3]^{2+}$ as photosensitizer, and $S_2O_8{}^{2-}$ as sacrificial electron acceptor, the cubane compound yields a TON over 40 after 60 minutes of irradiation, with a TOF close to 0.02 s^{-1}.[92] At pH 7 the chemical yield reaches a 50%, based on the amount of oxidant.[93] However, Britt

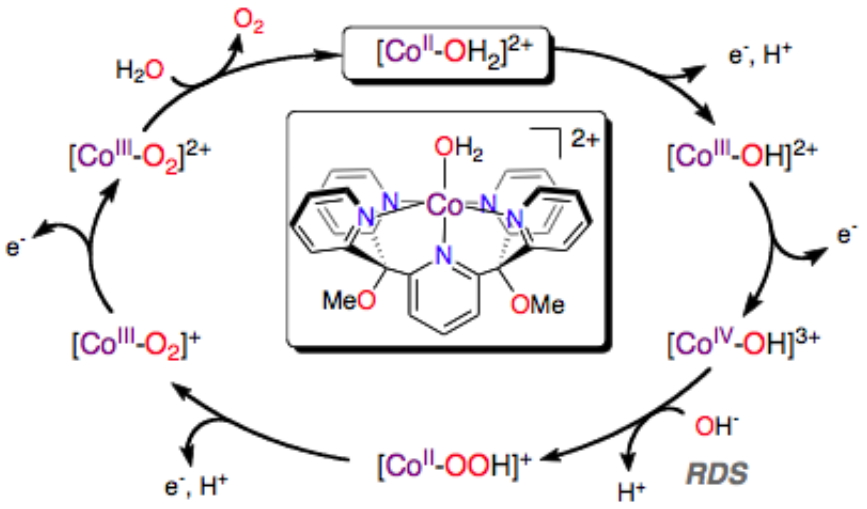

Figure 1.21: Structure of $[Co(Py5)(OH_2)]^{2+}$, and the proposed reaction mechanism.[89,90]

et al. found that the same complex did not yield oxygen production when oxidized electrochemically.[94] Recently, Nocera et al. found that catalysis with this complex arises from impurities of cobalt(II), supported by NMR, EPR, and electrochemistry experiments.[95]

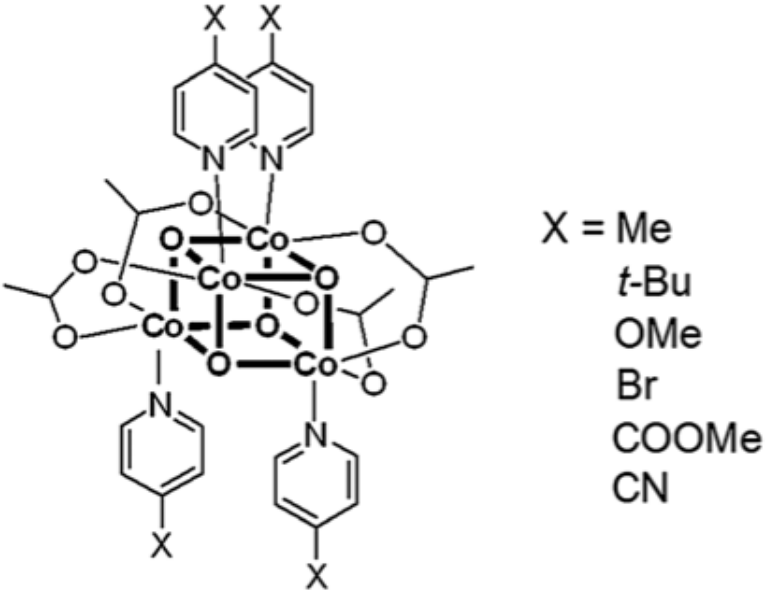

Figure 1.22: Structure of the $[Co_4O_4(OAc)_4(py)_4]$complex.[91]

Interestingly, Patzke et al. recently reported the $[Co^{II}_3Ln(hmp)_4(OAc)_5H_2O]$ (where Ln = Ho−Yb, hmp = 2-(hydroxymethyl)pyridine) cubane series as active WOCs under homogeneous light−driven conditions, employing $[Ru(bpy)_3]^{2+}$ as photosensitizer, and $S_2O_8{}^{2-}$ as sacrificial electron acceptor.[96] pH−dependent WOC performance showed maximum TON values at pH 8, whereas maximum TOF values were obtained at pH 9. Therefore, at pH 8 the Er and Ho derivatives performed a maximum TON of 221 and 163, respectively. These WOCs also showed the highest TOF values among the series at pH 9 with 9.6 s^{-1} and 8.9 s^{-1} for the Ho and Er derivatives, respectively. Kinetic studies suggested a pseudo first-order oxygen evolution with respect to the catalyst concentration along the cubane series. Stability tests confirmed the nature of the cubane structure as responsible for the oxygen evolution. Computational studies showed that Ln^{3+} centers are active catalytic promoters with flexible ligand binding modes in close analogy to OEC mechanisms. This cubane series supposed the first molecular 3d−4f catalysts for key light−induced processes with tunable Ln^{3+} centers.

1.5.2 Solid-state Water Oxidation Catalysts

Due to their higher stability and the easier implementation in devices, heterogeneous catalysts have been extensively studied, including metal oxides (particularly spinels, perovskites, and layered double hydroxides) and more recently prussian blues analogues.[30,32,33,97–104] Most active metal oxides are based on rare and precious metal ions, while first transition metal oxides operate only in highly basic conditions. However, development of metal oxides based on Earth-abundant materials operating in mild conditions has been carried out during the last decade.[22,100,105–110] These metal oxides have been prooved to catalytically oxidize water employing chemical oxidants, and in either electrochemical[22,109–112] or photo-electrochemical cells.[105,113]

Ruthenium Oxides

Grätzel et al. reported in 1979 the use of colloidal RuO_2 nanoparticles as water oxidation catalyst driven by Ce(IV), where the rates of oxygen evolution found were 100 times higher than those obtained with bulk RuO_2 powder.[114] These nanoparticle were also active under light-driven conditions employing $[Ru(bpy)_3]^{2+}$ as photosensitizer and dimethylviologen as sacrificial electron acceptor.[115] Afterwards, the RuO_2 nanoparticles were deposited onto Pt-doped TiO_2 nanoparticles, obtaining a system able to perform water oxidation and reduction simultaneously.[116]

The catalytic activity was affected by the hydration grade of the RuO_2, so thus the best performances were achieved in the optimal hydration range of 12-14%.[117–120] Recently, a simple, novel method for photodeposition of RuO_2 nanoparticles on titania surface led to a material able to catalytically oxidize water with a TON of 16 under dark conditions using Ce(IV) as the oxidant.[120]

A light-induced oxygen-generating gel system was constructed using the electrostatic interactions of ionic functional groups and steric effects of a polymer network. By using a graft polymer chain with $[Ru(bpy)_3]^{2+}$ as photosensitizer to closely ar-

range RuO_2 nanoparticles as catalyst, the functional groups transmit multiple electrons cooperatively to generate oxygen (Figure 1.23).[121]

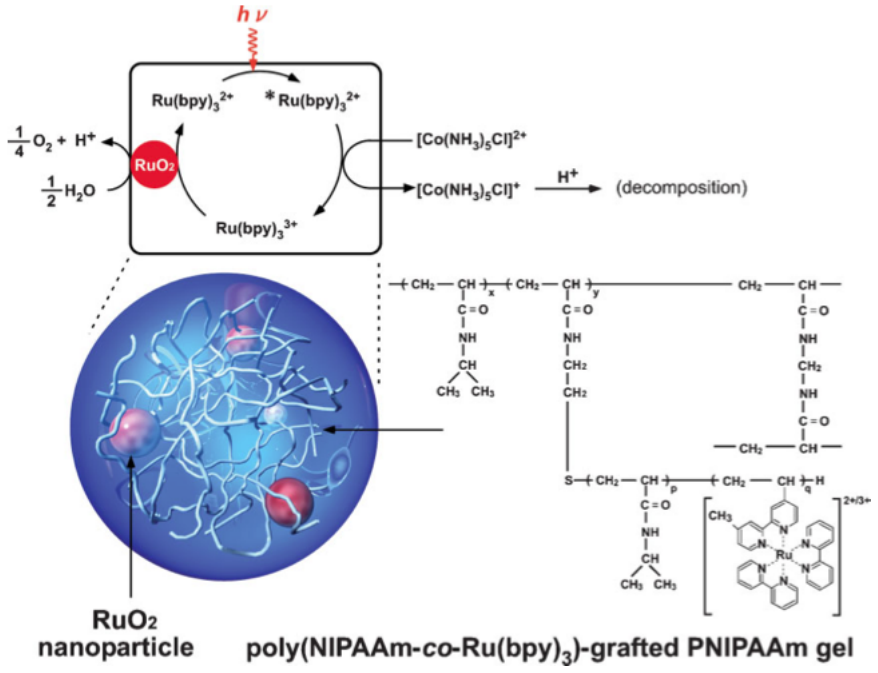

Figure 1.23: Oxygen-generating system formed by using a poly(NIPAAm-*co*-Ru(bpy)$_3$)-grafted PNIPAAm gel that contains RuO_2 nanoparticles.[121]

As a part of a Nafion membrane, colloidal RuO_2 was also deposited on a glassy carbon electrode, and then dipped in a $[Ru(bpy)_3]^{2+}$ solution. Water electrolysis let to oxygen evolution at an applied potential of 1.14 V vs NHE in acetate buffer at pH 4.6.[122]

Iridium Oxides

Iridium Oxide, IrO_2, was reported as water oxidation catalyst for the first time in 1978 by Grätzel and co-workers.[123] With a great stability, IrO_2 is one of the most efficient catalyst working at low overpotentials.

A citrate-stabilized IrO_2 colloid was self-assembled onto an ITO electrode forming a monolayer of the colloidal catalyst by dip coating. The self-assembly could be

achieved by a chemical interaction between carboxylate groups on the citrate stabilizer, and hydroxyl groups on the ITO surface to form ester bonds. Electrocatalysis performed with these modified electrodes yielded a TOF = $(2.3-2.5)x10^4$ h^{-1}, based on the surface concentration of catalyst, when applying 1.24 V vs NHE at pH 5.2.[34] Mesoporous films of 2 nm diameter of IrO_x nanoparticles were formed on glassy carbon electrodes. These films catalyze water oxidation achieving 100% current efficiency, at overpotentials 0.15 and 0.25 V higher, respectively, than the reversible H_2O/O_2 potential. The overpotentials, measured at 0.5 mA/cm^2, were independent of the pH.[124]

Citrate-stabilized IrO_2 colloids have also been investigated to yield dioxygen during light-driven experiments, in the presence of a photosensitizer such a $[Ru(bpy)_3]^{2+}$ in sodium hexafluosillicate-based (Na_2SiF_6) buffers.[125] For example, turnover numbers reached 290 employing a Na_2SiF_6-$NaHCO_3$ buffer at pH 5, whereas changing the buffer to Na_2SiF_6-$Na_2B_4O_7$ the turnover number decreased to 100, remarking the importance of the buffer regarding photosensitizer decomposition. The use of polymeric ruthenium photosensitizers decreased the turnover numbers due to polymer aggregation. These systems were improved employing $[Ru(bpy)_3]^{2+}$ sensitizers containing malonate and succinate groups in the 4,4'-positions, that stabilize 2 nm diameter particles of IrO_2.[126] The quenching of the excited-state of the bound sensitizer molecules was within the 30 ns time scale, most likely by electron transfer to Ir(IV), indicating a good electronic coupling between the sensitizer and IrO_2. Electron transfer from Ir(IV) to Ru(III) occurs with a first-order rate constant of $8x10^2 s^{-1}$, and oxygen is evolved.

Later, Mallouk et al. were able to construct an overall water splitting system that uses visible light to convert water to hydrogen and oxygen, assisted by a small applied voltage.[127] A multi-funtional ruthenium polypyridyl sensitizer was synthesized, with phosphonates substituents that are chemically selective for TiO_2, and with malonate groups selective for $IrO_2 \cdot nH_2O$. Therefore, the photoanode integrates TiO_2 (anatase)

with IrO_2 hydrated nanoparticles (2 nm) (Figure 1.24). Low quantum efficiency was observed due to slow electron transfer from the $IrO_2 \cdot nH_2O$ nanoparticle to the oxidized dye. Hence, this reaction did not compete effectively with back transfer electron from TiO_2 to the dye. The performance of the system can be improved by changing the sensitizer nature, and the electrode material with respect to the semiconductor nature.[128–130]

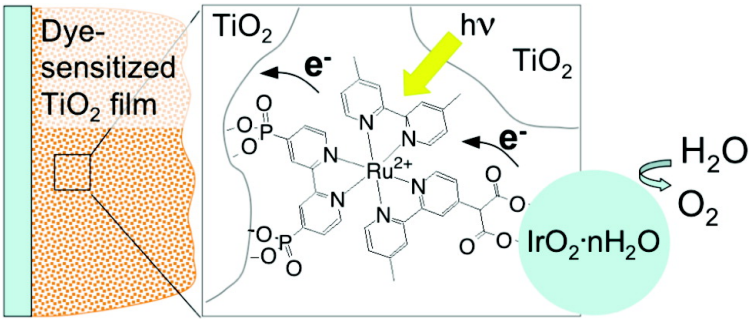

Figure 1.24: Schematic of the water splitting dye sensitized solar cell.[127]

Despite the good performance of IrO_2 in terms of rates and efficiencies, Ir is one of the most rare metals, and therefore it is not suitable for large-scale applications due to its high price in the market. Ir-based water splitting devices cannot compete in price with commercially available water electrolyzers.

Manganese Oxides

Identification of the active MnO_x forms is particularly difficult. The catalytic activity towards water oxidation employing manganese oxides has been attributed to layered oxides,[30,105,131] rutile phases,[132] spinels,[133–135] and perovskites.[136,137] However, due to the stable formation of inactive MnO_2 domains, MnO_x catalysts exhibit lower activity compared with that obtained with CoO_x and NiO_x.[138] This deactivation can be avoided by potential cycling during electrodeposition of MnO_x films, as reported by Dau and co-workers. The formed MnO_2 is modified into a mixed-valency Mn(III/IV) oxide during reduction potential sweeping.[139] This mixed-valency oxide

remains active even under mildly acidic solutions. However, problems related with the stability still exists due to the rapid dissolution at neutral pH, which cannot be avoided.

In order to promote water oxidation, the presence of Mn(III) species is crucial.[140] Unfortunately, below pH 9 Mn(III) is unstable due to disproportionation reaction into Mn(II) and Mn(IV). Therefore, it is necessary additional strategies to improve the long-term catalytic activity, such the use of electrolytes, for example Li^+, to stabilize the conversion of MnO_x into layered structures.[141] Catalytic activity can also be tuned by interleaving organic molecules in layered MnO_x.[142] It has been reported that Mn(III) can be stabilized by coordinating amine groups on the surface of MnO_2, so thus shifting the electrocatalytic activity by approximately 500 mV.[143,144] Defects in the oxide, arising from oxygen vacancies, also increase the catalytic activity.[145] Interestingly, birnessite-type MnO_2 nanostructures have shown photocurrent activity,[131,146] with a strong dependence on the selected precursors.

In acidic media, MnO_x shows a unique self-repairing mechanism, whereby Mn(II) ions from solution are reoxidized at OER potentials.[147] In addition, MnO_x electrodes can even be screen printed.[148] Hybrid composites of MnO_x catalysts on gold or $CoSe_2$ surfaces,[35,149] and as Ca^{2+}-doped nanostructures,[150] also increase the water oxidation activity.

Iron Oxides

Iron oxide films are very attractive, because they are the cheapest possible catalyst.[151] Doyle et al. studied in detail these catalysts performing kinetic and mechanistic investigations.[152–154] Beyond their catalytic activity, FeO_x films can also been use in the fabrication of photoelectrochemical anodes, since the hematite band gap should be sufficient to promote water oxidation (2.1 eV).[32,155] However, the mismatch between hole diffusion, slow interfacial electron transfer, and optical penetration leads to poor efficiency.[156–158] FeO_x performs lower catalytic activity compared

to that obtained with Co or Ni, although Fe content dramatically improves the activity of NiO_x.

In general, photoelectrodes can be improved by nanostructuration.[159,160] Combined with solid-state supports, such as Nafion, or single-walled carbon nanotube composites, the activity of FeO_x increases, showing a decrease in overpotential of up to 50 mV.[161] Interestingly, when covering the hematite photoanodes with amorphous FeOOH, the photocurrent doubles,[162] exhibiting catalytic activity and long-term stability comparable to that obtained with the best CoO_x catalyst.[163]

Cobalt Oxides

Co_3O_4 is a typical electrocatalyst with interesting properties and many applications.[164] Electrochemical deposition of CoO_x from a buffered solution was first reported in 1902.[165,166] The use of CoO_x as electrocatalyst for water oxidation was reported in the 1970s.[167] An important breakthrough in cobalt oxide-based WOC was achieved when Nocera et al. discover a self-reparing mechanism operating at neutral pH (above pH 6) in a phosphate (P_i) electrolyte.[22,168] The robustness of this catalyst, referred as CoP_i, relies in the structural role of the P_i anions in stabilizing the CoO_x catalytic domains to avoid Co leaching.[169] Actually, the catalyst may be described as layered CoO_x with molecular dimensions, stabilized at neutral pH by the PO_4 groups,[111] where the P_i electrolyte also plays a role by facilitating rapid proton transfer,[170] and by improving the kinetics of the process.[171]

The growth mechanism of CoP_i films depends on many parameters, including pH, applied voltage, and electrolyte. Moreover, it was claimed that better performances were obtained by growing the films from acetate-buffered solution,[172] or when cobaloximes were used as cobalt source.[171] An optimal film thickness of 1.44 mm was defined in high buffer concentration solutions. It reached currents over 100 mA/cm^2 working in buffered natural waters, when deposited on large surface area electrodes.[173]

Dynamic potential-pH diagrams were used to compare the activities of Co_3O_4 and CoP_i catalysts.[174] CoP_i performs higher activity, probably due to its higher hydration, leading to an increase in the number of accessible sites,[175] but a current drop is observed at high overpotentials, occurring up to pH 12, probably due to the self-healing process, in which cobalt ions need to be reoxidized from solution to the electrode. On the contrary, due to a better mechanical strength and better adhesion to the support, Co_3O_4 did not show such instability. Therefore, it seems clear that the method of electrode preparation is a key factor.

The reaction mechanism of oxygen production from CoP_i is still unknown. However, electrochemical studies suggest that the O−O bond formation is a turnover-limiting chemical step, which is preceded by a PCET equilibrium step (Figure 1.25). Cyclic voltammetry experiments support the operative catalytic intermediate a formal oxidation state of Co(IV), whereas spectroscopic results indicate a resting state composed of Co(III/IV) mixed valence clusters.[19,171]

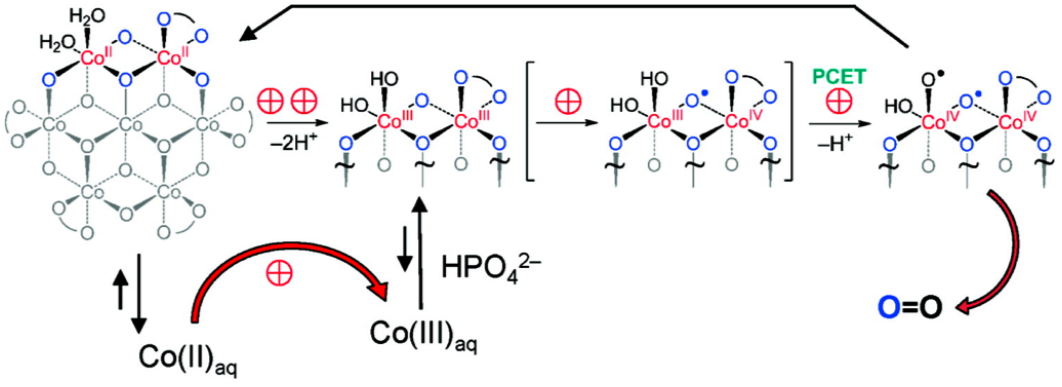

Figure 1.25: Proposed pathway for water splitting by Co-OEC. PCET equilibrium proceeds the turnover-limiting O−O bond-forming step. Curved lines denote pohosphate or terminal oxygen (from water or hydroxide). The oxyl radical in the far right structure is shown for emphasis. If the hole is completely localized on oxygen, then the Co oxidation state is Co(III) and not Co(IV).[19]

Nickel Oxides

The research of nickel oxides has been more limited when compared to CoO_x,[176] probably due to the need for a highly basic medium, and a complex evolution of the catalyst with aging.[177] Starting from the stable α-NiO(OH), it dehydrates into β-NiO(OH), and then applying oxidation potential in alkali media it evolves into a mixture β and γ-NiO(OH).[178] However, the presence of another unknown phase cannot be discarded.[179] Presumably, the formation of Ni(IV) under turnover conditions in alkali media at high overpotentials deactivates the β-NiO(OH) phase, which is commonly accepted as the active phase.[180,181]

Employing a borate electrolyte, NiO_x films can be electrodeposited in a controllable maner,[109,182] leading to oxygen evolution at pH 9.2, with the requirement of pre-electrolysis treatment to increase two orders of magnitude their efficiency.[108] This has been initially related to an increase in the oxidation state of Ni enters, from Ni(III) to Ni(IV), at least on the surface of the films, although Ni(IV) was though to be inactive.

Mixed Oxides

Most studies made on mixed oxides are based on the synergistic effect between Ni and Fe. A simple procedure to prepare nanostructured mixed metal oxides by solution casting, was reported by Boettcher and co-workers.[183] These optimized films of $Ni_{0.9}Fe_{0.1}O_x$, led to a 30 mV/decade Tafel slope, and reached 1 mA/cm^2 at just 300 mV overpotential at pH 14. Moreover, these films are compatible with photoanodes.[184,185]

In 1987 Corrigan reported the enhancement of the water oxidation activity of NiO_x films with the incorporation of Fe impurities from the KOH electrolyte after several catalytic cycles.[186] Bell et al. also corroborated the positive effect of Fe upon the features of NiO_x.[187] Additionally, Kitchin et al. identified the presence

of a mixed $NiO/NiFe_2O_4$ phase at low Fe concentrations as a key component for enhanced activity.[188] In fact, recent studies demonstrate that NiO_x is not as active as it was supposed when water oxidation experiments are performed in Fe-free KOH solutions.[189] The lack of water oxidation activity of NiO_x up to very positive potentials in the absence of Fe(III) reveals an electronic contribution. Therefore, Fe has an electron-withdrawing effect upon Ni centers, giving more oxidizing power to the Ni(III/IV) sites.

Double perovskites have been described as highly active WOCs that are stable in alkaline solutions,[190–203] although the need to include rare earths precludes their extended use.[194,195] For example, Ba−Sr−Co−Fe perovskite proved to be 10 times faster than IrO_x.[196] Some of these perovskites exhibited structural changes during the water oxidation reaction, going from crystalline to amorphous, which could be due to conversion of the local structure from corner-sharing octahedral to edge-sharing octahedral, associated with enhanced activity.[197,198] Low-temperature annealing optimizes the performance, promoting lower concentration of charged cations and increased OH surface coverage.[199] It is worth mentioning that perovskite are bifunctional catalysts that are also active for the oxygen reduction reaction.[200]

Prussian Blue Derivatives

The catalytic activity of Prussian blue analogues (PBAs) in redox chemistry has been well documented for many years.[204] Despite being used intensively as oxidation catalysts, the activity of PBAs for the OER was not established until 2013, when Galán-Mascarós et al. reported the electrocatalytic activity of $K_{2x}Co_{(3-x)}[Fe(CN)_6]_2$ (CoFePB).[104] At neutral pH, this PBA exhibited kinetics that are comparable (if not superior) to those of metal oxides, with unparalleled long-term stability. Electrodes coated with CoFePB maintained a persistent catalytic activity for weeks at neutral pH under ambient conditions.

Characterization experiments were conducted to these modified electrodes after

electrochemical water oxidation, including surface-sensitive techniques such as Raman or X-ray photoelectron spectroscopy, confirming the absence of any trace of transition metal oxide. Therefore, the participation of metal oxide nanostructures evolved during the catalysis, that would be responsible for the catalytic activity was ruled out.[205] In addition, the materials remained active in acid media, in which MO_x participation would not be possible.

PBAs appear to be a viable WOC alternative to metal oxides for promoting water oxidation in artificial photosynthesis devices. They present competitive kinetics, are obtained from Earth-abundant metals, and can easily be processed as powders, thin-films or nanoparticles, with classic coordination chemistry tools. Furthermore, they are active at neutral or acidic pH, without the need for additional electrolytes, because their stability resides in the strong cyanide bridge in the solid state, with no participation of oxo or hydroxo groups in their skeleton.

1.6 Polyoxometalate Chemistry

Oxygen is one of the most abundant elements in the Earth's Crust. It represents the 55 atom % from which only the 8 atom % is attributed to H_2O, silicate-based rocks (SiO_2), and clays (Al_2O_3). The bulk of the chemistry of combined oxygen is either solid-state and surface chemistry of insoluble metal oxides (*e.g.* Co_3O_4, Fe_2O_3), or nonmetal oxoanions in aqueous solution such a H_3PO_4 or H_2SO_4. Moreover, there is a third aspect of the oxygen chemistry which combines both solution and metal oxide fields, that are polyoxometalates (POMs).[206]

Polyoxometalates are discrete anionic clusters made of early transition metal oxides building blocks, that are formed spontaneously in water when either soluble, molecular monomeric transition metal precursors, or insoluble metal hydroxides or oxides are adjusted to the appropriate pH. The most common POMs are based on molybdenum or tungsten, less frequently vanadium, niobium, or tantalum (or mixtures of these elements), all of them in their highest oxidation state (d^0, d^1).[207,208]

The general formula of POMs is $\{MO_x\}_n$, where M stands for the metal (*addenda atom*) and x = 4-7. Commonly, polyoxometalates are characterized by MO_6 octahedra with the ability to form short terminal M=O ($d\pi$-$p\pi$) bonds, resulting in discrete structures with such bonds directed outwards. These structures are governed by electrostatic and radius-ratio principles, also observed for extended ionic lattices, and are described as assemblages of MO_x polyhedra linked *via* shared corners, edges, and less frequently faces, with the metal displaced towards the exterior of the polyanion structure (vertex or edge of its own polyhedron).[206]

Polyoxometalates have low surface charge densities resulting in weak anion-cation attractions. This property confers to POMs an extensive solution chemistry in both aqueous and nonaqueous solvents. Two different types of oxygen atoms can be found in the surface, terminal (M=O) and bridging (M-O-M). Those placed in a bridging position carry a greater negative charge, providing a higher basicity and

the tendency of being protonated in preference to terminal oxygen.

Although polyoxometalates were discovered in 1783 by the spanish Delhuyar brothers,[209] and the first reported structure was in 1826 by Berzelius,[210] it is only within the last decades that modern experimental techniques and synthetic approaches have allowed for a more exhaustive study of structure and reactivity. Polyoxometalates raised in popularity thanks to a Review by Pope and Müller in 1991,[211] and afterwards when a special issue about POMs in *Chemical Reviews* organized by Hill in 1998[212] presented the history, developments, and applications of the many areas covered by POM chemistry. Later in 2010 Cronin presented a "polyoxometalate periodic table" in a POMs' review,[213] where it is presented a classification of the different structures known since the date and the relation to each other. In this table it is highlighted the huge amount of compounds which fall into the polyoxometalate category, with different shapes and sizes.

All these structures can be classified, with some limitations and exceptions, in thee different classes:[213]

- *Heteropolyanions:* Most POMs can incorporate primary (central) and/or secondary (peripheral) heteroatoms. There is no restriction on the element that can serve as heteroatom with the exception of the noble gases. Typically these elements belong to the p or d block (*e.g.* P(V), Si(IV), or V(V)). Heteropoly compounds tend to be stable hydrolitically over a wide pH range. They also represent the most studied type of POMs, with special emphasis on the archetypal Keggin $[XM_{12}O_{40}]^{n-}$ and Wells-Dawson $[X_2M_{18}O_{62}]^{n-}$ anions (Figure 1.26), where M = W or Mo, and X is a tetrahedral template that can be most of the elements in the periodic table. In addition, tungsten-based Keggin and Wells-Dawson anions can allow one, two, or three vacancies, where the original tungsten atom can be replaced with other p or d block elements, including those with appended organic groups in a predictable manner. Lacunary POMs have high negative charge densities and can serve as inorganic

ligands to stabilize transition metal clusters.

- *Isopolyanions:* These metal-oxide frameworks do not have heteroatoms, which result in a lower stability than heteropolyanions. Still they have interesting physical properties such as high charges and strongly basic oxygen surfaces, which means they can be used as building blocks. In Figure 1.26 are shown two examples of isopoly compounds, the Lindqvist archetype and the decavanadate.

- *Molybdenum blue and molybdenum brown reduced POM clusters:* Based on molybdenum-oxide building blocks, these POMs are spherically shaped molecular systems with nanoscale size. They are constructed by intertwining pentagonal {(Mo)Mo_5}-type building blocks with linker entities of different size that bridge those pentagonal units. Their composition was unknown until Müller in 1995 reported the composition of a very-high-nuclearity cluster {Mo_{154}}, which has a ring topology. This highly reduced POMs have many potential applications in nanoscience. An example of these giant polyoxometalates is shown in Figure 1.26, where the structure of the {Mo_{132}} clearly shows the pentagonal {(Mo)Mo_5} building blocks (in blue) and the linker moieties (in red) composed by two Mo(V).

1.6.1 The Keggin Archetype

J. F. Keggin reported for the first time in 1933 the crystal structure of the polyoxometalate 12-tungstophosphoric acid employing powder X-ray analysis.[214] Nowadays, this structure is known as α-Keggin (Figure 1.27) and presumably is the most studied archetype among polyoxometalates, since the majority of the heteropolytungstates are based on that structure or from derived fragments. With general formula α-$[XM_{12}O_{40}]^{n-}$, it has overall T_d symmetry with a central XO_4 tetrahedron, acting as a template, surrounded by twelve MO_6 octahedra arranged in four

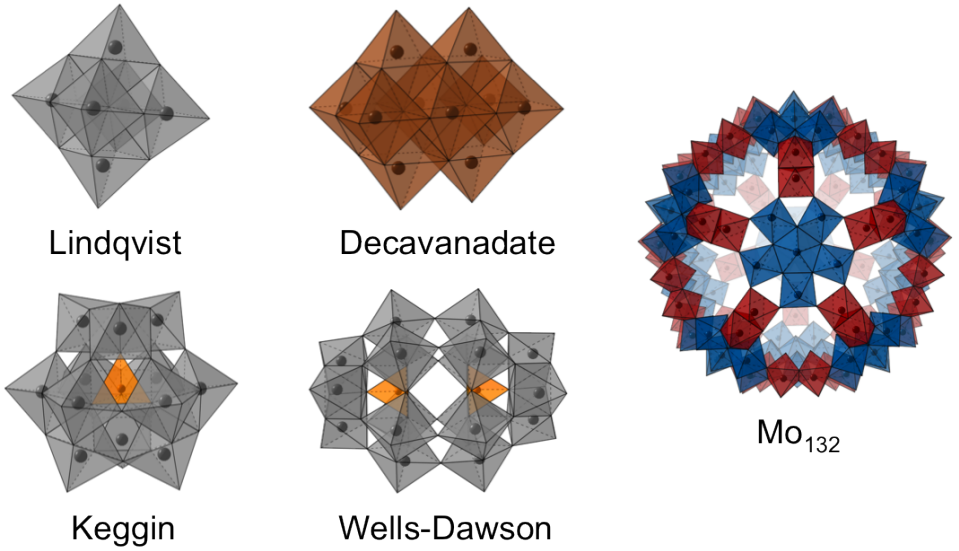

Figure 1.26: Example of some typical archetypes of polyoxometalates. Top left: Lindqvist $[M_6O_{19}]^{2-}$; Top center: Decavanadate $[V_{10}O_{28}]^{6-}$; Bottom left: Keggin $[XM_{12}O_{40}]^{n-}$; Bottom center: Wells-Dawson $[X_2M_{18}O_{62}]^{n-}$; Right: $\{Mo_{132}\}$ as $[Mo_{132}O_{372}]^{12-}$, with the pentagonal units in blue $[Mo_6{}^{VI}O_{21}]$, and the linkers in red $[Mo_2{}^{V}O_4]$.

edge-shared trimers M_3O_{13}. These trimers are linked to each other and to the central heteroatom by corner shared bridges.[207]

Moreover, the Keggin polyoxometalate has five different isomers, the so-called Baker-Figgis isomers,[215] labeled as α-, β-, γ-, δ-, and ϵ-structures as shown in Figure 1.27. These isomers are obtained by a rotation of 60° of a three edge-shared M_3O_{13} trimers. Therefore, starting from the α isomer, when one of its trimers is rotated 60° it is obtained the β-Keggin structure, thereby reducing the overall symmetry from T_d to C_{3v}. Next, upon rotation of the second trimer it is obtained the γ-Keggin isomer with an overall C_{2v} symmetry. As a result new corner-shared M−O−M linkages are formed with a reduction of the M$\cdots$M distance and a more acute M−O−M angles, which confer a lower stability of the γ-isomer due to an increase of the coulombic repulsions, and less favorable pπ-dπ interactions. Rotation of the third and the fourth trimer yields to the δ-, and ϵ-Keggin structures, respectively. The δ-isomer has a C_{3v} symmetry, whereas the ϵ one has a T_d symmetry. These rotations increase

the number of M···M contacts decreasing, hence, the stability of the isomers upon rotation of the triads.

Theoretical DFT calculations carried out for different Keggin polyanions showed that α and β isomers have comparable stabilities, due to the absence of M···M contacts. On the contrary, for Keggin structures with 2, 3 and 4 rotated triads (*i.e.*, γ, δ, and ϵ isomers, respectively) the number of M···M contacts formed increase, namely 1, 3 and 6. It was computed a destabilization of 8-9 kcal mol^{-1} per M···M contact, therefore, in general the relative energy of the five isomers follows the trend $\alpha < \beta < \gamma < \delta < \epsilon$.[216]

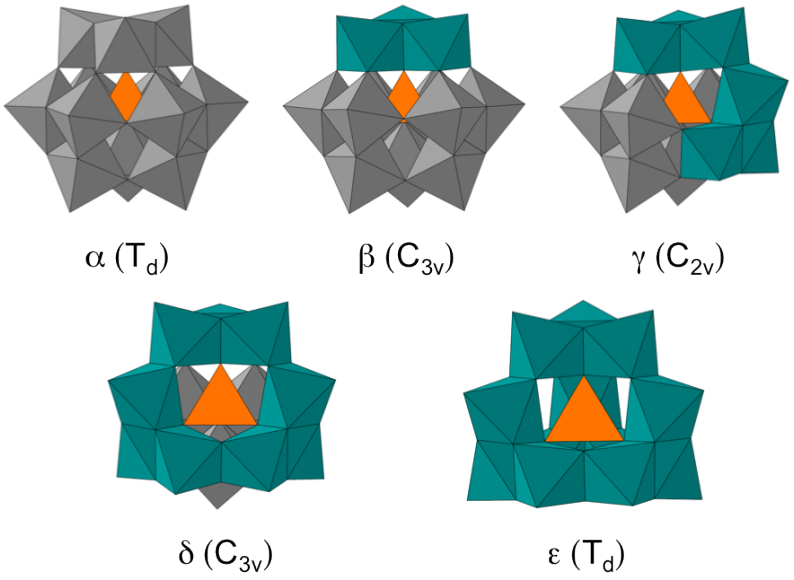

Figure 1.27: Polyhedral representation of the five Baker-Figgis isomers of the Keggin archetype with their overall symmetry.

Polyoxometalates are known to be stable in a wide range of pH, from acid to moderate alkaline. However, increasing the pH of an aqueous solution containing the POM leads to a progressive degradation of the polyanion towards lacunary structures, where 1, 2 or 3 octahedral units have been removed. These new vacancies can be filled with $[M^{n+}{=}O]^{(n-2)+}$ fragments or organic groups. Hence, lacunary polyoxometalates are used as polydentate inorganic ligands since they are independently

stable and isolable.[207,216] Lacunary species of the Keggin structure are know for the α, β, and γ, as shown in Figure 1.28. DFT calculations reveal that in monolacunary Keggin tungstates, the internal heteroatom has an influence in the relative energies of the α and β isomers, with a preference for the β isomer when decreasing the oxidation state of the heteroatom. For example, the β-monolacunary Keggin, β-$[XW_{11}O_{39}]^{n-}$, is more stable when employing Si(IV) than with P(V) as heteroatom. Moreover, the use of different countercations can favor the formation of one isomer over the other, as in the case of Na^+, which has a preference on the α isomer over the β.[216]

Figure 1.28 shows the different lacunary Keggin structures that can be isolated. The monolacunary $\{\alpha\text{-}XW_{11}O_{39}\}$ archetype is formed by removal of one of the twelve octahedra, whereas trilacunary species are formed either by loosing three corner-shared octahedral $\{A\text{-}\alpha\text{-}XW_9O_{34}\}$, or by removal of three edge-shared octahedral $\{B\text{-}\alpha\text{-}XW_9O_{34}\}$. Three different monolacunary structures of the β isomer can be obtained due to the its C_{3v} symmetry. Hence, the $\{\beta_1\text{-}XW_{11}O_{39}\}$ is obtained when one octahedral opposite to the rotated trimer is subtracted. Removal of an octahedral unit located in the central belt yields the $\{\beta_2\text{-}XW_{11}O_{39}\}$, whilst loosing one octahedral of the rotated trimer leads to the $\{\beta_2\text{-}XW_{11}O_{39}\}$ lacunary Keggin. As seen in the case of the α isomer, two trilacunary β-Keggin can be isolated, reaching the $\{A\text{-}\beta\text{-}XW_9O_{34}\}$ upon removal of the corner-shared trimer opposite to the rotated trimer, and the $\{B\text{-}\beta\text{-}XW_9O_{34}\}$ obtained by subtraction of an edge-shared trimer, with none of the rotated octahedra involved. Finally, only a divancant species is found in the case of the γ isomer, namely $\{\gamma\text{-}XW_{11}O_{36}\}$, and it is reached by taking out two corner-shared octahedral belonging to the two rotated trimers.

As said before, lacunary species can be used as multidentate ligands that can stabilize small metal oxide frameworks or organic groups. This ability confers the POMs a huge range of physical and chemical properties, with potential applications in diverse fields as, magnetism, medicine, analysis, biochemistry, chirality or

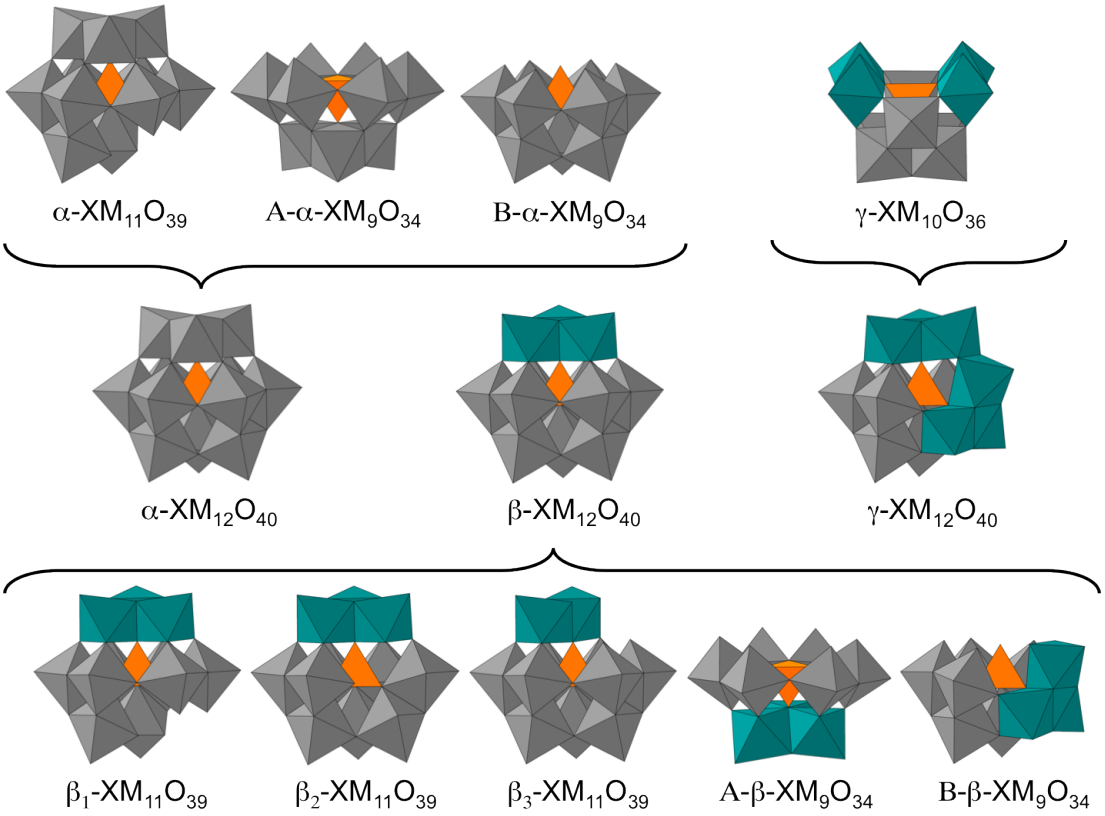

Figure 1.28: Lacunary Keggin species obtained from the α, β, and γ isomers than have been isolated.

materials science.[206–208,213,216,217] Nevertheless, the field in which POMs have been commonly used is in catalysis, for example: oxidation of aromatic hydrocarbons; olefin polymerization and epoxidation; and Friedel-Crafts-type alkylation, acylation and sulfonation of aromatics. Moreover, during the last decade, POMs have also been identified as good water oxidation catalysts.[218–220]

1.6.2 Polyoxometalates as Water Oxidation Catalysts

Polyoxometalates are very interesting compounds as water oxidation catalysts, since they can serve as all-inorganic multidentate ligands to stabilize transition metal oxide clusters, with high stability under strong oxidizing conditions.[206,213,217] POMs are also known as strong Brœnsted acids and as fast reversible multielectron ox-

idants, stabilizing high-valent intermediates and assisting deprotonation equilibria on the polyoxygenated surface.[216,221–223] Moreover, they have the ability of stabilize adjacent d-electrons centers through multiple-μ-hydroxo/oxo bridging units, which is one of the most important features that natural enzymes posses to effect multiple electron/cascade transformations.[10] Hence, polyoxometalates can be employed as bifunctional (acid and redox) catalysts, with the stability of heterogeneous catalysts and with the tunability and processing of homogeneous catalysts.

A Tetraruthenium(IV)oxo-core Stabilized by Polyoxometalate Ligands

The first breakthrough in water oxidation catalyzed by POMs was achieved in 2008, when two different groups reported, separately, the synthesis and the activity of a tetraruthenate core stabilized by two $[\gamma\text{-}SiW_{10}O_{36}]^{8-}$ polyanions as $[Ru_4(\mu\text{-}O)_4(\mu\text{-}OH)_2(H_2O)_4(\gamma\text{-}SiW_{10}O_{36})_2]^{10-}$ (**Ru_4Si**).[218,224] As shown in Figure 1.30, the ruthenium core, $[Ru_4{}^{IV}(\mu\text{-}O)_4(\mu\text{-}OH)_2(H_2O)_4]^{6+}$, has an adamantane-like arrangement with the four ruthenium atoms forming a tetrahedron. The core is stabilized by the two γ-SiW_{10} units, where the ruthenium centers are corner-sharing and not ligated to the central SiO_4 unit. The γ-SiW_{10} archetypes are rotated 90° around the vertical C_2 axis relative to one another, yielding an overall D_{2d} symmetry to the POM. Two oxygen atoms of the core are monoprotonated, hence two adjacent Ru atoms joined to the POM are linked *via* hydroxo bridges, with a Ru−O−Ru bond angle of *ca.* 131.2°. Additionally, they each form a strong three-center H-bond with two proximal Si−O−W bridges. Finally, four aqua ligands are found in the terminal oxygen atoms bound to each Ru(IV) center.

The catalytic activity of the polyoxometalate was tested employing different chemical oxidants. In short, Bonchio evaluated the oxygen evolution with an excess of Ce(IV) in strong acidic media (pH = 0.6) at 20°C. Under these conditions, 385 μmol of O_2 were obtained after 2 hours, reaching an overall 90% on the added oxidant. Moreover, equivalent activity was obtained upon addition of Ce(IV), what

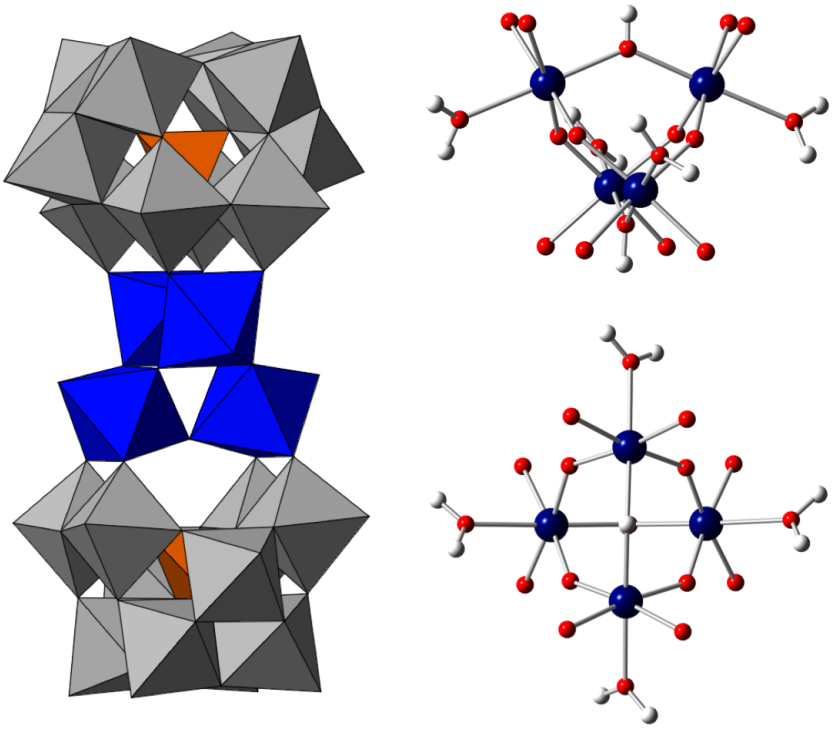

Figure 1.29: Polyhedral representation of the polyanion **Ru_4Si** (left). Top-front views of the central tetraruthenium-oxo-core (right). The polytungstate fragments are shown as gray octahedra, Si as brown tetrahedra, Ru as blue octahedra and balls, and O and H as red and white balls, respectively.

highlights the stability of the catalyst under catalytic conditions. The POM showed excellent evolution rates, reaching a maximum TOF > 450 h^{-1}.[218] A different strategy was employed by Hill, who carried out dark reactions using $[Ru(bpy)_3]^{3+}$ as chemical oxidant at pH 7.[224] In this case, due to the instability under oxidizing conditions of $[Ru(bpy)_3]^{3+}$,[225] the O_2 yield was substantially lower (maximum of 75%). Posterior studies revealed that the catalyst is stable under turnover conditions in neutral to mildly acidic pH, whereas it slowly decomposes in strong acid (pH < 1.5),[226] contrary to that observed by Bonchio and co-workers.[218] **Ru_4Si** shows several voltammetric peaks corresponding to the oxidation of the Ru(IV) centers to Ru(V) centers, followed by a catalytic wave assigned to the oxidation of H_2O to O_2. The overall 4-electron reduction potential of the $Ru(V)_4/Ru(IV)_4$ couple was

estimated to be ∼0.95 V at neutral pH, whereas, at the same pH the 4-electron oxidation of water to molecular oxygen is ∼0.82 V, hence the reduction potential obtained with the POM is sufficient to allow water oxidation catalysis. Additionally, light-driven water oxidation experiments with $[Ru(bpy)_3]^{2+}$ as photosensitizer, and sodium persulfate as sacrificial electron acceptor, showed outstanding catalytic performance of **Ru_4Si**.[227] Furthermore, flash photolysis experiments were carried out to study the kinetics of electron transfer from the catalyst to the oxidized photosensitizer $[Ru(bpy)_3]^{3+}$. The experiments confirmed that hole scavenging between **Ru_4Si** and $[Ru(bpy)_3]^{3+}$ occurs at a very fast rate, so thus limiting side reactions that yield into decomposition of the photosensitizer; results also showed that **Ru_4Si** is able to multiply scavenge $[Ru(bpy)_3]^{3+}$ within milliseconds, leading to high turnover frequencies for oxygen production, close to those found for the oxygen evolving center into the photosystem II.[228]

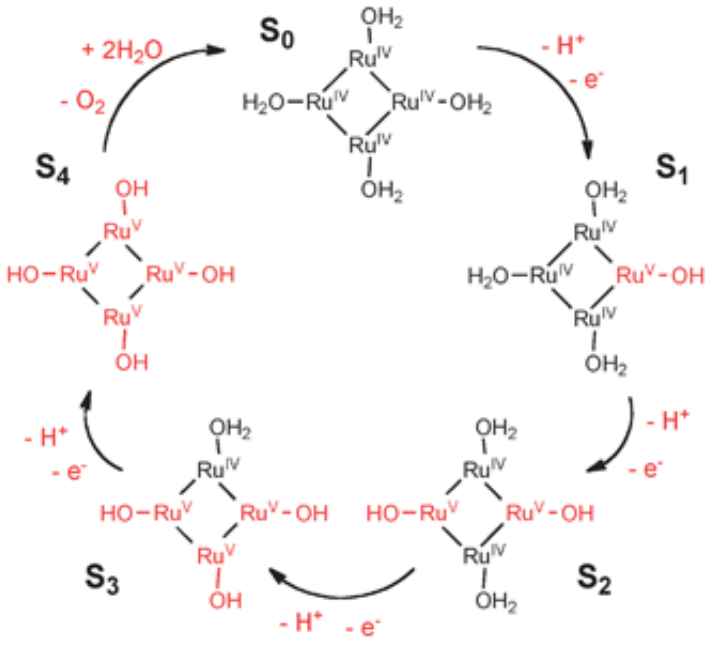

Figure 1.30: Schematic representation of the studied stepwise mechanism for the water oxidation in the oxygen-evolving complex (OEC): $[Ru^{IV}{}_4(\mu\text{-}OH)_2(H_2O)_4(\gamma\text{-}SiW_{10}O_{36})_2]^{10-}$ polyoxometalate. It is assumed that from the S_0 to the S_4 state each Ru moiety undergoes one electron oxidation and loses one proton.[216]

DFT calculations, at the BP86 and OLYP/TZP/COSMO level, were carried out by Bo to study electronic structures of the intermediate species suggested by electrochemical experiments.[229] A model of the polyanion was employed as a tetraruthenate core capped with eight chloride atoms replacing the POM ligands, since calculations for the entire molecule were not possible. The Ru_4 core undergoes four stepwise oxidations, where the starting state involves four Ru(IV) centers (S_0), yielding a high valent $Ru(V)_4$ reactive oxygen evolving state (S_4). Hence, each Ru^{IV}-(H_2O) moiety would undergo a PCET event to reach a Ru^{V}-(OH) state. Calculations for S_0, S_1, and S_3 species, confirm EPR data, where the low-spin state was found to be the most stable. On the contrary, for the second oxidation (species S_2) calculations predict a *cis* conformation of the Ru^{V}-(OH) moiety in the triplet state as the most stable, which disagrees with EPR data. Additionally, Musaev also carried out DFT calculations (at the RI-BP86/TZ/COSMO level) on the **Ru_4Si** polyoxometalate and the intermediate oxidized species.[230] In this case the loss of protons was not considered. Calculations confirm the high stability of the catalyst during the four subsequent one-electron oxidations, since the most closely lying HOMOs and LUMOs of the species S_0 are characterized to be bonding and antibonding MOs of the central tetraruthenium-oxo-core.

Moreover, hybrid Carr-Parrinello/Moleular Dynamics (QM/MM) simulations with explicit solvation of the S_0 species show a solvent-induced structural distortion of the central tetraruthenium-oxo-core, that brings the calculated average distances in excellent agreement with the experimental values.[231] The thermodynamic profile of the reaction was also examined by means of DFT (B3LYP and HSE06 functionals), where the computed free energy difference between the S_0 and S_3 species fairly reproduces within 0.25 eV with the corresponding experimental value. Although there is no experimental data for the fourth PCET event (S_3 to S_4), the computed free energies values for overall oxidation (3.38 eV and 4.00 eV using B3LYP and HSE06 functionals, respectively) are significantly lower than the thermodynamic

limit for water oxidation (4.92 eV). This might suggest that the S_0/S_4 couple is not the responsible for the catalytic water splitting observed experimentally. Therefore, one way to promote the water splitting with four PCET events would involve a catalytic cycle with higher oxidation states than the Ru^{IV}-$(H_2O)/Ru^{V}$-(OH) of the S_0/S_4 couple.

A Tetracobalt(II)oxo-core Weakley Sandwich

The use of water oxidation catalysts based on noble metals should be avoid due to their high price in the market. The high costs of fabrication of water splitting devices that incorporate noble metal-based catalysts would lead to hydrogen production at such high price that would make it impossible to compete with the hydrogen produced by fossil fuels, that industry is employing nowadays. Therefore, in order to reduce production costs and make the process competitive, it is easy to assume that it is required the use of Earth abundant materials for the fabrication of water oxidation devices for real industrial applications.

Another breakthrough came out in 2010, when Hill reported the catalytic water oxidation activity of the tetracobalt-oxo-core sandwich-type POM $[Co_4(H_2O)_2(\alpha\text{-}PW_9O_{34})_2]^{10-}$ (**Co_4P**).[219] The structure of this polyanion was already described by Weakley *et al.* in 1973,[232] which consists in a rhomb-like tetracobalt-oxo-core build of edge-linked $Co^{II}O_6$ octahedra with coplanar cobalt atoms, stabilized by two trilacunary Keggin units, $[B\text{-}\alpha\text{-}PW_9O_{34}]^{9-}$, as inorganic ligands. Contrary to the observed in the **Ru_4Si** structure, the disposition of the four cobalt atoms leads to a conformation where two of them occupy internal positions without terminal Co-O bonds, whereas the other two cobalt atoms are occupying the external positions linked each one to a water ligand (Figure 1.31).

The activity of **Co_4P** was examined using $[Ru(bpy)_3]^{3+}$ as chemical oxidant in 30 mM sodium phosphate buffer at pH 8. The oxygen production was monitored with gas chromatography, obtaining a TOF > 5 s^{-1}, that supposed the highest rate

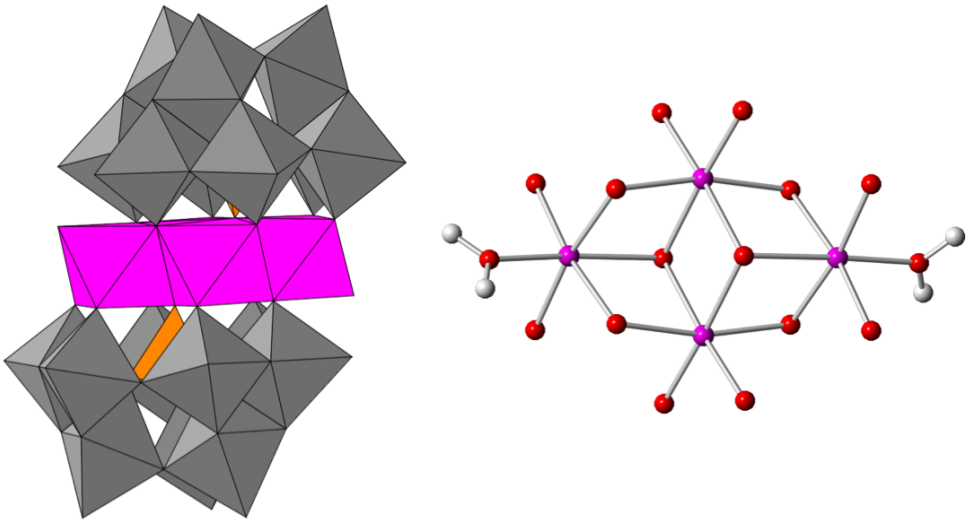

Figure 1.31: Polyhedral representation of the polyanion **Co$_4$P** (left). Top view of the central tetracobalt-oxo-core with the two external water ligands (right). The polytungstate fragments are shown as gray octahedra, P as orange tetrahedra, Co as pink octahedra and balls, and O and H as red and white balls, respectively.

observed for a molecular WOC at that time.[219] Oxygen evolution yields were found to be highly pH and buffer dependent. In the same work several cobalt-containing polyoxometalates were tested as water oxidation catalysts under the same experimental conditions, as for example, the analogue tetracobalt-oxo-core stabilized by two trilacunary Wells-Dawson units. Surprisingly, none of them showed catalytic activity but the **Co$_4$P**, highlighting the importance not only of the nature of the ligands employed to stabilize the core, but also the structure of the active cobalt centers and synthesis conditions. Later, the same group reported the catalytic activity of this POM under light-driven conditions, employing $[Ru(bpy)_3]^{2+}$ as photosensitizer and sodium persulfate as sacrificial electron acceptor, in a 80 mM sodium borate buffer at pH 8. Experiments were also carried out with **Ru$_4$Si** for comparison, demonstrating that **Co$_4$P** is more efficient under the same conditions.[233]

During the last years, the molecular nature of the catalyst has been put into question,[234–237] since $Co^{2+}(aq)$ cations may exist in solution equilibrium along with the

cobalt-containing polyoxometalates.[238] Aqueous cobalt ions and cobalt oxide/hydroxide that form in situ from the former, under certain turnover conditions, are known to be water oxidation catalysts.[22,118,225] Therefore, it is important to carefully identify the nature of the true catalyst and differentiate homogeneous and heterogeneous water oxidation catalysis.[238] Hill and co-workers demonstrated with several lines of evidences that $\mathbf{Co_4P}$ is an authentic POM WOC, in both $[Ru(bpy)_3]^{3+}$ and $[Ru(bpy)_3]^{2+}/S_2O_8{}^{2-}$ systems, despite the presence of Co^{2+}(aq) in solution.[219,238] Lower catalytic activity of Co^{2+}(aq) and CoO_x compared with that of $\mathbf{Co_4P}$ was found under the same experimental conditions, so thus identifying the POM as the only responsible of the high oxygen evolution rates. This finding was also confirmed through careful studies by Finke.[234,236] On the contrary, $\mathbf{Co_4P}$ and cobalt-containing polyoxometalates in general, used in solution as electrochemical water oxidation catalysts are not stable. Finke provided experimental evidences that a CoO_x WOC film is formed in situ on the working electrode surface under oxidizing conditions, due to the leaching of Co^{2+}(aq) from the POM.[234,235] Therefore, the observed catalytic activity is the result of this released Co^{2+}(aq). Nevertheless, prevention of the CoO_x film formation can be achieved by selective catalyst poisoning, adding stoichiometric amounts of 2,2'-bipyridine (bpy) as an inhibitor.[219] Therefore, bpy reacts with the released Co^{2+}(aq) resulting in the precipitation of the inactive water oxidation salt of $[Co(bpy)_3]^{2+}$.[239] Under these conditions it has been identify the $\mathbf{Co_4P}$ as the actual molecular water oxidation catalyst.

All these experiments highlight the importance, and the challenge of identifying the nature of the catalyst under working conditions, to avoid drawing erroneous conclusions. Determining whether a material acts as a homogeneous or heterogenous catalyst is particularly complicated when employing POMs under oxidizing conditions, due to the possible formation of metal oxides along the experiment, which are known as active species for WOC.

A High Nuclearity Nonacobalt(II) Polyoxometalate

In 2012 our group reported the water oxidation catalytic activity of a high nuclearity cobalt-containing polyoxometalate: the nonanuclear $[Co_9(H_2O)_6(OH)_3(HPO_4)_2(PW_9O_{34})_3]^{16-}$ cluster (**Co$_9$**).[220] The synthesis and structure of this POM was already described by Weakley *et al.* in 1984.[240] This polyanion is composed by three trilacunary B-α-Keggin units, where three Co^{2+} ions occupy the octahedral vacant positions, in each Keggin fragment, yielding triangular edge-sharing Co_3O_{12} moieties, as seen in Figure 1.32 The three Keggin fragments are then connected by three hydroxyl bridges and two $HPO_4{}^{2-}$ anions forming a triangle of triangles. Six of the nine Co ions complete their coordination sphere with terminal water molecules prone to be oxidized. The higher nuclearity of **Co$_9$** compared with that of the **Co$_4$P** allow to draw four main structural differences:

- A triangle of triangles versus rhombohedral core structure
- Presence of hydroxyl bridges versus only oxo bridges
- Available hydrogen phosphate bridges that are not embedded in the POM structure
- Higher percentage of terminal water molecules

The electrochemical water oxidation activity of **Co$_9$** was tested in homogeneous conditions carrying out bulk water electrolysis experiments in a two-chamber cell separated by a glass frit. Fluorine-doped tin oxide (FTO) coated glass was used as anode, whereas platinum mesh electrodes were employed as cathode. The experiments were performed in 50 mM sodium phosphate buffer at pH 7 with 1 M $NaNO_3$ as the electrolyte. With the absence of catalysts the current densities obtained when applying 1.41 V vs NHE were negligible. However, with the addition of **Co$_9$** (1 mM) to the anode compartment, the current density increased over 1 order of magnitude.

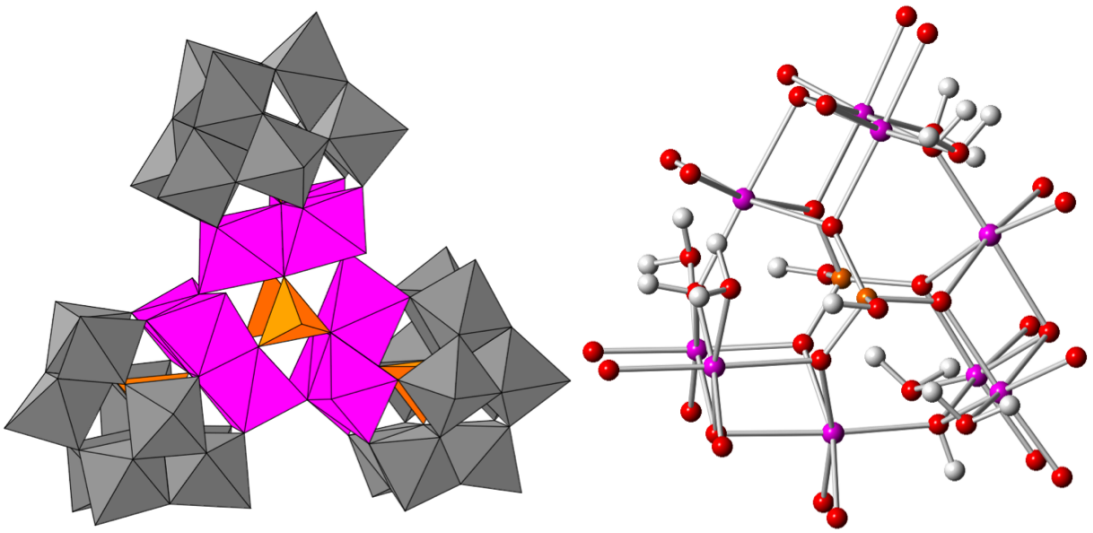

Figure 1.32: Polyhedral representation of the polyanion **Co$_9$** (left). Detailed view of the central cobalt-oxo-core forming the triangle of triangles (right). The polytungstate fragments are shown as gray octahedra, P as orange tetrahedra, Co as pink octahedra and balls, and O and H as red and white balls, respectively.

During experiments a brown film grew on the anode, characterized as cobalt oxide with some phosphate traces. The activity of the deposited film was tested under the same conditions in the absence of **Co$_9$**. The current density reached in this case was essentially the same as observed in the previous experiment, indicating that the deposited cobalt oxide is the main active WOC under these conditions. The cobalt oxide film deposition arises from the oxidation of free Co^{2+} ions leached from the POM. The loss of the initial **Co$_9$** concentration during water electrolysis was estimated through UV-vis spectroscopy to be about 15 %. Therefore, addition of chelating ligands, as 2,2'-bipyridyl (bpy), during the experiment, prevented the formation of the cobalt oxide film since the bpy trapped the Co^{2+} ions to form $[Co(bpy)_3]^{2+}$, which under oxidizing conditions yields the highly inert $[Co(bpy)_3]^{3+}$ species. Repeating the experiments upon addition of bpy, the current density also increased by less than one-third that observed in the absence of bpy. This suggested that the main catalyst was different in both experiments. No traces of cobalt were

found on the surface of the FTO electrode. In addition, by repeating the experiment with the same "as used" electrode in a buffer solution without **Co$_9$**, the current density obtained was very close to the original blank. The efficiency of oxygen evolution under these conditions was determined employing a fluorescence probe, reaching a 90 % for over 1 h. The current not involved in the catalytic process accounts for the oxidation of the $[Co(bpy)_3]^{2+}$ species generated in solution to $[Co(bpy)_3]^{3+}$. At the end of the experiments a highly insoluble pink precipitate appeared that was confirmed to be a $[Co(bpy)_3]^{3+}$ salt of the **Co$_9$**. The kinetics of the reaction was studied by means of Tafel experiments from steady state current density experiments. Results showed a clear dependence on the concentration of **Co$_9$**, since for concentrated solutions (1 mM) the Tafel slope was 130-140 mV/decade, indicating that the rate-determining step is electrochemical (electron- or mass-transport issues),[37,241] with an overpotential of 776 mV needed to reach 1 mA/cm^2. On the contrary, in diluted conditions (**Co$_9$** 0.06 mM) the slope was in the 55-65 mV/decade range, indicating that a chemical step is the rate-limiting one in this case,[38,171] with an overpotential of 695 mV to reach 1 mA/cm^2. These overpotentials are higher than those observed for the cobalt oxide, but due to the concentration-dependent current density obtained for **Co$_9$**, a direct comparison is not fair to the homogeneous catalyst. Finally, the calculation of the diffusion layer to determine the number of molecules interacting with the electrode at a given time was not possible due to the absence of a noncatalytic redox process.[27,242] Therefore the TOF could not be directly calculated from the electrochemical data.

In the same work, the catalytic activity of **Co$_9$** was tested employing NaClO as chemical oxidant. Oxygen evolution starts immediately after adding **Co$_9$** to a solution of sodium hypochlorite with a 0.9 M sodium phosphate buffer at pH 8. Online mass spectrometry (MS) confirmed that only oxygen was evolved during the reaction. Additionally, quantitative oxygen evolution was monitored with differential manometry at different oxidant/catalyst ratios, and confirmed with gas chromatog-

raphy (GC), showing excellent agreement. In these experiments a maximum TON of over 400 and an initial TOF of 350 h^{-1} were found when a $3.3x10^3$:1 oxidant/$\mathbf{Co_9}$ ratio was employed. However, low efficiencies were obtained, indicating the presence of competing reactions, probably disproportionation of hypochlorite to yield chloride and chlorite (vide infra). Experiments were also carried out at different temperatures, where the optimum performance was found at 35°C, with 50 % efficiency. An increase of 2-fold on the initial TOF was observed when changing the pH of the reaction from 7 to 9. After oxidation, no change in the absorbance by UV-vis was detected, and dynamic light scattering (DLS) analysis also ruled out the presence of heterogeneous nanoparticles. The $\mathbf{Co_9}$ was recystallized after the experiments showing identical IR spectrum and X-ray diffraction compared to that obtained with fresh $\mathbf{Co_9}$. Moreover, $\mathbf{Co_4P}$ was employed as water oxidation catalyst under the same experimental conditions for comparison. Calculated initial TOF data indicate that $\mathbf{Co_9}$ is at least 8 times faster than $\mathbf{Co_4P}$, carrying out the experiments with the same POM concentration.Taking into account the molecular weigh of each POM salt, it was estimated that 250 and 29 mg of O_2 can be obtained per gram of POM with a 1000:1 oxidant/POM ration for $\mathbf{Co_9}$ and $\mathbf{Co_4P}$, respectively. The latest indicates that $\mathbf{Co_9}$ is much more efficient, although both catalyst show similar kinetics, with comparable turns per second. In addition, $\mathbf{Co_9}$ shows remarkable stability in solution. The catalyst remains completely active upon addition of additional equivalents of oxidant after long periods of time and in the presence of a 10-fold excess of bpy, with no sign of fatigue or decomposition.

Recently, in 2015 a deeper study about the stability and solution speciation of the $\mathbf{Co_9}$ in both neat water and phosphate buffer, was reported by Goberna-Ferrón and co-workers.[243] Small angle X-ray scattering (SAXS) experiments were carried out reproducing the experimental conditions previously reported,[220] that is 50 mM sodium phosphate buffer at pH 7 with 1 M $NaNO_3$ as the electrolyte, and 0.9 M sodium phosphate buffer at pH 8. Additionally, experiments were also performed

in neat water to benchmark the **Co$_9$** speciation in the simplest of solutions. SAXS data, together with high energy X-ray scattering (HEXS), and compared with the simulated data from the crystal structure, confirmed that **Co$_9$** is maintained intact in solution, not only in neat water, but also in the buffered conditions, and these solutions are monodisperse. Moreover, SAXS experiments demonstrated that in water exists an inter-particle repulsion that disappears in the presence of buffer due to a screening of the electrostatic forces between the cluster.[244] The influence of the pH on the speciation of **Co$_9$** was also studied, demonstrating that the cluster remains stable in a wide range of pH, from 5.5 to 11, whereas by decreasing between 4.4 and 4.0 appears a change in speciation. Moreover, at pH 1.5 dimension and shape of particles correspond to the plenary Keggin ion. Trivacant lacunary Keggin species are stable at basic pH, meanwhile lowering the pH to acidic conditions yields the plenary archetype. Additionally, the color of the solution changed from intense pink at near neutral pH to reddish at pH 1.5, which resembles the color of $[Co(H_2O)_6]^{2+}$. This evidences that **Co$_9$** dissociates to release $[Co(H_2O)_6]^{2+}$ in strong acidic conditions, as reported previously for other cobalt-containing polyoxometalates.[245] To further study the homogeneous species present in solution under chemical reaction, SAXS data was collected reproducing the conditions mentioned above, by addition of 0.1 M of NaClO to a 1 mM solution of **Co$_9$** in 0.9 M sodium phosphate buffer at pH 8. Results show that **Co$_9$** remains stable after 3 h reaction, with no evidence of nanoparticles in solution. On the contrary, under extreme conditions, that is additions of oxidant equivalents every 2.5 h-cycle reaction, a decrease of **Co$_9$** concentration was observed and/or the presence of smaller species, consistent with the leaching of Co^{2+} ions from the POM and subsequent precipitation that would be favored by the large excess of phosphate buffer. However, after 4 additions of oxidant (10.5 h of reaction), the species in solution is predominantly **Co$_9$**. Therefore, high concentrations of phosphate buffer may accelerate the degradation of **Co$_9$**, since the precipitation of highly insoluble cobalt oxide phosphate will shift the equilibrium towards the release of more Co^{2+} ions into solution. In fact, in the absence

of phosphate buffer, results show that $\mathbf{Co_9}$ remains stable cycle after cycle, with no evidence of any other species present in solution. So thus, it was demonstrated that the stability of $\mathbf{Co_9}$ is strongly influenced by pH, buffer and buffer concentration, due to the solution equilibria and Co^{2+} leaching. However, it has remarkable redox stability.

1.7 Thesis Goals and Outline

Meeting the global energetic demands in the future will only be possible with a good implementation of renewable sources of energy. The most exploitable source is solar energy. Hence, mimicking photosynthesis, an artificial photosynthesis platform should convert sunlight into spatially separated electron/hole pairs and use the electric potential to mediate water splitting into H_2 (reduction) and O_2 (oxidation) at catalytic centers. However, the water oxidation reaction is considered the bottleneck in such water splitting scheme. Therefore, the discovery of water oxidation catalysts able to work at low overpotentials, with high stability under high oxidizing conditions, and in a cost-effective manner for the implementation into the market is mandatory. Moreover, the state-of-the-art in terms of feasible industrials applications is leaded by heterogeneous catalysis, so these catalysts have to be able to work in the solid-sate.

In this work we will show how the POM $[Co_9(H_2O)_6(OH)_3(HPO_4)_2(PW_9O_{34})_3]^{16-}$ (**Co_9**), which has been already identified that it is active as homogeneous WOC, is also active in the solid-state. Moreover, by means of DFT calculations we propose a plausible reaction mechanism for the water oxidation reaction catalyzed by Co-containing POMs.

- In Chapter 2 we show that precipitation of the POM with Cs^+ leads to an insoluble salt in water at room temperature which, blended with a solid-state matrix (*i.e.* carbon paste), and incorporated into an electrode, promote heterogeneous electrocatalytic water oxidation in mild conditions without signs of fatigue or decomposition.

- In Chapter 3 we present the heterogeneous catalytic activity of **Co_9** for light-driven water oxidation at pH 7. Moreover, the use of chromophore as countercation (**$RuCo_9$**) yields improved oxygen evolution under the same conditions,

without the presence of the photosensitizer in a solution containing the electron acceptor.

- In Chapter 4 we investigate by computational means the full catalytic cycle of the water oxidation catalyzed by $\mathbf{Co_4P}$ and its vanadium derivative $\mathbf{Co_4V}$ treated as single-site catalysts. In addition we present some preliminary results analyzing the effect of POM nuclearity on the water oxidation catalysis.

This Thesis serves as a proof of concept for the use of Co-containing POMs in solid-state water oxidation catalysis, and shed some light into the unknown water oxidation mechanism catalyzed by cobalt-substituted POMs.

Chapter 2

Heterogeneous Water Oxidation Catalysis with Modified Co_9*/Carbon Paste Electrodes*

UNIVERSITAT ROVIRA I VIRGILI
HIGH NUCLEARITY POLYOXOMETALATES AS WATER OXIDATION CATALYSTS: FROM EXPERIMENTS TO THEORY
Joaquín Soriano López

2.1 Introduction

Electrochemical water splitting, with the goal of molecular hydrogen production, has become a real clean alternative to replace fossil fuels. This process requires the oxidation of water, producing molecular oxygen 2.1, and, at the same time, the reduction of protons to molecular hydrogen 2.2. On this regard, water oxidation catalysis, compared with hydrogen production, is a challenging reaction due to its high energetic demand (it is an endothermic process with $\Delta G = 4.92\ eV$).[241] It is commonly accepted that water oxidation is bottleneck in water splitting. The state-of-the-art in terms of feasible industrial applications is led by electrochemical heterogeneous catalysis. Therefore the research for a robust, fast, and inexpensive heterogeneous water oxidation catalyst (WOC) seems to be mandatory in order to increase the commercial impact of water electrolysis, which accounts for less than 4% of the total worldwide hydrogen production.[23]

$$2H_2O \rightarrow O_2 + 4H^+ + 4e^- \qquad (E = +1.229 - 0.059(pH)\ V\ vs\ NHE\ at\ 25°C) \quad (2.1)$$

$$4H^+ + 4e^- \rightarrow 2H_2 \qquad (E = 0.000 - 0.059(pH)\ V\ vs\ NHE\ at\ 25°C) \quad (2.2)$$

Polyoxometalates (POMs) present a formidable opportunity in the research of a good WOC, since it is demonstrated that they are genuine homogeneous catalysts thanks to their rich redox chemistry and offering a good processability, optimization, fast kinetic rates, working in a large range of pH. Their molecular nature also allows for computational investigations.[218–220,224] Moreover, POMs can also be immobilized into modified electrodes to be employed as heterogeneous water oxidation catalysts, with high surface area, allowing for a close contact between the electrode surface and the POM which increases the rate of electron-transfer, and with more stability than most homogeneous catalysts. Therefore, it seems clear that immobilization of POM into a conductive supporting material is the most plausible alternative to advance

in the research of a good electrolyzer device, since POMs are insulating salts with low electrical conductivity.

The first example of electrode modification employing a POM supported into a conductive material was reported by Bonchio and co-workers in 2010.[246] They employed the polyanion $Li_{10}[Ru_4(H_2O)_4(\mu\text{-}OH)_2(\gamma\text{-}SiW_{10}O_{36})_2]$ (**Ru$_4$Si**) to construct nanostructured oxygen-evolving anodes by electrostatic assembly of this POM to water-soluble multiwalled carbon nanotubes (MWCNTs) previously decorated with polyamidoamine (PAMAM) ammonium dendrimers (**Ru$_4$Si**@MWCNT). They also integrated the (**Ru$_4$Si**) into amorphous carbon (AC) functionalized with the PAMAM dendrimers (**Ru$_4$Si**@AC) to evaluate the role of the MWCNTs. Indium tin oxide (ITO) electrodes were then modified by drop-casting a water solution containing the hybrid composite. These **Ru$_4$Si**@MWCNT modified electrodes showed high surface area, good mechanical properties, and good thermal stability. ITO electrodes were also modified with a lipophilic salt of **Ru$_4$Si** to benchmarking the effect of the MWCNT, and also with MWCNT-PAMAM to explore the activity of the POM-free modified ITO electrode. Cyclic voltammetries were carried out to check the oxygen evolving activity of these modified electrodes. As expected bare ITO electrodes and the POM-free MWCNT-PAMAM modified electrodes were complete inactive under water oxidation conditions. On the other hand, modified electrodes with the POM were always active in oxygen production, showing a strong dependency on the environment with an increase on the activity as **Ru$_4$Si**<**Ru$_4$Si**@AC$\ll$**Ru$_4$Si**@MWCNT, confirming the good synergetic effect between the POM and the dendrimer decorated MWCNT. Chronoamperometric experiments were carried out to determine the turnover frequency (TOF) of these **Ru$_4$Si**@MWCNT modified electrodes, in a pH 7 phosphate buffer. The TOF efficiency was 0.01 s^{-1} and 0.085 s^{-1} at overpotentials of 0.35 V and 0.6 V, respectively. The authors did not evaluated neither the long-term stability of these electrodes including the POM electrostatic retention on the MWCNTs.

Shortly after, in 2011, the same group developed a new strategy to functionalize MWCNTs and single-walled CNTs (SWCNTs) with positive charges under microwave (MW) solvent-free conditions. Moreover, a non-covalent bonding route was also explored to functionalize the MWCNTs employing an amphiphilic trimethylammonium acetyl pyrene in water, through π-π stacking interactions. Again, the $\mathbf{Ru_4Si}$ was electrostatically assembled to these functionalized CNTs in water at pH 5. In the same way as described above, the oxygen evolving anodes were modified by drop-casting a water solution of the hybrid composite on ITO and disk screen-printed carbon (SPC) electrodes. The catalytic efficiency of these modified electrodes yield higher electrocatalytic activity at $\eta > 0.4$ V. This was attributed to an improved stability and reduced ohmic losses of the SPC electrode with respect to ITO. As pointed before, long-term stability and POM retention were no studied.

Xie et al. reported in 2012, the immobilization in ordered mesoporous carbon nitride (MCN) of the POM $[Co_4(H_2O)_2(PW_9O_{34})_2]^{10-}$ ($\mathbf{Co_4P}$).[247] The choice of MCN was made based on its uniform nanochannels, high surface area, and outstanding conductivity. All these together with the presence of $-NH_2$ and $-NH$ groups on the mesoporous walls, that can be protonated to positive charged $-NH_3^+$ groups, where the $\mathbf{Co_4P}$ can be electrostatically absorbed. Therefore, the MCN was left under vacuum to remove air trapped inside the mesopores and impurities. Then the MCN was immersed in a aqueous solution containing $\mathbf{Co_4P}$ for 24 h. The POM was well-dispersed inside the mesopores with no alteration of the shape and diameter of the MCN nanochannels. ITO electrodes were modified by casting aqueous solutions of the $\mathbf{Co_4P}$@MCN and the catalytic activity was explored. For comparison, ITO electrodes were also modified with POM-free, and with a lipophilic salt of $\mathbf{Co_4P}$. Cyclic voltammetries were carried out in a phosphate buffer solution at pH 7, where, as expected, bare ITO electrodes were found to be inactive. The $\mathbf{Co_4P}$@MCN@ITO led to higher catalytic current compared with the deposited TBA$\mathbf{Co_4P}$ salt. The POM-free MCN@ITO also showed to be active but current densities obtained were much

lower than in presence of the $\mathbf{Co_4P}$. Long-term chronoamperometry over 10000 s was performed at an applied potential of 1.6 V vs NHE in a phosphate buffer solution at pH 7, producing 12.1 μmol of O_2 by passing 5 C of charge during electrolysis, reaching a 95 % of Faradaic efficiency. The TOF during this experiment was estimated to be 0.3 s^{-1}. Data obtained when carrying out X-ray absorption near edge structure (XANES) spectroscopy suggest a possible bond formation between the $\mathbf{Co_4P}$ and the MCN. The authors suggest such bonds are probably the responsible for the highly catalytic water oxidation activity. No obvious changes were found in the $\mathbf{Co_4P}$ structure when characterizing the hybrid compound after the experiments, although long-term stability tests were not carried out.

Again, Bonchio and co-workers presented in 2013 a graphene functionalized nanosheets that integrated the tetra-ruthenium polyoxometalate $\mathbf{Ru_4Si}$.[248] Pristine graphene was functionalized with a first generation polyaminoamide (PAMAM) dendron *via* direct 1,3-dipolar cyclo-addition. Therefore, as explained before, the polyanion $\mathbf{Ru_4Si}$ was electrostatically assembled to the positive ammonium groups of the dendrimer at pH 5 ($\mathbf{Ru_4Si}$@d-G). Modification of ITO and SPC electrodes was carried out by drop-casting an aqueous solution of the $\mathbf{Ru_4Si}$@d-G. Cyclic voltammograms and chronoamperometric experiments employing $\mathbf{Ru_4Si}$@d-G@SPC, allowed a comparison between this new modified electrodes and the already reported $\mathbf{Ru_4Si}$@MWCNT@SPC electrodes. These new $\mathbf{Ru_4Si}$@d-G@SPC modified electrodes led to a decrease on the overpotential with a 2-fold enhancement of the maximum TOF, compared with the previously reported $\mathbf{Ru_4Si}$@MWCNT@SPC electrodes. So thus, it was demonstrated that employing graphene nanosheets is more convenient than using MWCNTs as supporting material for electrode modification. The stability of the $\mathbf{Ru_4Si}$@d-G@SPC electrodes was tested by a sequence of chronoamperometric experiments, leading to a 1% current loss after 4 h of experiment. The stability and high water oxidation activity of these modified electrodes is suggested by the author to be due to the noninvasive and highly dispersed sur-

face modification, which enables for electron transport and accumulation across the extended π-bond network.

Still in 2013, the group of Hill studied a similar approach of electrode modification by **Ru_4Si** supported on graphene.[249] First, graphene oxide was reduced and deposited electrochemically on both ITO and glassy carbon (GC) electrodes. At this point, two different graphene electrodes were prepared: wet graphene modified electrodes (wG) and dried graphene modified electrode (dG), that were prepared in the same way but the dG were dried in air prior to use. After that, **Ru_4Si** was immobilized electrostatically into the graphene by soaking overnight the graphene modified electrodes into a aqueous solution containing the POM. Both, **Ru_4Si**@wG@GC and **Ru_4Si**@dG@GC modified electrodes were tested, together with a bare GC electrode with **Ru_4Si** solution, by cyclic voltammetry employing 0.5 M H_2SO_4 as electrolyte. Peak currents obtained with **Ru_4Si**@dG@GC were similar to those obtained with the bare GC, while the peaks currents observed for the **Ru_4Si**@wG@GC were much larger. Authors attribute this difference to the highly porous structure of wet graphene, leading to significant contributions from thin layer and surface-confined processes to the overall voltametric response. In addition, the higher porosity of the wet graphene allows for a much higher loading of the POM compared with the dried graphene, as shown by EDX data. Stability tests with the **Ru_4Si**@wG@GC were performed by chronoamperometric measurements at pH 7.5 with 0.1 M sodium borate buffer and 1 M $Ca(NO_3)_2$ as electrolyte, at an applied potential of 1.5 V vs NHE. During the experiment a decay on the current density was observed as O_2 bubbles accumulated on the electrode surface, resulting in a decrease on the surface area as active sites of the catalyst were blocked. The stability of the **Ru_4Si**@wG was confirmed after the experiments by EDX spectroscopy. Moreover, *in situ* formation of RuO_2 nanoparticles, that could be responsible for the catalysis, was rule out by using RuO_2-graphene modified electrodes, since no catalytic wave is observed during the voltammetries and no oxygen bubbles were observed. TOF was obtained

for the $\mathbf{Ru_4Si}$@wG using rotating ring-disk voltammetry, where it was measured to be 0.82 s^{-1} at an overpotential of 0.35 V, which is 80 times more active than the $\mathbf{Ru_4Si}$@MWCNT modified electrodes at the same overpotential. Therefore authors suggest that the presence of a non-conducting PAMAM dendrimer on the graphene surface has a negative impact on the activity of the catalyst.

In this chapter we present the incorporation of an insoluble salt of $\mathbf{Co_9}$ into carbon paste mixtures to prepare modified electrodes for water oxidation catalysis. These modified electrodes yield high catalytic activity with no signs of fatigue during electrolysis in a wide range of pH, and represent a convenient way to explore the catalytic activity of $\mathbf{Co_9}$ in the solid state, as required for technological applications.

2.2 Results and Discussion

The insoluble salt of $\mathbf{Co_9}$ was obtained by the addition of CsCl to a $\mathbf{Co_9}$ water solution.[250] The number of water molecules was determined by thermogravimetric analysis (TGA), showing 41 molecules of water in the unit cell. Metal analysis was carried out with an inductively coupled plasma optical emission spectrometer (ICP-OES). Both analysis together allowed us to calculate the molecular formula as $Cs_{15}K[Co_9(OH)_3(H_2O)_6(HPO_4)_2(PW_9O_{34})_3]\cdot 41H_2O$ ($M_w = 10341.31$) (see Figure 2.17 and Table 2.4 in the Experimental Section).

As prepared, scanning electron microscope (SEM) shows that this salt contains a homogeneous particle size distribution in the 5−10-μm-diameter range, as can be seen in Figure 2.1. Whereas in a water suspension, dynamic light scattering measurements indicate an average particle size of 267.2 nm (Figure 2.2).

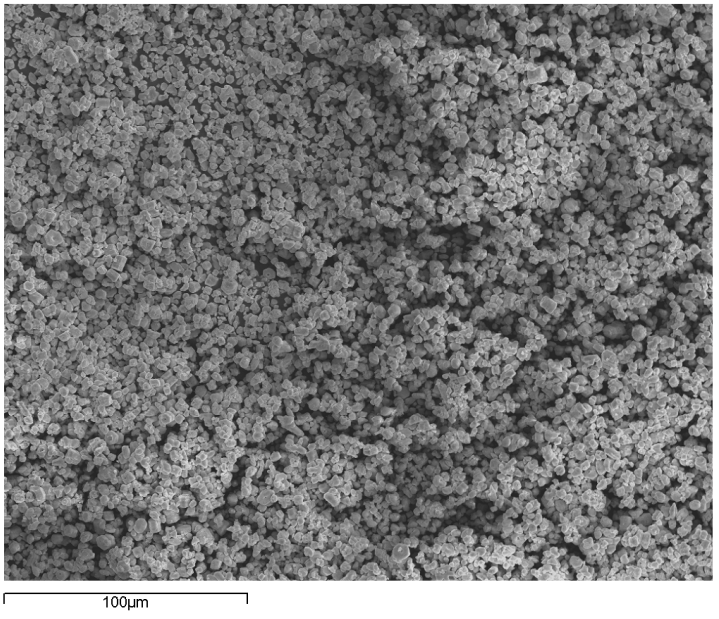

Figure 2.1: SEM image of a typical freshly prepared $\mathbf{CsCo_9}$ sample.

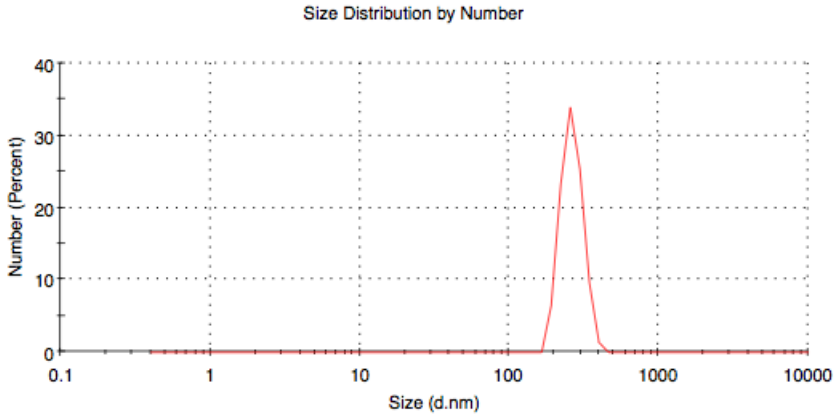

Figure 2.2: Size distribution by number measured for the $\mathbf{CsCo_9}$ in suspension before experiments.

This salt is insoluble in water at room temperature or any other common solvents, and thus it is a good material to test if the WOC activity is retained in the solid state, or if this POM is only active in homogeneous conditions. Without further treatment, this polycrystalline solid was blended with carbon paste to prepare POM modified amorphous carbon (POM-C) electrodes with a POM content between 1 and 60% in weight. Blends above 60% catalyst became too brittle. Cyclic voltammetry with a POM-C working electrode, a Pt wire as counter electrode, and a Ag/AgCl (3.5 M) reference electrode, showed a strong water oxidation wave, indicating participation of a catalytic process (Figure 2.3).

During successive cycles, gas bubbles formed on the electrode, and the typical oxygen reduction wave below -0.3 V appeared at negative potentials, confirming oxygen evolution. These preliminary results suggest that $\mathbf{Co_9}$ can also work as a WOC in heterogeneous conditions.

2.2.1 Steady-State Water Oxidation Analysis

Controlled potential water electrolysis with these POM-C electrodes was carried out in a two-compartment cell with a pH 7 sodium phosphate buffer (NaP_i, 50

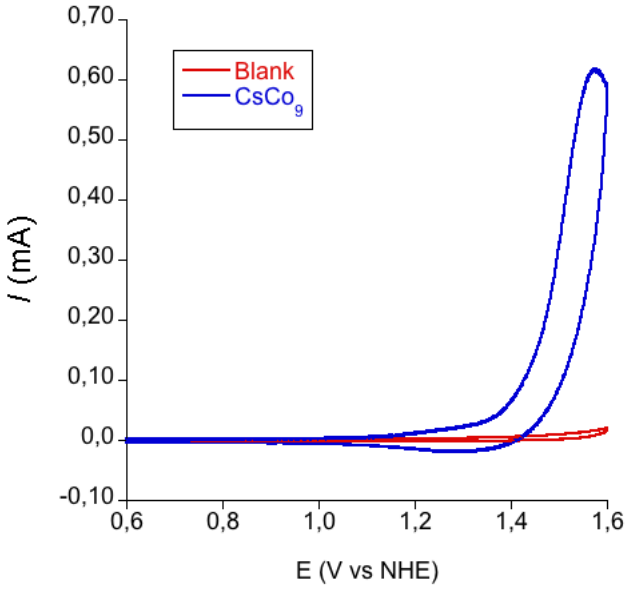

Figure 2.3: Cyclic voltammogram acquired in a pH 7 NaP_i buffer (50 mM) water solutions with $NaNO_3$ (1 M) as electrolyte with a 57.1% POM-C working electrode, a Pt wire counter electrode, and a Ag/AgCl (3.5 M) reference electrode. Scan rate = 100 mV/s.

mM)/water solution with $NaNO_3$ (1 M) as electrolyte. Steady-state currents were reached after a few minutes. At these steady-state, the current density (j) follows a linear Tafel law in the $0.2 < \eta < 0.6$ V range, as shown in the Figure 2.4.

The Tafel slope decreases very rapidly for a very small catalyst content, indicating faster kinetics and the appearance of a catalytic process (Table 2.1, Figure 2.5). The 1.5% blend already shows 148 mV/decade, from the 178 mV/decade found for a pure carbon paste electrode. Above 3% catalyst content, the slope remains essentially constant in the 90-110 mV/decade range. These values are in between the expected values for an electron-transfer rate-limited process (60 mV/decade) and a chemical rate-limited process (120 mV/decade). Our hypothesis is that this intermediate slope appears from the competition between the catalytic oxidation and from the electron transfer in the blend. The kinetics of the different blends can also be compared by

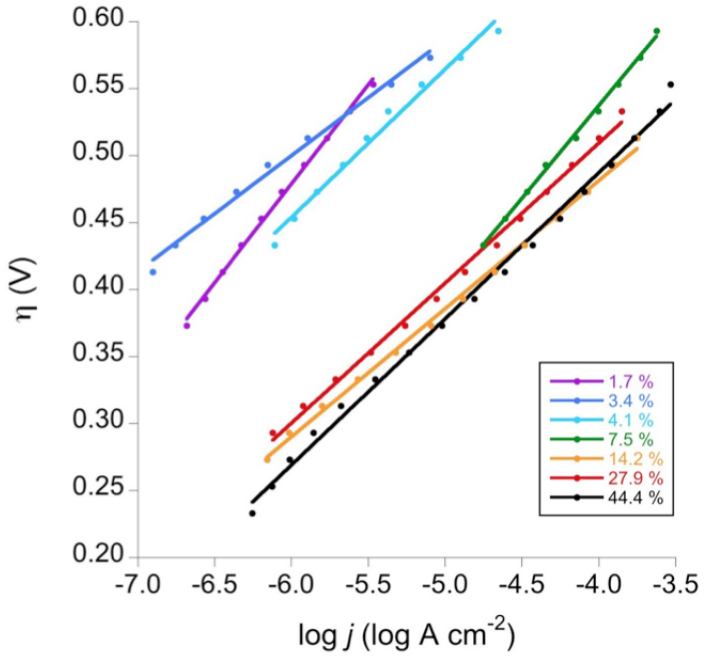

Figure 2.4: Steady-state Tafel data acquired in a pH 7 NaP_i buffer (50 mM) water solution with $NaNO_3$ (1 M) as electrolyte with POM-C anodes at different **$CsCo_9$**/carbon paste weight ratios. Ohmic drop was compensated using a positive feedback compensation.

POM Co_9 (weight %)	η **(mV)** **(j = 1 mA/cm^2)**	**j_0 (A/cm^2)**	**Tafel slope (mV/decade)**
1.7	841	2.01 $x10^{-6}$	148
3.4	712	5.56 $x10^{-9}$	86
4.1	725	2.70 $x10^{-7}$	110
7.5	600	4.51 $x10^{-5}$	138
14.2	525	3.27 $x10^{-6}$	96
27.9	557	4.66 $x10^{-6}$	104
44.4	537	1.19 $x10^{-5}$	109

Table 2.1: Results acquired from the Tafel Plots. The amount of catalyst content in each modified electrode is shown, as well as the overpotential needed to reach a current density of 1 mA/cm^2, the exchange current and, the Tafel slope for each case.

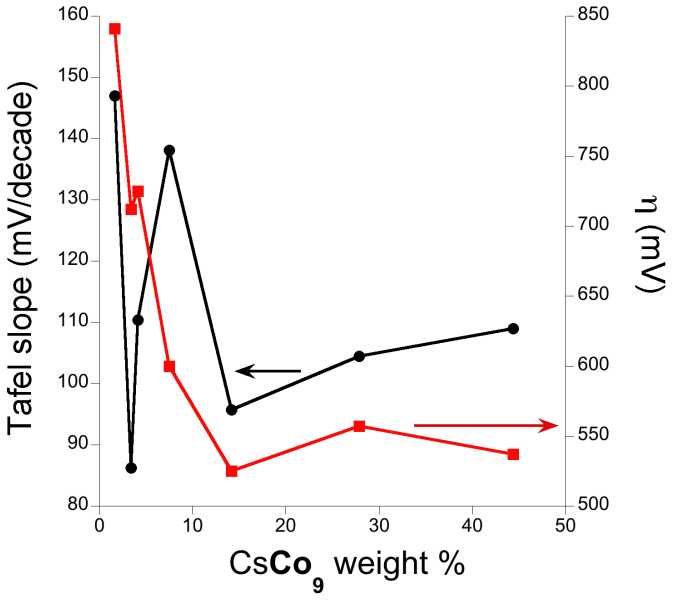

Figure 2.5: Tafel slope (black) and overpotential needed to reach 1 mA/cm^2 (red) for catalytic water electrolysis with a POM-C working electrode as a function of the $\mathbf{Co_9}$ content.

the overpotential (η) needed to reach $j = 1$ mA/cm^2. The result is analogous to that observed for the Tafel slope, reaching a minimum value above 14% (525 mV).

2.2.2 Oxygen Evolution

Bulk water electrolysis with a POM-C electrode shows remarkable stability. After a induction period of ≈30 min, where the intensity decreases, probably due to capacitance, the current remains constant for the rest of the experiment for over 8 h, as shown in Figure 2.6. This demonstrates the long-term stability of $\mathbf{Co_9}$ in heterogeneous conditions.

During these experiments, we monitored oxygen evolution with a fluorescence probe. The final yield reaches over 90% compared with the theoretical amount

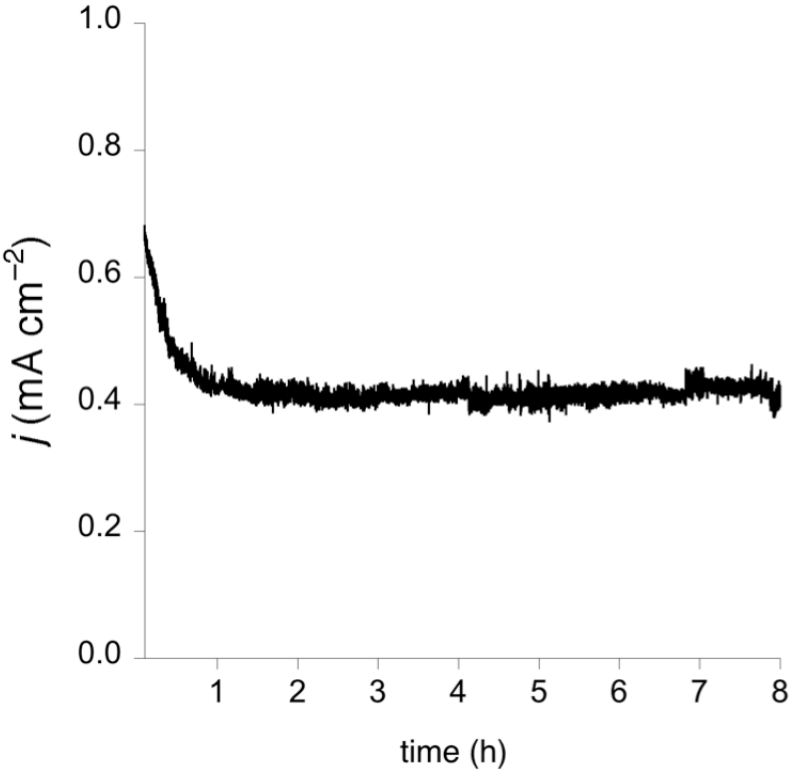

Figure 2.6: Current density at +1.3 V (vs NHE) with a 44% POM-C modified electrode.

of oxygen expected for a stoichiometric reaction ($4e^-$ per oxygen molecule). The rest can be assigned to the oxidation of the carbon component, because no other component can be oxidized at these potentials (up to +1.5 V vs NHE).

Once the bulk water electrolysis finished, the buffer solution was rotaevaporated and the solid residue obtained was analyzed by EDX analysis to confirm any leaching from the electrode. The results show that just the electrolyte buffer salts are present with no signals of cobalt or tungsten, confirming that the POM remains in the blend. The sensitivity of EDX ($>$ 1000 ppm) cannot rule out minimum traces, but such leaching is not significant. It does not affect catalytic current.

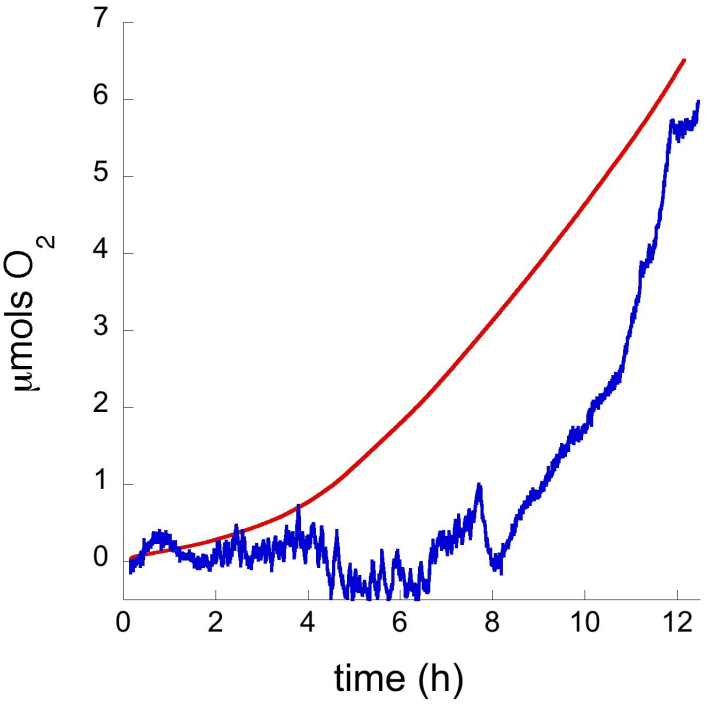

Figure 2.7: O_2 production measured with a fluorescence sensor (blue line) and theoretical production calculated for a quantitative Faradaic efficiency (red line) for water electrolysis with a 22% POM-C anode electrode at pH 7, with 50 mM NaP_i buffer, and $NaNO_3$ (1M) as electrolyte applying a potential of 1.5 V vs NHE. The very long lag time arises from the complex experimental setup. The position of the electrode, perpendicular to the surface, traps the oxygen bubbles even at high stirring speed. Thus, the oxygen content increases following a very irregular pattern, as gas bubbles escape randomly from the electrode.

2.2.3 Recovery of the Catalyst

After bulk water electrolysis experiments the $\mathbf{CsCo_9}$ salt was recovered from the carbon paste. The POM-C blend was suspended in acetone and sonicated until $\mathbf{CsCo_9}$ detached from the carbon paste, appearing as a pink precipitate. The recovered catalyst was characterized by infrared spectroscopy (IR), powder X−ray diffraction (PXRD) , and energy−dispersive X−ray spectroscopy (EDX). Results were compared with those obtained for the freshly prepared $\mathbf{CsCo_9}$. Figure 2.8 shows a typical IR spectra of the $\mathbf{Co_9}$ cluster in the 1100−400 cm^{-1} range (blue line), in this case that obtained from a powder sample of freshly prepared $\mathbf{CsCo_9}$. The red line shows the IR spectra of the recovered catalyst after the experiment, which perfectly fits with the freshly prepared $\mathbf{CsCo_9}$. Comparison of the collected PXRD pattern (Figure 2.9) also supports the integrity of the POM cluster under catalytic conditions. Finally, EDX analysis (Figure 2.10 and Table 2.2) shows similar elemental abundance for the constituent atoms of the $\mathbf{CsCo_9}$ salt before and after bulk water electrolysis. These techniques highlight the stability of $\mathbf{CsCo_9}$ under turnover conditions.

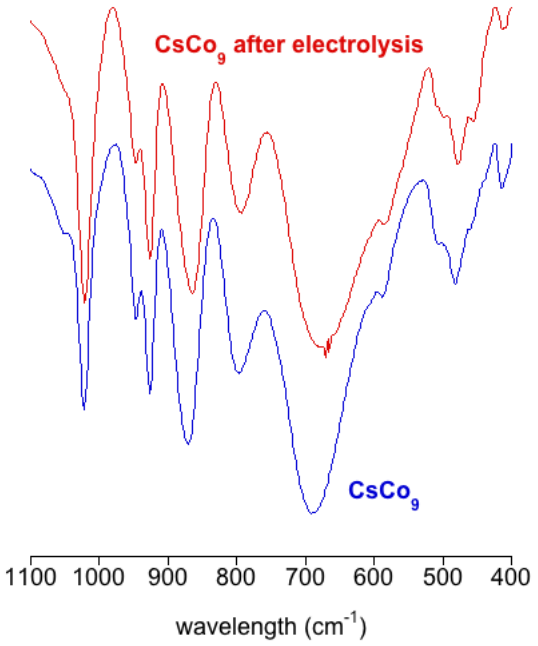

Figure 2.8: Comparison between the IR spectra of freshly prepared **CsCo$_9$** and of the salt recovered after 8 hours of water electrolysis.

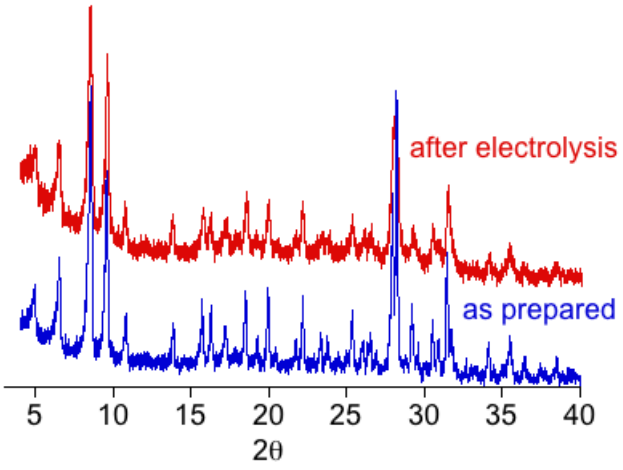

Figure 2.9: Typical PXRD of pristine **CsCo$_9$** salt and of collected compound after 8 hours of water electrolysis.

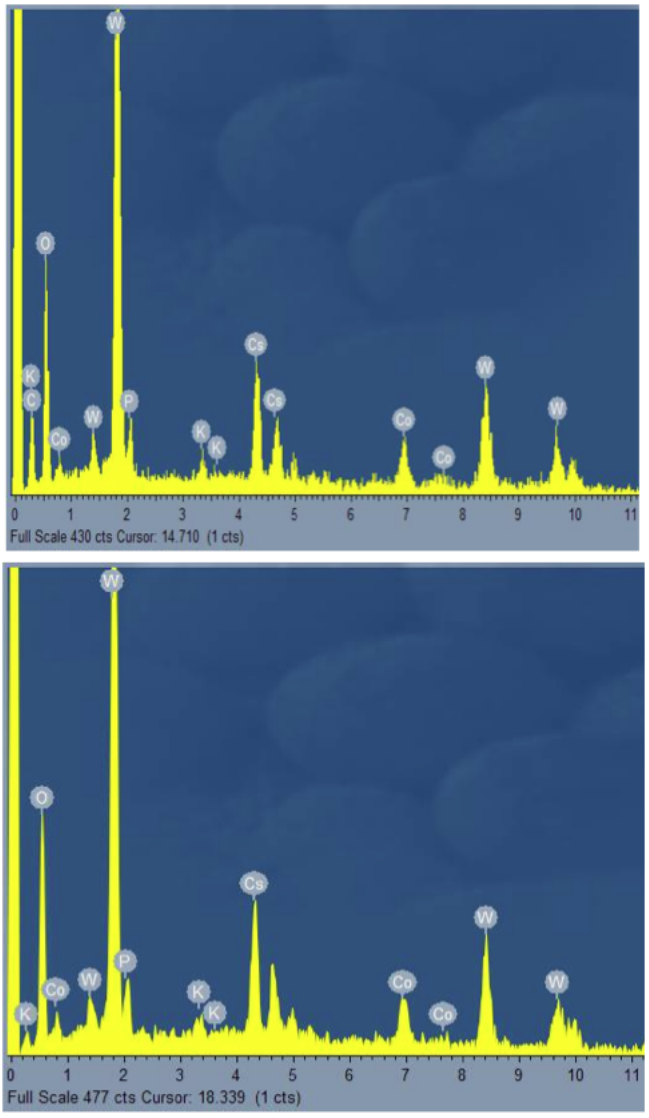

Figure 2.10: Typical EDX histogram of freshly prepared $\mathbf{CsCo_9}$ (top) and of a POM-C blend after 8 hours of $\mathbf{CsCo_9}$ catalyzed water electrolysis (bottom).

	Before		**After**	
Element	atomic % (found)	stoichiometry (estimated)	atomic % (found)	stoichiometry (estimated)
P	2.8	5.4	1.7	4.9
K	0.8	1.6	0.4	1.1
Co	4.9	9.5	3.2	9.2
Cs	7.8	15.2	5.3	15.2
W	13.9	27	9.4	27

Table 2.2: Elemental abundance for the constituent atoms of the $\mathbf{CsCo_9}$ salt estimated for the EDX analysis before and after 12 hours bulk water electrolysis. Data averaged for four different samples.

2.2.4 Comparison with Cobalt Oxide

It has been shown that WOCs can suffer important changes in turnover conditions to yield highly active WOCs as cobalt oxide.[198,234] However, our data indicate that cobalt oxide is not being formed in situ, according to several observations. During bulk water electrolysis at POM-C electrodes, the current decreases with time. However, oxide formation should increase the catalytic activity because cobalt oxide is a better catalyst than $\mathbf{Co_9}$.[234] However, the presence of traces of CoO_x cannot be ruled out.

In order to get additional evidence, we performed analogous experiments with Co_3O_4 carbon paste blends (CoX-C).[251? –253] Figure 2.11 shows the Tafel plots performed employing CoX-C modified electrodes with different amounts of Co_3O_4, using a NaP_i buffer (50 mM) water solution with $NaNO_3$ (1 M) as electrolyte at pH 7. It is clearly shown that CoX-C electrodes performs very different than POM-C electrodes, since for higher contents of Co_3O_4 the slope of the Tafel plot of current density increases, opposite to what was observed for $\mathbf{Co_9}$.

The Tafel slope increases very rapidly when increasing the content of oxide in the electrode. The 7.1% blend already shows 87 mV/decade, while the 40.7% blend shows a Tafel slope of 346 mV/decade, which is too high for a catalytic process. (Table 2.3, Figure 2.12). Looking at the overpotential (η) needed to reach a j= 1 mA/cm^2 we also can observe differences from the results found with the POM-C electrodes. Using the CoX-C electrodes the overpotential decreases from 643 mV to 489 mV for the 7.1% and for the 40.7% blends, respectively.

These experiments compare % weight of POM or Co_3O_4 in the electrode, where the moles of Co are not the same, since for a same weight of catalyst there are more Co centers in the oxide than in the POM. Therefore, in order to perform a more fairly comparison we compared data taking into account the moles of Co that we were using in each experiment.

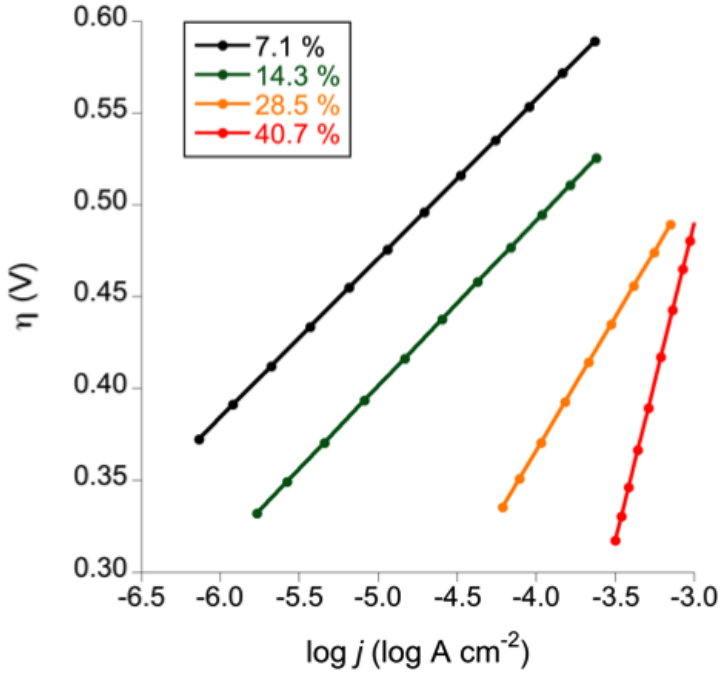

Figure 2.11: Steady-state Tafel data acquired in a pH 7 NaP_i buffer (50 mM) water solution with $NaNO_3$ (1 M) as electrolyte with CoX-C anodes at different Co_3O_4/carbon paste weight ratios. Ohmic drop was compensated using a positive feedback compensation.

Co_3O_4 (weight %)	**η (mV) (j = 1 mA/cm^2)**	**j_0 (A/cm^2)**	**Tafel slope (mV/decade)**
7.1	643	2.01 $x10^{-6}$	87
14.3	580	5.56 $x10^{-9}$	90
28.5	510	2.70 $x10^{-7}$	145
40.7	489	4.51 $x10^{-5}$	346

Table 2.3: Results acquired from the Tafel Plots. The amount of Co_3O_4 content in each modified electrode is shown, as well as the overpotential needed to reach a current density of 1 mA/cm^2, the exchange current and, the Tafel slope for each case.

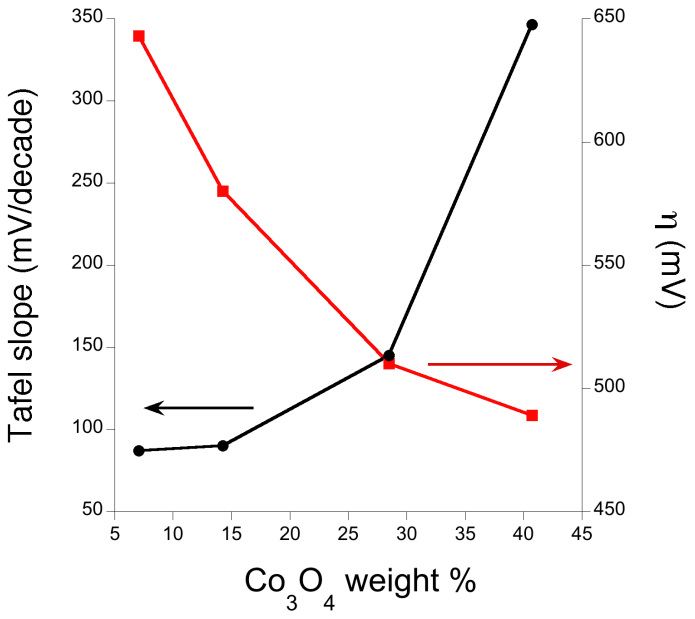

Figure 2.12: Tafel slope (black) and overpotential needed to reach 1 mA/cm^2 (red) for catalytic water electrolysis with a CoX-C working electrode as a function of the Co_3O_4 content.

POM-C electrodes yield 2 orders of magnitude larger current densities than the corresponding CoX-C blends for equimolar amounts of cobalt content (Figure 2.13). Actually, a huge excess of cobalt oxide is needed to reach similar activity. For example, we obtained a much larger current density with just 2 μmol of total cobalt as **Co$_9$** (20 mg, 0.22 μmol) than with 125 μmol of total cobalt as Co_3O_4 (20 mg, 41.7 μmol of oxide). Although direct correlations are difficult to draw because the formation of cobalt oxide nanoparticles could yield higher activity than the fine cobalt oxide powder that we used for the blend preparation, our experiments suggest that most of the POM had to be converted into oxide to reach such a high catalytic activity. The POM-C blends after 8 h of water oxidation showed features identical with those of the freshly prepared **CsCo$_9$** This supports that the catalyst remains essentially intact in turnover conditions for very long periods of time. If very small,

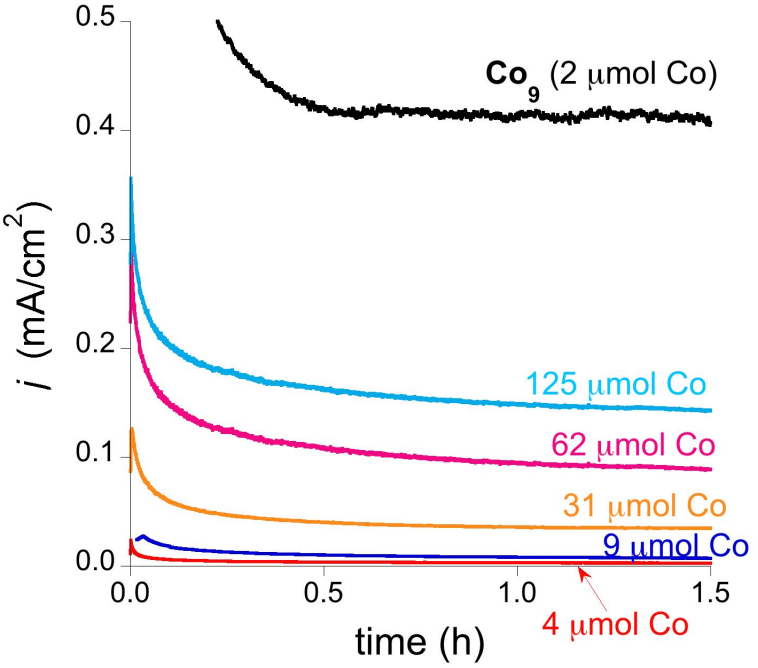

Figure 2.13: Current density at +1.3 V (vs NHE) with a 44% POM-C electrode (black) and with CoX-C working electrodes at different Co_3O_4 contents (color lines). Labels indicate the total amount of Co in the blends.

undetected amounts of **Co**$_9$ decompose into cobalt oxide during water oxidation, such small traces cannot justify the high activity exhibited by the POM-C blends.

2.2.5 Effect of the pH on the Catalytic Performance

Catalytic water electrolysis with a POM-C blend electrode shows very small variations with pH (see Figure 2.14). Starting from acid pH j increases up to pH 4 and then remains essentially constant. The catalytic current is over 1 order of magnitude higher than for a carbon paste electrode, and the pH dependence shows a different trend. In the absence of catalyst, it reaches a maximum above pH 6, and the variation at low pH is much more pronounced.

The cyclic voltammograms of the POM-C blends as a function of the pH (Fig-

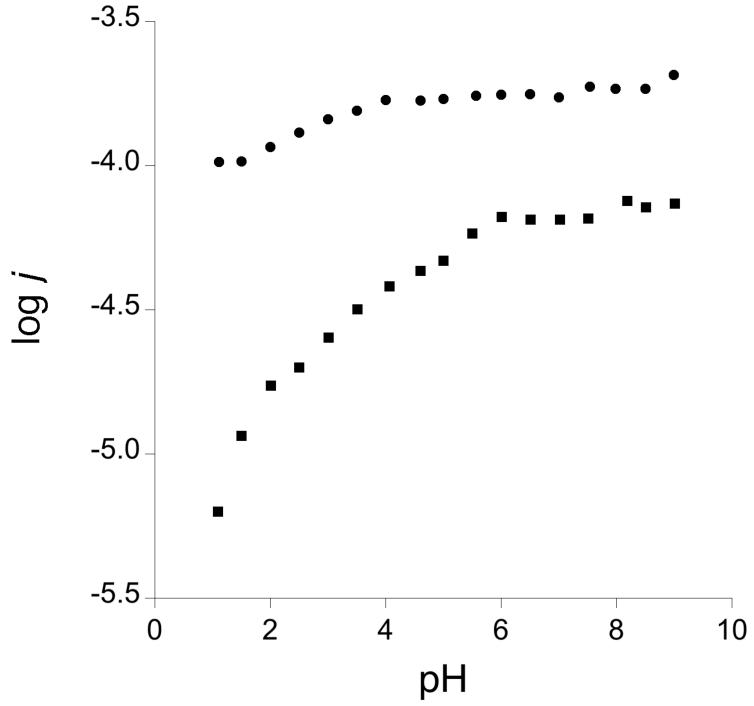

Figure 2.14: Dependence on pH at +1.5 V for a carbon paste (squares) and a 14% POM-C electrode (circles).

ure 2.15) show remarkable differences from the pH dependence reported for the CoO_x catalysts.[37] Cobalt oxide is inactive at low pH, and the water oxidation wave increases until pH >8.[174] The POM-C catalytic water oxidation wave shows no significant changes in intensity or position. On the contrary, cyclic voltammograms reported by Gerken *et al.* showed that the number of redox couples and their positions are dependent on pH. At pH 8 and above, two different redox processes are clearly shown, while from pH 3 to 8 just one redox couple is observed at lower potentials than the catalytic wave. Below pH 3 no redox couple appears. The different behavior of the modified electrodes reported by Gerken *et al.* in contrast with the ones reported in this work, confirm that in situ formation of CoO_x is not getting place in our system.

In addition, the difference in the catalytic activity between POM-C and CoX-C blends is even more remarkable when bulk electrolysis is performed at pH 1, where

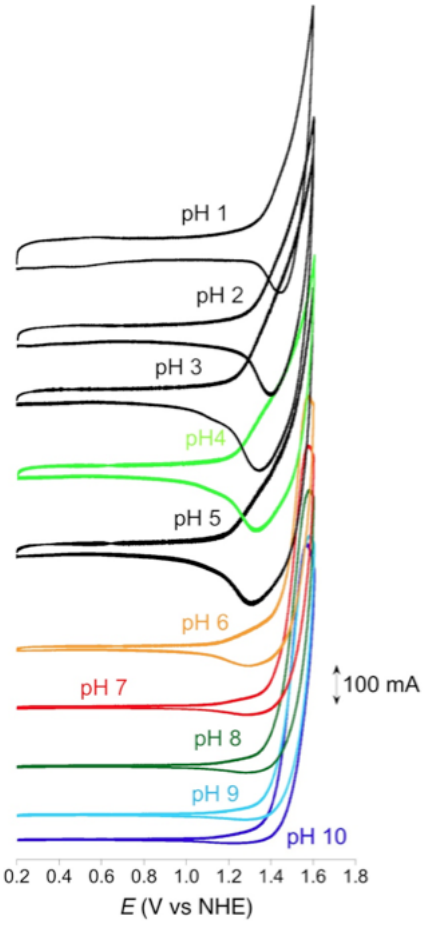

Figure 2.15: Cyclic voltammograms acquired in H_2SO_4 (0.1 M) as electrolyte at different pH with a 14.2% POM-C anode, a Pt wire cathode and a Ag/AgCl (3.5 M) reference electrode. Scan rate = 100 mV/s. The pH was adjusted with NaOH.

cobalt oxide is unstable (Figure 2.16). Indeed, the CoX-C blend shows no significant effect on the current density, yielding j values identical with those of the pure carbon paste electrodes. In the case of the POM-C electrodes, catalytic water oxidation proceeds with current densities 100 times higher for just a total cobalt content of 2 μmol. This high activity of the POM-C blends in acidic media is a unique feature for a metal oxide-based catalyst and additional evidence that no adventitious cobalt oxide is significantly participating in the catalytic process. Because Co^{2+} can engage in water oxidation in acidic media *via* ephemerally absorbed species, we also studied

water electrolysis at pH 1 with the addition of $Co(NO_3)_2$ to the electrolyte. In this case, j increases up to maximum values for a total content of $\approx$18 μmol, just twice the activity exhibited by the carbon paste itself and far from the rates found for the POM-C blends. After this maximum, j decreases upon further addition of the cobalt salt. This also supports that adventitious aqueous Co^{2+} ions cannot be responsible for the high activity of the POM-C electrodes in acidic media. Moreover, they were not detected in the leached solutions from the electrodes, taking into account that the limit of detection of EDX is 1000 ppm.

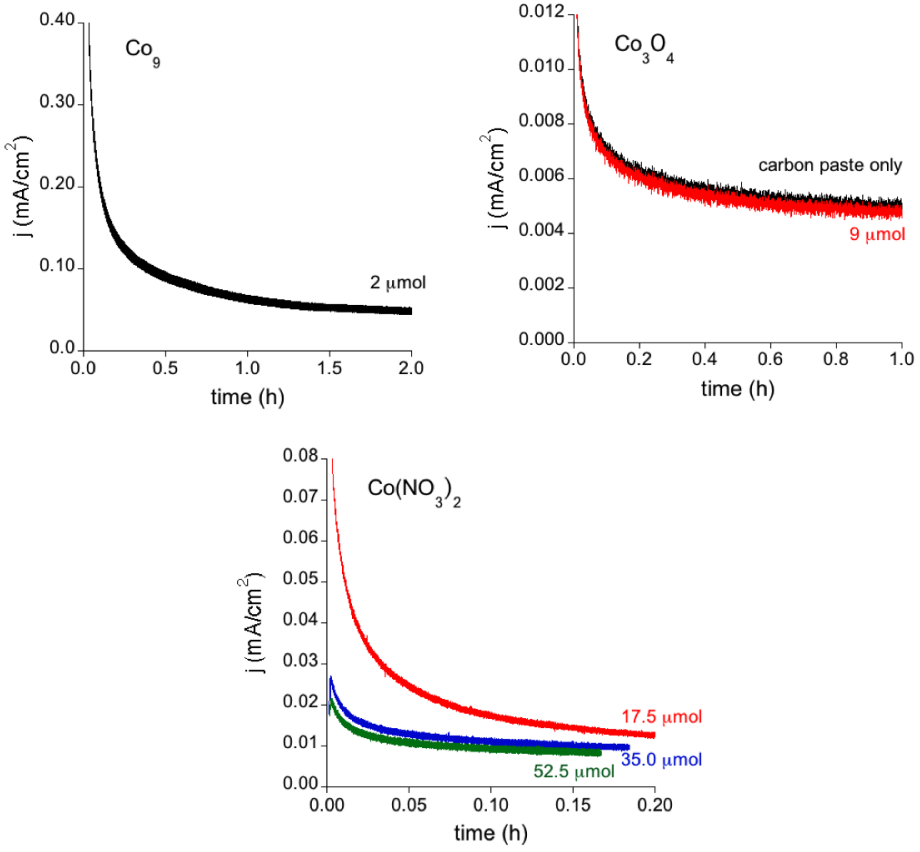

Figure 2.16: Bulk water electrolysis at pH 1 (H_2SO_4 0.1 M) applying a potential of 1.5 V vs NHE with different anode electrodes: POM-C blend (0.22 μmol **CsCo$_9$**); CoX-C blend (3 μmol Co_3O_4); and with a carbon paste electrode, adding to the solution $Co(NO_3)_2$ (17.5, 35 and 52.5 μmol). The numbers quoted in the plots indicate the total amount of cobalt content.

UNIVERSITAT ROVIRA I VIRGILI
HIGH NUCLEARITY POLYOXOMETALATES AS WATER OXIDATION CATALYSTS: FROM EXPERIMENTS TO THEORY
Joaquín Soriano López

2.3 Conclusions

In this chapter we show that precipitation of the POM with Cs^+ leads to a water insoluble salt (**CsCo$_9$**) which, blended with a solid-state conducting matrix (i.e. carbon paste), promotes heterogeneous electrocatalytic water oxidation in mild conditions (pH 7). The electrochemical data indicates that a current density of 1 mA/cm^2 needs an overpotential of ca. 525 mV in optimum conditions for this catalyst. These electrodes show a remarkable stability, with no signs of fatigue for at least 8 hours with Faradaic O_2 evolution. Interestingly, these modified electrodes are also active even in strong acidic conditions (pH 1), where cobalt oxide is unstable. Comparison with Co_3O_4/Carbon Paste modified electrodes show different electrochemical behavior, than that observed with the POM modified electrode. Multiple experimental evidences support the stability of the **CsCo$_9$** catalyst under working conditions inside the carbon paste matrix, with consistent analytical and structural data obtained before and after water electrolysis.

UNIVERSITAT ROVIRA I VIRGILI
HIGH NUCLEARITY POLYOXOMETALATES AS WATER OXIDATION CATALYSTS: FROM EXPERIMENTS TO THEORY
Joaquín Soriano López

2.4 Experimental

2.4.1 Synthesis

All reagents were commercially available and used without further purification. The $Na_8K_8[Co_9(H_2O)_6(OH)_3(HPO_4)_2(PW_9O_{34})_3]\cdot 43H_2O$ salt was obtained by dissolving in 100 mL of an aqueous solution $Na_2WO_4\cdot 2H_2O$ (33 g, 100 mmol) and Na_2HPO_4 (3.3 g, 22 mmol). The pH of that solution was adjusted at 7.1 with acetic acid, and 30 mL of an aqueous solution of $Co(OOC\text{-}CH_3)_2\cdot 4H_2O$ (9 g, 35 mmol) was then added. The violet solution obtained was refluxed at 100°C for 2 hours, and then hot filtered. An excess of $K(OOC\text{-}CH_3)_2$ (2 g) was added and the solution was filtered again. The solution was cooled at room temperature and, after some days, crystals of the anions $[Co_4(H_2O)_2(PW_9O_{34})_2]^{10-}$ and $[Co_9(H_2O)_6(OH)_3(HPO_4)_2(PW_9O_{34})_3]^{16-}$ appeared. The desired anion was extracted with cold water. From the resulting solution large pink needles were obtained, being these crystals the $\mathbf{Co_9}$.[250]

The Cs^+ salt was prepared by metathesis. An stoichiometric excess of a 0.1 M solution of CsCl was added to a solution of the potassium/sodium salt. The desired Cs salt precipitated immediately. This precipitate was filtered, washed with water and air-dried. Typical yield $\approx 20\%$.

2.4.2 Characterization

- **Analysis:** The stoichiometry of the Cs salt was determined by metal analysis and thermogravimetry. Metal analysis was carried out with a Perkin Elmer, Optima 8300 model, inductively coupled plasma optical emission spectrometer (ICP-OES). Thermogravimetry analysis was performed with powder samples using TGA/SDTA851 Mettler Toledo with MT1 microbalance.

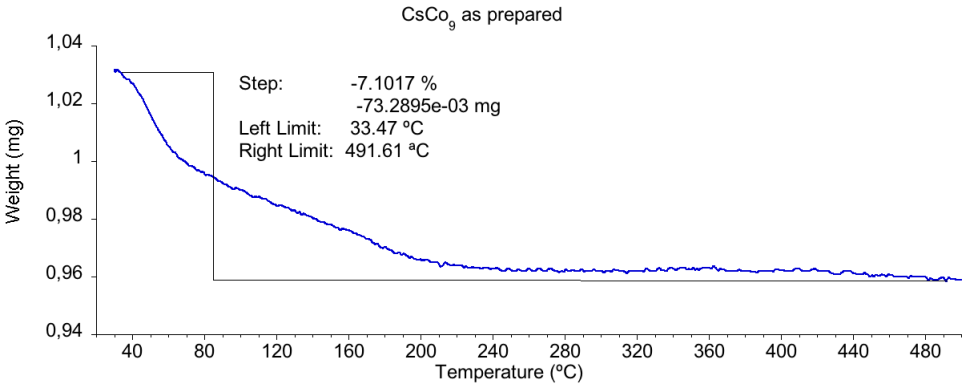

Figure 2.17: Thermogravimetric analysis of the pristine **CsCo$_9$** salt.

Element	Calculated (%)	Found (%)
Cs	19.28	19.30
Co	5.13	5.28
W	48.00	47.52
P	1.50	1.36

Table 2.4: ICP-OES analysis of the pristine **CsCo$_9$** salt.

- **Dynamic Light Scattering:** The nanoparticle size distribution of **CsCo$_9$** was measured using a Malvern nanoZS analyzer.

- **Infrared Spectroscopy:** Infrared spectra were collected in the $3600-400$ cm^{-1} range with a Bruker Optics FTIR Alpha spectrometer equipped with a DTGS

detector, KBr beamsplitter at 4 cm^{-1} resolution.

- **Powder X−Ray Diffraction:** Powder X−Ray diffraction patterns of the **$CsCo_9$** salt before and after the catalysis were collected with a Bruker 8D Advance Series equipped with a VÅNTEC-1PSD detector.

- **Scanning Electron Microscopy and Energy−Dispersive X−Ray Spectroscopy:** Comparison of the metal content of the freshly prepared **$CsCo_9$** and of the collected salt was analyzed with a Scanning Electron Microscope JEOL−JMS6400 equipped with an Oxford EDX analyzer (Oxford Instruments).

2.4.3 Electrochemistry

All experiments were performed with a Biologic SP-150 potentiostat. Ohmic drop was compensated using the positive feedback compensation implemented in the instrument. For cyclic voltammetry experiments, an amorphous carbon paste working electrode (0.07 cm^2), a Pt wire counter electrode, and a Ag/AgCl (3.5 M) reference electrode were placed in a beaker with a sodium phosphate buffer solution (50 mM) and $NaNO_3$ (1 M) electrolyte. The carbon paste mixture were prepared in a mortar by mixing amorphous carbon paste (Biologic Carbon paste oil base) and $\mathbf{CsCo_9}$, or Co_3O_4, in the desired proportion. Bulk water electrolysis was carried out with stirring in a two-chamber cell, with a porous frit connecting both chambers. In one chamber we placed a Pt mesh counter electrode, and in the other chamber the modified carbon paste working electrode (0.07 cm^2) and the reference electrode. Typical electrolysis experiments were carried out in a 50 mM NaP_i buffer solutions. For pH dependent electrolysis, a 0.1 M H_2SO_4 solution was used as electrolyte, and the pH was adjusted by addition of NaOH. Oxygen evolution was detected with an Ocean Optics NeoFOX oxygen sensing system equipped with a FOXY probe inserted into the anodic compartment.

Chapter 3

Heterogeneous Light-Driven Water Oxidation Catalysis with Insoluble Salts of Co_9

UNIVERSITAT ROVIRA I VIRGILI
HIGH NUCLEARITY POLYOXOMETALATES AS WATER OXIDATION CATALYSTS: FROM EXPERIMENTS TO THEORY
Joaquín Soriano López

3.1 Introduction

Several polyoxometalates have been reported as active light−driven water oxidation catalysts during the last years. In all cases ruthenium(II) polypyridine complexes were employed as photosensitizer, being the tris(bipyridine) ruthenium(II) chloride ($[Ru(bpy)_3]Cl_2$) the most extensively used. The presence of sacrificial electron acceptors such $Na_2S_2O_8$ was always needed. A schematic representation of the reaction mechanism of light−driven water oxidation catalysis is shown in Figure 3.1. The reaction is initiated with the absorption of one photon by one $[Ru(bpy)_3]^{2+}$, producing an excited state $[Ru(bpy)_3]^{2+*}$ (Eq. 3.1). The last is quenched by a molecule of $S_2O_8^{2-}$, producing two strong oxidants $[Ru(bpy)_3]^{3+}$ [$E^0([Ru(bpy)_3]^{3+}/[Ru(bpy)_3]^{2+})$ = +1.26 V vs NHE[254]] and $SO_4{}^{-\bullet}$ [E^0 ($SO_4{}^{-\bullet}/SO_4{}^{2-}$) ≈ 2.4 V vs NHE[255]], and a molecule of $SO_4{}^{2-}$ (Eq. 3.2). Then the radical specie $SO_4{}^{-\bullet}$ is able to oxidize an additional molecule of $[Ru(bpy)_3]^{2+}$ to give $[Ru(bpy)_3]^{3+}$ (Eq. 3.3). This oxidation occurs via photoinduced electron transfer from the excited state of the photosensitizer to the sacrificial electron acceptor.[256] In addition, flash photolysis experiments carried out to study the kinetics of hole transfer from the oxidized sensitizer to the catalyst, show that the $SO_4{}^{-\bullet}$ specie is strong enough to oxidize not only the $[Ru(bpy)_3]^{2+}$, but may also compete to oxidize the catalyst.[93,257] Finally, four molecules of $[Ru(bpy)_3]^{3+}$ oxidize the catalyst removing four electrons, which in turn oxidizes one molecule of H_2O to O_2, regenerating the $[Ru(bpy)_3]^{2+}$ (Eq. 3.4). It is worthy to mention that during the previously described steps, not only side reactions can take place due to the low selectivity of the oxidative species, but also oxidative degradation of the organic ligands of the $[Ru(bpy)_3]^{2+}$ is observed, resulting in a decrease of the final yield of the oxygen production.

$$Ru(bpy)_3^{2+} + h\nu \rightarrow Ru(bpy)_3^{2+*} \tag{3.1}$$

$$Ru(bpy)_3^{2+*} + S_2O_8^{2-} \rightarrow Ru(bpy)_3^{3+} + SO_4^{2-} + SO_4^{-\bullet} \tag{3.2}$$

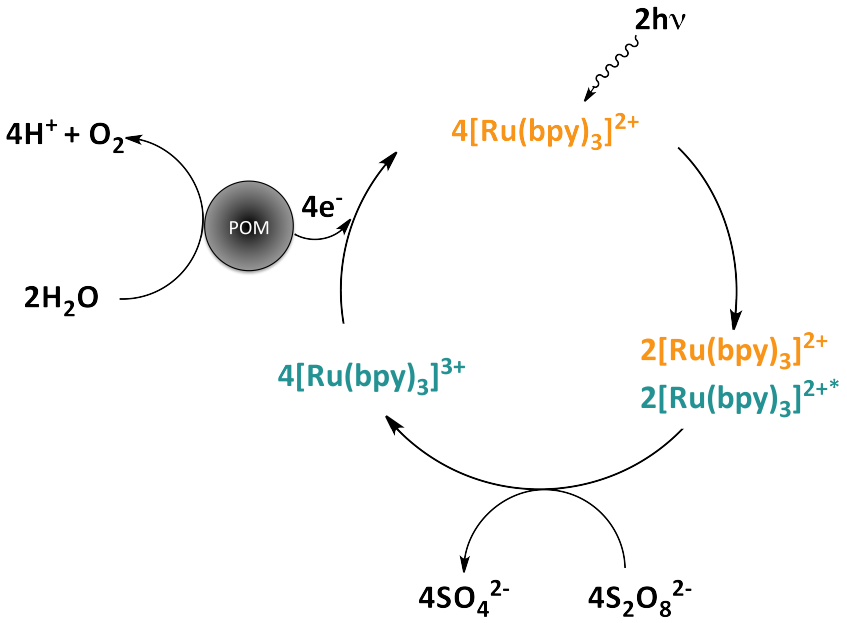

Figure 3.1: Schematic representation of the Light−Driven Catalytic Water Oxidation using a Polyoxometalate as catalyst, $[Ru(bpy)_3]^{2+}$ as photosensitizer, and persulfate as sacrificial electron acceptor.

$$Ru(bpy)_3^{2+} + SO_4^{-\bullet} \rightarrow Ru(bpy)_3^{3+} + SO_4^{2-} \tag{3.3}$$

$$4\ Ru(bpy)_3^{3+} + Catalyst + 2\ H_2O \rightarrow 4\ Ru(bpy)_3^{2+} + Catalyst + O_2 + 4\ H^+ \tag{3.4}$$

The first active polyoxometalate under light−driven water oxidation conditions was reported in 2009 by the group of Hill.[227] They reported the activity of a tetraruthenium polytungstate, $[Ru_4O_4(OH)_2(H_2O)_4(\gamma\text{-}SiW_{10}O_{36})_2]^{10-}$ (**Ru_4Si**), in homogeneous conditions. To carry out the experiments they employed a concentration of 5.0 μM of **Ru_4Si** in a 20 mM sodium phosphate buffer with an initial pH of 7.2, and $[Ru(bpy)_3]^{2+}$ (1.0 mM) as a photosensitizer and $S_2O_8^{2-}$ (5.0 mM) as a sacrificial electron acceptor. Under these conditions they obtained a maximum turnover number (TON) of 350, with an initial turnover frequency (TOF) and quantum yield ($\Phi(O_2)$) of 0.08 s^{-1} and 9%, respectively. The authors observed a decrease in the pH during the reaction from 7.2 to 6.3 and a decomposition of the

$[Ru(bpy)_3]^{2+}$ below the 15%. Moreover, they observed a precipitation of an adduct between the polyoxometalate and the $[Ru(bpy)_3]^{2+}$ when the concentration of the **Ru_4Si** was increased. The decomposition of the polyoxometalate yielding to RuO_2 particles (known as a good WOC) was ruled out by repeating the experiments with $RuCl_3$ as a precursor of the oxide. This experiment resulted in a oxygen evolution rate up to 20-fold lower than employing the **Ru_4Si**.

Later on, in 2010, it was reported by the same group the water oxidation activity under light−driven conditions of the polyanion $[Ru_4(\mu\text{-}O)_4(\mu\text{-}OH)_2(H_2O)_4(\gamma\text{-}PW_{10}O_{36})_2]^{n-}$ (**Ru_4P**).[258] This polyoxometalate is an isostructural phosphorous analogue of **Ru_4Si**, therefore they studied the influence of the heteroatom on the homogeneous light−driven water oxidation catalysis. The experiments were carried out employing both **Ru_4Si** and **Ru_4P** in a 20 mM Na_2SiF_6 buffer at a pH 5.8. Under these conditions, both catalysts show oxygen evolution, being the water oxidation activity of **Ru_4P** a 20% lower than that obtained with **Ru_4Si**. So thus, when employing **Ru_4P** the TON was up to 120, with an initial TOF of 0.13 s^{-1}, and a chemical yield (CY) close to 25%.

A cobalt−based polyoxometalate was reported to be a WOC under light−driven conditions, by Hill and co-workers in 2011.[233] This polyoxometalate, $[Co_4(H_2O)_2(PW_9O_{34})_2]^{10-}$ (**Co_4P**), supposed an important breakthrough since it was the first POM containing exclusively Earth−abundant metals acting as efficient water oxidation catalyst known to date. It was demonstrated that **Co_4P** was the true water oxidation catalyst when the homogeneous light−induced experiments were performed in a 80 mM sodium borate buffer at pH 8.0 with $[Ru(bpy)_3]^{2+}$ (1.0 mM) acting as a photosensitizer and $S_2O_8{}^{2-}$ (5.0 mM) as a sacrificial electron acceptor, yielding a maximum TON up to 224, with a CY of *ca.* 45%, and a initial $\Phi(O_2)$ of 30%.

In an attempt to synthesize the silicon analogue of **Co_4P**, in 2012 the group of Hill obtained the complex $[Co_4(\mu{-}OH)(H_2O)_3(Si_2W_{19}O_{70})]^{11-}$ (**Co_4SiW$_{19}$**).[259] The

crystallographic shown a 1:1 mixture of two isomers, with a disorder between a Co and a W atoms, and a occupation factor of 1/2 for each polyanion. The catalytic activity of $\mathbf{Co_4SiW_{19}}$ in homogeneous conditions was tested with four different 25 mM buffer solutions, being sodium phosphate buffer at pH 7.2, a 1:1 mixture of sodium phosphate and sodium borate buffers at pH 8, a sodium borate buffer at pH 8, and a sodium borate buffer at pH 9. The use of $[Ru(bpy)_3]^{2+}$ (1.0 mM) and $S_2O_8{}^{2-}$ (5.0 mM) was needed in order to achieve O_2 evolution. The highest rates were obtained when employing sodium borate buffer at pH 9 with a TON close to 80 and an initial TOF of 0.1 s^{-1}. Nevertheless, $\mathbf{Co_4SiW_{19}}$ has a low stability and hydrolyzes into other products which are less active as water oxidation catalysts.

Again in 2012, Sakai et al. reported the water oxidation catalytic activity under homogeneous light−driven conditions of two molybdenum−based polyoxometalates with one and two cobalt (III) atoms,[260] $[CoMo_6O_{24}H_6]^{3-}$ (**CoMo**) and $[Co_2Mo_{10}O_{38}H_4]^{4-}$ (**Co$_2$Mo**). In this study they used an aqueous borate buffer 0.1 M at pH 8.0, obtaining initial TOF and $\Phi(O_2)$ of 0.11 s^{-1} and 54%, respectively for **CoMo**, and 0.16 s^{-1} and 42%, respectively when employing **Co$_2$Mo**. The use of these POMs as source of CoO_x being the true catalyst was ruled out since experiments performed with $[Co(H_2O)_6]^{2+}$ did not lead to an increase in the oxygen yield.

Still in 2012, the group of Patzke synthesized a trivacant triruthenium-substituted Keggin-type polyoxometalate, $[\{Ru_3O_3(H_2O)Cl_2\}(SiW_9O_{34})]^{7-}$ (**Ru$_3$Si**), and two sandwich-type analogue to the previously described **Co$_4$P**, $[M_4(H_2O)_2(SiW_9O_{34})_2]^{10-}$ being M = Co^{2+} (**Co$_4$Si**) or Ni^{2+} (**Ni$_4$Si**).[261] The buffer of choice was a 20 mM Na_2SiF_6 buffer at pH 5.8, so thus when carrying out the experiments employing 50 μM of the **Ru$_3$Si** polyoxometalate they obtained a maximum TON of 23 with an initial TOF of 0.7 s^{-1}. When using **Co$_4$Si** as catalyst under the same conditions the highest TON value obtained with only 20 μM of catalyst was 42, while the highest initial TOF reached was 0.4 s^{-1} for a concentration of

42 μM of the catalyst. However, the use of **Ni$_4$Si** showed no activity as WOC under the same conditions. After running those experiments POM−photosensitizer complexes were identified, showing slightly shifted bands of the POM in the IR together with characteristic bands of the $[Ru(bpy)_3]^{2+}$ countercation. Therefore the structure of the POM remains intact within the complex. The recycling of these complexes yield to comparable oxygen evolution obtained with the pristine catalyst. Control experiments were performed to rule out the possibility that leaching of ruthenium or cobalt lead to the formation of the corresponding oxides, acting as true water oxidation catalysts.

Shortly after, it was reported a new Ni−containing polyoxometalate as active water oxidation catalyst under light−driven conditions by Hill and co-workers.[262] Contrary to **Ni$_4$Si** reported by Patzke, this new polyoxometalate, $[Ni_5(OH)_6(H_2O)_3(Si_2W_{18}O_{66})]^{12-}$ (**Ni$_5$Si**), shows catalytic activity. The authors identified the POM−photosensitizer complex as the active specie since filtering the complex before photo−illumination no O_2 was evolved from the supernatant solution. The experiments were carried out employing a 80 mM sodium borate buffer at pH 8.0, yielding to a maximum TON of 60 with a $\Phi(O_2)$ of 3.8%.

In 2013 a study of the activity under light−driven conditions upon different Keggin−type polyoxometalates was published by the group of Ma.[263] The six different polyoxometalates tested were $[Co^{II}W_{12}O_{40}]^{6-}$, $[Co^{III}W_{12}O_{40}]^{5-}$, $[Co^{II}(H_2O)SiW_{11}O_{39}]^{6-}$, $[Co^{II}(H_2O)PW_{11}O_{39}]^{5-}$, $[Co^{II}(H_2O)Co^{II}W_{11}O_{39}]^{8-}$, and $[Co^{II}(H_2O)Co^{III}W_{11}O_{39}]^{7-}$, where only the later, with a tetrahedral Co^{III} as heteroatom, showed efficient O_2 evolution. Experiments were performed in homogeneous conditions with a 80 mM sodium borate buffer at pH 9.0, where they reached a TON as high as 360, and an initial TOF of 0.5^{-1}. It is worthy to mention that initial chemical yields in this work are calculated as $(2{\cdot}n_{O_2})/(n_{Na_2S_2O_8})$ leading to values four times higher than the real ones.

In 2013 Zhang et al. explored the cluster−size−dependent dye−sensitized poly-

oxometalate cluster employing three different polyoxometalates with different size with ruthenium sensitizers acting as charge−balancing cations.[264] The polyoxometalates of choice were $[Mo_6O_{19}]^{2-}$ (**Mo**$_6$) as the smallest one, $[Mo_5S_2O_{23}]^{4-}$ (**Mo**$_5$), and the largest one $\alpha-[Mo_8O_{26}]^{4-}$ (**Mo**$_8$). As photosensitizer they employed tris(1,10−phenanthroline) ruthenium (II) $[Ru(phen)_3]^{2+}$. The results show a clear cluster−size−dependence for the oxygen production, being the largest complex, **Mo**$_8$, the most efficient as water oxidation catalyst, while the **Mo**$_6$ leads to the lowest rates of oxygen production. Authors claim that this result agrees with the fact that in these POMs the Mo=O_t (terminal oxygen) bonds are the active sites for light−driven catalysis, therefore **Mo**$_8$, which contains 14 bonds of this type is more active than **Mo**$_6$, which only has 6 bonds. From our point of view it is no possible that these polyoxometalates can act as water oxidation catalysts. The most reasonable explanation for the oxygen evolution observed is a decomposition of the polyoxometalates yielding to molybdenum oxide species which are the responsible for the catalysis. Therefore, the **Mo**$_8$ leads to higher oxygen evolution rates because it contains more Mo atoms and the decomposition products have more active centers than the other two polyoxometalates.

Again in 2013 it was published by Patzke and co-workers the water oxidation activity under light−driven conditions of three new isostructural cobalt-containing tungstobismutates,[265] being $[\{Co(H_2O)_3\}_2\{CoBi_2W_{19}O_{66}(OH)_4\}]^{10-}$ (**Co**$_3$**Bi**), $[Co_{2.5}(H_2O)_6Bi_2W_{19.5}O_{66}(OH)_4]^{8-}$ (**Co**$_{2.5}$**Bi**), and $[Mn_{1.5}(H_2O)_6Bi_2W_{20.5}O_{68}(OH)_2]^{6-}$ (**MnBi**). Surprisingly, only the **Co**$_3$**Bi** showed catalytic activity, demonstrating that subtile changes into the POM structure can lead to very different behavior in the water oxidation catalysis activity. When employing the **Co**$_3$**Bi** TON can reach a maximum value of 21 with a CY of 97 % in a 20 mM Na_2SiF_6 buffer at pH 5.8.

In this chapter we investigated in collaboration with Prof. Greta R. Patzke's Group (University of Zurich, Switzerland) the water oxidation catalysis under light−driven conditions of the **Co**$_9$ in the solid state. For that purpose two insoluble salts

of $\mathbf{Co_9}$ were tested as heterogeneous light-driven water oxidation catalysts at a pH close to neutrality. The employed salts were the $\mathbf{CsCo_9}$, already described in Chapter 2, and the $[Ru(bpy)_3]^{2+}$ salt which shows a better performance and stability than the cesium salt, namely $\mathbf{RuCo_9}$.

UNIVERSITAT ROVIRA I VIRGILI
HIGH NUCLEARITY POLYOXOMETALATES AS WATER OXIDATION CATALYSTS: FROM EXPERIMENTS TO THEORY
Joaquín Soriano López

3.2 Results and Discussion

3.2.1 Catalytic activity of $CsCo_9$

In Chapter 2 it was demonstrated that the **$CsCo_9$** is active as heterogeneous WOC as a part of a modified electrode. Therefore, it seem to be worthy to test its activity under light−driven water oxidation conditions. Light−driven experiments were carried out with different amounts of the **$CsCo_9$** salt in a pH 7 KP_i buffer (40 mM), with 5 mM of $Na_2S_2O_8$ as sacrificial electron acceptor, and 1 mM of $[Ru(bpy)_3]Cl_2$ as photosensitizer. Molecular oxygen evolution was monitored upon light irradiation ($\lambda > 400$ nm).

Figure 3.2 and Table 3.1 show the oxygen evolution for different amounts of **$CsCo_9$**. The reaction starts with fast kinetics, and slows down until oxygen evolution stops. The highest values of TON (n_{O2}/n_{cat}) and TOF ($n_{O2}/(n_{cat} \cdot \text{time})$) are obtained when using 1 mg of catalyst, being 14.2 and 10.8 h^{-1}, respectively. On the contrary, when employing higher amounts of **$CsCo_9$** these values decrease until a TON value of 0.2 and a TOF of 0.2 h^{-1} when carrying out the experiment with 50 mg of catalyst. These TON and TOF values are not well defined for a heterogeneous catalysts since only the surface of the catalyst is active to evolve oxygen and the values are given for total mass. Therefore we are underestimating the characteristic values as not all the catalytic centers are taking part in the reaction. The final O_2 chemical yield ($n_{O2}/2 \cdot n_{S2O8}$) is 2.3%, obtained when employing 10 mg of **$CsCo_9$**.

The **$CsCo_9$** was recovered after performing the experiments. The catalyst was characterized by infrared spectroscopy (IR), raman spectroscopy and X−ray photoelectron spectroscopy (XPS), showing important changes in the salt. IR spectra obtained from powder samples of **$CsCo_9$** before and after the experiments are shown in Figure 3.3. The IR spectrum before the catalysis shows typical **Co_9** bands within the 1100−400 cm^{-1} range. After the experiments the IR spectrum shows that the

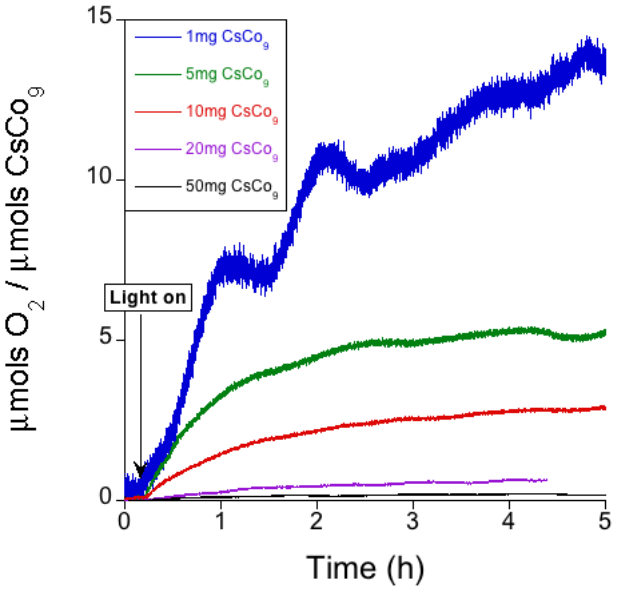

Figure 3.2: Oxygen evolution obtained employing different quantities of the **$CsCo_9$**, in KP_i buffer 40 mM at pH 7, with $[Ru(bpy)_3]Cl_2$ (1 mM) as photosensitizer, and $Na_2S_2O_8$ (5 mM) as sacrificial electron acceptor.

$CsCo_9$ (mg)	**TON**	**TOF** (h^{-1})	**CY** (%)
1	14.2	10.8	1.1
5	5.3	4.0	2.1
10	2.9	1.4	2.3
20	0.7	0.3	1.0
50	0.2	0.2	0.9

Table 3.1: Turnover number (TON), Turnover frequency number (TOF), and Chemical Yield (CY) for heterogeneous light−driven water oxidation catalyzed by **$CsCo_9$**. The experiment was carried out in KP_i buffer 40 mM at pH 7, with $[Ru(bpy)_3]Cl_2$ (1 mM) as photosensitizer, and $Na_2S_2O_8$ (5 mM) as sacrificial electron acceptor.

Co$_9$ structure remains stable. Additional bands are found in the region between 1200 and 1600 cm^{-1} which are attributed to $[Ru(bpy)_3]^{2+}$. These additional bands indicate that during the catalysis a cation exchange occurs as some of the Cs^+ cations have been replaced by $[Ru(bpy)_3]^{2+}$ cations. Comparison of the raman spectra of the pristine **CsCo$_9$** salt and of the collected complex after experiments is shown in Figure 3.4. Typical ν(W=O) bands of freshly **CsCo$_9$** appear around 960 cm^{-1} and a band assigned to the PO_4 moiety appears at 1075 cm^{-1}. Cation exchange during the catalytic experiments is also confirmed since these bands appear shifted to higher wavelengths, arising from an electrostatic interaction between the POM and the photosensitizer. In addition characteristic bands of the $[Ru(bpy)_3]^{2+}$ are found in the collected sample. XPS spectra (Figure 3.5) shows the absence of $[Ru(bpy)_3]^{2+}$ as countercation in the **CsCo$_9$** salt before running light−driven water oxidation experiments. On the contrary, after performing water oxidation catalysis the XPS spectra of the collected salt clearly shows the appearance of peaks assigned to Ru 3d, indicating again a cation exchange during turnover cycles.

These techniques confirm that part of the $[Ru(bpy)_3]^{2+}$ present in solution, acting as photosensitizer, appears incorporated into the structure of the catalyst. This behavior can explain the low chemical yield obtained in the experiments since, although the concentration of $[Ru(bpy)_3]^{2+}$ is not directly related with the chemical yield, the ion-pairing with the **CsCo$_9$** salt decreases the number of molecules of $[Ru(bpy)_3]^{2+}$ dissolved in the media able to be oxidized by the persulfate. Moreover, in presence of neutral or alkali media $[Ru(bpy)_3]^{3+}$ suffer of irreversible decomposition by attack of nucleophyles such a OH^-.[125] For these reason we decided to substitute the use of the Cs^+ salt, and to carry out the light−driven experiments employing the $[Ru(bpy)_3]^{2+}$ as counter cation of the **Co$_9$**, without the need of adding photosensitizer into the solution.

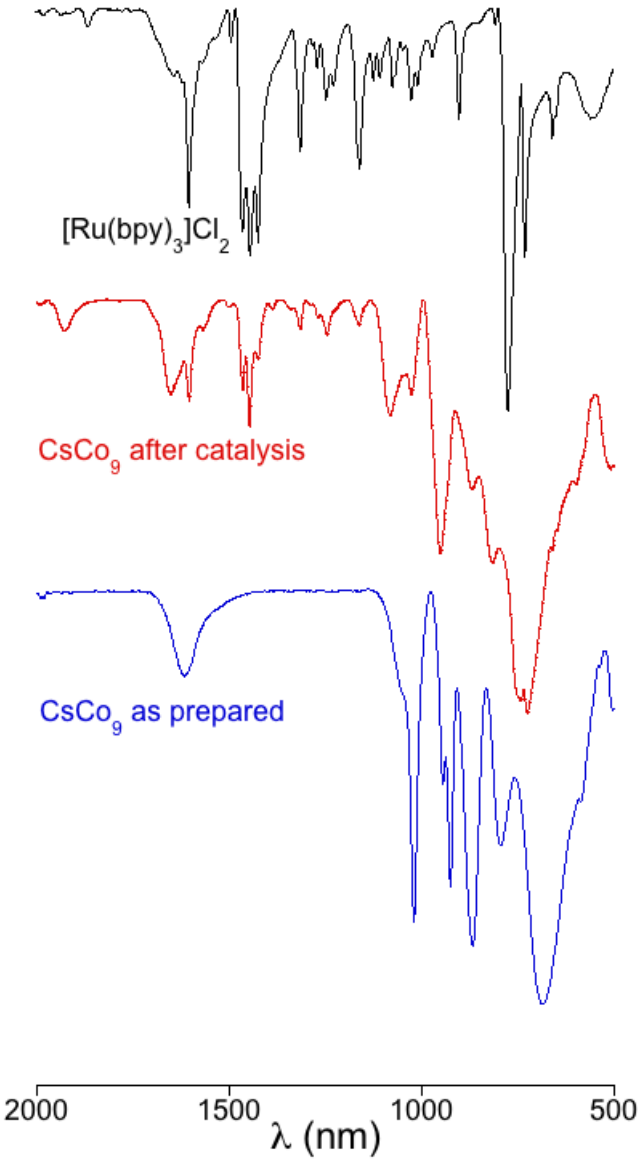

Figure 3.3: FTIR spectra of the **$CsCo_9$** salt before (blue) and after (red) the light−driven water oxidation experiments.

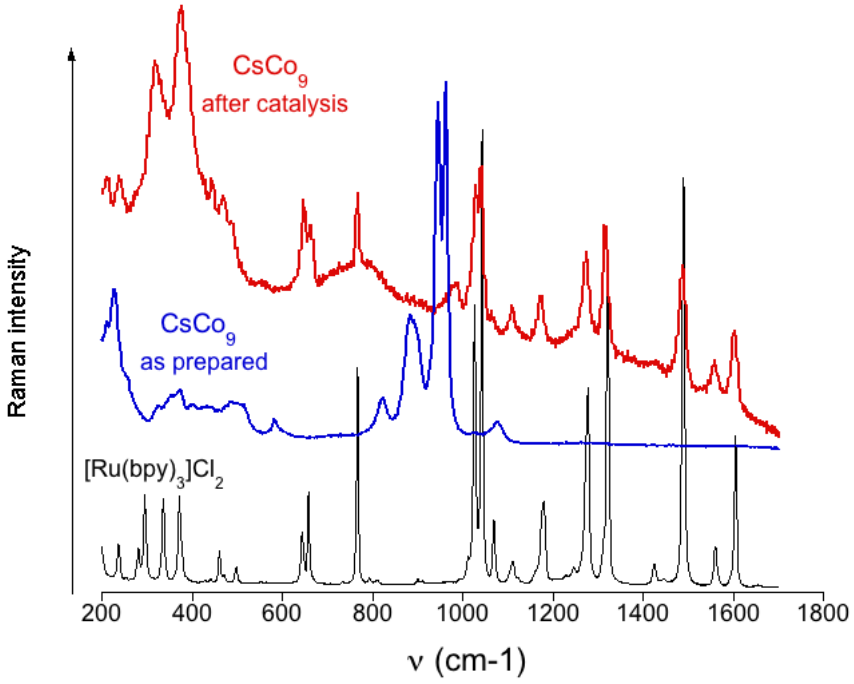

Figure 3.4: Raman spectra of the **CsCo$_9$** salt before (blue) and after (red) the light−driven water oxidation experiments. Raman spectrum of $[Ru(bpy)_3]Cl_2$ (black) is included for comparison.

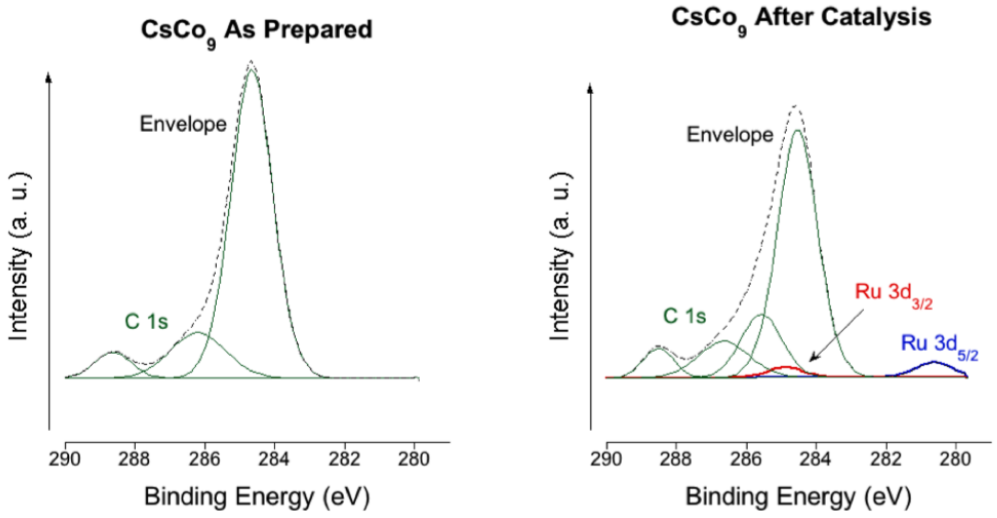

Figure 3.5: Ru 3d (blue and red) and C 1s (green) XPS spectra of **CsCo$_9$** as prepared and collected after catalysis.

3.2.2 Catalytic activity of $RuCo_9$

The **$RuCo_9$** salt obtained by the addition of $[Ru(bpy)_3]Cl_2$ to a **Co_9** water solution. The determination of the counter cations and water content of the **$RuCo_9$** salt was made with CHN analysis and thermogravimetry (TGA), respectively. Data allowed to calculate the molecular formula as $[Ru(bpy)_3]_6K_4[Co_9(H_2O)_6(OH)_3(HPO_4)_2(PW_9O_{34})_3]\cdot 40H_2O$ (M_w = 11821.24) (see Table 3.5 and Figure 3.18 in the Experimental Section). Dynamic light scattering measurements of the **$RuCo_9$** salt in a water suspension indicate an average particle size of 373.5 nm (Figure 3.6).

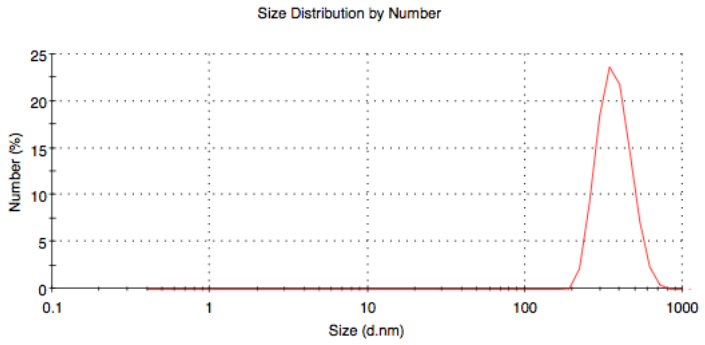

Figure 3.6: Size distribution by number measured for the **$RuCo_9$** in suspension before experiments.

Without further treatment this salt was employed as heterogeneous light−driven water oxidation catalyst. In the experiments we could avoid the use of photosensitizer in solution as it was already present as counteranion of the catalyst. This ion-pairing allows a closer contact between the catalyst and the photosensitizer, increasing the final oxygen production yield, and preventing somehow the degradation of the organic ligands of the $[Ru(bpy)_3]^{2+}$.

The measured oxygen evolution employing different quantities of **$RuCo_9$** is shown in Figure 3.7. The turnover number (TON) decreases from 27.3 to 2.7 as the amount of catalyst increases, for 1 mg of catalyst and 50 mg, respectively (Ta-

ble 3.2). The same behavior is found for the turnover frequency since a TOF of 19.1 h^{-1} is obtained when employing 1 mg of catalyst and 4.31 h^{-1} for 50 mg. We observed a particularity when using 10 mg of **RuCo$_9$**, since the initial evolution rate is higher than employing 5 mg. The highest chemical yield (CY) was obtained when 10 mg of catalyst were employed, where we found a yield of 11.9%.

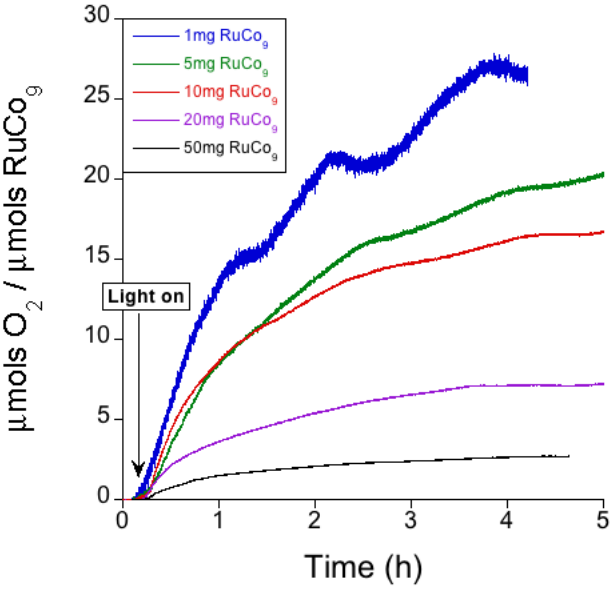

Figure 3.7: Oxygen evolution obtained employing different quantities of the **RuCo$_9$**, in KP_i buffer 40 mM at pH 7, and $Na_2S_2O_8$ (5 mM) as sacrificial electron acceptor.

Comparing the **RuCo$_9$** versus the **CsCo$_9$** salt, we observe higher rates of molecular oxygen conversion obtained for the PS/Catalyst system, as the TON has been increased from 14.2 to 27.3 when employing 1 mg of catalyst (see Figure 3.8). In the same way the TOF value increased from 10.8 h^{-1} to 19.8 h^{-1}, and the maximum chemical yield increased one order of magnitude, from 2.3 % until a 11.9 % when 10 mg of catalyst were employed.

$RuCo_9$ (mg)	**TON**	**TOF** (h^{-1})	**CY** (%)
1	27.3	19.1	1.9
5	20.3	11.9	7.1
10	16.7	17.0	11.9
20	7.2	9.0	10.6
50	2.7	4.3	9.1

Table 3.2: Turnover number (TON), Turnover frequency number (TOF), and Chemical Yield (CY) for heterogeneous light−driven water oxidation catalyzed by **$RuCo_9$**. The experiment was carried out in KP_i buffer 40 mM at pH 7, with $Na_2S_2O_8$ (5 mM) as sacrificial electron acceptor.

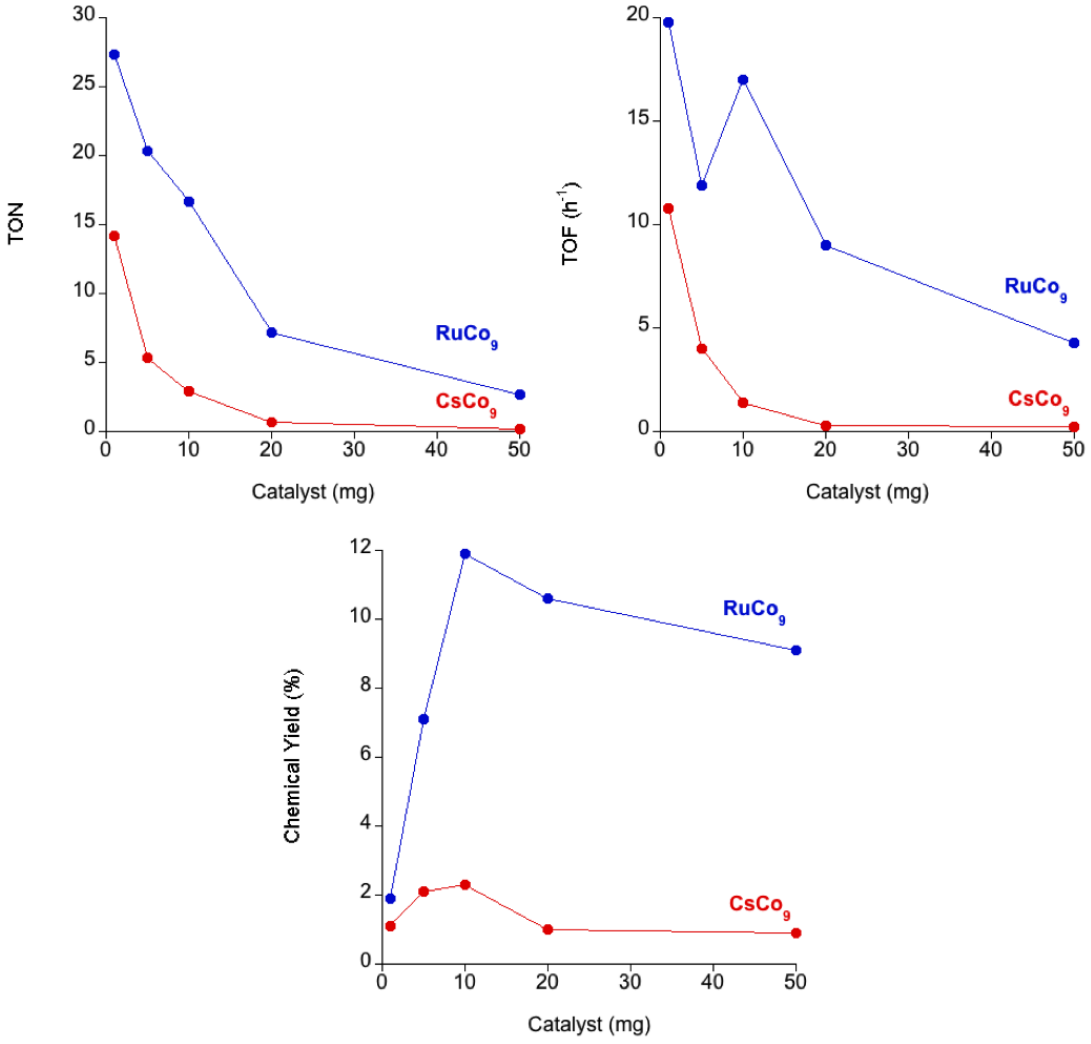

Figure 3.8: Comparison of Turnover number (TON), Turnover frequency number (TOF), and Chemical Yield (CY) obtained with **RuCo$_9$** and **CsCo$_9$**. The experiment was carried out in KP$_i$ buffer 40 mM at pH 7, with $Na_2S_2O_8$ (5 mM) as sacrificial electron acceptor. In the case of **CsCo$_9$** $[Ru(bpy)_3]Cl_2$ (1 mM) was employed as photosensitizer, while for the **RuCo$_9$** the use of photosensitizer un solution was no needed.

Successive additions of $Na_2S_2O_8$ (5 mM) to the reaction vessel after a experiment carried out with 10 mg of **RuCo$_9$** indicate that the catalyst is being deactivated in each cycle. As seen in Figure 3.9 and Table 3.3 in a second cycle the **RuCo$_9$** is still active, but with lower performance than that obtained with a freshly prepared catalyst. The activity decreased again when performing a third cycle. This behavior is explained by the fact that not only part of the $[Ru(bpy)_3]^{2+}$ is being oxidized to $[Ru(bpy)_3]^{3+}$, but also suffering of oxidative degradation of the organic ligands.

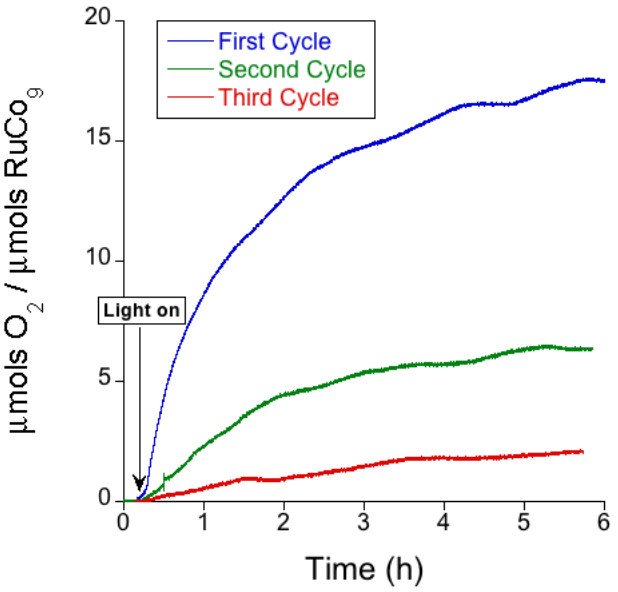

Figure 3.9: Oxygen evolution measured for the successive addition of $Na_2S_2O_8$ (5 mM) to 10 mg of **RuCo$_9$** in in KP$_i$ buffer 40 mM at pH 7.

We also carried out pulse experiments to ensure that the oxygen is only being produced when light is switched on. In these experiments 10 mg of **RuCo$_9$** were suspended in KP$_i$ buffer 40 mM at pH 7 with $Na_2S_2O_8$ (5 mM) as sacrificial electron acceptor. As shown in Figure 3.10 when the light was switched on for three minutes the oxygen concentration in the gas−space increased during 70 minutes where it reaches a plateau. Then, the light was switched on again for three more minutes

$RuCo_9$ (10 mg)	**TON**	**TOF (h^{-1})**	**CY (%)**
1st. Cycle	16.7	17.0	11.9
2nd. Cycle	6.4	2.7	4.4
3rd. Cycle	2.1	0.7	1.4

Table 3.3: Turnover number (TON), Turnover frequency number (TOF), and Chemical Yield (CY) for the successive addition of $Na_2S_2O_8$ (5 mM) to 10 mg of **$RuCo_9$** in KP_i buffer 40 mM at pH 7.

and the same behavior was observed. This procedure was repeated four times, until no oxygen production was detected by the oxygen probe. This experiment clearly shows that the light is the only driving force for oxygen production under these conditions.

In addition, control experiments were carried out in absence of catalyst where negligible amounts of molecular oxygen were obtained, indicating that the true catalyst under our conditions is the **$RuCo_9$** (Figure 3.11).

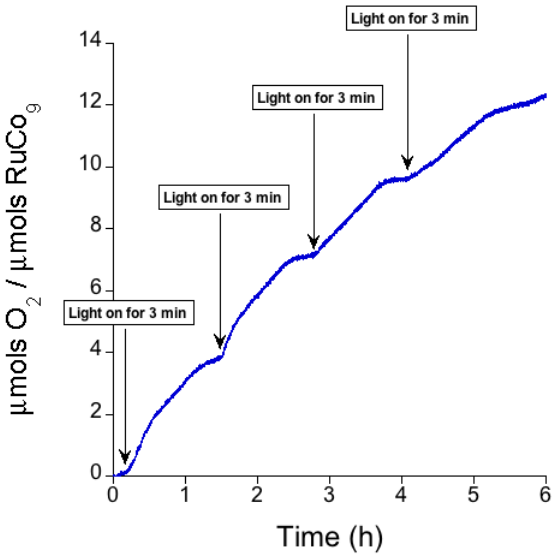

Figure 3.10: Pulse experiments for oxygen evolution employing 10 mg of **RuCo$_9$** in KP$_i$ buffer 40 mM at pH 7 with $Na_2S_2O_8$ (5 mM) as sacrificial electron acceptor.

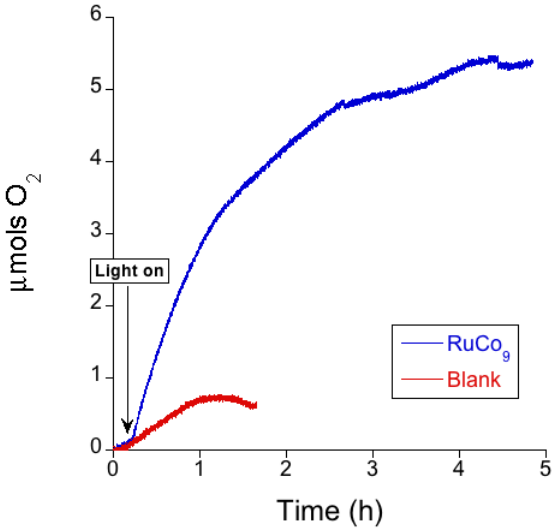

Figure 3.11: Control experiment in absence of catalyst in KP$_i$ buffer 40 mM at pH 7, with $[Ru(bpy)_3]Cl_2$ (1 mM) as photosensitizer, and $Na_2S_2O_8$ (5 mM) as sacrificial electron acceptor, compared with 20 mg of **RuCo$_9$** under the same conditions.

3.2.3 Comparison with Cobalt Oxide

In order to rule out the possibility of having Co^{2+} leaching from the **Co$_9$** structure, and the subsequent formation of cobalt oxide under catalytic conditions, we compared the oxygen evolution of the **RuCo$_9$** salt with that obtained when employing Co_3O_4. To allow a fairly comparison between both catalysts, we carried out the experiments taking into account the number of mols of Co employed in the experiments. Therefore, both experiment were performed under the same conditions in KP_i buffer 40 mM at pH 7, with $[Ru(bpy)_3]Cl_2$ (1 mM) as photosensitizer, $Na_2S_2O_8$ (5 mM) as sacrificial electron acceptor, and 13.99 μmols of Co in the form of **RuCo$_9$** (20 mg, 1.55 μmols), or Co_3O_4 (1.13 mg, 4.66 μmols).

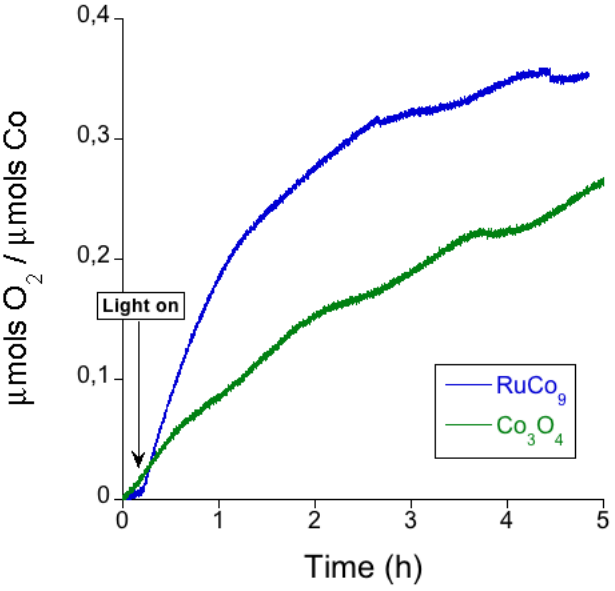

Figure 3.12: Comparison of the oxygen evolution obtained employing the same amount of mols of Co as **RuCo$_9$** and as Co_3O_4. The experiments were performed in KP_i buffer 40 mM at pH 7, with $[Ru(bpy)_3]Cl_2$ (1 mM) as photosensitizer, and $Na_2S_2O_8$ (5 mM) as sacrificial electron acceptor.

	TON	**TOF (h^{-1})**	**CY (%)**
$RuCo_9$	3.2	2.3	4.3
Co_3O_4	0.9	0.3	3.2

Table 3.4: Comparison of Turnover number (TON), Turnover frequency number (TOF), and Chemical Yield (CY) for heterogeneous light−driven water oxidation catalyzed by **$RuCo_9$** and by Co_3O_4. The experiment was carried out in KP_i buffer 40 mM at pH 7, with $[Ru(bpy)_3]Cl_2$ (1 mM) as photosensitizer, and $Na_2S_2O_8$ (5 mM) as sacrificial electron acceptor.

Figure 3.12 and Table 3.4 show the results obtained from the experiments. We can see a higher activity when using the **$RuCo_9$** salt than when the Co_3O_4 is employed as catalyst. The results suggest that in the case of having leaching of Co^{2+} from the **$RuCo_9$** salt, it is not responsible for the oxygen evolution observed during the reaction time, since higher amounts of cobalt are needed to reach the activity shown by the **$RuCo_9$**.

3.2.4 Recovery of $RuCo_9$ After the Experiments

$RuCo_9$ was recovered after the experiments. We performed CHN analysis and TGA to this salt, which showed the molecular formula $[Ru(bpy)_3]_5K_6[Co_9(H_2O)_6(OH)_3(HPO_4)_2(PW_9O_{34})_3]\cdot 25H_2O$ (M_w = 11081.58) (see Table 3.5 and Figure 3.18 in the Experimental Section). This salt was also characterized by IR spectroscopy, raman spectroscopy and XPS. Figure 3.13 shows the IR spectra obtained from the **$RuCo_9$** samples before and after the catalysis. As we can see, the structure of the **Co_9** is maintained while some decomposition of the $[Ru(bpy)_3]^{2+}$ counter cation is observed. Raman spectra acquired from the **$RuCo_9$** salt in both fresh and collected after catalysis samples show that the POM structure is retained during the experiments (Figure 3.14). Electrostatic interactions between

the POM and the photosensitizer lead to a shift to higher wavelengths compared to that obtained with the **CsCo$_9$** salt. Figure 3.15 shows a comparison of the raman spectrum of the collected **RuCo$_9$** after catalytic experiments with that of the Co_3O_4. It supports that the POM structure remains unchanged during experiments with no sign of Co_3O_4 formation, discarding the possibility of having cobalt oxide as the true catalyst under experimental conditions. The presence of $[Ru(bpy)_3]^{2+}$ as countercation was also confirmed by XPS, as shown in Figure 3.16. Figure 3.17 shows the XPS Co($2p_{3/2}$) spectra of **RuCo$_9$** as prepared, and after the experiments. For comparison, the XPS spectra acquired with pristine Co_3O_4 is also shown. The Co_3O_4 has a spinel structure and contains magnetic Co^{2+} ions in the tetrahedral sites and diamagnetic Co^{3+} ions in the octahedral sites. These two sites appear very close in energy in the XPS spectra. Normally, compounds containing high-spin Co^{2+} ions have strong satellite peaks in Co 2p spectra, as obtained in both salts of our catalyst, before and after the experiments. Interestingly, typical Co_3O_4 XPS spectra only has weak satellites in this region, which occur about 7−9 eV higher in binding energy from the main bands.[266,267] Therefore, we identify in the XPS spectra of Co_3O_4 one main peak at 779.7 eV attributed to the Co^{3+} ions in the octahedral sites, whereas the peak of the Co^{2+} ions in the tetrahedral sites lies very close in energy (781.4 eV), appearing as a shoulder of the former peak. Moreover, two weak satellite peaks appear at higher binding energies, at 785.7 and 789.9 eV. On the contrary, XPS spectra of our catalysts show an intense band between 780−781 eV, attributed to the Co^{2+} ions in octahedral sites of the POM. In addition, strong satellite peaks typical of high-spin Co^{2+} ions appear at higher binding energies. The differences in the spectra acquired before and after the catalytic cycles arise from the observed changes in the countercations, and not from the structure of the POM.

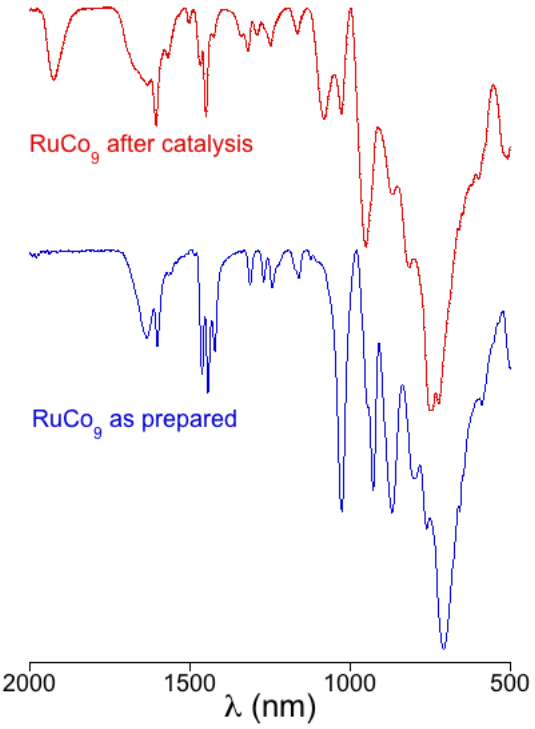

Figure 3.13: FT−IR spectra of the **RuCo$_9$** salt before (blue) and after (red) the light−driven water oxidation experiments.

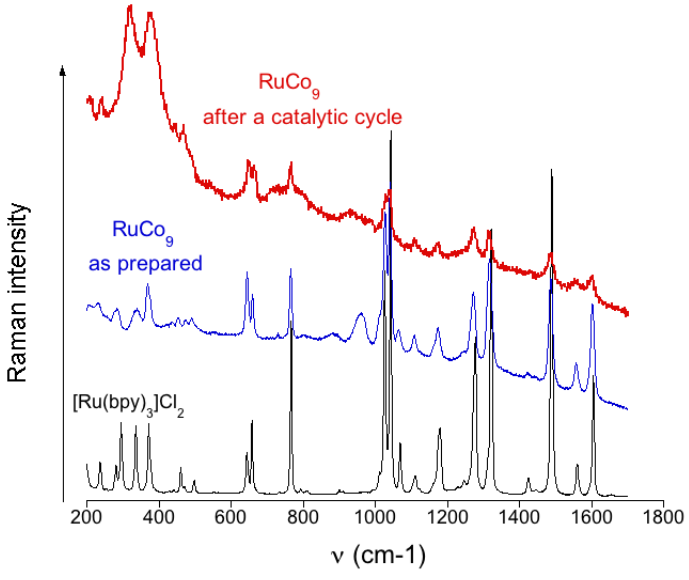

Figure 3.14: Raman spectra of the **RuCo$_9$** salt before (blue) and after (red) the light−driven water oxidation experiments. Raman spectrum of $[Ru(bpy)_3]Cl_2$ (black) is included for comparison.

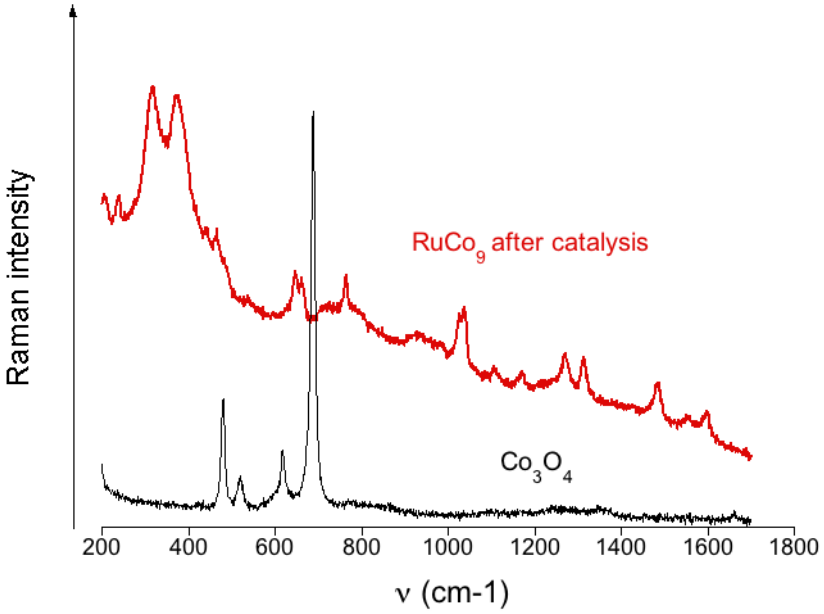

Figure 3.15: Comparison of the raman spectra of the collected **RuCo**$_9$ salt after the light−driven water oxidation experiments and of pristine Co_3O_4.

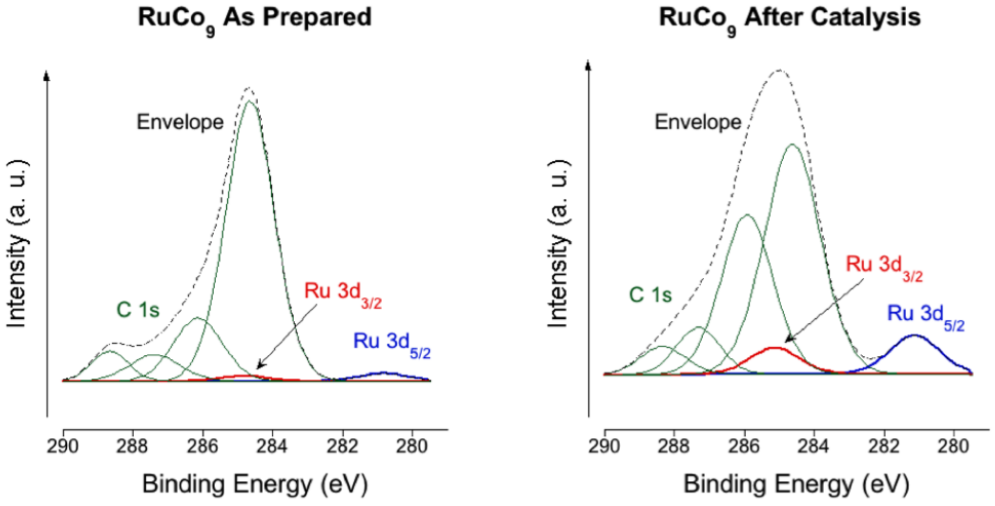

Figure 3.16: Ru 3d (blue and red) and C 1s (green) XPS spectra of **RuCo**$_9$ as prepared and collected after catalysis.

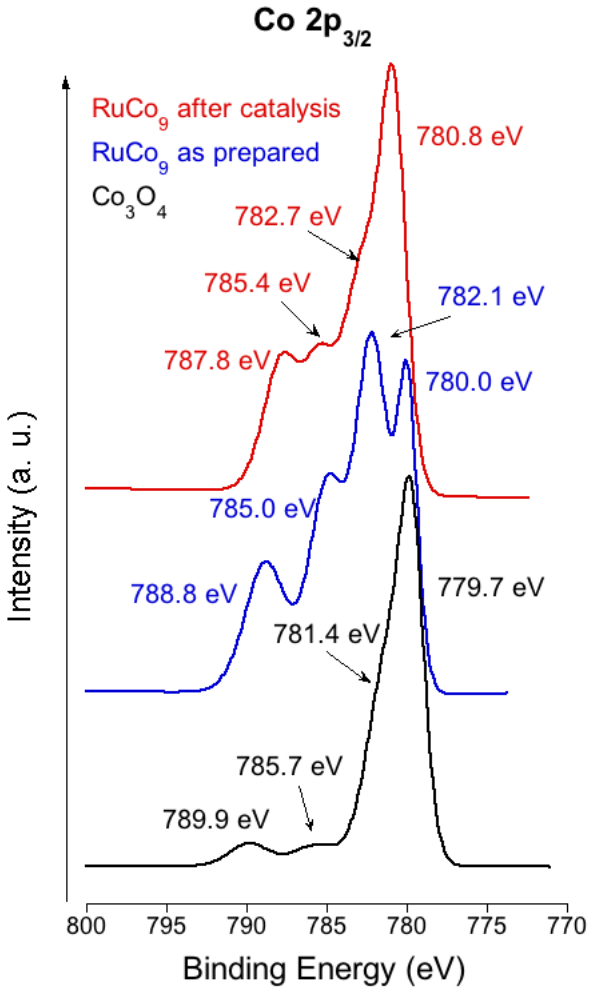

Figure 3.17: Co $2p_{3/2}$ XPS spectra of **RuCo$_9$** as prepared (blue) and collected after catalysis (red), and of pristine Co_3O_4 (black) for comparison.

3.3 Conclusions

In this chapter we present the heterogeneous catalytic activity of **CsCo$_9$** for light-driven water oxidation at pH 7 employing $[Ru(bpy)_3]^{2+}$ as photosensitizer, and $(S_2O_8)^{2-}$ as sacrificial electron acceptor. This catalyst yields a maximum turnover number (TON) of 14.2 and an maximum turnover frequency (TOF) of 10.8 per hour. Characterization of the collected catalyst after running the experiments confirms that the structure of the **Co$_9$** remains stable under experimental conditions, whereas cation exchange occurs during the experiment. Indeed, a suspension of the insoluble salt of **Co$_9$** with the chromophore $[Ru(bpy)_3]^{2+}$ as countercation (**RuCo$_9$**) in a solution containing an electron acceptor, yields improved oxygen evolution under the same conditions. The maximum TON and TOF obtained with the photosensitizer/catalyst solid (**RuCo$_9$**) increase to 27.3 and 19.1 per hour, respectively. However, degradation of the organic ligand of the photosensitizer, due to the highly oxidation environment, leads to its deactivation. **RuCo$_9$** exhibits superior activity when compared with Co_3O_4 under the same working conditions. The later, combined with the characterization of the catalyst, supports the genuine catalytic activity of **Co$_9$** for water oxidation, ruling out the in situ formation of cobalt oxide.

UNIVERSITAT ROVIRA I VIRGILI
HIGH NUCLEARITY POLYOXOMETALATES AS WATER OXIDATION CATALYSTS: FROM EXPERIMENTS TO THEORY
Joaquín Soriano López

3.4 Experimental

3.4.1 Synthesis

Tris(2,2'−bipyridyl)dichlororuthenium(II) hexahydrate and sodium persulfate were purchased from TCI and Sigma-Aldrich (>99% purity) and used without further purification.

The synthesis of **CsCo$_9$** was already described in Chapter 2. In the same way, the $[Ru(bpy)_3]^{2+}$ salt was also prepared by methatesis. An stoichiometric excess of $[Ru(bpy)_3]Cl_2$ was added to a solution containing $Na_8K_8[Co_9(H_2O)_6(OH)_3(HPO_4)_2(PW_9O_{34})_3]\cdot 43H_2O$ salt. The desired salt precipitated immediately. This orange precipitate was filtered, washed with water and acetone, and air−dried.

3.4.2 Characterization

- **Analysis:** The content of $[Ru(bpy)_3]^{2+}$ was determined with a Elemental Microanalyzer Flash model 1112. Thermogravimetry analysis was performed with powder samples using TGA/SDTA851 Mettler Toledo with MT1 microbalance.

	Before		**After**	
RuCo$_9$	atomic % (found)	stoichiometry (estimated)	atomic % (found)	stoichiometry (estimated)
C	17.75	180	15.92	150
H	1.87	241	1.43	217
N	3.99	36	3.82	30

Table 3.5: CHN analysis of the **RuCo$_9$** salt before and after the light-driven water oxidation experiments.

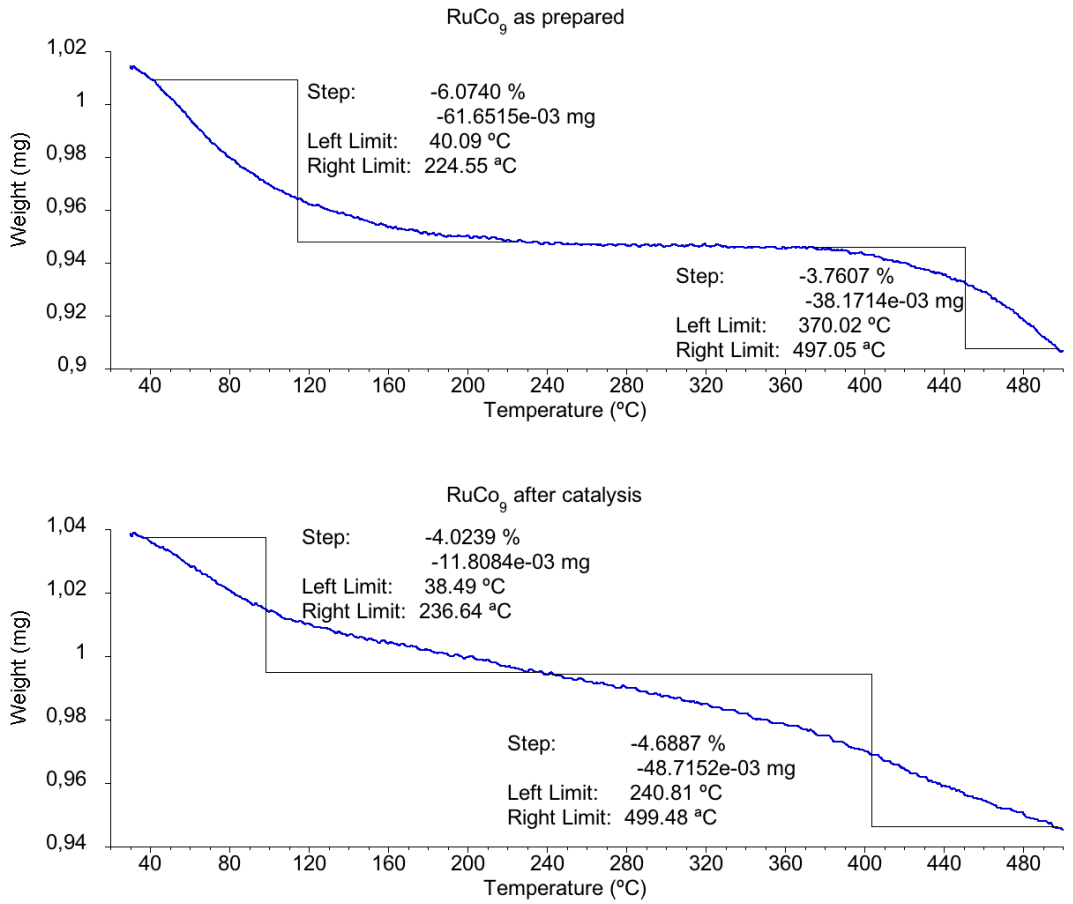

Figure 3.18: Thermogravimetric analysis of the **RuCo$_9$** salt before (top) and after (bottom) the light-driven water oxidation experiments.

- **Dynamic Light Scattering:** The nanoparticle size distribution of **RuCo$_9$** was measured using a Malvern nanoZS analyzer.

- **Infrared Spectroscopy:** IR spectra were collected in the 3600−400 cm^{-1} range with a Bruker Optics FTIR Alpha spectrometer equipped with a DTGS detector, KBr beamsplitter at 4 cm^{-1} resolution.

- **Raman:** Raman measurements were acquired using a Renishaw inVia Reflex Raman confocal microscope (Gloucester-Shire, UK) equipped with a diode laser emitting at 785 nm at a nominal power of 300 mW, and a Peltier-cooled

CCD detector (-70°C) coupled to a Leica DM-2500 microscope.

- **X-Ray Photoelectron Spectroscopy:** XPS (K-ALPHA, Thermo Scientific, SSTTI at University of Alicante) was used to analyze the sample surfaces. All spectra were collected using Al-K_α radiation (1486.6 eV), monochromatized by a twin crystal monochromator, yielding a focused X-ray spot with a diameter of 400 μm, at 3 mA x 12 kV. The alpha hemispherical analyzer was operated in the constant energy mode with survey scan pass energies of 200 eV to measure the whole energy band, and 50 eV in a narrow scan to selectively measure the particular elements.

3.4.3 Light−Driven Water Oxidation Catalysis Tests

Water oxidation experiments were performed in a 6.7 mL headspace Schlenk tube sealed with a rubber septum (PFTE). The Schlenk tube was covered with an aluminum foil, in order to avoid an early light−induced reaction of the system, and filled with 1 mM (9.4 mg) $[Ru(bpy)_3]Cl_2$, 5 mM (14.9 mg) $Na_2S_2O_8$, the desired amount of catalyst, and 12.5 mL of 40 mM KP_i buffer solution at pH 7.0, with a remaining gas−space of 6.7 mL. The experiment employing the **RuCo$_9$** as catalyst, did not required the addition of $[Ru(bpy)_3]Cl_2$ to the buffer solution, except for comparison with Co_3O_4 where the same concentration (5 mM) was employed in both experiments. The solution was completely deaerated by purging with nitrogen. A baseline of 20 min was recorded to guarantee no oxygen leakage or side reaction and, then the system was exposed to the light of a blue LED lamp (wavelength at peak emission = 465 nm; OSRAM Opto Semiconductors) working at 0.20 A and 11.4 V. The concentration of oxygen in the headspace was measured by employing a O_2−sensor probe (Ocean Optics NeoFOX oxygen−sensing system equipped with a FOXY probe).

The **number of mols of O$_2$ produced** during the experiments were calculated from the $\%O_2$ given by the oxygen−sensing probe employing the Dalton's law of partial pressures:

$$\%O_2 = \frac{P_{O2}}{P_T} \cdot 100 \tag{3.5}$$

Where P_{O2} is the partial pressure of the O_2 in the gas−space, and P_T is the total pressure and equal to 1 atm.

Therefore, substituting P_{O2} into the Ideal gas law we can calculate the number of mols of O_2 produced as:

$$n_{O2} = \frac{\frac{\%O_2}{100} V_{gs}}{RT} \tag{3.6}$$

Where n_{O2} = number of moles of O_2; $\%O_2$ = percentage of O_2 present in the gas−space; V_{gs} = gas−space volume (in L); R (gas constant) = 0.082 atmL/molK; and T = 298K.

The **chemical yield** (CY, %) and the **quantum yield** ($\Phi(O_2)$, %) were calculated as:

$$CY = \frac{n_{O2}}{2 \cdot n_{S2O8}} \cdot 100 \tag{3.7}$$

$$\Phi(O_2) = \frac{2 \cdot n_{O2}}{I} \cdot 100 \tag{3.8}$$

Where n_{O2} = number of moles of O_2, and n_{S2O8} = number of moles of $Na_2S_2O_8$, and I is the rate of absorption of incident photons. In both equations the number two arises because the formation of O_2 requires four electrons, but the photochemical act using the $[Ru(bpy)_3]^{2+}$−$S_2O_8^{2-}$ assay produces only two electrons.[118]

The **Turnover number** (TON) was calculated as:

$$TON = \frac{n_{O2}}{n_{cat}} \tag{3.9}$$

Where n_{O2} = number of moles of O_2, and n_{cat} = number of moles of catalyst.

Finally, the **Turnover frequency** (TOF, s^{-1}) was calculated by plotting n_{O2}/n_{cat} vs. time. The slope at beginning of the O_2 evolution follows a linear fit, and it is equal to the TOF, following the relationship:

$$TOF = \frac{n_{O2}}{n_{cat} \cdot t} = slope \tag{3.10}$$

UNIVERSITAT ROVIRA I VIRGILI
HIGH NUCLEARITY POLYOXOMETALATES AS WATER OXIDATION CATALYSTS: FROM EXPERIMENTS TO THEORY
Joaquín Soriano López

Chapter 4

Tetracobalt-Polyoxometalate: A Mechanistic Proposal

UNIVERSITAT ROVIRA I VIRGILI
HIGH NUCLEARITY POLYOXOMETALATES AS WATER OXIDATION CATALYSTS: FROM EXPERIMENTS TO THEORY
Joaquín Soriano López

4.1 Introduction

Atomistic level understanding of mechanisms and governing factors of water oxidation by transition metal catalysts is expected to advance us on design of more efficient, stable, fast and cost-effective water oxidation catalysts. The mechanism of water oxidation catalyzed by Ru-based systems has been subject of extensive studies.[65,230,231,268–276] However, the mechanism and governing factors of the Co-containing catalysts still remain elusive, and computational approaches are expected to play a crucial role in solution of these problems.

Regarding polyoxometalates, Piccinin and Fabris have carried out computational mechanistic studies of the water oxidation catalyzed by $[Ru_4(\mu\text{-}O)_4(\mu\text{-}OH)_2(H_2O)_4(\gamma\text{-}SiW_{10}O_{36})_2]^{10-}$ (**Ru$_4$Si**) by means of DFT calculations.[231,273] In a first approximation, authors studied a reaction cycle involving four consecutive proton-coupled electron transfer (PCET) events where the four $Ru^{IV}-OH_2$ units (initial state $\mathbf{S}_0$) are successively oxidized to four $Ru^{V}-OH$ centers of the activated intermediate ($\mathbf{S}_4$).[231] Among these states the frontiers molecular orbitals are located in the tetraruthenium-oxo core. This fact highlight not only the stability of the all-inorganic ligands (two lacunary γ-Keggin units in this case) under turnover conditions, but also supports the metal-oxo core as the catalytic site for water oxidation. The predicted thermodynamics of the reaction is in good agreement with the available experimental cyclic voltammetry measurements up to $\mathbf{S}_3$, but the calculated free energy difference between the initial and the activated state ($\mathbf{S}_0/\mathbf{S}_4$) turns out to be significantly lower than the thermodynamic limit for water oxidation. This suggests that promoting this reaction would require cycling between higher oxidation states. Following the study, Piccinin and Fabris demonstrated that further oxidations are needed to form an O−O bond, and posterior O_2 evolution (Figure 4.1).[273] Therefore, further oxidation of $\mathbf{S}_4$ to $\mathbf{S}_5$ leads to the formation of one formal $Ru^{VI}-O$ through a PCET event. However, a net spin polarization appears on the

oxo ligand, suggesting that the $Ru^{VI}-O$ group is formally closer to being $Ru^{V}-O^{\bullet}$. Another PCET event leads to species $\mathbf{S}_6$, with two $Ru^{V}-$oxyl moieties. The reaction proceeds with the key O−O bond formation via nucleophilic attack of water to the oxyl ligand reaching a $Ru^{V}-OOH$, with a proton transfer in a concerted manner to the other oxyl ligand leading to a $Ru^{V}-OH$ group ($\mathbf{S}_6{}^{*}$). Two further steps are needed for oxygen evolution. First, one of the $Ru^{V}-OH$ is converted back to a $Ru^{IV}-OH_2$ through the migration of a proton and an electron from the hydroperoxo ligand. This leads to a $O_2{}^{\bullet-}$ superoxo bound to the Ru(V) center. Then, molecular oxygen is evolved when an electron transfer from the superoxo to the neighboring Ru ion, and a water molecule displaces the O_2. It is worthy to mention that authors suggest that in reaction pathways from multicenter metal-oxo cores, minimum overpotentials can also be achieved by single-site catalysis with the remaining metal centers promoting multielectron processes.

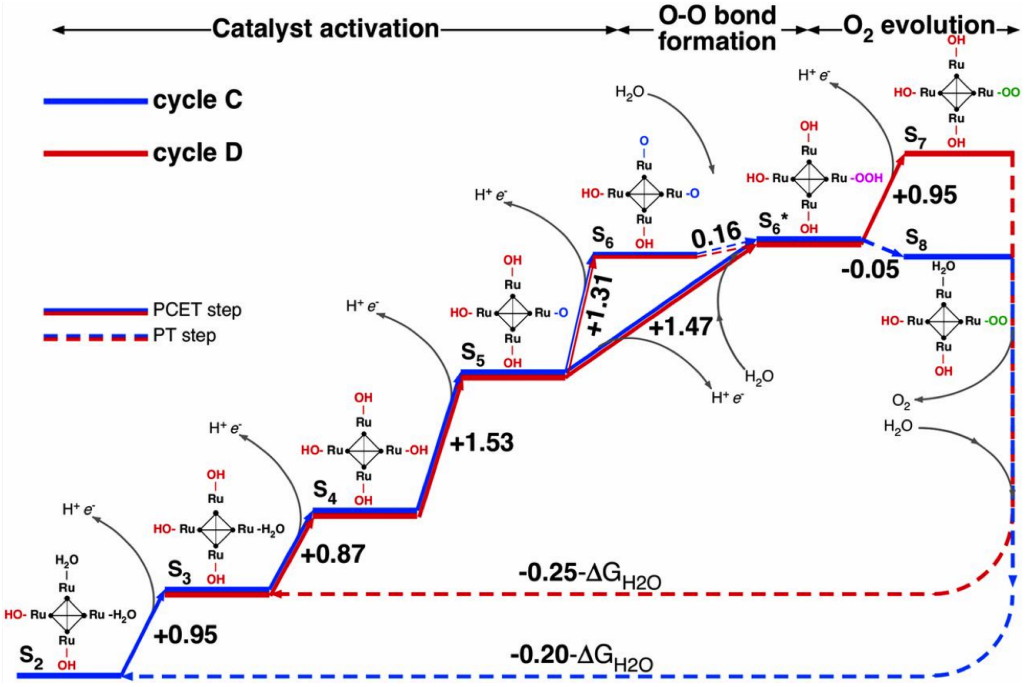

Figure 4.1: Free energy diagram for the proposed reaction cycle (C) and an alternative cycle (D) with a schematic representation of the reaction intermediates. $\Delta G(H_2O)$ is the free energy change in the reaction $2H_2O \rightarrow O_2 + 2H_2$ at pH = 0 and room temperature.[273]

The mechanism of water oxidation catalyzed by single-Ru-substituted Keggin anions ($[Ru^{III}(H_2O)XW_{11}O_{39}]^{n-}$; X = Si(IV), Ge(IV)) was investigated through DFT calculations by Su and co-workers.[274] The reaction mechanism was already proposed by Fukuzumi et al.,[277] based on kinetic analysis and detection of the catalytic intermediates. As shown in Figure 4.2, the reaction starts with the oxidation of Ru(III) to Ru(IV), followed by the loss of two protons and one more oxidation reaching the highly oxidized species Ru^{V}=O. Authors analyzed the electronic characteristics of the Ru^{V}−oxo species and found a substantial radical character of the fragment, which is in agreement with that reported by Piccinin and Fabris.[273] The next step is the formation of the O−O bond from a water nucleophilic attack to the active species Ru^{V}=O, with a proton transfer from the water molecule to a basic oxygen of the polyoxometalate ligand. The O−O bond formation leads to the species Ru^{III}−OOH, which followed by a PCET event yields Ru^{IV}−OO. For simplicity, the proton transferred to the basic oxygen of the POM at the formation of the O−O bond was ignored. Molecular oxygen is released upon oxidation of the ruthenium center to the species Ru^{V}−OO followed by water displacement. Different isomers were studied for the key intermediates peroxo-species, $[Ru^{IV}(OO)SiW_{11}O_{39}]^{6-}$ and $[Ru^{V}(OO)SiW_{11}O_{39}]^{5-}$, considering six- or seven-coordinate Ru species. Results indicate that and open terminal geometry (six-coordinate species) is more favorable than the seven-coordinate species. The effect of changing the heteroatom (from Si(IV) to Ge(IV)) on the catalytic activity was also explored in the rate determining step, *i.e.* O−O bond formation. Employing Ge(IV) as heteroatom leads to a slightly lower energy barrier for the O−O bond formation, than that obtained with Si(IV). Authors claim that this difference mainly arises from the different electronegativity of the heteroatoms. Hence, decreasing the electronegativity from Ge to Si will lead to a decrease of the charge of the Ru=O moiety. As a result, increasing the electronegativity of the heteroatom leads to an improvement of the electrophilic activity of the Ru^{V}−O site.

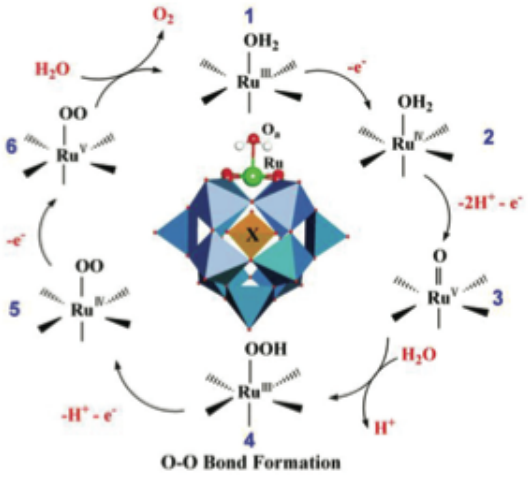

Figure 4.2: Proposed single-site water oxidation mechanism catalyzed by Ru-substituted polyoxometalates, X = Si, Ge.[277]

Recent mechanistic studies on heterogeneous cobalt oxide catalysts have focused on various model system of the cobalt phosphate WOC (CoP_i),[94,278,279] including the cluster[280] and periodic[281] models. In general, these studies have shown that water oxidation by CoP_i were initiated by successive Proton Coupled Electron Transfer (PCET) events (concerted or sequential) leading to the formation of the active $Co^{IV}-$oxo or $Co^{III}-$oxyl species, which involved in the formation of the O−O bond. Two different mechanisms for the O−O formation have been proposed: (i) "water-assisted" mechanism, involving intermolecular nucleophilic attack of external water to the electrophilic $Co^{IV}-$oxo or $Co^{III}-$oxyl species,[278] and (ii) "direct O−O coupling" mechanism proceeding via intramolecular direct coupling of two $Co^{IV}-$oxo sites.[230,231,273–276] These initial discrepancies were later attributed to the structural differences in the used models.[282]

In this chapter we investigate by computational means the full catalytic cycle of the water oxidation catalyzed by Co-containing POMs treated as single-site catalysts. Because of bulkiness and structural stability of Co-POM anions one can eliminate the O−O bond formation mechanism by direct coupling between two Co groups and we focused on the "water-assisted" mechanism. We propose a reaction mecha-

nism of the water oxidation catalyzed by the well known $[Co_4^{II}(H_2O)_2(PW_9O_{34})_2]^{10-}$ (**PCo**$_4$) POM, identifying all the intermediate species. Then a comparison with the recently reported analogous system $[Co_4^{II}(H_2O)_2(VW_9O_{34})_2]^{10-}$ (**VCo**$_4$) is done. We do not analyze the magnetic coupling among the Co atoms because it is beyond the scope of the present study. In addition we present some preliminary results for water oxidation catalysis by $[Co(H_2O)PW_{11}O_{39}]^{5-}$ (**PCo**$_1$) and $[Co_9(H_2O)_6(OH)_3(HPO_4)_2(PW_9O_{34})_3]^{16-}$ (**Co**$_9$) aiming to analyze the effect of POM nuclearity.

UNIVERSITAT ROVIRA I VIRGILI
HIGH NUCLEARITY POLYOXOMETALATES AS WATER OXIDATION CATALYSTS: FROM EXPERIMENTS TO THEORY
Joaquín Soriano López

4.2 Computational Details

All reported calculations were performed with the Gaussian09 package[283] at density functional theory (DFT) level by utilizing B3LYP functional.[284–286] For Co, W, P, V, and Al atoms, the LANL2DZ effective core potential (ECP) and associated basis sets were used.[287] The 6-31g(d,p) basis set was used for O atoms directly bound to Co, and the 6-31g basis set for the rest of atoms.[288–290] All the structures were optimized in water using IEF-PCM approach to model the solvent effects ($\epsilon = 78.36$ and UFF radii).[291] Theoretical magnetic analysis of the anion is beyond the scope of the present study. The nature of all stationary points was verified by vibrational frequencies, which were also used for calculation of free energy contributions. In order to investigate the energies required to reach each step in the catalytic cycle we adopted the energetic scheme proposed by Voorhis:[272]

$$E^0 = \frac{1}{F}(\Delta G^0_{(g)} + \Delta G_{solv} - n_{H^+} G^{0H^+}_{(aq)}) - 4.24\ V \tag{4.1}$$

where F is the Faraday constant, $\Delta G^0_{(g)}$ is the free energy change associated with oxidation in vacuum, ΔG_{solv} is the free energy of solvation, $G^{0H^+}_{(aq)}$ is the standard free energy of a proton in aqueous solution for which we adopted a value of -11.803 eV, and the negative term references the potentials to the NHE (E_{abs} = -4.24 V with Fermi-Dirac statistics).

In addition, electrochemical steps that involve a proton transfer the measured potential at experimental pH conditions is related to standard condition (pH = 0) by the Nernst equation that a room temperature is in V:

$$E = E^0 - 0.059 * pH \tag{4.2}$$

Calculated pK_a's were obtained from the free energy of deprotonation ($\Delta G_d{}^0$) using the standard equation:[269,292,293]

$$pK_a = -log_{10}\, e^{\frac{-\Delta G_d^0}{RT}} \tag{4.3}$$

where,

$$\Delta G_d^0 = \Delta G_{(g)}^0 + \Delta G_{solv} - n_{H^+} G_{(aq)}^{0H^+} \tag{4.4}$$

4.3 Results and Discussion

4.3.1 Electronic and Structural Properties of the PCo_4 and VCo_4 Catalysts

We selected to elucidate mechanism of the sandwich species $[Co_4(H_2O)_2(PW_9O_{34})_2]^{10-}$ (**PCo_4**) and $[Co_4(H_2O)_2(VW_9O_{34})_2]^{10-}$ (**VCo_4**) for which the water oxidation was extensively studied by experiment.[219,238,294] These experiments have shown that at the resting stages of **PCo_4** and **VCo_4** anions all four Co atoms are in their 2+ oxidation states with a formal $d^{\,7}$ configuration and three unpaired electrons. From these three unpaired electrons two occupy and e_g-like and one a t_{2g}-like orbitals. As said above, magnetic coupling among the Co centers is beyond the present study. Therefore, we assume a high-spin configuration and discuss only the electronic state of **PCo_4** and **VCo_4** with their twelve (three per Co-center) unpaired electrons. Furthermore, for simplicity of our analysis we fixed C_{2h} symmetry in the ground state ($\mathbf{S}_0$) of both anions, in which the water ligand is linked to the external Co(II) centers with a relatively long bond length (2.24 Å), and adopted an orientation to accentuate the interaction between the hydrogen atoms and the terminal oxo sites of the POM (with O−H$\cdots$O=W distance ∼2.01 Å, as shown in Figure 4.3). The calculated geometry parameters of **PCo_4** and **VCo_4** are well agreed with their X-ray values.

	POM	$\mathbf{S_0}$	$\mathbf{S_1}$'	$\mathbf{S_1}$	$\mathbf{S_2}$	**TS**	$\mathbf{S_3}$'	$\mathbf{S_3}$	$\mathbf{S_4}$
d(Co-O_t)	PCo_4	2.240	1.956	1.820	1.760	1.730	1.876	1.832	2.060
	VCo_4	2.220	1.968	1.821	1.761	1.734	1.867	1.833	2.013
d(Co-O_c)	PCo_4	2.240	1.969	2.100	2.100	2.070	2.097	2.106	2.164
	VCo_4	2.150	1.938	2.064	2.062	2.018	2.066	2.062	2.117
ρ(Co)	PCo_4	2.73	0.00	0.00	-0.04	1.15	1.01	0.01	0.79
	VCo_4	2.78	0.00	-0.01	-0.06	1.35	1.03	-0.01	0.71
ρ(O)	PCo_4	0.03	0.00	-0.01	1.00	-0.14	-0.06	-0.01	0.09
						(-0.10)	(-0.01)	(0.00)	(0.15)
	VCo_4	0.03	0.00	0.01	1.01	-0.26	-0.08	0.00	0.11
						(-0.17)	(-0.01)	(0.00)	(0.21)

Table 4.1: Structural (in Å) and electronic (in $|e|$) parameters for the different species (S_i) involved in the water oxidation by the polyanions $[Co_4(H_2O)_2(XW_9O_{34})_2]^{10-}$, X = P(V), V(V). Values in parentheses are for the second oxygen atom after the O−O bond is formed.

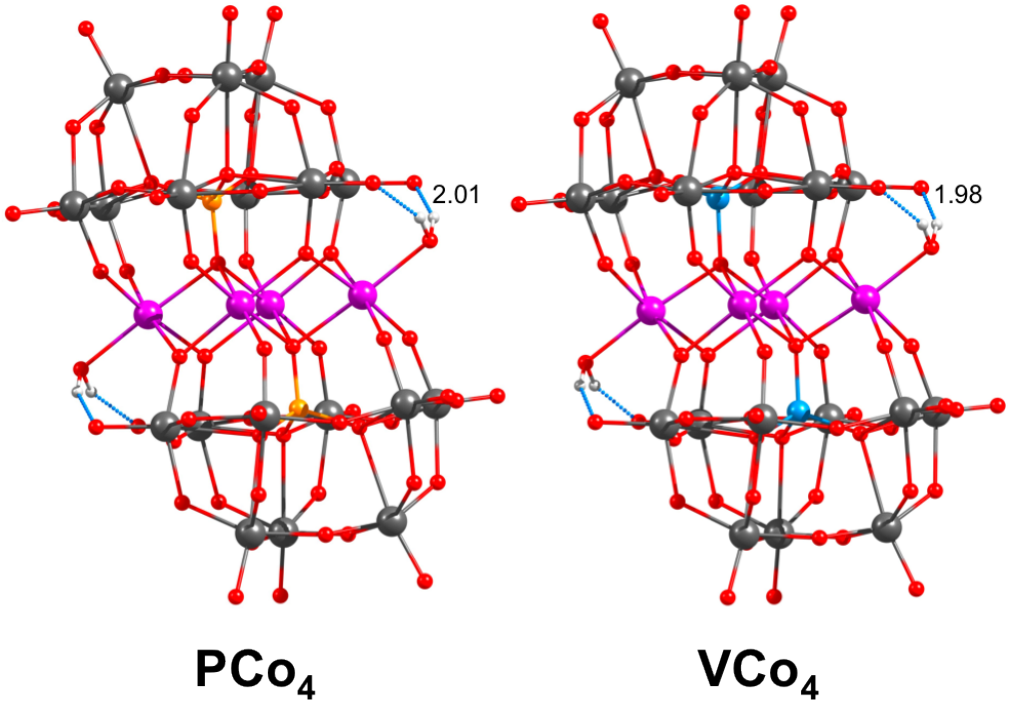

Figure 4.3: Ball and stick representations for $\mathbf{PCo_4}$ and $\mathbf{VCo_4}$ anions. Some selected bond distances are given in Å. In sandwich POMs water ligands linked to TM ions are stabilized by hydrogen bonds with terminal oxo ligands.

4.3.2 Water Oxidation by the $\mathbf{PCo_4}$ anion

A. Initial Steps

Taking as starting point the mechanism proposed for single-site cobalt[295–297] and ruthenium[65,268–272] catalysts, we analyzed each step of the $\mathbf{PCo_4}$-catalyzed water oxidation cycle (Figure 4.4). Calculations show that first PCET step of the overall water oxidation process starts from the resting $Co^{II}-OH_2$ ($\mathbf{S_0}$) state of the system and leads to the $Co^{III}-OH$ species ($\mathbf{S_1}$). The following second PCET event leads to the $Co^{III}-$Oxyl species ($\mathbf{S_2}$). For these two steps of the reaction we computed both the *coupled* (or *concerted*) and *uncoupled* (or *stepwise*) pathways. The computed free energies, shown in Figure 4.5, indicate that the first *coupled* PCET step, *i.e.* $\mathbf{S_0}\rightarrow\mathbf{S_1}$ transition, requires a potential of 1.98 V vs NHE at pH 0. In contrast, the

same step of the reaction proceeding *via* the *uncoupled* electron-then-proton transfer mechanism ($\mathbf{S}_0 \rightarrow \mathbf{S}_1$') requires only 1.27 V, which is 0.71 V lower as a result of the relatively high pK_a (+12.1) of the deprotonation step ($\mathbf{S}_1$'$\rightarrow\mathbf{S}_1$). Thus, at pH 0 the process starts from $\mathbf{S}_0$ with the oxidation of the Co(II) center. However, the equilibrium for the deprotonation step is only shifted to the deprotonated form if the pH is basic enough. Indeed, most of the catalytic processes utilizing cobalt-containing POMs occur in neutral or basic media (often pH 8). Therefore, elucidating contribution from the pH of solution to the calculated oxidation potentials is rather important affecting to the *coupled* events (see Equation 4.2) and to the equilibrium of the deprotonation steps. As shown in Figure 4.5, for the first PCET event the increase of pH from 0 to 8 reduces the potential from 1.98 V to 1.51 V.

Once it reached the $\mathbf{S}_1(Co^{III}-OH)$ state, the cobalt center is expected to further oxidized (the second PCET event, *i.e.* $\mathbf{S}_1 \rightarrow \mathbf{S}_2$). Following the aforementioned procedure, we computed again *coupled* ($\mathbf{S}_1 \rightarrow \mathbf{S}_2$) and *uncoupled* ($\mathbf{S}_1 \rightarrow \mathbf{S}_2$'$\rightarrow\mathbf{S}_2$) events. We found that the second *coupled* PCET event requires to apply a potential of 1.95 V, whereas the *uncoupled* electron-then-proton transfer needs a 2.59 V potential, both at pH 0. Thus, the second oxidation proceeds *via* a *coupled* PCET step, $\mathbf{S}_1(Co^{III}-OH) \rightarrow \mathbf{S}_2(Co^{III}-O^{\bullet})$. Change of pH from 0 to 8 reduced the calculated potential to 1.48 V (Figure 4.5).

In short, aforementioned discussions show that at the pH in which the reaction occurs (pH 8) the initial PCET step (from $\mathbf{S}_0$ to $\mathbf{S}_1$) proceeds *via* the *uncoupled* electron-then-proton transfer ($\mathbf{S}_0 \rightarrow \mathbf{S}_1$'$\rightarrow\mathbf{S}_1$) pathway and leads to one-electron oxidation of the Co(II) center. However, the following second PCET (*i.e.* $\mathbf{S}_1 \rightarrow \mathbf{S}_2$) event proceeds *via* the *coupled* pathway and leads to the POM-$Co^{III}-O^{\bullet}$ *active* species.

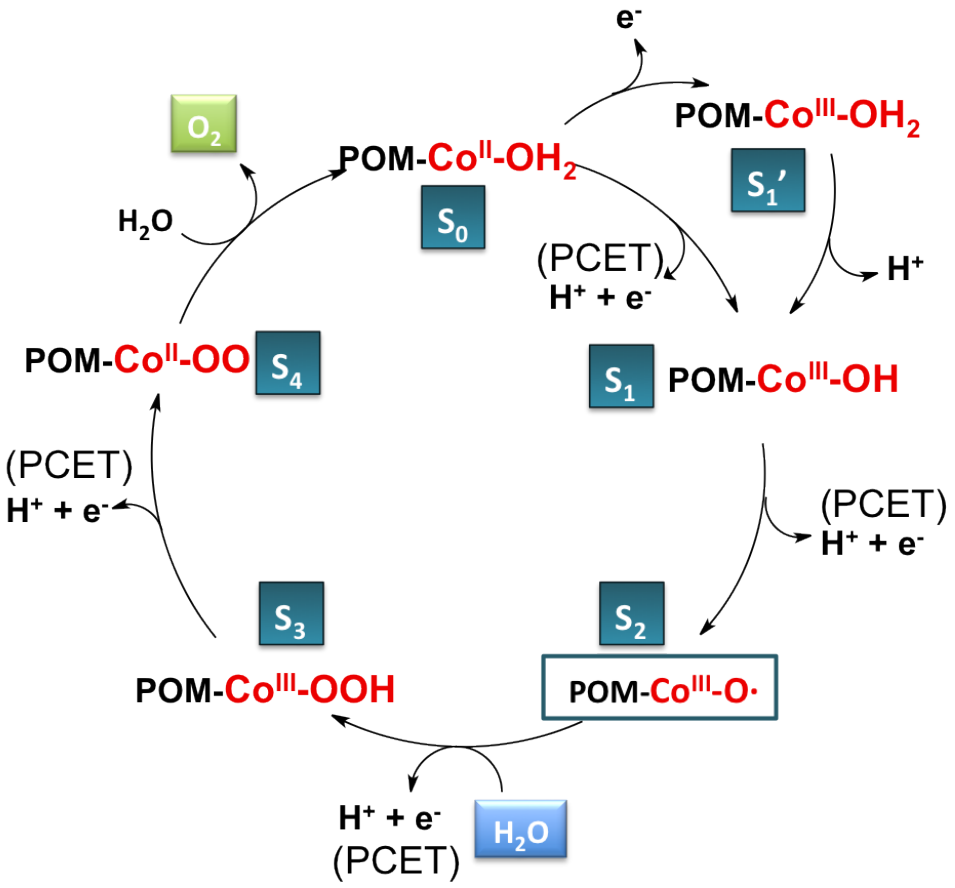

Figure 4.4: Schematic representation of the water oxidation mechanism for single-site cobalt-containing polyoxometalates. Energies associated are given in Table 4.2.

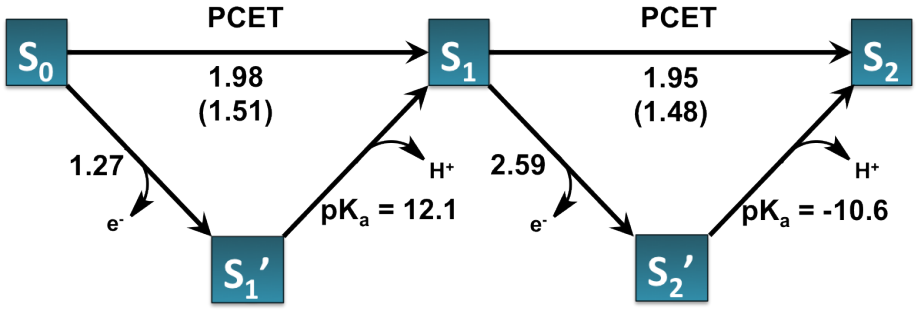

Figure 4.5: Computed potentials (in V vs NHE) of the *coupled* and *uncoupled* first and second PCET events for **PCo$_4$**. The pH-dependent potentials for the *coupled* events are given at pH 0 and pH 8 without and with parenthesis (determined employing equation 4.2), respectively. The pK_a were calculated employing equation 4.3.

According to the present calculations, the first and second oxidation steps require 1.27 V and 1.48 V applied potentials, respectively. In electrochemical catalysis the potentials are not additives as energies are in chemical catalysis. Therefore, one may conclude that the formation of the *active* species $\mathbf{S}_2$ ($Co^{III}-O^{\bullet}$) requires a 1.48 V an applied potential at pH 8. These findings are consistent with the electrochemical analysis of $\mathbf{PCo}_4$. Indeed, cyclic voltammetry experiments show an onset potential of 1.46 V vs NHE at pH 7.8 for water oxidation using $\mathbf{PCo}_4$ as catalyst.[235] Beyond the difficulty of drawing a straightforward comparison between the computed energetics in our model and electrochemical experimental data, our result agrees surprisingly well with the experimental values found for water oxidation employing $\mathbf{PCo}_4$ as a catalyst. Even if this agreement arises from errors cancellation in our calculations, we believe that the approximations made in the computational model are suitable to propose a plausible reaction mechanism for the $\mathbf{PCo}_4$-catalyzed water oxidation.

Close examination of geometry parameters of various intermediate PCET states of $\mathbf{PCo}_4$ shows that the change of external Co−O bond distance (it is established that in the sandwich POMs the external TM-OH_2 sites are reactive sites[277]) along the water oxidation cycle is consistent with above presented PCET events. Indeed, oxidation of the cobalt center (*i.e.* $\mathbf{S}_0(Co^{II}-OH_2)\rightarrow\mathbf{S}_1$'$(Co^{III}-OH_2)$) shortens the Co−$OH_2$ bond distance from 2.24 Å to 1.96 Å. The following loss of the proton (*i.e.* $\mathbf{S}_1$'$(Co^{III}-OH_2)\rightarrow\mathbf{S}_1(Co^{III}-OH)$) reduces this distance to 1.82 Å(see Figure 4.6 and Table 4.1).

These geometry changes are also consistent with the nature of the frontiers orbitals of these species. In fact, as seen in Figure 4.7, the the contribution of ligand p(O) orbital to the HOMO becomes significant in $\mathbf{S}_1$ species, and, consequently, the next PCET event is expected to occur on the OH-fragment leading to the $Co^{III}-O^{\bullet}$ species $\mathbf{S}_2$ ($Co^{III}-O^{\bullet}$), rather than oxidize the metal center. Consistently, in $\mathbf{S}_2$ ($Co^{III}-O^{\bullet}$) the calculated spin population of the Oxyl-center is 1.00 $|e|$ (Figures 4.6

and 4.7). One should mention that the oxidation of $Co^{III}-OH$ leads to the $Co^{III}-O^{\bullet}$ species rather than the $Co^{IV}-O$ unit. Similar result was previously described for cobalt oxide cubane models[278] and single-site Co-corrole catalysts.[295–297] More recently, DFT and CASSCF studies carried out on the Co derivatives of POMs also revealed that the formation of a Co^{IV} species is energetically unfavorable. To remove an electron from the oxo ligand is easier than to stabilize a Co^{IV} with a ligand field created by oxo ligands.[298] Similarly, for Ru-containing POMs, it was suggested that the $Ru^{VI}-$oxo groups are formally closer to being $Ru^{V}-$oxyl radicals.[273]

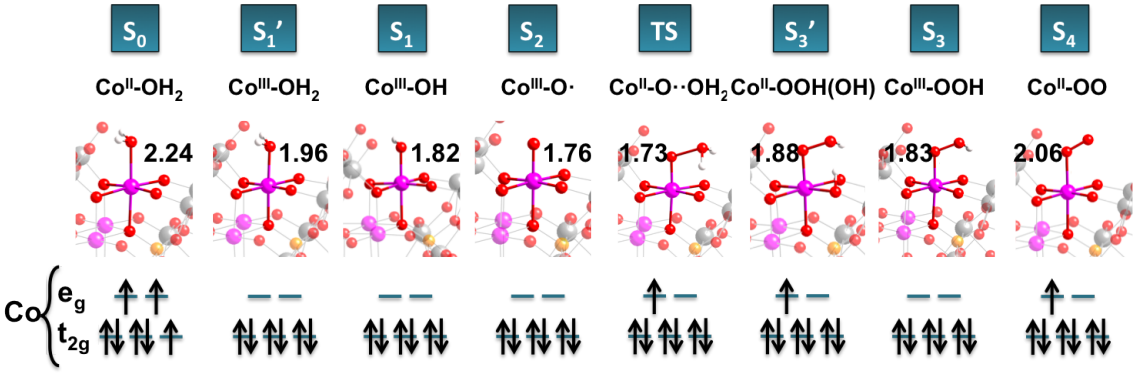

2S+1	13	10	10	11	11	11	10	11
ρ (Co)	2.73	0.00	0.00	-0.04	1.15	1.01	0.01	0.79
ρ (O)	0.03	0.00	-0.01	1.00	-0.14	-0.06	-0.01	0.09

Figure 4.6: Structural representation and schematic electronic structure of the active Co site for the different species involved in the water oxidation mechanism. Values correspond to the $\mathbf{PCo_4}$ anion.

B. Nucleophilic attack of water to the $Co^{III}-$oxyl (S_2) species: O−O bond formation

Once the active cobalt-oxyl species ($\mathbf{S_2}$) is formed, the next step of the water oxidation is the O−O bond formation. As already said, in transition metals substituted POM systems, this process is expected to occur via the "water-assisted" mechanism. It will be initiated by the nucleophilic attack of water molecule to the $Co^{III}-$oxyl

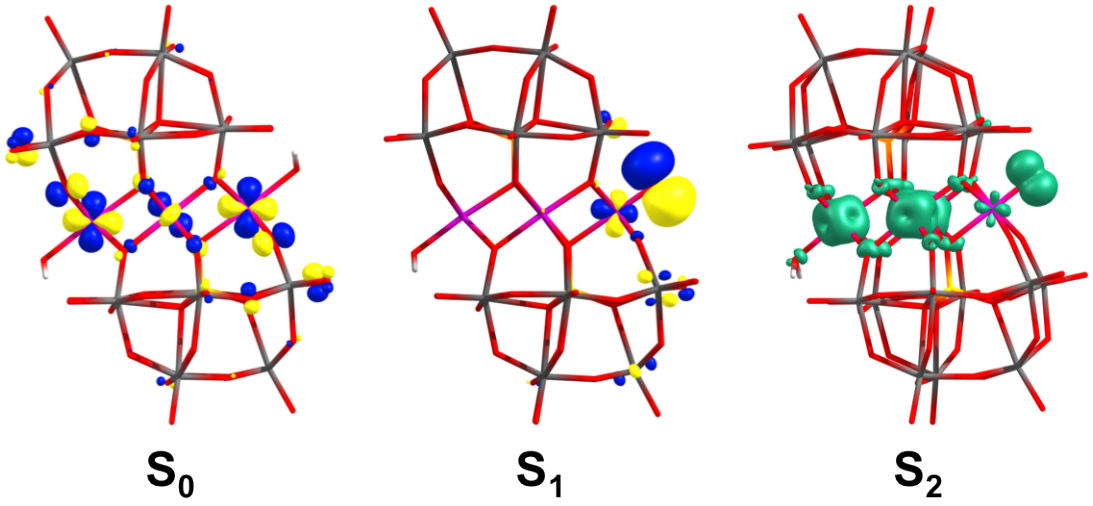

Figure 4.7: The HOMOs of species $\mathbf{S}_0$ and $\mathbf{S}_1$, and spin density of species $\mathbf{S}_2$ of the water oxidation cycle catalyzed by $\mathbf{PCo_4}$.

POM		$\mathbf{S_0}\rightarrow\mathbf{S_1}$'	$\mathbf{S_1}$'$\rightarrow\mathbf{S_1}$	$\mathbf{S_1}\rightarrow\mathbf{S_2}$	$\mathbf{S_2}\rightarrow\mathbf{TS}$	$\mathbf{S_2}\rightarrow\mathbf{S_3}$'	$\mathbf{S_3}$'$\rightarrow\mathbf{S_3}$	$\mathbf{S_3}\rightarrow\mathbf{S_4}$
		V [a]	pK_a [b]	V [a]	eV [c]	eV [c]	V [a]	V [a]
PCo_4	pH 0	+1.27	+12.1	+1.95	+0.99	+0.22	+0.73	+0.52
VCo_4	pH 0	+1.58	+13.4	+2.09	+0.73	-0.11	+0.89	+0.54
PCo_4	pH 8	+1.27	-	+1.48	+0.99	+0.22	+0.26	+0.05
VCo_4	pH 8	+1.58	-	+1.62	+0.73	-0.11	+0.42	+0.07

Table 4.2: Computed free energies required to reaching each step (S_i) of the water oxidation cycle by $\mathbf{PCo_4}$ and $\mathbf{VCo_4}$ catalysts. a) For the electrochemical steps the potentials are given in V vs NHE; b) Value corresponding to the pK_a of the deprotonation step; c) Energy values for the chemical steps are given in eV.

intermediate ($\mathbf{S}_2$), proceeds through two more PCET events, and releases a O_2 molecule. We ruled out the intramolecular formation of O−O bond from two Co-oxyl groups of the same POM because of large distance between the two oxo atoms in the core (>9.6 Å).

As shown in Figures 4.6 and 4.8, nucleophilic attack of water to intermediate

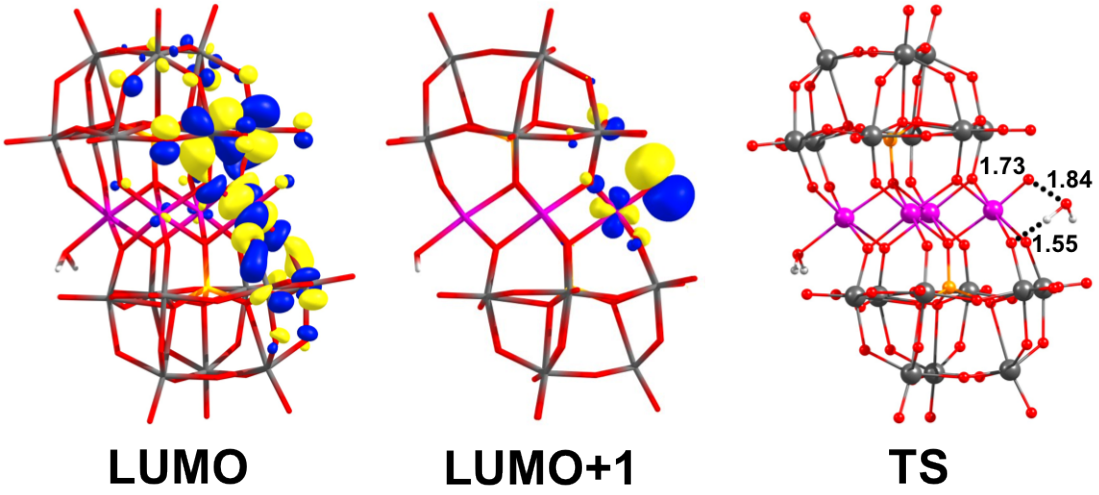

Figure 4.8: LUMO and LUMO+1 representation for $\mathbf{S}_2$ species, and transition state (**TS**) molecular structure of the $\mathbf{PCo}_4$ system, highlighting the O−O bond formation and the proton transfer to the basic oxygen of the polyoxometalate in a concerted manner; distances in Å.

$\mathbf{S}_2$ yields species $[Co^{II}(OOH)Co_3{}^{II}(H_2O)(PW_9O_{34})_2H]^{10-}$ ($\mathbf{S}_3$**'**), where one of the protons of coordinated (external) water is transferred to a basic oxygen atom of the POM in a concerted manner. Since the Co−O−W bridging oxygens are the most basic ones, they are most likely to be protonated.[299–301] The free energy barrier for this HO−H bond activation is calculated to be 0.99 eV at the transition state **TS** (see Table 4.2 and Figure 4.10). We have identified the LUMO+1 of the active $\mathbf{S}_2$ ($Co^{III}-O^{\bullet}$) species as the acceptor orbital for the nucleophilic attack of water (Figure 4.8). This orbital has a Co−O π-antibonding character, and is significantly polarized toward the oxyl ligand, fact that clearly favors the nucleophilic attack of a water molecule at relatively low energy.[65,274,302] The following PCET event from species $\mathbf{S}_3$**'** forms the species $\mathbf{S}_3$ ($[Co^{III}(OOH)Co_3{}^{II}(H_2O)(PW_9O_{34})_2]^{10-}$), the ground state of which has nine unpaired electrons (three electrons on each Co^{II} centers) and a Co^{III} ion, which retains its six electrons coupled (Figure 4.6). This PCET step requires a relatively low energy of 0.26 V at pH 8.

The last PCET step leads to the formation of $Co^{II}-OO$ moiety ($\mathbf{S}_4$,

$[Co^{II}(OO)Co_3{}^{II}(H_2O)(PW_9O_{34})_2]^{10-}$), and requires only 0.05 V at pH=8. The $\mathbf{S}_4$ species has ten unpaired electrons, one of them is localized in the reactive cobalt center, and three electrons in each of the remaining cobalt atoms. Then, the molecular oxygen is released from species $\mathbf{S}_4$ upon coordination of water molecule, which also regenerate the catalyst. Thus, based on above presented data, if the $Co^{III}-O^{\bullet}$ species ($\mathbf{S}_2$) had been formed, the O−O bond formation from this species would occur with less energy demand.

Previous studies have proposed that water molecules of solvation shells can act as proton acceptor,[270,273,295–297] but here we adopted the bridging oxygen of the Co−O−W moiety to be proton acceptor, as that was proposed for the Ru-substituted Keggin anions.[274] However, the selection of the proton acceptor should not be crucial to get a general picture of the reaction mechanism. Importantly, the energy required for this chemical event is significantly lower than those for the previous steps. Thus, if other proton acceptor will participate in the process, the barrier of this step would be even lower.

Summarizing, in this mechanism, the $\mathbf{S}_1(Co^{III}-OH)\rightarrow\mathbf{S}_2(Co^{III}-O^{\bullet})$ step determines the potential required to form the *active* species, which in turns determines the overpotential for the water oxidation catalysis. On the other hand, the kinetics of the reaction is governed by the *chemical step* corresponding to the O−O bond formation.[282] This latter step requires overcoming a barrier of 0.99 eV (22.8 kcal/mol), energy that is clearly affordable at room temperature. In an *electrochemical driven* process, the formation of the active species $\mathbf{S}_2$ ($Co^{III}-O^{\bullet}$) requires a 1.95 V and 1.48 V apply potential at pH 0 and 8, respectively, which would correspond to an overpotential of 0.72 V. Note that overpotential (η) is simply the difference between $\Delta G(\mathbf{S}_1\rightarrow\mathbf{S}_2)$ and $\Delta G(2H_2O\rightarrow O_2+2H_2)/4$. It is worth mentioning that often the WOC reactions are activated photochemically. Formally, the process is rather similar, but in the energetic balance is necessary to incorporate the oxi-reduction of the sacrificial electron acceptor.

Comparison of these findings for $\mathbf{PCo_4}$ catalyst with those for the Ru(III) based catalysts (both those in organometallic and POM frameworks) show that Ru oxidation occurs at lower potentials than Co centers. Indeed, the one-electron oxidation potential for $[Ru^{III}(H_2O)SiW_{11}O_{39}]^{5-}$ was reported to be 0.64 V vs SCE (0.88 V vs NHE),[277] while its computed value was estimated to be 0.45 V.[274] For the tetraruthenium-POM, $[Ru_4O_4(OH)_2(H_2O)_4(\gamma\text{-}SiW_{10}O_{36})_2]^{10-}$, first two oxidation events which transform of two $Ru^{IV}-OH_2$ moieties to the $Ru^{V}-OH$, was found to require only 0.76 and 0.88 V.[229] Computational studies showed that the PCET event leading to formation of $Ru^{V}-O^{\bullet}$ species require a potential of 1.53 V (pH 0),[273] which is 400 mV lower than the potential we have found for $\mathbf{PCo_4}$. For the *chemical step*, the activation free energy was reported to be 0.79 eV and 0.96 eV depending on the computational level.[273] These values are somewhat lower than the energy we have computed for $\mathbf{PCo_4}$, but the two set of energies cannot be directly compared because of different approaches used. Indeed, experimental TOF values measured for the tetraruthenium and $\mathbf{PCo_4}$ anions show a higher catalytic activity of $\mathbf{PCo_4}$, suggesting a lower free energy barrier for the later.[208]

4.3.3 Water Oxidation Catalyzed by the VCo_4 Polyoxometalate

As mentioned above, the replacement of P(V) in $\mathbf{PCo_4}$ by V(V) leads to the formation of $[Co_4(H_2O)_2(VW_9O_{34})_2]^{10-}$ ($\mathbf{VCo_4}$) anion, which exhibits a greater stability than $\mathbf{PCo_4}$. Furthermore, $\mathbf{VCo_4}$ demonstrates a significant increase in rate of catalytic water oxidation compared to the parent anion $\mathbf{PCo_4}$ in processes activated photochemically.[294] Such a dramatic change in stability and reactivity upon going from $\mathbf{PCo_4}$ to $\mathbf{VCo_4}$ could closely relate the change of electronic structure of polyoxometalate anion, in spite of the fact that both POMs have a same overall charge and similar geometry.[219,238,294] Actually, previously reported UV-vis spectrum has shown transitions involving orbitals of cobalt and heteroatom for $\mathbf{VCo_4}$, which could

indicate involvement of vanadium d orbitals in its redox chemistry.[294] In order to elucidate factors causing the difference in stability and reactivity of $\mathbf{PCo_4}$ and $\mathbf{VCo_4}$ systems, we also computed the water oxidation mechanism for the $\mathbf{VCo_4}$ POM and compared the obtained data with that for $\mathbf{PCo_4}$.

The calculated geometry and their X-ray values for $\mathbf{PCo_4}$ and $\mathbf{VCo_4}$ are well agreed (see Table 4.1).[294] Meanwhile, there exist several remarkable differences in the calculated free energies of the analogous steps of the $\mathbf{PCo_4}-$ and $\mathbf{VCo_4}-$catalyzed water oxidation cycles (Table 4.2). The most significant difference are in: (a) the oxidation of $Co^{II}-OH_2$ to $Co^{III}-OH_2$ ($\mathbf{S_0}\rightarrow\mathbf{S_1}$'), and (b) the reduction upon the nucleophilic attack of water to the $Co^{III}-O^{\bullet}$ *active* species ($\mathbf{S_2}\rightarrow\mathbf{TS}$). Indeed, the $\mathbf{S_0}\rightarrow\mathbf{S_1}$' transition for $\mathbf{VCo_4}$ requires a 1.58 V apply potential, which is 0.31 V larger than that required for the $\mathbf{PCo_4}$. Interestingly, upon going from $\mathbf{PCo_4}$ to $\mathbf{VCo_4}$ the spin density on each heteroatom increase to 0.02 |e| from almost zero. These findings could be explained by coupling of d orbitals of V and Co atoms in $\mathbf{VCo_4}$ that results in stabilization of high-oxidation states, increase of oxidation potential of Co-center, and renders an additional structural stability of $\mathbf{VCo_4}$ anion upon the catalysis.

To support this conclusion we analyzed the electronic structure (frontier orbitals and their energies) of the reactive Co-center in several intermediate states of the reaction. Unfortunately, the occupied canonical orbitals are difficult to interpret in such a large molecular systems because they are largely delocalized along the structure. However, since the unoccupied orbitals are usually more localized, we discuss the $\mathbf{S_0}\rightarrow\mathbf{S_1}$' oxidation process by mainly concentrating on the unoccupied (LUMO and LUMO+1) orbitals of the $\mathbf{S_1}$' state, which mostly are the d_{z2} and d_{x2-x2} orbitals of the Co-center. Interestingly, LUMO and LUMO+1 of the $\mathbf{S_1}$' state are the HOMO and HOMO-1 of the $\mathbf{S_0}$ state, since the electronic configuration of the cobalt changes from a high spin ${t_{2g}}^5{e_g}^2$ to a closed shell ${t_{2g}}^6{e_g}^0$ one during the $\mathbf{S_0}\rightarrow\mathbf{S_1}$' oxidation. As Figure 4.9 illustrates, in the $\mathbf{S_1}$' state of $\mathbf{VCo_4}$ the LUMO

lowers its energy by ∽0.17 eV respect to the LUMO+1, because of a significant mixture by vanadium d orbitals and cobalt d_{z2} orbital. Similar splitting of the e_g orbitals is expected in the $\mathbf{S}_0$ state of $\mathbf{VCo}_4$, explaining the increase in the redox potential. However, these orbitals are nearly degenerated in the $\mathbf{S}_1$' state of $\mathbf{PCo}_4$. The existence of the relatively large LUMO − LUMO+1 energy gap in the $\mathbf{S}_1$' state of $\mathbf{VCo}_4$ is indicative for presence of some degree of interaction between the vanadium d orbitals and cobalt d_{z2} orbital.

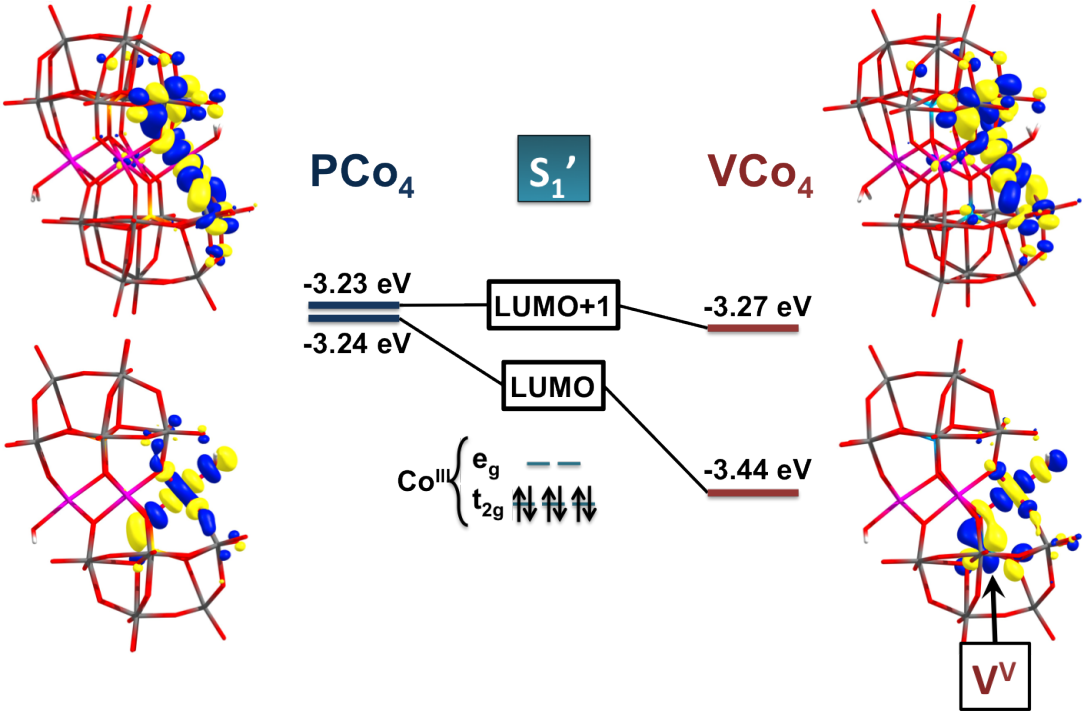

Figure 4.9: Schematic representation of Frontier Molecular Orbitals (FMO) energies and isodensity plots of LUMO and LUMO+1 orbitals for species $\mathbf{S}_1$' of $\mathbf{PCo}_4$ and $\mathbf{VCo}_4$ systems.

In addition, although the (Co^{II}/Co^{III}) (*i.e.* $\mathbf{S}_0 \rightarrow \mathbf{S}_1$' step) oxidation potential increases upon going from $\mathbf{PCo}_4$ to $\mathbf{VCo}_4$, this change is not expected to have significant influence to the overall catalytic performance of the tetracobal-POM systems, since this associates with the formation of the $Co^{III}-O^{\bullet}$ species, *i.e.* $\mathbf{S}_1 \rightarrow \mathbf{S}_2$ step, which appears later in the catalytic cycle.

Once the Co^{II} species ($\mathbf{S}_0$) is oxidized to the Co^{III} species ($\mathbf{S}_1$'), the next two events of the water oxidation cycle do not directly involve the active Co center, and, consequently, the energy required for these steps are very similar for the $\mathbf{PCo}_4$ and $\mathbf{VCo}_4$ catalysts. For $\mathbf{VCo}_4$, the deprotonation ($\mathbf{S}_1$'→$\mathbf{S}_1$) displays a pK_a somewhat higher than the one computed for $\mathbf{PCo}_4$, whereas the second PCET step ($\mathbf{S}_1$→$\mathbf{S}_2$) is 0.14 V higher in energy (Table 4.2).

The next event of the reaction is the O−O bond formation initiated by the nucleophilic attack of external water to the $Co^{III}-O^{\bullet}$ group. The computed activation free energy for $\mathbf{VCo}_4$ is significantly lower (0.73 eV, 16.8 kcal/mol), energy that is about 6 kcal/mol lower than that found for the $\mathbf{PCo}_4$ anion, see Figure 4.10. These computed values agree very well with the observed kinetic behavior reported by Hill and co-workers.[294] Therefore, the O−O bond formation is significantly faster for $\mathbf{VCo}_4$ than $\mathbf{PCo}_4$. This suggests that the O−O bond formation might be the turnover-limiting chemical step, similar to that proposed in the mechanistic studies for cobalt-phosphate catalyst.[171]

In order to elucidate the reason of the aforementioned reduction of the O−O bond formation barrier upon going from $\mathbf{PCo}_4$ to $\mathbf{VCo}_4$, we analyzed a set of lowest unoccupied orbitals of their $\mathbf{S}_2$ species, because these orbitals could be the acceptor orbitals upon the nucleophilic attack of water. For $\mathbf{PCo}_4$, we found that LUMO and LUMO+1 orbitals have -2.88 eV and -2.75 eV energies, respectively. Among these orbitals, the LUMO+1 has a strong p(Oxyl) contribution and, therefore, is a best candidate to accept electrons from the coordinated water molecule (Figures 4.8 and co4s2). However, in the case of $\mathbf{VCo}_4$, three unoccupied orbitals, namely LUMO, LUMO+1, and LUMO+2, have a strong contributions from the oxyl oxygen (Figure 4.11) and are good candidates for being an acceptor orbitals. Amazingly, all these three orbitals are lying lower in energy (at the positions of -2.95 eV, -2.78 eV, and -2.77 eV, respectively) than LUMO and LUMO+1 orbitals of the $\mathbf{S}_2$ species of $\mathbf{PCo}_4$, as shown in Figure 4.12. Therefore, due to the orbital coupling

between the d orbitals of the vanadium and cobalt, the set of acceptor orbitals for $\mathbf{VCo_4}$ decrease their energies favoring the nucleophilic attack of water and therefore increase reactivity of the POM with V(V) as heteroatom.

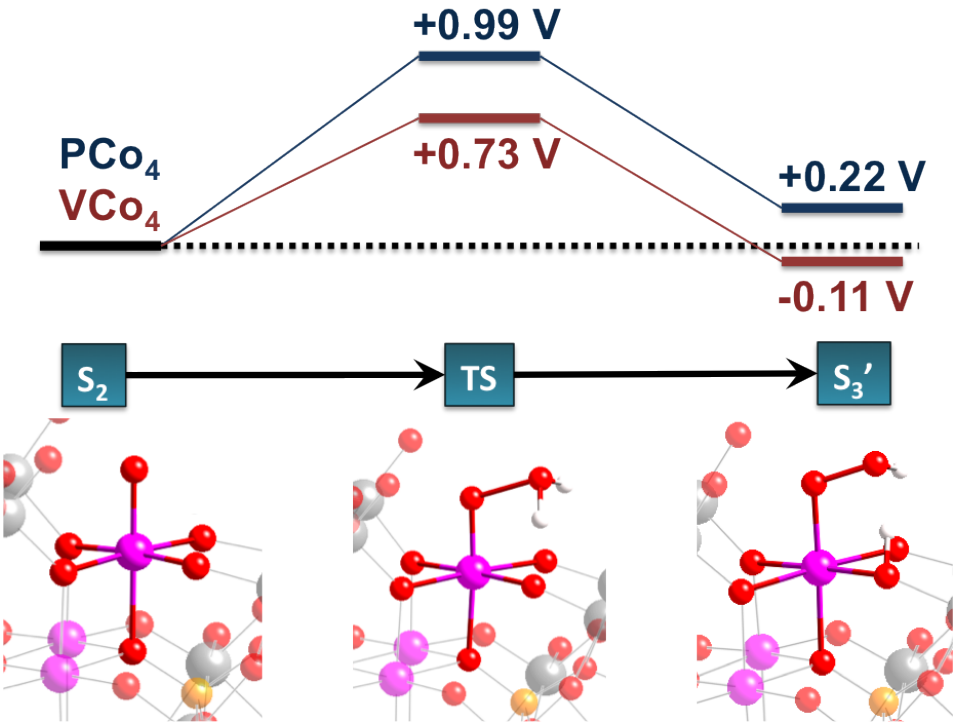

Figure 4.10: Energy profile corresponding to the nucleophilic attack of water to $Co^{III}-O^{\bullet}$ $\mathbf{S_2}$ species, and subsequent proton transfer to the basic oxygen, $\mathbf{S_3}$' species.

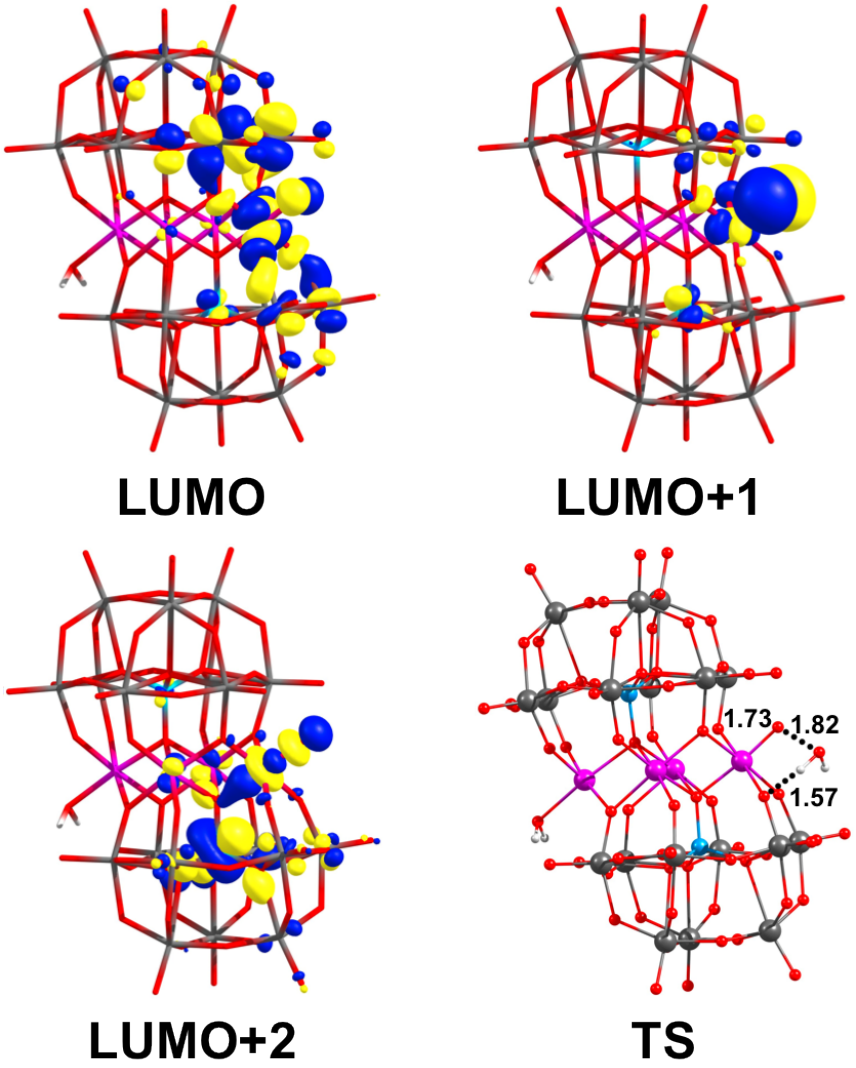

Figure 4.11: LUMO, LUMO+1, and LUMO+2 representation for $\mathbf{S}_2$ species, and transition state (**TS**) molecular structure of the $\mathbf{VCo}_4$ system, highlighting the O−O bond formation and the proton transfer to the basic oxygen of the polyoxometalate in a concerted manner; distances in Å.

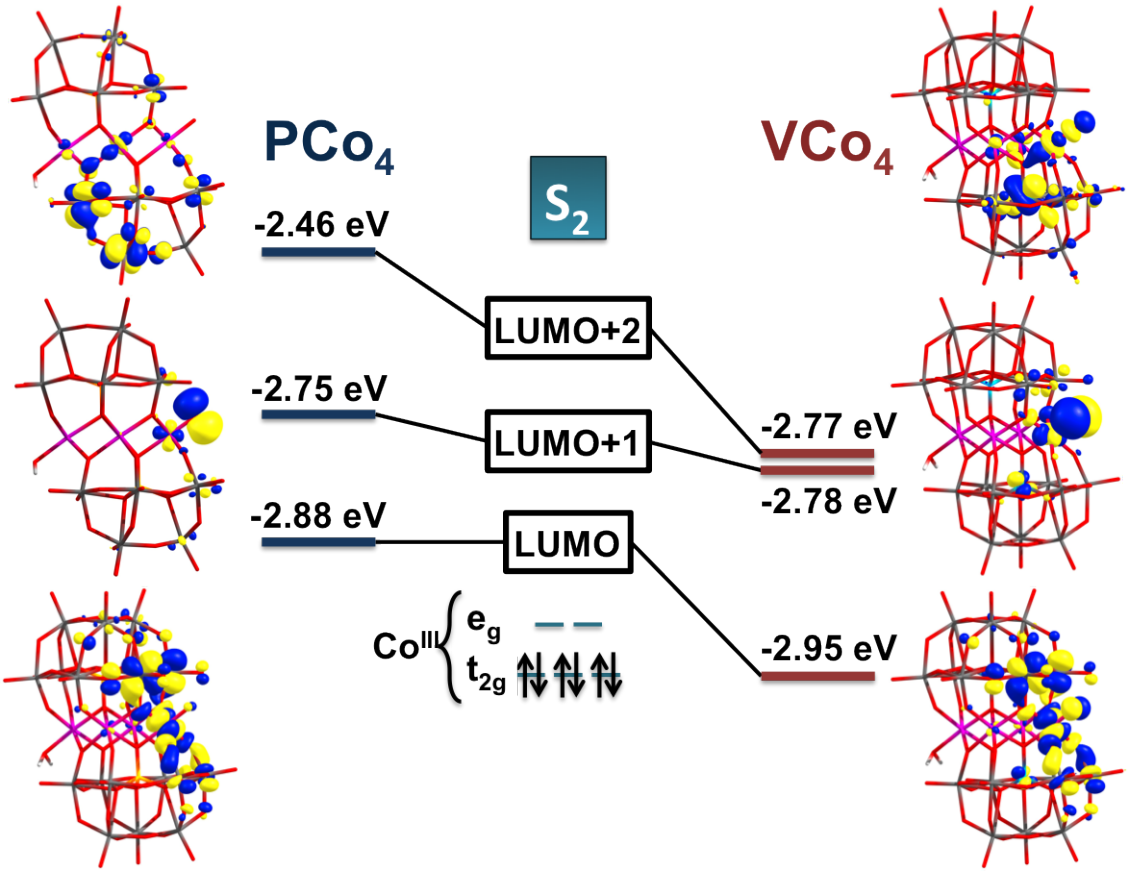

Figure 4.12: Schematic representation of Frontier Molecular Orbitals (FMO) energies and isodensity plots of LUMO, LUMO+1, and LUMO+2 orbitals for species $\mathbf{S}_2$ of $\mathbf{PCo}_4$ and $\mathbf{VCo}_4$ systems.

4.3.4 The Effect of the Nuclearity

It has been demonstrated that the effect of the nuclearity of Cobalt-substituted POMs based on the Keggin archetype is important for the catalyst activity towards water oxidation. Thus, monocobalt-substituted POM ($[Co(H_2O)PW_{11}O_{39}]^{5-}$ **PCo$_1$**) has been reported to be inert as water oxidation catalyst,[219] whereas the tetrasubstituted **PCo$_4$** and the nonasubstituted **Co$_9$** POMs are well known as active catalysts, with two and three Keggin units, respectively.[219,220] In the study of the reaction mechanism catalyzed with **PCo$_4$**, we have identified the formation of the *active* species $Co^{III}-O^{\bullet}$, *i.e.* the $\mathbf{S}_1 \rightarrow \mathbf{S}_2$ step, as the step which controls the overall overpotential of the catalytic cycle. Therefore, we compare the thermodynamics involved in this step for the three different POMs, **PCo$_1$**, **PCo$_4$**, and **Co$_9$**, as shown in Figure 4.13.

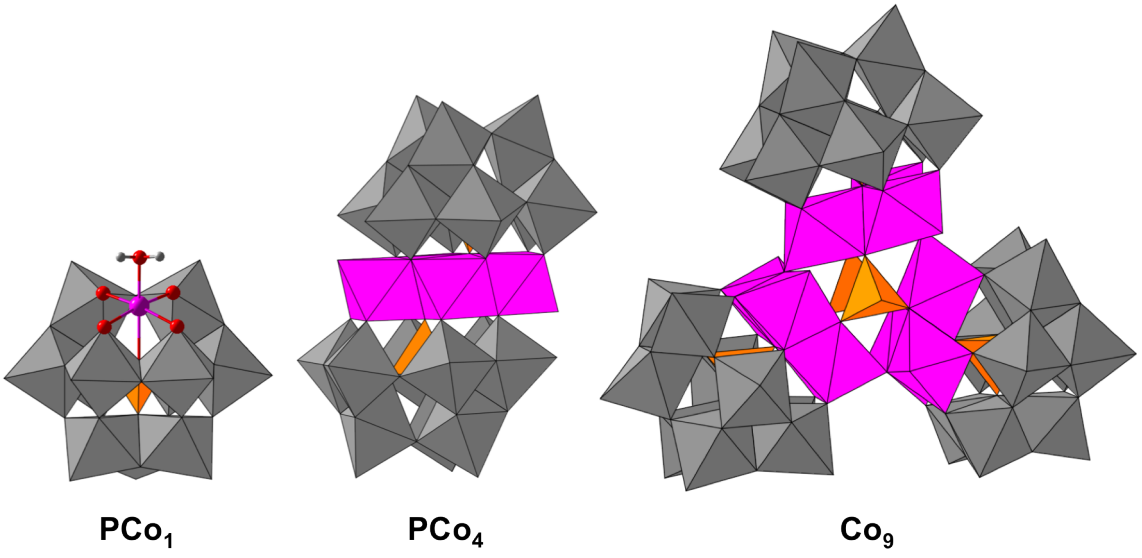

Figure 4.13: Polyhedral representation of **PCo$_1$** (left), **PCo$_4$** (center), and **Co$_9$** (right).

Unfortunately, **Co$_9$** ($[Co_9(H_2O)_6(OH)_3(HPO_4)_2(PW_9O_{34})_3]^{16-}$) is a large POM with a rather complex electronic structure with 27 unpaired electrons. In order to get some insight into this cluster, we decided to simplify its electronic structure by replacing eight of the Co(II) ions by eight Zn(II) ions,

$[Co(H_2O)Zn_8(H_2O)_5(OH)_3(HPO_4)_2(PW_9O_{34})_3]^{16-}$ (**ZnCo$_9$**, Figure 4.14). The resulting complex can be regarded as a single-site cobalt catalyst with three unpaired electrons that requires a significant computational effort, but still affordable with DFT methods. Moreover, looking into more detail to the structure of **ZnCo$_9$**, we observe an intramolecular hydrogen−bond between the OH of the phosphate link and the oxygen atom of the WOC active center. Thus, in state $\mathbf{S}_1$, the phosphate proton is almost transferred to the Co−hydroxo group, the O−H$\cdots$O(H)Co distance being ≈1.60 Å. In addition, in the case of the species $\mathbf{S}_1$, a second hydrogen−bond is found between the OH ligand of the active center and a basic oxygen of the closer Keggin archetype, with a hydrogen−bond distance of ≈1.99 Å. This might cause an overstabilization of the species $\mathbf{S}_1$ of ca. 0.5 eV with respect to the real situation, in which the explicit water molecules might form a complex net of hydrogen bonding. In fact, if we turn off these hydrogen bonds just by changing the orientation of the OH groups, the thermodynamics of the $\mathbf{S}_1 \rightarrow \mathbf{S}_2$ step change dramatically. Therefore, we believe that under experimental conditions an intermediate situation is operative, and that the two different calculated values can be viewed as the upper and lower limits. Herein we refer as **ZnCo$_9$**$^{\mathrm{H}}$ to the structures in which the hydrogen−bonds are formed, and as **ZnCo$_9$** to the structures without the formation of these bonds.

Table 4.3 summarizes the computed structural and electronic parameters for **PCo$_1$**, **PCo$_4$**, **ZnCo$_9$**$^{\mathrm{H}}$, and **ZnCo$_9$**. We found similar structural parameters for the surroundings of the cobalt active center. In general, the Co−O_t distance in the $\mathbf{S}_1$ species is ≈1.82 Å, which after the PCET event it is decreased to ≈1.76 Å in the $\mathbf{S}_2$ state. Particularly, these distances are slightly larger (0.02 Å) in the case of **ZnCo$_9$**$^{\mathrm{H}}$ in both $\mathbf{S}_1$ and $\mathbf{S}_2$ species as a result of the partial H-transfer from phosphate to the terminal ligand of Co. Regarding the electronic structures, we found the same results in all the structures. Therefore, as previously discussed for **PCo$_4$**, the Co active center of the $\mathbf{S}_1$ species is a Co(III) ion with a formal $d^{\,6}$ low-spin configuration where the six electrons occupy a t_{2g}-like orbital. Moreover,

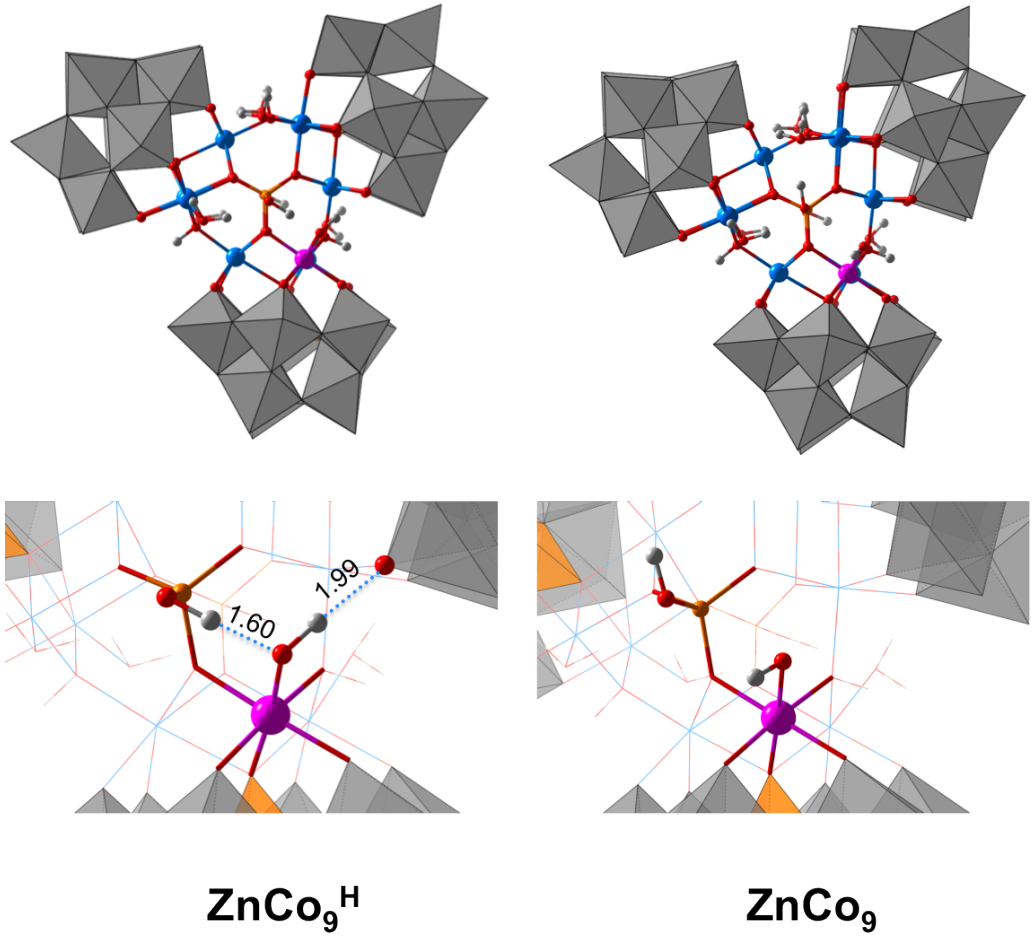

Figure 4.14: Structure of $\mathbf{ZnCo_9}^{H}$ (top-left), and $\mathbf{ZnCo_9}$ (top-right). Detailed view of the local conformation of the Co-reactive center in both structures showing the hydrogen−bond formation for $\mathbf{ZnCo_9}^{H}$ (bottom). Distances in Å.

the oxidation of $\mathbf{S}_1$ species yields the $\mathbf{S}_2$ *active* species ($Co^{III}-O^{\bullet}$), with a spin population of the oxyl center of ca. 1.00 e, highlighting the radical character of the *active* species, as shown in Figure 4.15. This also supports that the formation of $Co^{IV}=O$ species is not realistic to occur in POMs.

The energetics required to reach de *active* species ($\mathbf{S}_2$) beginning from the $\mathbf{S}_1$ state with the different POMs are shown in Table 4.4. As previously discussed, $\mathbf{PCo_4}$ requires to apply 1.48 V at pH 8. Surprisingly, the inactive POM $\mathbf{PCo_1}$ needs only a 1.53 V potential for reaching the *active* species, which is 0.05 V higher

	POM	$\mathbf{S}_1$	$\mathbf{S}_2$
		$Co^{III}-OH$	$Co^{III}-O^{\bullet}$
d(Co-O_t)	PCo_1	1.818	1.759
	PCo_4	1.820	1.760
	$ZnCo_9{}^H$	1.859	1.784
	$ZnCo_9$	1.820	1.760
d(Co-O_c)	PCo_1	2.072	2.078
	PCo_4	2.100	2.100
	$ZnCo_9{}^H$	2.084	2.095
	$ZnCo_9$	2.113	2.128
ρ(Co)	PCo_1	–	0.00
	PCo_4	0.00	-0.04
	$ZnCo_9{}^H$	–	-0.01
	$ZnCo_9$	–	-0.05
ρ(O)	PCo_1	–	1.02
	PCo_4	-0.01	1.00
	$ZnCo_9{}^H$	–	0.98
	$ZnCo_9$	–	1.01

Table 4.3: Structural (in Å) and electronic (in $|e|$) parameters for species $\mathbf{S}_1$, and $\mathbf{S}_2$ for Mono-, Tetra-, and Nona-substituted POMs.

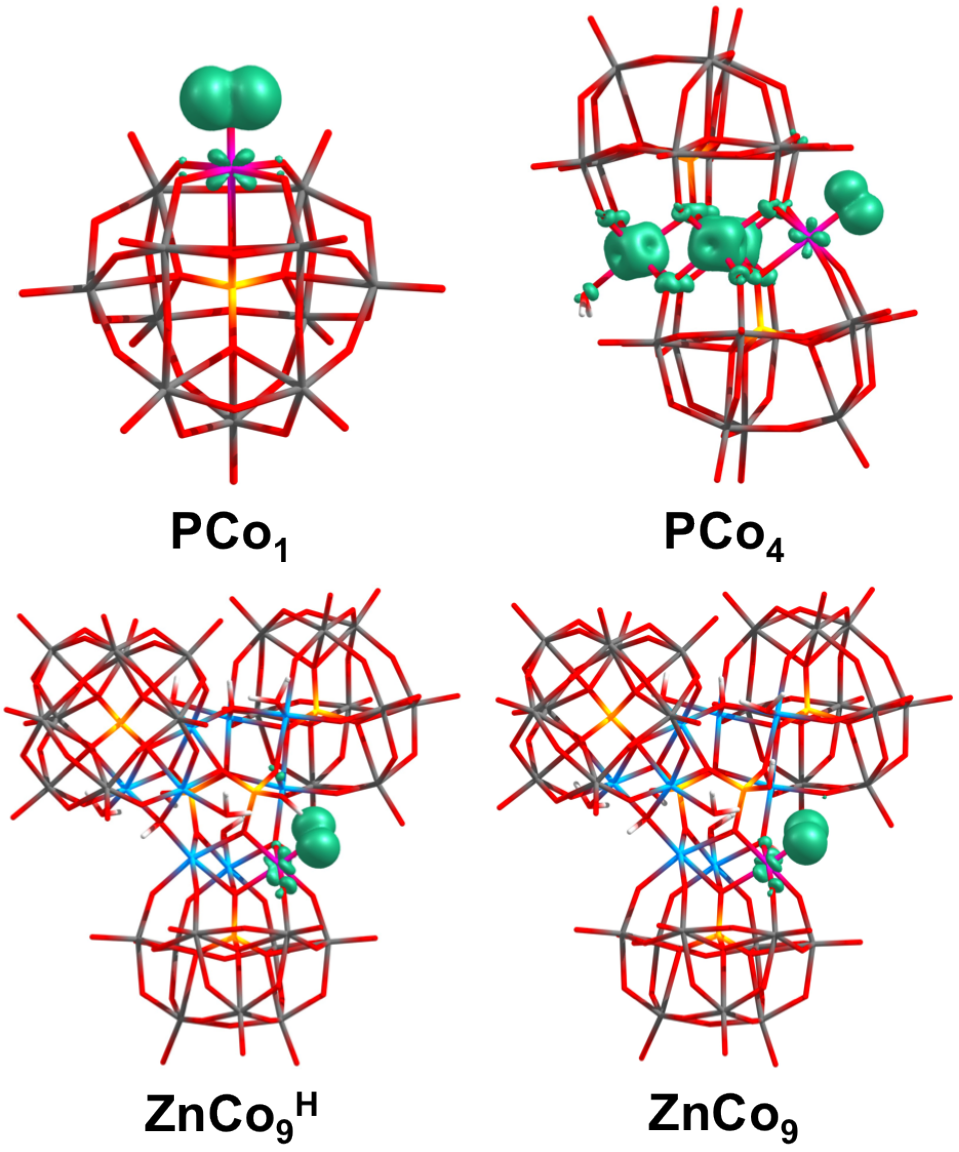

Figure 4.15: Spin densities of the $\mathbf{S}_2$ state found for the four studied structures.

than the potential found for $\mathbf{PCo_4}$. In the case of the model of $\mathbf{Co_9}$, we observe a strong influence of the formed hydrogen−bonds on the energetics. Thus, in the case of $\mathbf{ZnCo_9}$, where the formation of hydrogen−bonds on the surroundings of the reactive center is avoided, the obtained energy is 0.05 V lower than the obtained with the $\mathbf{PCo_4}$, being 1.43 V at pH 8. On the contrary, upon the formation of the hydrogen−bonds ($\mathbf{ZnCo_9}^{\mathrm{H}}$), the energy increases until 1.69 V, which is the highest energy found along the four studied structures. The later supports the hypothesis that the formation of the hydrogen−bonds overstabilizes the species $\mathbf{S}_1$ of $\mathbf{ZnCo_9}^{\mathrm{H}}$, so thus increasing the energy required to reach the *active* species.

	$\mathbf{S}_1 \rightarrow \mathbf{S}_2$	
POM	pH 0	pH 8
PCo_1	2.00	1.53
PCo_4	1.95	1.48
$ZnCo_9{}^{\mathrm{H}}$	2.16	1.69
$ZnCo_9$	1.90	1.43

Table 4.4: Computed potentials (in V vs NHE) required to reach the *active* species $\mathbf{S}_2$ from $\mathbf{S}_1$ state.

This overstabilization of the state $\mathbf{S}_1$ in $\mathbf{ZnCo_9}^{\mathrm{H}}$ is also evidenced when looking into detail the HOMO orbital, which is the orbital where the second oxidation takes place. As expected, the HOMO orbitals for $\mathbf{PCo_1}$, $\mathbf{PCo_4}$, and $\mathbf{ZnCo_9}$ have a Co−O π-antibonding character, with the major contribution of the ligand p(O) orbital (Figure 4.16). However, as can be seen in Figure 4.17, in the case of $\mathbf{ZnCo_9}^{\mathrm{H}}$ we have identified this ligand-based π-antibonding orbital as HOMO−15, which has an energy 0.42 eV lower than the HOMO level. The stabilization of the orbital is mainly due to the formation of the already mentioned hydrogen-bond in the structure. Overall, the $\mathbf{S}_1$ species in $\mathbf{ZnCo_9}^{\mathrm{H}}$ is stabilized respect to that in $\mathbf{ZnCo_9}$

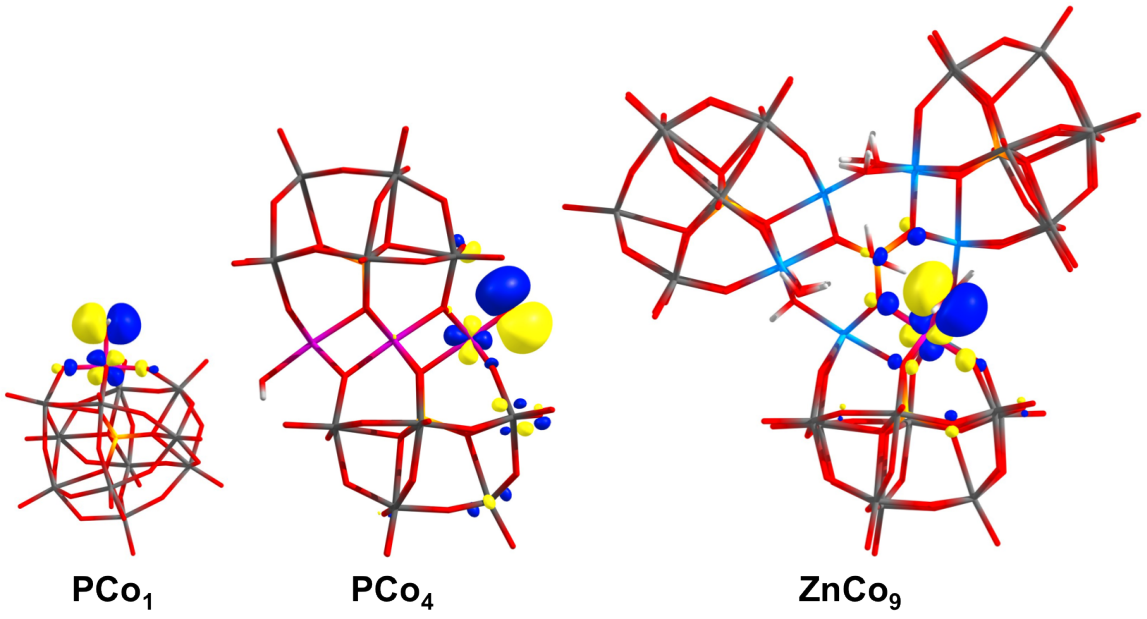

Figure 4.16: HOMO representation for $\mathbf{S}_1$ species of the structures $\mathbf{PCo}_1$, $\mathbf{PCo}_4$, and $\mathbf{ZnCo}_9$.

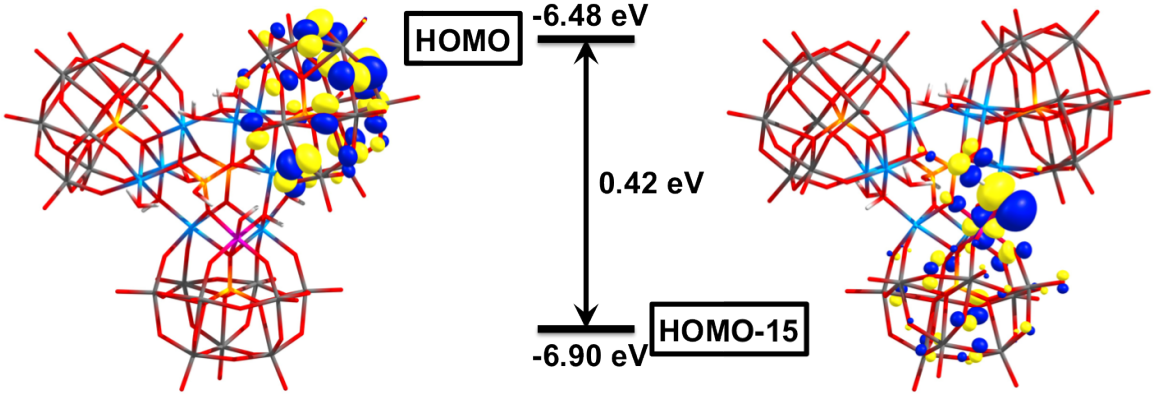

Figure 4.17: HOMO and HOMO−15 representation for $\mathbf{S}_1$ species of $\mathbf{ZnCo}_9{}^{\mathrm{H}}$.

Thermodynamically, we do not observe any substantial difference on the formation of the *active* species, beginning from species $\mathbf{S}_1$, that may cause the differences in the water oxidation catalysis activity experimentally observed. Therefore, the inactivity towards water oxidation observed for $\mathbf{PCo}_1$ may arise from POM stability issues, as decomposition may occur under turnover conditions. Regarding the differences between $\mathbf{PCo}_4$ and $\mathbf{Co}_9$ it has been observed that under the same experimental conditions both catalysts show similar kinetics, while $\mathbf{Co}_9$ is much more efficient than $\mathbf{PCo}_4$.[220,243] Combining both, our experimental observations, and our thermodynamic study, we can conclude that the difference between $\mathbf{Co}_9$ and $\mathbf{PCo}_4$ is regarded to the POM stability, being $\mathbf{Co}_9$ much more stable than $\mathbf{PCo}_4$. Therefore, these preliminary results indicate that the nuclearity of Co-substituted POMs has a minor influence on the single-site catalytic cycle, while the POM stability may be significantly affected, increasing as the nuclearity increases.

UNIVERSITAT ROVIRA I VIRGILI
HIGH NUCLEARITY POLYOXOMETALATES AS WATER OXIDATION CATALYSTS: FROM EXPERIMENTS TO THEORY
Joaquín Soriano López

4.4 Conclusions

In this chapter we have computationally studied the reaction mechanism of the water oxidation catalyzed by cobalt-containing polyoxometalates. In particular we have performed a detailed DFT analysis for sandwich polyoxometalates, $[Co_4(H_2O)_2(PW_9O_{34})_2]^{10-}$ (**PCo**$_4$), and $[Co_4(H_2O)_2(VW_9O_{34})_2]^{10-}$ (**VCo**$_4$). Experiments have shown that at the resting stages of **PCo**$_4$ and **VCo**$_4$ anions all four Co atoms are in their 2+ oxidation states with a formal d^7 configuration and three unpaired electrons. From these three unpaired electrons two occupy and e_g-like and one a t_{2g}-like orbitals. Therefore, we assume a high-spin configuration and discuss only the electronic state of **PCo**$_4$ and **VCo**$_4$ with their twelve (three per Co-center) unpaired electrons for the initial species $\mathbf{S}_0$.

The initial PCET step $\mathbf{S}_0(Co^{II}-OH_2)\rightarrow\mathbf{S}_1(Co^{III}-OH)$ proceeds via the *uncoupled* electron-then-proton pathway and leads to the one-electron oxidize species $\mathbf{S}_1$. However, the second PCET, which is overall catalysis-determining step, is a *coupled* process and does not impact oxidation state of the reactive Co-center, forming the $Co^{III}-O^{\bullet}$ *active* species $\mathbf{S}_2$. The overall $\mathbf{S}_0\rightarrow\mathbf{S}_2$ transformation requires to apply a potential of 1.48 V and 1.62 V at pH 8 for **PCo**$_4$ and **VCo**$_4$ anions, respectively. These potentials determine the overpotential of the overall catalytic reaction since in PCET events the activation barriers are usually very small and contain large quantum-mechanical tunneling prefactors.[282] The following O−O bond formation controls the kinetics of the reaction and occurs *via* the "water-assisted" mechanism that is initiated by water nucleophilic attack to the $Co^{III}-$oxyl intermediate $\mathbf{S}_2$ with a proton transfer from the water molecule to a basic oxygen of the POM in a concerted manner. This process involves a barrier of 0.99 eV (22.8 kcal/mol) for the HO−H bond activation for **PCo**$_4$, and is particularly low, 0.73 eV (16.8 kcal/mol), for **VCo**$_4$. The following deprotonation and the next two PCET steps are less energetically demanding. Hence, once the O−O bond is formed the reaction proceeds

smoothly, and the molecular oxygen is released upon water displacement, so thus recovering the catalyst $\mathbf{S}_0$.

Comparison of the calculated energetics for the $\mathbf{PCo}_4$ and $\mathbf{VCo}_4$ anions shows that coupling of d orbitals of V a Co atoms in $\mathbf{VCo}_4$ results in a stabilization of high-oxidation states, increase of oxidation potential of Co-center, and renders an additional structural stability of $\mathbf{VCo}_4$ anion upon the catalysis. Orbital coupling also improve the catalytic activity observed for the V-derivative making $\mathbf{VCo}_4$ one of the most active WOC.

The nuclearity of Cobalt-substituted POMs has a minor influence on the $\mathbf{S}_1 \rightarrow \mathbf{S}_2$ step, which controls the overall overpotential of the water oxidation catalytic cycle. Nevertheless, increasing the nuclearity leads to an increase on the stability of the POM towards water oxidation catalysis, so thus increasing its efficiency.

Bibliography

[1] N. S. Lewis and D. G. Nocera. Powering the planet: Chemical challenges in solar energy utilization. *Proc. Natl. Acad. Sci. U.S.A.*, 103:15729–15735, 2006.

[2] *The EU in the world 2013 - A statistical portrait.* Luxembourg: Publications Office of the European Union, 2012.

[3] W. Steffen, K. Richardson, J. Rockström, S. E. Cornell, I. Fetzer, E. M. Bennett, R. Biggs, S. R. Carpenter, W. de Vries, C. A. de Wit, C. Folke, Gerten D., J. Heinke, G. M. Mace, L. M. Persson, V. Ramanathan, B. Reyers, and S. Sörlin. Planetary boundaries: Guiding human development on a changing planet. *Science*, 347:736, 2015.

[4] J. Rockström, W. Steffen, K. Noone, Å. Person, F. S. Chapin III, E. F. Lambin, T. M. Lenton, M. Scheffer, C. Folke, H. J. Schellnhuber, B. Nykvist, C. A. de Wit, T. Hughes, S. van der Leeuw, H. Rodhe, S. Sörlin, P. K. Snyder, R. Costanza, U. Svedin, M. Falkenmark, L. Karlberg, R. W. Corell, V. J. Fabry, J. Hansen, B. Walker, D. Liverman, K. Richardson, P. Crutzen, and J. A. Foley. A safe operating space for humanity. *Nature*, 461:472–475, 2009.

[5] T. R. Cook, Dogutan D. K., S. Y. Reece, Y. Surendranath, T. S. Teets, and D. G. Nocera. Solar energy supply and storage for the legacy and nonlegacy worls. *Chem. Rev.*, 110:6474–6502, 2010.

[6] M. G. Walter, E. L. Warren, J. R. McKone, S. W. Boettcher, Q. Mi, E. A. Santori, and N. S. Lewis. Solar water splitting cells. *Chem. Rev.*, 110:6446–6473, 2010.

[7] *World Energy Assessment Report: Energy and The Challenge of Sustainability.* United Nations Developement Programme, 2003.

[8] N. S. Lewis. Toward cost-effective solar energy use. *Science*, 315:798–801, 2007.

[9] R. E. Blankenship and H. Hartman. The origins and evolution of oxygenic photosynthesis. *Trends Biochem. Sci.*, 23:94–97, 1998.

[10] J. P. McEvoy and G. W. Brudvig. Water-splitting chemistry of photosystem II. *Chem. Rev.*, 106:4455–4483, 2006.

[11] H. Dau and I. Zaharieva. Principles, efficiency, and blueprint character of solar-energy conversion in photosynthetic water oxidation. *Acc. Chem. Res. Chem. Res.*, 42:1861–1870, 2009.

[12] L. N. M. Duysens, J. Amesz, and B. M. Kamp. Two photochemical systems in photosynthesis. *Nature*, 190:510–511, 1961.

[13] *Artificial Photosynthesis-From Basic Biology to Industrial Application.* WILEY-VCH Verlag GmbH & Co. KGaA, Weinheim, 2005.

[14] K. N. Ferreira, T. M. Iverson, K. Maghlaoui, J. Barber, and S. Iwata. Architecture of the photosynthetic oxygen-evolving center. *Science*, 303:1831–1838, 2004.

[15] I. Szabó, E. Bergantino, and G. M. Giacometti. Light and oxygenic photosynthesis: energy dissipation as a protection mechanism against photo-oxidation. *EMBO reports*, 6:629–634, 2005.

[16] Y. Umena, K. Kawakami, J.-R. Shen, and N. Kamiya. Crystal structure of oxygen-evolving photosystem II at a resolution of 1.9 Å. *Nature*, 473:55–63, 2011.

[17] M. Haumann, P. Liebish, C. Müller, M. Barra, M. Grabolle, and H. Dau. Photosynthetic O_2 formation tracked by time-resolved X-ray experiments. *Science*, 310:1019–1021, 2005.

[18] S. V. Baranov, G. M. Ananyev, V. V. Klimov, and C. Dismukes. Bicarbonate accelerates assembly of inorganic core of the water-oxidizing complex in manganese-depleted photosystem II: A proposed biogeochemical role for atmospheric carbon dioxide in oxygenic photosynthesis. *Biochemistry*, 39:6060–6065, 2000.

[19] D. G. Nocera. The artificial leaf. *Acc. Chem. Res.*, 45:767–776, 2012.

[20] *Fuels from solar energy. A dream of Giacomo Ciamician, the father of photochemistry*, 2005.

[21] G. Ciamician. The photochemistry of the future. *Science*, 36:385–394, 1912.

[22] M. W. Kanan and D. G. Nocera. In situ formation of an oxygen-evolving catalyst in neutral water containing phosphate and Co^{2+}. *Science*, 321:1072–1075, 2008.

[23] J. R. Galán-Mascarós. Water oxidation at electrodes modified with earth-abundant transition-metal catalysts. *ChemElectroChem*, 2:37–50, 2015.

[24] S. W. Gersten, G. J. Samuels, and T. J. Meyer. Catalytic oxidation of water by an oxo-bridged ruthenium dimer. *J. Am. Chem. Soc.*, 104:4029–4030, 1982.

[25] X. Liu and F. Wang. Transition metal complexes that catalyze oxygen formation from water: 1979-2010. *Coordin. Chem. Rev.*, 256:1115–1136, 2012.

[26] L. Duan, F. Bozoglian, S. Mandal, B. Stewart, T. Privalov, A. Llobet, and L. Sun. A molecular ruthenium catalyst with water-oxidation activity comparable to that of photosystem II. *Nat. Chem.*, 4:418–423, 2012.

[27] S. M. Barnett, K. I. Goldberg, and J. M. Mayer. A soluble copper-bipyridine water-oxidation electrocatalyst. *Nat. Chem.*, 4:498–502, 2012.

[28] W. C. Ellis, N. D. McDaniel, S. Bernhard, and T. J. Collins. Fast water oxidation using iron. *J. Am. Chem. Soc.*, 132:10990–10991, 2010.

[29] M. Grätzel. Photoelectrochemical cells. *Nature*, 414:338–344, 2001.

[30] R. K. Hocking, R. Brimblecombe, L.-Y. Chang, A. Singh, M. H. Cheah, C. Glover, W. H. Casey, and L. Spiccia. Water-oxidation catalysis by manganese in a geochemical-like cycle. *Nat. Chem.*, 3:461–466, 2011.

[31] K. Maeda, T. Ohno, and K. Domen. A copper and chromium based nanoparticulate oxide as a noble-metal-free cocatalyst for photocatalytic water splitting. *Chem. Sci.*, 2:1362–1368, 2011.

[32] K. Sivula, F. Le Formal, and M. Grätzel. Solar water splitting: Progress using hematite (α-Fe_2O_3) photoelectrodes. *ChemSusChem*, 4:432–449, 2011.

[33] F. Jiao and H. Frei. Nanostructured cobalt oxide clusters in mesoporous silica as efficient oxygen-evolving catalysts. *Angew. Chem. Int. Edit.*, 48:1841–1844, 2009.

[34] M. Yagi, E. Tomita, S. Sakita, T. Kuwabara, and K. Nagai. Self-assembly of active IrO_2 colloid catalyst on an ITO electrode for efficient electrochemical water oxidation. *J. Phys. Chem. B*, 109:21489–21491, 2005.

[35] M.-R. Gao, Y.-F. Xu, J. Jiang, Y.-R. Zheng, and S.-H. Yu. Water oxidation electrocatalyzed by an efficient $Mn_3O_4/CoSe_2$ nanocomposite. *J. Am. Chem. Soc.*, 134:2930–2933, 2012.

[36] T.-L. Wee, B. D. Sherman, D. Gust, A. L. Moore, T. A. Moore, Y. Liu, and J. C. Scaiano. Photochemical synthesis of a water oxidation catalyst based on cobalt nanostructures. *J. Am. Chem. Soc.*, 133:16742–16745, 2011.

[37] J. B. Gerken, J. G. McAlpin, J. Y. C. Chen, M. L. Rigsby, W. H. Casey, R. D. Britt, and S. S. Stahl. Electrochemical water oxidation with cobalt-based electrocatalysts from pH 0-14: The thermodynamic basis for catalyst structure, stability, and activity. *J. Am. Chem. Soc.*, 133:14431–14442, 2011.

[38] J. J. H. Pijpers, M. T. Winkler, Y. Surendranath, T. Buonassisi, and D. G. Nocera. Light-induced water oxidation at silicon electrodes functionalized with a cobalt oxygen-evolving catalyst. *Proc. Natl. Acad. Sci. U.S.A.*, 108:10056–10061, 2011.

[39] J. A. Gilbert, D. S. Eggleston, W. R. Murphy, D. A. Geselowitz, S. W. Gersten, D. J. Hodgson, and T. J. Meyer. Structure and redox properties of the water-oxidation catalyst $[(bpy)_2(OH_2)RuORu(OH_2)(bpy)_2]^{4+}$. *J. Am. Chem. Soc.*, 107:3855–3864, 1985.

[40] J. P. Collin and J. P. Sauvage. Synthesis and study of mononuclear Ruthenium(II) complexes of sterically hindering diimine chelates. implications for the catalytic oxidation of water to molecular oxygen. *Inorg. Chem.*, 25:135–141, 1986.

[41] R. Ramaraj, A. Kira, and M. Kaneko. Electrochemistry and stability studies of oxo-brigded dinuclear ruthenium(III) complexes for water oxidation. *J. Chem. Soc., Faraday Trans. 1*, 82:3515–3524, 1986.

[42] F. P. Rotzinger, S. Munavalli, P. Comte, J. K. Hurst, M. Grätzel, F.-J. Pern, and A. J. Frank. A molecular water-oxidation catalyst derived from ruthenium diaqua bis(2,2'-bipyridil-5,5'-dicarboxylic acid). *J. Am. Chem. Soc.*, 109:6619–6626, 1987.

[43] M. K. Nazeeruddin, F. P. Rotzinger, P. Comte, and M. Grätzel. Spontaneous oxidation of water to oxygen by the mixed-valence μ-oxo ruthenium dimer $L_2(H_2O)Ru^{III}$-O-$Ru^{IV}(OH)L_2$ (L = 2,2'-bipyridyl-5,5'-dicarboxylic acid). *J. Chem. Soc., Chem. Commun.*, pages 872–874, 1988.

[44] P. Comte, M. K. Nazeeruddin, F. P. Rotzinger, A. J. Frank, and M. Grätzel. Artificial analogues of the oxygen-evolving complex in photosynthesis: the oxo-bridfed ruthenium dimer $L_2(H_2O)Ru^{III}$-O-$Ru^{III}(H_2O)L_2$, L = 2,2'-bipyridyl-4,4'dicarboxylate. *J. Mol. Cat.*, 52:63–84, 1989.

[45] H. H. Petach and C. M. Elliott. Characterization and catalytic activity of covalently linked bipyridyl ruthenium oxo dimers. *J. Electrochem. Soc.*, 139:2217–2221, 1992.

[46] Y.-K. Lai and K.-Y. Wong. Electrochemistry of oxo-bridged ruthenium dimers with 4,4'-dichloro- and 5,5'-dichloro-2,2'bipyridine and their catalytic properties towards water oxidation. *J. Electroanal. Chem.*, 380:193–200, 1995.

[47] C. W. Chronister, R. A. Binstead, J. Ni, and T. J. Meyer. Mechanism of water oxidation catalyzed by the μ-oxo dimer $[(bpy)_2(OH_2)Ru^{III}ORu^{III}(OH_2)(bpy)_2]^{4+}$. *Inorg. Chem.*, 36:3814–3815, 1997.

[48] R. A. Binstead, C. W. Chronister, J. Ni, C. M. Hartshorn, and T. J. Meyer. Mechanism of water oxidation by the μ-oxo dimer $[(bpy)_2(H_2O)Ru^{III}ORu^{III}(H_2O)(bpy)_2]^{4+}$. *Inorg. Chem.*, 122:8464–8473, 2000.

[49] Z. Deng, H.-W. Tseng, R. Zong, D. Wang, and R. Thummel. Preparation and study of a family of dinuclear Ru(II) complexes that catalyze the decomposition of water. *Inorg. Chem.*, 47:1835–1848, 2008.

[50] M. Huynh and T. J. Meyer. Proton-coupled electron transfer. *Chem. Rev.*, 107:5004–5064, 2007.

[51] H. Yamada, W. F. Siems, T. Koike, and J. K. Hurst. Mechanism of water oxidation catalyzed by the *cis,cis*-$[(bpy)_2Ru(OH_2)]_2O^{4+}$ ion. *J. Am. Chem. Soc.*, 126:9786–9795, 2004.

[52] J. J. Concepcion, J. W. Jurss, J. L. Templeton, and T. J. Meyer. One site is enough. Catalytic water oxidation by $[Ru(tpy)(bpm)(OH_2)]^{2+}$ and $[Ru(tpy)(bpz)(OH_2)]^{2+}$. *J. Am. Chem. Soc.*, 130:16462–16463, 2008.

[53] F. Liu, J. J. Concepcion, J. W. Jurss, T. Cardolaccia, J. L. Templeton, and T. J. Meyer. Mechanism of water oxidation from the blue dimer to photosystem II. *Inorg. Chem.*, 47:1727–1752, 2008.

[54] J. L. Cape and J. K. Hurst. Detection and mechanistic relevance of transient ligand radicals formed during $[Ru(bpy)_2(OH_2)]_2O^{4+}$-catalyzed water oxidation. *J. Am. Chem. Soc.*, 130:827–829, 2008.

[55] B. Limburg, E. Bouwman, and S. Bonnet. Molecular water oxidation catalysts based on transition metals and their decomposition pathways. *Coord. Chem. Rev.*, 256:1451–1467, 2012.

[56] C. Sens, I. Romero, M. Rodríguez, A. Llobet, T. Parella, and J. Benet-Buchholz. A new ru complex capable of catalytically oxidizing water to molecular dioxygen. *J. Am. Chem. Soc.*, 126:7798–7799, 2004.

[57] F. Bozoglian, S. Romain, M. Z. Ertem, T. K. Todorova, C. Sens, J. Mola, M. Rodríguez, I. Romero, J. Benet-Buchholz, X. Fontrodona, C. J. Cramer,

L. Gagliardi, and A. Llobet. The ru-hbpp water oxidation catalyst. *J. Am. Chem. Soc.*, 131:15176–15187, 2009.

[58] S. Romain, F. Bozoglian, X. Sala, and A. Llobet. Oxygen-oxygen bond formation by the ru-hbpp water oxidation catalyst occurs solely via an intramolecular reaction pathway. *J. Am. Chem. Soc.*, 131:2768–2769, 2009.

[59] X. Yang and M.-H. Baik. The mechanism of water oxidation catalysis promoted by $[tpyRu(IV)=O]_2L^{3+}$: A computational study. *J. Am. Chem. Soc.*, 130(16231-16240), 2008.

[60] R. Zong and R. P. Thummel. A new family of ru complexes from water oxidation. *J. Am. Chem. Soc.*, 127:12802–12803, 2005.

[61] J. D. Blakemore, R. H. Crabtree, and G. W. Brudvig. Molecular catalysts for water oxidation. *Chem. Rev.*, 115:12974–13005, 2015.

[62] L. Duan, A. Fischer, Y. Xu, and L. Sun. Isolated seven-coordinate Ru(IV) dimer complex with $[HOHOH]^-$ bridging ligand as an intermediate for catalytic water oxidation. *J. Am. Chem. Soc.*, 131:10397–10399, 2009.

[63] L. Li, L. Duan, Y. Xu, M. Gorlov, A. Hagfeldt, and L. Sun. A photoelectrochemical device for visible light driven water splitting by a molecular ruthenium catalyst assembled on dye-sensitized nanostructured TiO_2. *Chem. Commun.*, 46:7307–7309, 2010.

[64] F. Li, B. Zhang, X. Li, J. Jiang, L. Chen, Y. Li, and L. Sun. Highly efficient oxidation of water by a molecular catalyst immobilized on carbon nanotubes. *Angew. Chem. Int. Ed.*, 50:12276–12279, 2011.

[65] S. Goberna-Ferrón, B. Peña, J. Soriano-López, J. J. Carbó, H. Zhao, J. M. Poblet, K. R. Dunbar, and J. R. Galán-Mascarós. A fast metal-metal bonded water oxidation catalyst. *Journal of Catalysis*, 315:25–32, 2014.

[66] N. D. McDaniel, F. J. Coughlin, L. L. Tinker, and S. Bernhard. Cyclometalated iridium(III) aquo complexes: Efficient and tunable catalysts for the homogeneous oxidation of water. *J. Am. Chem. Soc.*, 130:210–217, 2008.

[67] J. F. Hull, D. Balcells, J. D. Blakemore, C. D. Incarvito, O. Eisenstein, G. W. Brudvig, and R. H. Crabtree. Highly active and robust Cp* iridium complexes for catalytic water oxidation. *J. Am. Chem. Soc.*, 131:8730–8731, 2009.

[68] D. G. H. Hetterscheid and J. N. H. Reek. Me_2-NHC based robust Ir catalyst for efficient water oxidation. *Chem. Commun.*, 47:2712–2714, 2011.

[69] J. D. Blakemore, N. D. Schley, D. Balcells, J. F. Hull, G. W. Olack, C. D. Incarvito, O. Eisenstein, G. W. Brudvig, and R. H. Crabtree. Half-sandwich iridium complexes for homogeneous water-oxidation catalysis. *J. Am. Chem. Soc.*, 132:16017–16029, 2010.

[70] A. Savini, P. Belanzoni, G. Bellachioma, C. Zuccaccia, D. Zuccaccia, and A. Macchioni. Activity and degradation pathways of pentamethylcyclopentadienyl-iridium catalysts fro water oxidation. *Green Chem.*, 13:3360–3374, 2011.

[71] D. B. Grotjahn, D. B Brown, J. K. Martin, D. C. Marelius, M.-C. Abadjian, H. N. Tran, G. Kalyuzhny, K. S. Vecchio, Z. G. Specht, S. A. Cortes-Llamas, V. Miranda-Soto, C. van Niekerk, C. E. Moore, and A. L. Rheingold. Evolution of iridium-based molecular catalysts during water oxidation with ceric ammonium nitrate. *J. Am. Chem. Soc.*, 133:19024–19027, 2011.

[72] N. D. Schley, J. D. Blakemore, N. K. Subbaiyan, C. D. Incarvito, F. D'Souza, R. H. Crabtree, and G. W. Brudvig. Distinguishing homogeneous from heterogeneous catalysis in electrode-driven water oxidation with molecular iridium complexes. *J. Am. Chem. Soc.*, 133:10473–10481, 2011.

[73] J. D. Blakemore, N. D. Schley, G. W. Olack, C. D. Incarvito, G. W. Brudvig, and R. H. Crabtree. Anodic deposition of a robust iridium-based water-oxidation catalyst from organometallic precursors. *Chem. Sci.*, 2:94–98, 2011.

[74] S. Mukhopadhyay, S. K. Mandal, S. Bhaduri, and W. H. Armstrong. Manganese clusters with relevance to photosystem II. *Chem. Rev.*, 104:3981–4026, 2004.

[75] M. Wiechen, H.-M. Berends, and P. Kurz. Water oxidation catalysed by manganese compounds: from complexes to 'biomimetic rocks'. *Dalton Trans.*, 41:21–31, 2012.

[76] J. Limburg, J. S. Vrettos, L. M. Liable-Sands, A. L. Rheingold, R. H. Crabtree, and G. W. Brudvig. A functional model for O-O bond formation by the O_2-evolving complex in photosystem II. *Science*, 283:1524–1527, 1999.

[77] M. Yagi and K. Narita. Catalytic O_2 evolution from water induced by adsorption of $[(OH_2)(Terpy)Mn(\mu\text{-}O)_2Mn(Terpy)(OH_2)]^{3+}$. *J. Am. Chem. Soc.*, 126:8084–8085, 2004.

[78] W. F. Ruettinger, C. Campana, and G. C. Dismukes. Synthesis and characterization of $Mn_4O_4L_6$ complexes with cubane-like core structure: A new class of models of the active site of the photosynthetic water oxidase. *J. Am. Chem. Soc.*, 119:6670–6671, 1997.

[79] W. F. Ruettinger, D. M. Ho, and G. C. Dismukes. Protonation and dehydration reactions of the $Mn_4O_4L_6$ cubane and synthesis and crystal structure of the oxidized cubane $[Mn_4O_4L_6]^+$: A model for the photosynthetic water oxidizing complex. *Inorg. Chem.*, 38:1036–1037, 1999.

[80] M. Yagi, K. V. Wolf, P. J. Baesjou, S. L. Bernasek, and G. C. Dismukes. Selective photoproduction of O_2 from the Mn_4O_4 cubane core: A structural

and funtional model for the photosynthetic water-oxidizing complex. *Angew. Chem. Int. Ed.*, 40:2925–2928, 2001.

[81] R. Brimblecombe, G. F. Swiegers, C. Dismukes, and L. Spiccia. Sustained water oxidation photocatalysis by a bioinspired manganese cluster. *Angew. Chem. Int. Ed.*, 47:7335–7338, 2008.

[82] R. Brimblecombe, A. Koo, G. C. Dismukes, G. F. Swiegers, and L. Spiccia. A tandem water-splitting device based on a bio-inspired manganese catalyst. *ChemSusChem*, 3:1146–1150, 2010.

[83] K. J. Young, Y. Gao, and G. W. Brudvig. Photocatalytic water oxidation using manganese compounds immobilized in nafion polymer membranes. *Aust. J. Chem.*, 64:1221–1228, 2011.

[84] A. Singh and L. Spiccia. water oxidation catalysts based on abundant 1st row transition metals. *Coord. Chem. Rev.*, 257:2607–2622, 2013.

[85] J. Lloret Fillol, Z. Codolà, I. Garcia-Bosch, L. Gómez, J. J. Pla, and M. Costas. Efficient water oxidation catalysts based on readily available iron coordination complexes. *Nat. Chem.*, 3:807–813, 2011.

[86] T. Abe, K. Nagai, S. Kabutomori, M. Kaneko, A. Tajiri, and T. Norimatsu. An organic photoelectrode working in the water phase: Visible-light-induced dioxygen evolution by a perylene derivative/cobalt phthalocyanine bilayer. *Angew. Chem. Int. Ed.*, 45:2778–2781, 2006.

[87] Dogutan D. K., R. McGuire Jr., and D. G. Nocera. Electrocatalytic water oxidation by cobalt(III) hangman β-octofluoro corroles. *J. Am. Chem. Soc.*, 133:9178–9180, 2011.

[88] D. Wang and J. T. Groves. Efficient water oxidation catalyzed by homogeneous cationic cobalt porphyrins with critical roles for the buffer base. *Proc. Natl. Acad. Sci. U.S.A.*, 110:15579–15584, 2013.

[89] D. J. Wasylenko, C. Ganesamoorthy, J. Borau-Garcia, and C. P. Berlinguette. Electrochemical evidence for catalytic water oxidation mediated by high-valent cobalt complex. *Chem. Commun.*, 47:4249–4251, 2011.

[90] D. J. Wasylenko, R. D. Palmer, E. Schott, and C. P. Berlinguette. Interrogation of electrocatalytic water oxidation mediated by a cobalt complex. *Chem. Commun.*, 48:2107–2109, 2012.

[91] A. Sartorel, M. Bonchio, S. Campagna, and F. Scandola. Tetrametallic molecular catalysts for photochemical water oxidation. *Chem. Soc. Rev.*, 42:2262–2280, 2013.

[92] N. S. McCool, D. M. Robinson, J. E. Sheats, and G. C. Dismukes. A co_4o_4 "cubane" water oxidation catalyst inspired by photosynthesis. *J. Am. Chem. Soc.*, 133:11446–11449, 2011.

[93] G. La Ganga, F. Puntoriero, S. Campagna, I. Bazzan, S. Berardi, M. Bonchio, A. Sartorel, M. Natali, and F. Scandola. Light-driven water oxidation with a molecular tetra-cobalt(III) cubane cluster. *Faraday Discuss.*, 155:177–190, 2012.

[94] J. G. McAlpin, T. A. Stich, Y. Surendranath, D. G. Nocera, W. H. Casey, and R. D. Britt. Electronic structure description of a $[Co(III)_3Co(IV)O_4]$ cluster: A model for the paramagnetic intermediate in cobalt-catalyzed water oxidation. *J. Am. Chem. Soc.*, 133:15444–15452, 2011.

[95] A. M. Ullman, Y. Liu, M. Huynh, D. K. Bediako, H. Wang, B. L. Anderson, D. C. Powers, J. J. Breen, H. D. Abruña, and D. G. Nocera. Water oxidation catalysis by Co(II) impurities in $Co(III)_4O_4$ cubanes. *J. Am. Chem. Soc.*, 136:17681–17688, 2014.

[96] F. Evangelisti, R. Moré, F Hodel, S. Luber, and G. R. Patzke. $3d-4f$

$\{Co^{II}{}_3Ln(OR)_4\}$ cubanes as bio-inspired water oxidation catalysts. *J. Am. Chem. Soc.*, 137:11076–11084, 2015.

[97] Y. Matsumoto and E. Sato. Electrocatalytic properties of transition metal oxides for oxygen evolution reaction. *Mater. Chem. Phys.*, 14:397–426, 1986.

[98] J. O'M. Bockris and T. Otagawa. Mechanism of oxygen evolution on perovskites. *J. Phys. Chem.*, 87:2960–2971, 1983.

[99] J. O'M. Bockris and T. Otagawa. The electrocatalysis of oxygen evolution on perovskites. *J. Electrochem. Soc*, 131:290–302, 1984.

[100] S. Trasatti. Electrocatalysis in the anodic evolution of oxygen and chlorine. *Electrochim. Acta*, 29:1503–1512, 1984.

[101] P. Rasiyah and A. C. C. Tseung. The role of the lower metal oxide/higher metal oxide couple in oxygen evolution reactions. *J. Electrochem. Soc*, 131:803–808, 1984.

[102] S. M. Jasem and A. C. C. Tseung. A potentiostatic pulse study of oxygen evolution on teflon-bonded nickel-cobalt oxide electrodes. *J. Electrochem. Soc.*, 126:1353–1360, 1979.

[103] A. Walsh, S.-H. Wei, Y. Yan, M. M. Al-Jassim, and J. A. Turner. Structural, magnetic, and electronic properties of the Co-Fe-Al oxide spinel system: Density-functional theory calculations. *Phys. Rev. B Condens. Matter.*, 76:165119–165128, 2007.

[104] S. Pintado, S. Goberna-Ferrón, E. C. Escudero-Adán, and J. R. Galán-Mascarós. Fast and persistent electrocatalytic water oxidation by Co-Fe prussian blue coordination polymers. *J. Am. Chem. Soc.*, 135:13270–13273, 2013.

[105] B. A. Pinaud, Z. Chen, D. N. Abram, and T. F. Jaramillo. Thin films of

sodium birnessite-type MnO_2: Optical properties, electronic band structure, and solar photoelectrochemistry. *J. Phys. Chem. C*, 115:11830–11838, 2011.

[106] M. Morita, C. Iwakura, and H. Tamura. The anodic characteristics of massive manganese oxide electrode. *Electrochim. Acta*, 24:357–362, 1979.

[107] S. Trasatti. Electrocatalysis by oxides - attempt at a unifying approach. *J. Electroanal. Chem.*, 111:125–131, 1980.

[108] D. K. Bediako, B. Lassalle-Kaiser, Y. Surendranath, J. Yano, V. K. Yachandra, and D. G. Nocera. Structure-activity correlations in a nickel-borate oxygen evolution catalyst. *J. Am. Chem. Soc.*, 134:6801–6809, 2012.

[109] M. Dinca, Y. Surendranath, and D. G. Nocera. Nickel-borate oxygen-evolving catalyst that functions under benign conditions. *Proc. Natl. Acad. Sci. U.S.A.*, 107:10337–10341, 2010.

[110] M. Risch, K. Klingan, J. Heidkamp, D. Ehrenberg, P. Chernev, I. Zaharieva, and H. Dau. Nickel-oxido structure of a water-oxidizing catalyst film. *Chem. Commun.*, 47:11912–11914, 2011.

[111] M. W. Kanan, J. Yano, Y. Surendranath, M. Dinca, V. K. Yachandra, and D. G. Nocera. Structure and valency of a cobalt-phosphate water oxidation catalyst determined by in sity x-ray spectroscopy. *J. Am. Chem. Soc.*, 132:13692–13701, 2010.

[112] F. Zhou, A. Izgorodin, R. K. Hocking, L. Spiccia, and D. R. MacFarlane. Electrodeposited mno_x films from ionic liquid for electrocatalytic water oxidation. *Adv. Energy Mater.*, 2:1013–1021, 2012.

[113] N. Sakai, Y. Ebina, K. Takada, and T. Sasaki. Photocurrent generation from semiconducting manganese oxide nanosheets in response to visible light. *J. Phys. Chem. B*, 109:9651–9655, 2005.

[114] J. Kiwi and M. Grätzel. Colloidal redox catalysts for evolution of oxygen and for light-induced evolution of hydrogen from water. *Angew. Chem. Int. Ed. Engl.*, 18:624–626, 1979.

[115] K. Kalyanasundaram and M. Grätzel. Cyclic cleavage of water into H_2 and O_2 by visible light with coupled redox catalysts. *Angew. Chem. Int. Ed. Engl.*, 18:701–702, 1979.

[116] J. Kiwi, E. Borgarello, E. Pelizzetti, M. Visca, and M. Grätzel. Cyclic water cleavage by visible light: Drastic improvement of yield of H_2 and O_2 with bifunctional redox catalysts. *Angew. Chem. Int. Ed. Engl.*, 19:646–648, 1980.

[117] A. Harriman, M.-C. Richoux, P. A. Christensen, S. Mosseri, and P. Neta. Redox reactions with colloidal metal oxides. *J. Chem. Soc., Faraday Trans. 1*, 83:3001–3014, 1987.

[118] A. Harriman, I. J. Pickering, J. M. Thomas, and P. A. Christensen. Metal oxides as heterogeneous catalysts for oxygen evolution under photochemical conditions. *J. Chem. Soc., Faraday Trans. 1*, 84:2795–2806, 1988.

[119] A. Mills. Heterogeneous redox catalysts for oxygen and chlorine evolution. *Chem. Soc. Rev.*, 18:285–316, 1989.

[120] A. Mills, P. A. Duckmanton, and J. Reglinski. A simple, novel method for preparing an effective water oxidation catalyst. *Chem. Commun.*, 46:2397–2398, 2010.

[121] K. Okeyoshi and R. Yoshida. Oxygen-generating gel systems induced by visible light. *Adv. Funct. Mater.*, 20:708–714, 2010.

[122] K. C. Pillai, A. S. Kumar, and J.-M. Zen. Nafion-RuO_2-$Ru(bpy)_3{}^{2+}$ composite electrodes for efficient electrocatalytic water oxidation. *J. Mol. Catal. A: Chem.*, 160:277–285, 2000.

[123] J. Kiwi and M. Grätzel. Oxygen evolution from water via redox catalysis. *Angew. Chem. Int. Ed. Engl.*, 17:860–861, 1978.

[124] T. Nakagawa, C. A. Beasley, and R. W. Murray. Efficient electro-oxidation of water near its reversible potential by a mesoporous IrO_x nanoparticle film. *J. Phys. Chem. C*, 113:12958–12961, 2009.

[125] M. Hara, C. C. Waraksa, J. T. Lean, B. A. Lewis, and Mallouk. T. E. Photocatalytic water oxidation in a buffered tris(2,2'-bipyridyl)ruthenium complex-colloidal IrO_2 system. *J. Phys. Chem. A*, 104:5275–5280, 2000.

[126] P. G. Hoertz, Y.-I. Kim, W. J. Youngblood, and Mallouk. T. E. Bidentate dicarboxylate capping groups and photosensitizers control the size of IrO_2 nanoparticle catalytsts for water oxidation. *J. Phys. Chem. B*, 111:6845–6856, 2007.

[127] W. J. Youngblood, S.-H. A. Lee, Y. Kobayashi, E. A. Hernandez-Pagan, P. G. Hoertz, T. A. Moore, A. L. Moore, D. Gust, and Mallouk. T. E. Photoassisted overall water splitting in a visible light-absorbing dye-sensitized photoelectrochemical cell. *J. Am. Chem. Soc.*, 131:926–927, 2009.

[128] H. Han and H. Frei. In situ spectroscopy of water oxidation at Ir oxide nanocluster driven by visible TiOCr charge-transfer chromophore in mesoporous silica. *J. Phys. Chem. C*, 112:16156–16159, 2008.

[129] G. La Ganga, F. Nastasi, S. Campagna, and F. Puntoriero. Photoinduced water oxidation sensitized by a tetranuclear Ru(II) dendrimer. *Dalton Trans.*, 45:9997–9999, 2009.

[130] S. D. Tilley, M. Cornuz, K. Sivula, and M. Grätzel. Light-induced water splitting with hematite: Improved nanostructure and iridium oxide catalysis. *Angew. Chem. Int. Ed.*, 49:6405–6408, 2010.

[131] A. Ramírez, P. Bogdanoff, D Friedrich, and S. Flechter. Synthesis of $Ca_2Mn_3O_8$ films and their electrochemical studies for the oxygen evolution reaction (OER) of water. *Nano Energy*, 1:282–289, 2012.

[132] Y. Gorlin and T. F. Jamarillo. A bifunctional nonprecious metal catalyst for oxygen reduction and water oxidation. *J. Am. Chem. Soc.*, 132:13612–13614, 2010.

[133] K. Maeda, A. Xiong, T. Yoshinaga, T Ikeda, N. Sakamoto, T. Hisatomi, M. Takashima, D Lu, M. Kanehara, T. Setoyama, T. Teranishi, and K. Domen. Photocatalytic overall water splitting promoted by two different cocatalysts for hydrogen and oxygen evolution under visible light. *Angew. Chem.*, 122:4190–4193, 2010.

[134] F. Jiao and H. Frei. Nanostructured manganese oxide clusters supported on mesoporous silica as efficient oxygen-evolving catalysts. *Chem. Commun.*, 46:2920–2922, 2010.

[135] K. Maeda and K. Domen. Photocatalytic water splitting: Recent progress and future challenges. *J. Phys. Chem. Lett.*, 1:2655–2661, 2010.

[136] M. Morita, C. Iwakura, and H. Tamura. The anodic characteristics of manganese dioxide electrodes prepared by thermal decomposition of manganese nitrate. *Electrochim. Acta*, 22:325–328, 1977.

[137] M. Morita, C. Iwakura, and H. Tamura. The anodic characteristics of modified Mn oxide electrode: $Ti/RuO_x/MnO_x$. *Electrochim. Acta*, 23:331–335, 1978.

[138] A. Bergmann, I. Zaharieva, H. Dau, and P. Strasser. Electrochemical water splitting by layered and 3D crosslinked manganese oxides: correlating structural motifs and catalytic activity. *Energy Environ. Sci.*, 6:2745–2755, 2013.

[139] I. Zaharieva, P. Chernev, M. Risch, K. Klingan, M. Kohlhoff, A. Fischer, and H. Dau. Electrosynthesis, functional, and structural characterization of a water-oxidizing manganese oxide. *Energy Environ. Sci.*, 5:7081–7089, 2012.

[140] T. Takashima, K. Hashimoto, and R. Nakamura. Mechanistics of ph-dependent activity for water oxidation to molecular oxygen by mno_2 electrocatalysts. *J. Am. Chem. Soc.*, 134:1519–1527, 2012.

[141] M. M. Najafpour, B. Haghighi, D. J. Sedigh, and M. Z. Ghobadi. Conversions of Mn oxides to nanolayered Mn oxide in electrochemical water oxidation at near neutral pH, all to a better catalyst: catalyst evolution. *Dalton Trans.*, 42:16683–16686, 2013.

[142] M. M. Najafpour, M. A. Tabrizi, B. Haghighi, J. J. Eaton-Rye, R. Carpentier, and S. I. Allakhverdiev. Imidazolium or guanidinium/layered manganese (III, IV) oxide hybrid as a promising structural model for the water-oxidizing complex of Photosystem II for artificial photosynthetic systems. *Photosynth. Res.*, 117:413–421, 2013.

[143] T. Takashima, K. Hashimoto, and R. Nakamura. Inhibition of charge disproportionation of MnO_2 electrocatalysts for efficient water oxidation under neutral conditions. *J. Am. Chem. Soc.*, 134:18153–18156, 2012.

[144] M. M. Najafpour, B. Haghighi, M. Z. Ghobadi, and D. J. Sedigh. Nanolayered manganese oxide/poly(4-vinylpyridine) as a biomimetic and very efficient water oxidizing catalyst: toward an artificial enzyme in artificial photosynthesis. *Chem. Commun.*, 49:8824–8826, 2013.

[145] F. Cheng, T. Zhang, Y. Zhang, J. Du, X. Han, and J. Chen. Enhancing electrocatalytic oxygen reductio on MnO_2 with vacancies. *Angew. Chem. Int. Ed.*, 52:2474–2477, 2013.

[146] A. Singh, R. K. Hocking, S. L.-Y. Chang, B. M. George, M. Fehr, K. Lips, A. Schnegg, and L. Spiccia. Water oxidation catalysis by nanoparticulate manganese oxide thin films: Probing the effect of the manganese precursors. *Chem. Mater.*, 25:1098–1108, 2013.

[147] M. Huynh, D. K. Bediako, and D. G. Nocera. A functionally stable manganese oxide oxygen evolution catalyst in acid. *J. Am. Chem. Soc.*, 136:6002–6010, 2014.

[148] M. Fekete, R. K. Hocking, S. L. Y. Chang, C. Italiano, A. F. Patti, F. Arena, and L. Spiccia. Highly active screen-printed electrocatalysts for water oxidation based on β-manganese oxide. *Energy Environ. Sci.*, 6:2222–2232, 2013.

[149] Y. Gorlin, C.-J. Chung, J. D. Benck, D. Nordlund, L. Seitz, T.-C. Weng, D. Sokaras, B. M. Clemens, and T. F. Jamarillo. Understanding interactions between manganese oxide and gold that lead to enhanced activity for electrocatalytic water oxidation. *J. Am. Chem. Soc.*, 136,:4920–4926, 2014.

[150] M. M. Najafpour, K. C. Leonard, F.-R. F. Fan, M. A. Tabrizi, A. J. Bard, C. K. King'ondu, S. L. Suib, B. Haghighi, and S. I. Allakhverdiev. Nanosize layered manganese-calcium oxide as an efficient and biomimetic catalyst for water oxidation under acidic conditions: comparable to platinum. *Dalton Trans.*, 42:5085–5091, 2013.

[151] T. W. Hamann. Splitting water with rust: hematite photoelectrochemistry. *Dalton Trans.*, 41:7830–7834, 2012.

[152] R. L. Doyle and M. E. G. Lyons. Kinetics and mechanistic aspects of the oxygen evolution reaction at hydrous iron oxide films in base. *J. Electrochem. Soc.*, 160:H142–H154, 2013.

[153] M. E. G. Lyons and M. P. Brandon. The oxygen evolution reaction on passive

oxide covered transition metal electrodes in aqueous alkaline solution. Part III - Iron. *Int. J. Electrochem. Sci.*, 3:1463–1503, 2008.

[154] M. E. G. Lyons and R. L. Doyle. Oxygen evolution at oxidised iron electrodes: Atale of two slopes. *Int. J. Electrochem. Sci.*, 7:9488–9501, 2012.

[155] S. Shen. Toward efficient solar water splitting over hematite photoelectrodes. *J. Mater. Res.*, 29:29–46, 2014.

[156] B. Klahr, S. Gimenez, F. Fabregat-Santiago, J. Bisquert, and T. W. Hamann. Electrochemical and photoelectrochemical investigation of water oxidation with hematite electrodes. *Energy Environ. Sci.*, 5:7626–7636, 2012.

[157] L. M. Peter. Energetics and kinetics of light-driven oxygen evolution at semiconductor electrodes: the example of hematite. *J. Solid State Electrochem.*, 17:315–326, 2013.

[158] M. J. Katz, S. C. Riha, N. C. Jeong, A. B. F. Martinson, O. K. Farha, and J. T. Hupp. Toward solar fuels: Water splitting with sunlight and "rust"? *Coord. Chem. Rev.*, 256:2521–2529, 2012.

[159] F. E. Osterloh. Inorganic nanstructures for photoelectrochemical and photocatalytic water splitting. *Chem. Soc. Rev.*, 42:2294–2320, 2013.

[160] X. Zong, S. Thaweesak, H. Xu, Z. Xing, J. Zou, G. Lu, and L. Wang. A scalable colloidal approach to prepare hematite films for efficient solar water splitting. *Phys. Chem. Chem. Phys.*, 15:12314–12351, 2013.

[161] R. L. Doyle and M. E. G. Lyons. Redox and oxygen evolution electrocatalytic properties of nafion and single-walled carbon naotube/hydrous iron oxide composite films. *Electrocatal.*, 5:114–124, 2014.

[162] N. D. Carbonare, V. Cristino, S. Berardi, S. Carli, R. Argazzi, S. Caramori,

L. Meda, A. Tacca, and C. A. Bignozzi. Hematite photoanodes modified with an Fe^{III} water oxidation catalyst. *ChemPhysChem*, 15:1164–1174, 2014.

[163] W. D. Chemelewski, H.-C. Lee, J.-F. Lin, A. J. Bard, and C. B. Mullins. Amorphous FeOOH oxygen evolution reaction catalyst for photoelectrochemical water splitting. *J. Am. Chem. Soc.*, 136:2843–2850, 2014.

[164] R. Boggio, A. Carugati, and S. Trasatti. Electrochemical surface properties of Co_3O_4 electrodes. *J. App. Electrochem.*, 17:828–840, 1987.

[165] A. Coehn and M. Cläser. Studien über die bildung von metalloxyden I. Über das anodische verhalten von kobalt- und nickel-lösungen. *Z. Anorg. Chem.*, 33:9–24, 1902.

[166] F. W. Skirrow. Über oxydation durch elektrolytisch abgeschiedenes fluor. *Z. Anorg. Chem.*, 33:25–30, 1902.

[167] K. Jun, M. Takahashi, O. Suzuki, and T. Fukunaga. Novel cobalt oxide and an electrode having the cobalt oxide coating, 1968. US Patent 3,399,966.

[168] Y. Surendranath, M. Dinca, and D. G. Nocera. Electrolyte-dependent electrosynthesis and activity of cobalt-based water oxidation catalysts. *J. Am. Chem. Soc.*, 131:2615–2620, 2009.

[169] D. A. Lutterman, Y. Surendranath, and D. G. Nocera. A self-healing oxygen-evolution catalyst. *J. Am. Chem. Soc.*, 131:3838–3839, 2009.

[170] J. He, Y. Peng, Z. Sun, W. Cheng, Q. Liu, Y. Feng, Y. Jiang, F. Hu, Z. Pan, Q. Bian, and S. Wei. Realizing high water splitting activity on Co_3O_4 nanowire arrays under neutral environment. *Electrochim. Acta*, 119:64–71, 2014.

[171] Y. Surendranath, M. W. Kanan, and D. G. Nocera. Mechanistic studies of the oxygen evolution reaction by a cobalt-phophate catalyst at neutral pH. *J. Am. Chem. Soc.*, 132:16501–16509, 2010.

[172] A. Irshad and N. Munichandraiah. An oxygen evolution Co-Ac catalyst - the synergistic effect of phosphate ions. *Phys. Chem. Chem. Phys.*, 16:5412–5422, 2014.

[173] A. J. Esswein, Y. Surendranath, S. Y. Reece, and D. G. Nocera. Highly active cobalt phosphate and borate based oxygen evolving catalysts operating in neutral and natural waters. *Energy Environ. Sci.*, 4:499–504, 2011.

[174] A. Minguzzi, F.-R. F. Fan, A. Vertova, S. Rondinini, and A. J. Bard. Dynamic potential-pH diagrams application to electrocatalysts for water oxidation. *Chem. Sci.*, 3:217–229, 2012.

[175] L. Ouattara, S. Fierro, O. Frey, M. Koudelka, and C. Comninellis. Electrochemical comparison of IrO_2 prepared by anodic oxidation of pure iridium and IrO_2 prepared by thermal decomposition of H_2IrCl_6 precursor solution. *J. App. Electrochem.*, 39:1361–1367, 2009.

[176] M. E. G. Lyons and M. P. Brandon. The oxygen evolution reaction on passive oxide covered transition metal electrodes in aqueous alkaline solution. Part 1-Nickel. *Int. J. Electrochem. Sci.*, 3:1386–1424, 2008.

[177] M. R. Gennero de Chialvo and A. C. Chialvo. Oxygen evolution reaction on thick hydrous nickel oxide electrodes. *Electrochim. Acta*, 33:825–830, 1988.

[178] X. Wang, H. Luo, H. Yang, P. J. Sebastian, and S. A. Gamboa. Oxygen catalytic evolution reaction on nickel hydroxide electrode modified by electroless cobalt coating. *Int. J. Hydrogen Energy*, 29:967–972, 2004.

[179] B. S. Yeo and A. T. Bell. In situ raman study on nickel oxide and gold-supported nickel oxide catalysts for the electrochemical evolution of oxygen. *J. Phys. Chem. C*, 116:8394–8400, 2012.

[180] P. W. T. Lu and S. Srinivasan. Electrochemical-ellipsometric studies of oxide film formed on nickel during oxygen evolution. *J. Electrochem. Soc*, 125:1416–1422, 1978.

[181] A. G. Marrani, V. Novelli, S. Sheehan, D. P. Dowling, and D. Dini. Probing the redox states at the surface of electroactive nanoporous NiO thin films. *ACS Appl. Mater. Interfaces*, 6:143–152, 2014.

[182] D. K. Bediako, Y. Surendranath, and D. G. Nocera. Mechanistic studies of the oxygen evolution reaction mediated by a nickle-borate thin film electrocatalyst. *J. Am. Chem. Soc.*, 135:3662–3674, 2013.

[183] L. Trotochaud, J. K. Ranney, K. N. Williams, and S. W. Boettcher. Solution-cast metal oxide thin film electrocatalysts for oxygen evolution. *J. Am. Chem. Soc.*, 134:17253–17261, 2012.

[184] T. W. Kim and K.-S. Choi. Nanoporous $BiVO_4$ photoanodes with dual-layer oxygen evolution catalysts for solar water splitting. *Science*, 343:990–994, 2014.

[185] L. Trotochaud, T. J. Mills, and S. W. Boettcher. An optocatalytic model for semiconductor-catalyst water-splitting photoelectrodes based on in situ optical measurements on operational catalysts. *J. Phys. Chem. Lett.*, 4:931–935, 2013.

[186] R. D. L. Smith, M. S. Prévot, R. D. Fagan, S. Trudel, and C. P. Berlinguette. Water oxidation catalysis: Electrocatalytic response to metal stoichiometry in amorphous metal oxide films containing iron, cobalt, and nickel. *J. Am. Chem. Soc.*, 135:11580–11586, 2013.

[187] M. W. Louie and A. T. Bell. An investigation of thin-film Ni-Fe oxide catalysts for the elctrochemical evolution of oxygen. *J. Am. Chem. Soc.*, 135:12329–12337, 2013.

[188] J. Landon, E. Demeter, N. Inoglu, C. Keturakis, I. E. Wachs, R. Vasic, A. I. Frenkel, and J. R. Kitchin. Spectroscopic characterization of mixed Fe-Ni oxide electrocatalysts for the oxygen evolution reaction in alkaline electrolytes. *ACS Catal.*, 2:1793–1801, 2012.

[189] L. Trotochaud, S. L. Young, J. K. Ranney, and S. W. Boettcher. Nickel-iron oxyhydroxide oxygen-evolution electrocatalysts: The role of intentional and incidental iron incorporation. *J. Am. Chem. Soc.*, 136:6744–6753, 2014.

[190] D. G. Shchukin, A. A. Yaremchenko, M. G. S. Ferreira, and V. V. Kharton. Polymer gel templating synthesis of nanocrystalline oxide anodes. *Chem. Mater.*, 17:5124–5129, 2005.

[191] R. N. Singh, S. K. Tiwari, S. P. Singh, N. K. Singh, G. Poillerat, and P. Chartier. Synthesis of (La, Sr)CoO_3 perovskite films via a sol-gel route and their physicochemical and electrochemical surface characterization for anode application in alkaline water electrolysis. *J. Chem. Soc., Faraday Trans.*, 92:2593–2597, 1996.

[192] H. Arai, S. Müller, and O. Haas. AC impedance analysis of bifunctional air electrodes for metal-air batteries. *J. Electrochem. Soc.*, 147:3584–3591, 2000.

[193] A. Wattiaux, J. C. Grenier, M. Pouchard, and P. Hagenmuller. Electrolytic oxygen evolution in alkaline medium on $La_{1-x}Sr_xFeO_{3-y}$ perovskite-related ferrites I. Electrochemical study. *J. Electrochem. Soc.*, 134:1714–1718, 1987.

[194] C. O. Soares, M. D. Carvalho, M. E. Melo Jorge, A. Gomes, R. A. Silva, C. M. Rangel, and M. I. da Silva Pereira. High surface area $LaNiO_3$ electrodes for oxygen electrocatalysis in alkaline media. *J. Appl. Electrochem.*, 42:325–332, 2012.

[195] A. Grimaud, K. J. May, C. E. Carlton, Y.-L. Lee, M. Risch, W. T. Hong, J. Zhou, and Y. Shao-Horn. Double perovskites as a family of highly active

catalysts for oxygen evolution in alkaline solution. *Nat. Commun.*, 4:2439, 2013.

[196] J. Suntivich, K. J. May, H. A. Gasteiger, J. B. Goodenough, and Y. Shao-Horn. A perovskite oxide optimized for oxygen evolution catalysis from molecular orbital principles. *Science*, 334:1383–1385, 2011.

[197] M. Risch, A. Grimaud, K. J. May, K. A. Stoerzinger, T. J. Chen, A. N. Mansour, and Y. Shao-Horn. Structural changes of cobalt-based perovskites upon water oxidation investigated by EXAFS. *J. Phys. Chem. C*, 117:8628–8635, 2013.

[198] K. J. May, C. E. Carlton, K. A. Stoerzinger, M. Risch, J. Suntivich, Y.-L. Lee, A. Grimaud, and Y. Shao-Horn. Influence of oxygen evolution during water oxidation on the surface of perovskite oxide catalysts. *J. Phys. Chem. Lett.*, 3:3264–3270, 2012.

[199] N.-L. Wu, W.-R. Liu, and S.-J. Su. Effect of oxygenation on electrocatalysis of $La_{0.6}Ca_{0.4}CoO_{3-x}$ in bifunctional air electrode. *Electrochim. Acta*, 48:1567–1571, 2003.

[200] J. Suntivich, H. A. Gasteiger, N. Yabuuchi, H. Nakanishi, J. B. Goodenough, and Y. Shao-Horn. Design principles for oxygen-reduction activity on perovskite oxide catalysts for fuel cells and metal-air batteries. *Nat. Chem.*, 3:546–550, 2011.

[201] N. Fradette and B. Marsan. Surface studies of $Cu_xCo_{3-x}O_4$ electrodes for the electrocatalysis of oxygen evolution. *J. Electrochem. Soc.*, 145:2320–2327, 1998.

[202] J. Ponce, E. Ríos, J.-L. Rehspringer, G. Poillerat, P. Chartier, and J. L. Gautier. Preparation of nickel aluminum-manganese spinel oxides $Ni_xAl_{1-x}Mn_2O_4$

for oxygen electrocatalysis in alkaline medium: Comparison of properties stemming from different preparation methods. *J. Solid State Chem.*, 145:23–32, 1999.

[203] R. N. Singh, J. P. Singh, B. Lal, and A. Singh. Preparation and characterization of $CuFe_{2-x}Cr_xO_4$ ($0 \leq x \leq 1.0$) nano spinels for electrocatalysis of oxygen evolution in alkaline solutions. *J. Hydrogen Energy*, 32:11–16, 2007.

[204] N. R. de Tacconi and K. Rajeshwar. Metal hexacyanoferrates: Electrosynthesis, in situ characterization, and applications. *Chem. Mater.*, 15:3046–3062, 2003.

[205] S. Goberna-Ferrón, W. Y. Hernández, B. Rodríguez-García, and J. R. Galán-Mascarós. Light-driven water oxidation with metal hexacyanometallate heterogeneous catalysts. *ACS Catal.*, 4:1637–1641, 2014.

[206] M. T. Pope and A. Müller. *Polyoxometalate chemistry from topology via self-assembly to applications*. Kluwer Academic Publishers, 2001.

[207] M. T. Pope. *Heteropoly and isopoly oxometalates*. Springer-Verlag, 1983.

[208] H. Lv, Y. V. Geletii, C. Zhao, J. W. Vickers, G. Zhu, Z. Luo, J. Song, T. Lian, D. G. Musaev, and C. L. Hill. Polyoxometalate water oxidation catalysts and the production of green fuel. *Chem. Soc. Rev.*, 41:7572–7589, 2012.

[209] J. J. De Luyart Lubice and F. C. De Luyar Lubice. Análisis químico del volfram y examen de un nuevo metal que entra en su composición. pages 46–88, 1783.

[210] J. J. Berzelius. Beitrag zur näheren kenntnifs des molybdäns. *Pogg. Ann. Phys. Chem.*, 6:369–380, 1826.

[211] M. T. Pope and A. Müller. Polyoxometalate chemistry: An old field with

new dimensions in several disciplines. *Angew. Chem. Int. Ed. Engl.*, 30:34–48, 1991.

[212] C. L. Hill. Introduction: Polyoxometalates multicomponent molecular vehicles to probe fundamental issues and practical problems. *Chem. Rev.*, 98:1–2, 1998.

[213] D.-L. Long, R. Tsunashima, and L. Cronin. Polyoxometalates: Building blocks for functional nanoscale systems. *Angew. Chem. Int. Ed.*, 49:1736–1758, 2010.

[214] J. F. Keggin. Structure of the molecule of 12-phosphotungstic acid. *Nature*, 131:908–909, 1933.

[215] L. C. W. Baker and J. S. Figgis. A new fundamental type of inorganic complex: Hybrid between heteropoly and conventional coordination complexes. Possibilities for geometrical isomerisms in 11-, 12-, 17-, and 18-heteropoly derivatives. *J. Am. Chem. Soc.*, 92:3794–3797, 1970.

[216] X. López, J. J. Carbó, C. Bo, and J. M. Poblet. Structure, properties and reactivity of polyoxometalates: a theoretical perspective. *Chem. Soc. Rev.*, 41:7537–7571, 2012.

[217] D.-L. Long, E. Burkholder, and L. Cronin. Polyoxometalate clusters, nanostructures and materials: From self assembly to designer materials and devices. *Chem. Soc. Rev.*, 36:105–121, 2007.

[218] A. Sartorel, M. Carraro, G. Scorrano, R. De Zorzi, S. Geremia, N. D. McDaniel, S. Bernhard, and M. Bonchio. Polyoxometalate embedding of a tetraruthenium(IV)-oxo-core by template-directed metalation of [γ-$SiW_{10}O_{36}$]$^{8-}$: A totally inorganic oxygen-evolving catalyst. *J. Am. Chem. Soc.*, 130:5006–5007, 2008.

[219] Q. Yin, J. M. Tan, C. Besson, Y. V. Geletii, D. G. Musaev, A. E. Kuznetsov, Z. Luo, K. I. Hardcastle, and C. L. Hill. A fast soluble carbon-free molecular

water oxidation catalyst based on abundant metals. *Science*, 328:342–345, 2010.

[220] S. Goberna-Ferrón, L. Vigara, J. Soriano-López, and J. R. Galán-Mascarós. Identification of a nonanuclear Co^{II}_9 polyoxometalate cluster as a homogeneous catalyst for water oxidation. *Inorg. Chem.*, 51:11707–11715, 2012.

[221] S. Shaik, H. Hirao, and D. Kumar. Reactivity of high-valent iron-oxo species in enzymes and synthetic reagents: A tale of many states. *Acc. Chem. Res.*, 40:532–542, 2007.

[222] A. Sartorel, M. Carraro, A. Bagno, G. Scorrano, and M. Bonchio. Asymmetric tetraprotonation of γ-$[(SiO_4)W_{10}O_{32}]^{8-}$ triggers a catalytic epoxidation reaction: Perspectives in the assignment of the active catalyst. *Angew. Chem. Int. Ed.*, 46:3255–3258, 2007.

[223] X. Fang and C. L. Hill. Multiple reversible protonation of polyoxoanion surfaces: Direct observation of dynamic structural effects from proton transfer. *Angew. Chem. Int. Ed.*, 46:3877–3880, 2007.

[224] Y. V. Geletii, B. Botar, P. Kögerler, D. A. Hillesheim, D. G. Musaev, and C. L. Hill. An all-inorganic, stable, and highly active tetraruthenium homogeneous catalyst for water oxidation. *Angew. Chem. Int. Edit.*, 47:3896–3899, 2008.

[225] P. K. Ghosh, B. S. Brunschwig, M. Chou, C. Creutz, and N. Sutin. Thermal and light-induced reduction of $Ru(bpy)_3{}^{3+}$ in aqueous solution. *J. Am. Chem. Soc.*, 106:4772–4783, 1984.

[226] Y. V. Geletii, C. Besson, Y. Hou, Q. Yin, D. G. Musaev, D. Quiñonero, R. Cao, K. I. Hardcastle, A. Proust, P. Kögerler, and C. L. Hill. Structural, physicochemical, and reactivity properties of an all-inorganic, highly active tetraruthenium homogeneous catalyst for water oxidation. *J. Am. Chem. Soc.*, 131:1697–1699, 2009.

[227] Y. V. Geletii, Z. Huang, Y. Hou, D. G. Musaev, T. Lian, and C. L. Hill. Homogeneous light-driven water oxidation catalyzed by a tetraruthenium complex with all inorganic ligands. *J. Am. Chem. Soc.*, 131:7522–7523, 2009.

[228] M. Orlandi, R. Argazzi, A. Sartorel, M. Carraro, G. Scorrano, M. Bonchio, and F. Scandola. Ruthenium polyoxometalate water splitting catalyst: very fast hole scavenging from photogenerated oxidants. *Chem. Commun.*, 46:3152–3154, 2010.

[229] A. Sartorel, P. Miró, E. Salvadori, S. Romain, M. Carraro, G. Scorrano, M. Di Valentin, A. Llobet, C. Bo, and M. Bonchio. Water oxidation at a tetraruthenate core stabilized by polyoxometalate ligands: Experimental and computational evidence to trace the competent intermediates. *J. Am. Chem. Soc.*, 131:16051–16053, 2009.

[230] D. Quiñonero, A. L. Kaledin, A. E. Kuznetsov, Y. V. Geletii, C. Besson, C. L. Hill, and D. G. Musaev. Computational studies of the geometry and electronic structure of an all-inorganic and homogeneous tetra-Ru-polyoxotungstate catalyst for water oxidation and its four subsequent one-electron oxidized forms. *J. Phys. Chem. A*, 114:535–542, 2010.

[231] S. Piccinin and S. Fabris. A first principles study of water oxidation catalyzed by a tetraruthenium-oxo core embedded in polyoxometalate ligands. *Phys. Chem. Chem. Phys.*, 13:7666–7674, 2011.

[232] T. J. R. Weakley, H. T. Evans Jr., J. S. Showell, G. F. Tourné, and C. M. Tourné. 18-Tungstotetracobalto(II)diphosphate and related anions: a novel structural class of heteropolyanions. *J. Chem. Soc., Chem. Commun.*, 4:139–140, 1973.

[233] Z. Huang, Z. Luo, Y. V. Geletii, J. W. Vickers, Q. Yin, D. Wu, Y. Hou, Y. Ding, J. Song, D. G. Musaev, C. L. Hill, and T. Lian. Efficient light-driven

carbon-free cobalt-based molecular catalyst for water oxidation. *J. Am. Chem. Soc.*, 133:2068–2071, 2011.

[234] J. J. Stracke and R. G. Finke. Electrocatalytic water oxidation beginning with the cobalt polyoxometalate $[Co_4(H_2O)_2(PW_9O_{34})_2]^{10-}$: Identification of heterogeneous CoO_x as the dominant catalyst. *J. Am. Chem. Soc.*, 133:14872–14875, 2011.

[235] J. J. Stracke and R. G. Finke. Water oxidation catalysis beginning with 2.4 μM $[Co_4(H_2O)_2(PW_9O_{34})_2]^{10-}$: Investigation of the true electrochemically driven catalyst at $\geq$600 mV overpotential at a glassy carbon electrode. *ACS Catal.*, 3:1209–1219, 2013.

[236] J. J. Stracke and R. G. Finke. Water oxidation catalysis beginning with $[Co_4(H_2O)_2(PW_9O_{34})_2]^{10-}$ when driven by the chemical oxidant Ruthenium(III)tris(2,2'-bipyridine): Stoichiometry, kinetic, and mechanistic studies en route to identifying the true catalyst. *ACS Catal.*, 4:79–89, 2014.

[237] M. Natali, S. Berardi, A. Sartorel, M. Bonchio, S. Campagna, and F. Scandola. Is $[Co_4(H_2O)_2(\alpha\text{-}PW_9O_{34})_2]^{10-}$ a genuine molecular catalyst in photochemical water oxidation? Answers from time-resolved hole scavenging experiments. *Chem. Commun.*, 48:8808–8810, 2012.

[238] J. W. Vickers, H. Lv, J. M. Sumliner, G. Zhu, Z. Luo, D. G. Musaev, Y. V. Geletii, and C. L. Hill. Differentiating homogeneous and heterogeneous water oxidation catalysis: Confirmation that $[Co_4(H_2O)_2(\alpha\text{-}PW_9O_{34})_2]^{10-}$ is a molecular water oxidation catalyst. *J. Am. Chem. Soc.*, 135:14110–14118, 2013.

[239] F. H. Burstall and R. S. Nyholm. 681. studies in co-ordination chemistry. part XIII. magnetic moments and bond types of transition-metal complexes. *J. Chem. Soc.*, pages 3570–3579, 1952.

[240] T. J. R. Weakley. The identification and X-ray structure of the diphosphatotris(nonatungstophosphato)nonacobaltate(II) heteropolyanion. *J. Chem. Soc., Chem. Commun.*, pages 1406–1407, 1984.

[241] H. Dau, C. Limberg, T. Reier, M. Risch, S. Roggan, and P. Strasser. The mechanism of water oxidation: From electrolysis via homogeneous to biological catalysis. *ChemCatChem*, 2:724–761, 2010.

[242] C. Costentin, S. Drouet, M. Robert, and J.-M. Savéant. Turnover numbers, turnover frequencies, and overpotential in molecular catalysis of electrochemical reactions. cyclic voltammetry and preparative-scale electrolysis. *J. Am. Chem. Soc.*, 134:11235–11242, 2012.

[243] S. Goberna-Ferrón, J. Soriano-López, J. R. Galán-Mascarós, and M. Nyman. Solution speciation and stability of cobalt-polyoxometalate water oxidation catalysts by X-ray scattering. *Eur. J. Inorg. Chem*, pages 2833–2840, 2015.

[244] C. D. Putnam, M. Hammel, G. L. Hura, and J. A. Tainer. X-ray solution scattering (SAXS) combined with crystallography and computation: defining accurate macromolecular structures, conformations and assemblies in solution. *Q. Rev. Biophys.*, 40:191–285, 2007.

[245] C. A. Ohlin, Harley S. J., J. G. McAlpin, R. K. Hocking, B. Q. Mercado, R. L. Johnson, E. M. Villa, M. K. Fidler, M. M. Olmstead, L. Spiccia, R. D. Britt, and W. H. Casey. Rates of water exchange for two Cobalt(II) heteropolyoxotungstate compounds in aqueous solution. *Chem. Eur. J.*, 17:4408–4417, 2011.

[246] F. M. Toma, A. Sartorel, M. Iurlo, M. Carraro, P. Parisse, C. Maccato, S. Rapino, B. R. Gonzalez, H. Amenitsch, T. Da Ros, L. Casalis, A. Goldoni, M. Marcaccio, G. Scorrano, G. Scoles, F. Paolucci, M. Prato, and M. Bonchio. Efficient water oxidation at carbon nanotubes-polyoxometalate electrocatalytic interfaces. *Nat. Chem.*, 2:826–831, 2010.

[247] J. Wu, L. Liao, We. Yan, Y. Xue, Y. Sun, X. Yan, Y. Chen, and Y. Xie. Polyoxometalates immobilized in ordered mesoporous carbon nitride as highly efficient water oxidation catalysts. *ChemSusChem*, 5:1207–1212, 2012.

[248] M. Quintana, A. Montellano López, S. Rapino, F. M. Toma, M. Iurlo, M. Carraro, A. Sartorel, C. Maccato, X. Ke, C. Bittencourt, T. Da Ros, G. Van Tendeloo, M. Marcaccio, F. Paolucci, M. Prato, and M. Bonchio. Knitting the catalytic pattern of artificial photosynthesis to a hybrid graphene nanotexture. *ACS Nano*, 7:811–817, 2013.

[249] S.-X. Guo, Y. Liu, C.-Y. Lee, A. M. Bond, J. Zhang, Y. V. Geletii, and C. L. Hill. Graphene-supported $[Ru_4O_4(OH)_2(H_2O)_4(\gamma\text{-}SiW_{10}O_{36})_2]^{10-}$ for highly efficient electrocatalytic water oxidation. *Energy Environ. Sci.*, 6:2654–2663, 2013.

[250] J. R. Galán-Mascarós, C. J. Gómez-Garcia, J. J. Borrás-Almenar, and E. Coronado. High nuclearity magnetic clusters: Magnetic properties of a nine cobalt cluster encapsulated in a polyoxometalate, $[Co_9(OH)_3(H_2O)_6(HPO_4)_2(PW_9O_{34})_3]^{16-}$. *Adv. Mater.*, 6:221–223, 1994.

[251] J. Chen and A. Selloni. Water adsorption and oxidation at the Co_3O_4 (110) surface. *J. Phys. Chem. Lett.*, 3:2808–2814, 2012.

[252] A. J. Esswein, M. J. McMurdo, P. N. Ross, A. T. Bell, and T. D. Tilley. Size-dependent activity of Co_3O_4 nanoparticle anodes for alkaline water electrolysis. *J. Phys. Chem. C*, 113:15068–15072, 2009.

[253] B. S. Yeo and A. T. Bell. Enhanced activity of gold-supported cobalt oxide for the electrochemical evolution of oxygen. *J. Am. Chem. Soc.*, 133:5587–5593, 2011.

[254] A. Juris, V. Balzani, F. Barigelletti, S. Campagna, P. Belser, and A. von

Zelewsky. Ru(II) polypyridine complexes: photophysics, photochemistry, electrochemistry, and chemiluminiscence. *Coordin. Chem. Rev.*, 84:85–277, 1988.

[255] D. M. Stanbury. Reduction potentials involving inorganic free radicals in aqueous solution. *Adv. Inorg. Chem.*, 33:69–138, 1989.

[256] H. S. White, W. G. Becker, and A. J. Bard. Photochemistry of the tris(2,2'-bipyridine)ruthenium(II)-poroxydisulfate system in aqueous and mixed acetonitrili-water soutions. evidence for a long-lived photoexcited ion pair. *J. Phys. Chem.*, 88:1840–1846, 1984.

[257] M. Natali, M. Orlandi, S. Berardi, S. Campagna, M. Bonchio, A. Sartorel, and F. Scandola. Photoinduced water oxidation by a tetraruthenium polyoxometalate catalyst: Ion-paring and primary processes with $Ru(bpy)_3{}^{2+}$ photosensitizer. *Inorg. Chem.*, 51:7324–7331, 2012.

[258] C. Besson, Z. Huang, Y. V. Geletii, S. Lense, K. I. Hardcastle, D. G. Musaev, T. Lian, A. Proust, and C. L. Hill. $Cs_9[(\gamma\text{-}PW_{10}O_{36})_2Ru_4O_5(OH)(H_2O)_4]$, a new all-inorganic, soluble catalyst for the efficient visible-light-driven oxidation of water. *Chem. Commun.*, 46:2784–2789, 2010.

[259] G. Zhu, Y. V. Geletii, P. Kogerler, H. Schilder, J. Song, S. Lense, C. Zhao, K. I. Hardcastle, D. G. Musaev, and C. L. Hill. Water oxidation catalyzed by a new tetracobalt-substituted polyoxometalate complex: $[Co_4(\mu\text{-}OH)(H_2O)_3(Si_2W_{19}O_{70})]^{11-}$. *Dalton Trans.*, 41:2084–2090, 2012.

[260] S. Tanaka, M. Annaka, and K. Sakai. Visible light-induced water oxidation catalyzed by molybdenum-based polyoxometalates with mono- and dicobalt(iii) cores as oxygen-evolving centers. *Chem. Commun.*, 48:1653–1655, 2012.

[261] P.-E. Car, M. Guttentag, K. K. Baldridge, R. Alberto, and G. R. Patzke. Synthesis and characterization of open and sandwich-type polyoxometalates

reveals visible-light-driven water oxidation via pom-photosensitizer complexes. *Green Chem.*, 14:1680–1688, 2012.

[262] G. Zhu, E. N. Glass, C. Zhao, H. Lv, J. W. Vickers, Y. V. Geletii, D. G. Musaev, J. Song, and C. L. Hill. A nickel containing polyoxometalate water oxidation catalyst. *Dalton Trans.*, 41:13043–13049, 2012.

[263] F. Song, Y. Ding, Baochun Ma, C. Wang, Q. Wang, X. Du, S. Fu, and J. Song. $K_7[Co^{III}Co^{II}(H_2O)W_{11}O_{39}]$: a molecular mixed−valence Keggin polyoxometalate catalyst of high stability and efficiency for visible light−driven water oxidation. *Energy Environ. Sci.*, 6:1170–1184, 2013.

[264] J. Gao, S. Cao, Q. Tay, Y. Liu, L. Yu, K. Ye, P. C. S. Mun, Y. Li, G. Rakesh, S. C. J. Loo, Z. Chen, Y. Zhao, C. Xue, and Q. Zhang. Molecule-based water-oxidation catalysts (WOCs): Cluster-size-dependent dye-sensitized polyoxometalates for visible-light-driven O_2 evolution. *Sci. Rep.*, 3:1853, 2013.

[265] F. Evangelisti, P.-E. Car, O. Blacque, and G. R. Patzke. Photocatalytic water oxidation with cobalt-containing tungstobismutates: Tuning the metal core. *Catal. Sci. Technol.*, 3:3117–3129, 2013.

[266] T. J. Chuang, C. R. Brundle, and D. W. Rice. Interpretation of the X-ray photoemission spectra of cobalt oxides and cobalt oxide surfaces. *Surface Science*, 59:413–429, 1976.

[267] B. J. Tan, Klabunde K. J., and P. M. A. Sherwood. XPS studies of solvated metal atom dispersed catalysts. evidence for layered cobalt-manganese particles on alumina and silica. *J. Am. Chem. Soc.*, 113:855–861, 1991.

[268] R. Kang, K. Chen, J. Yao, S. Shaik, and H. Chen. Probing ligand effects on O−O bond formation of Ru-catalyzed water oxidation: A computational survey. *Inorg. Chem.*, 53:7130–7136, 2014.

[269] M. Hirahara, M. Z. Ertem, M. Komi, H. Yamazaki, C. J. Cramer, and M. Yagi. Mechanisms of photoisomerization and water-oxidation catalysis of mononuclear ruthenium(II) monoaquo complexes. *Inorg. Chem.*, 52:6354–6364, 2013.

[270] L. Vigara, M. Z. Ertem, N. Planas, F. Bozoglian, N. Leidel, H. Dau, M. Haumann, L. Gagliardi, C. J. Cramer, and A. Llobet. Experimental and quantum chemical characterization of the water oxidation cycle catalysed by $[Ru^{II}(damp)(bpy)(H_2O)]^{2+}$. *Chem. Sci.*, 3:2576–2586, 2012.

[271] J. J. Concepcion, M.-K. Tsai, J. T. Muckerman, and T. J. Meyer. Mechanism of water oxidation by single-site ruthenium complex catalysts. *J. Am. Chem. Soc.*, 132:1545–1557, 2010.

[272] L.-P. Wang, Q. Wu, and T. Van Voorhis. Acid-base mechanism for ruthenium water oxidation catalysts. *Inorg. Chem.*, 49:4543–4553, 2010.

[273] S. Piccinin, A. Sartorel, G. Aquilanti, A. Goldoni, M. Bonchio, and S. Fabris. Water oxidation surface mechanisms replicated by a totally inorganic tetraruthenium-oxo molecular complex. *Proc. Natl. Acad. Sci. U.S.A.*, 110:4917–4922, 2013.

[274] Z.-L. Lang, G.-C. Yang, N.-N. Ma, S.-Z. Wen, L.-K. Yan, W. Guan, and Z.-M. Su. DFT characterization on the mechanism of water splitting catalyzed by single-Ru-substituted polyoxometalates. *Dalton Trans.*, 42:10617–10625, 2013.

[275] A. E. Kuznetsov, Y. V. Geletii, C. L. Hill, K. Morokuma, and D. G. Musaev. The role of the heteroatom (X = Si^{IV}, P^{V}, and S^{VI}) on the reactivity of $\{\gamma\text{-}[(H_2O)Ru^{III}(\mu\text{-}OH)_2Ru^{III}(H_2O)][X^{n+}W_{10}O_{36}]\}^{(8-n)-}$ with the O_2 molecule. *Theor. Chem. Acc.*, 130:197–207, 2011.

[276] A. E. Kuznetsov, Y. V. Geletii, C. L. Hill, K. Morokuma, and D. G. Musaev. Dioxygen and water activation processes on multi-Ru-substituted polyoxomet-

alates: Comparison with the "blue-dimer" water oxidation catalyst. *J. Am. Chem. Soc.*, 131:6844–6854, 2009.

[277] M. Murakami, D. Hong, T. Suenobu, S. Yamaguchi, T. Ogura, and S. Fukuzumi. Catalytic mechanism of water oxidation with single-site ruthenium-heteropolytungstate complexes. *J. Am. Chem. Soc.*, 133:11605–11613, 2011.

[278] L.-P. Wang and T. Van Voorhis. Direct-coupling O_2 bond forming a pathway in cobalt oxide water oxidation catalysts. *J. Phys. Chem. Lett.*, 2:2200–2204, 2011.

[279] X. Li and P. E. M. Siegbahn. Water oxidation mechanism for synthetic Co-oxides with small nuclearity. *J. Am. Chem. Soc.*, 135:13804–13813, 2013.

[280] G. Mattioli, P. Giannozzi, A. A. Bonapasta, and L. Guidoni. Reaction pathways for oxygen evolution promoted by cobalt catalyst. *J. Am. Chem. Soc.*, 135:15353–15363, 2013.

[281] M. Bajdich, M. García-Mota, A. Vojvodic, J. K. Nørskov, and A. T. Bell. Theoretical investigation of the activity of cobalt oxides for the electrochemical oxidation of water. *J. Am. Chem. Soc.*, 135:13521–13530, 2013.

[282] M. G. Mavros, T. Tsuchimochi, T. Kowalczyk, A. McIsaac, L.-P. Wang, and T. Van Voorhis. What can density functional theory tell us about artificial catalytic water splitting? *Inorg. Chem.*, 53:6386–6397, 2014.

[283] M. J. Frisch, G. W. Trucks, H. B. Schlegel, G. E. Scuseria, M. A. Robb, J. R. Cheeseman, G. Scalmani, V. Barone, B. Mennucci, G. A. Petersson, H. Nakatsuji, M. Caricato, X. Li, H. P. Hratchian, A. F. Izmaylov, J. Bloino, G. Zheng, J. L. Sonnenberg, M. Hada, M. Ehara, K. Toyota, R. Fukuda, J. Hasegawa, M. Ishida, T. Nakajima, Y. Honda, O. Kitao, H. Nakai, T. Vreven, J. A. Montgomery, Jr., J. E. Peralta, F. Ogliaro, M. Bearpark, J. J. Heyd, E. Brothers,

K. N. Kudin, V. N. Staroverov, R. Kobayashi, J. Normand, K. Raghavachari, A. Rendell, J. C. Burant, S. S. Iyengar, J. Tomasi, M. Cossi, N. Rega, J. M. Millam, M. Klene, J. E. Knox, J. B. Cross, V. Bakken, C. Adamo, J. Jaramillo, R. Gomperts, R. E. Stratmann, O. Yazyev, A. J. Austin, R. Cammi, C. Pomelli, J. W. Ochterski, R. L. Martin, K. Morokuma, V. G. Zakrzewski, G. A. Voth, P. Salvador, J. J. Dannenberg, S. Dapprich, A. D. Daniels, Ö. Farkas, J. B. Foresman, J. V. Ortiz, J. Cioslowski, and D. J. Fox. Gaussian-09 Revision A.1. Gaussian Inc. Wallingford CT 2009.

[284] C. Lee, W. Yang, and R. G. Parr. Development of the Colle-Salvetti correlation-energy formula into a functional of the electron density. *Phys. Rev. B*, 37:785–789, 1988.

[285] A. D. Becke. Densityfunctional thermochemistry. III. The role of exact exchange. *J. Chem. Phys.*, 98:5648–5652, 1993.

[286] P. J. Stephens, F. J. Delvin, C. F. Chabalowski, and M. J. Frisch. *Ab initio* calculation of vibrational absorption and circular dichroism spectra using density functional force fields. *J. Phys. Chem.*, 98:11623–11627, 1994.

[287] P. J. Hay and W. R. Wadt. *Ab initio* effective core potentials for molecular calculations. potentials for the transition metal atosm Sc to Hg. *J. Chem. Phys.*, 82:270–283, 1985.

[288] M. M. Francl, W. J. Pietro, W. J. Hehre, J. S. Binkley, M. S. Gordon, D. J. DeFrees, and J. A. Pople. Self-consistent molecular orbital methods. XXIII. A polarization-type basis set for second-row elements. *J. Chem. Phys.*, 77:3654–3665, 1982.

[289] W. J. Hehre, R. Ditchfield, and J. A. Pople. Self-consistent molecular orbital methods. XII. Further extensions of Gaussian-type basis set for use in molecular orbital studies of organic molecules. *J. Chem. Phys.*, 56:2257–2261, 1972.

[290] P. C. Hariharan and J. A. Pople. The influence of polarization functions on molecular orbital hydrogenation energies. *Theoret. Chim. Acta*, 28:213–222, 1973.

[291] E. Cancès, B. Mennucci, and J. Tomasi. A new integral equation formalism for the polarizable continuum model: Theoretical background and applications to isotropic and anisotropic dielectrics. *J. Chem. Phys.*, 107:3032–3041, 1997.

[292] J Li, C. L. Fisher, J. L. Chen, D. Bashford, and L. Noodleman. Calculation of redox potentials and pK_a values of hydrated transition metal cations by a combined density functional and continuum dielectric theory. *Inorg. Chem.*, 35:4694–4702, 1996.

[293] J. R. Buchwald, S. Kal, and P. H. Dinolfo. Determinationn of the mechanism of electrocatalytic water oxidation by a dimanganese tetrakis-Schiff base complex: Comparison of density functional theory calculations with experiment. *J. Phys. Chem. C*, 118:25869–25877, 2014.

[294] H. Lv, J. Song, Y. V. Geletii, J. W. Vickers, J. M. Sumliner, D. G. Musaev, P. Kögerler, P. F. Zhuk, J. Bacsa, G. Zhu, and C. L. Hill. An exceptionally fast homogeneous carbon-free cobalt-based water oxidation catalyst. *J. Am. Chem. Soc.*, 136:9268–9271, 2014.

[295] M. Z. Ertem and C. J. Cramer. Quantum chemical characterization of the mechanism of a supported cobalt-based water oxidation catalyst. *Dalton Trans.*, 41:12213–12219, 2012.

[296] W. Lai, R. Cao, G. Dong, S. Shaik, J. Yao, and H. Chen. Why is cobalt the best transition metal in transition-metal hangman corroles for O−O bond formation during water oxidation. *J. Phys. Chem. Lett.*, 3:2315–2319, 2012.

[297] H. Lei, A. Han, F. Li, M. Zhang, Y. Han, P. Du, W. Lai, and R. Cao. Electrochemical, spectroscopic and theoretical studies of a simple bifunctional cobalt

corrole catalyst for oxygen evolution and hydrogen production. *Phys. Chem. Chem. Phys.*, 16:1883–1893, 2014.

[298] D. Barats-Damatov, L. J. W. Shimon, L. Weiner, R. E. Schreiber, P. Jiménez-Lozano, J. M. Poblet, C. de Graaf, and R. Neumann. Dicobalt-μ-oxo polyoxometalate compound, $[(\alpha\text{-}P_2W_{17}O_{61}Co)_2O]^{14-}$: A potent species for water oxidation, C−H bond activation, and oxygen transfer. *Inorg. Chem.*, 53:1779–1787, 2014.

[299] X. López, I. A. Weinstock, C. Bo, J. P. Sarasa, and J. M. Poblet. Structural evolution in polyoxometalates: A DFT study of dimerization processes in Lindqvist and Keggin cluster anions. *Inorg. Chem.*, 45:6467–6473, 2006.

[300] P. Jiménez-Lozano, I. D. Ivanchikova, O. A. Kholdeeva, J. M. Poblet, and J. J. Carbó. Alkene oxidation by Ti-containing polyoxometalates. Unambiguous characterization of the role of the protonation state. *Chem. Commun.*, 48:9266–9268, 2012.

[301] P. Jiménez-Lozano, J. J. Carbó, A. Chaumont, J. M. Poblet, A. Rodríguez-Fortea, and G. Wipff. Nature of Zr-monosubstituted monomeric and dimeric polyoxometalates in water solution at different pH conditions: Static density functional theory calculations and dynamic simulations. *Inorg. Chem.*, 53:778–786, 2014.

[302] Y. Jiang, F. Li, B. Zhang, X. Li, X. Wang, F. Huang, and L. Sun. Promoting the activity of catalysts for the oxidation of water with bridged dinuclear ruthenium complexes. *Angew. Chem. Int. Ed.*, 52:3398–3401, 2013.

UNIVERSITAT ROVIRA I VIRGILI
HIGH NUCLEARITY POLYOXOMETALATES AS WATER OXIDATION CATALYSTS: FROM EXPERIMENTS TO THEORY
Joaquín Soriano López

UNIVERSITAT ROVIRA I VIRGILI
HIGH NUCLEARITY POLYOXOMETALATES AS WATER OXIDATION CATALYSTS: FROM EXPERIMENTS TO THEORY
Joaquín Soriano López